



Durham E-Theses

Optical sensing of organic vapours using langmuir-blodgett films

Wilde, Jason N.

How to cite:

Wilde, Jason N. (1998) *Optical sensing of organic vapours using langmuir-blodgett films*, Durham theses, Durham University. Available at Durham E-Theses Online: <http://etheses.dur.ac.uk/4763/>

Use policy

The full-text may be used and/or reproduced, and given to third parties in any format or medium, without prior permission or charge, for personal research or study, educational, or not-for-profit purposes provided that:

- a full bibliographic reference is made to the original source
- a [link](#) is made to the metadata record in Durham E-Theses
- the full-text is not changed in any way

The full-text must not be sold in any format or medium without the formal permission of the copyright holders.

Please consult the [full Durham E-Theses policy](#) for further details.

**Optical Sensing of Organic Vapours Using Langmuir-
Blodgett Films**

by

Jason N. Wilde B.Eng. (Hons)

Graduate Society

A Thesis submitted in partial fulfilment
of the requirements for the degree of Ph.D.

Centre for Molecular Electronics

The copyright of this thesis rests
with the author. No quotation
from it should be published
without the written consent of the
author and information derived
from it should be acknowledged.

School of Engineering

University of Durham

March 1998



13 JAN 1999

Copyright © 1998 by J.N. Wilde

The copyright of this thesis rests with the author. No quotation from it should be published without his prior written consent and information derived from it should be acknowledged.

Declaration

I hereby declare that the work carried out in this thesis has not been previously submitted for any degree and is not currently being submitted in candidature for any other degree.

Signed.....



Candidate

The work in this thesis was carried out by the candidate.

Signed.....

Director of Studies

Signed.....



Candidate

Dedication

This thesis is dedicated to my parents

Acknowledgements

There are a great number of people I wish to thank for their help and support throughout my PhD. Firstly I would like to thank Professor Mike Petty for the time and effort he has invested throughout this project; Neotronics Limited for their kind support, both financial and intellectual; and the other members of the Molecular Electronics group (especially Mary and Chris), all of whom have made the last three years so enjoyable!

I would like to thank Dr J. Nagel and Dr L. Valli whose materials have formed the basis for this project; Dr A. Beeby and Allison Wigman for producing such fantastic Brewster Angle Microscopy images; and Lesley, Ian, Julie, Harry, Kay and John for all their help and assistance.

Finally, I must say 'cheers' to all my friends who, at one time or another, have dragged me out kicking and screaming for a pint of beer, Peter Davies, Joanna Kennady, Phil Thomas, Anna, Dave Lee, Daryl, Gail Radcliffe, Jo Garland, Caroline Smith, Rène Rodgers, Nic., Ken Thomson, Colin, Sanjay, Debbie Hales, Sarah Ruff, Steve Allan, Louise, Fraser Walker. A special mention goes to Mandy who has put up with me over the last few months whilst writing this thesis!

Abstract

This thesis describes hydrocarbon vapour sensing using Langmuir-Blodgett films prepared from: a co-ordination polymer; substituted phthalocyanines containing copper and zinc as the central metal ions; and a polysiloxane. The physical and chemical properties of the co-ordination polymer, 5,5'-methylenebis (N-hexadecylsalicylideneamine), at the air water interface were investigated using Brewster angle microscopy and surface pressure versus area measurements. Langmuir-Blodgett films were built-up on a variety of substrates. The addition of copper acetate to the subphase caused a change in both the physical and optical properties of the Langmuir-Blodgett layers. Film thickness data suggest that a true monolayer (thickness *ca* 2 nm) is only formed under these conditions. The multilayer films were studied using X-ray diffraction, UV/Visible spectroscopy, ellipsometry, surface plasmon resonance, surface profiling and electron spin resonance.

The response of each film when exposed to, benzene, toluene, ethanol and water vapours were recorded. Two optical systems were used, both based on surface plasmon resonance. The first incorporated a silicon photodiode to record the intensity of the reflected light. The second was similar to that of surface plasmon microscopy, using a charge coupled device camera to monitor the reflected light intensity from the Langmuir-Blodgett film/metal interface. The co-ordination polymer was found to be most sensitive to benzene and could reliably detect concentrations of this vapour down to 100 vapour parts per million. Data obtained when the co-ordination polymer was exposed to benzene and water vapour (using the latter system) were presented to a neural network for recognition.

Contents

Chapter One	1
Introduction	1
References	5
Chapter Two	6
Gas Sensing Review: Materials and Techniques	6
2.0 Preface	6
2.1 Materials	6
2.1.1 Organic materials	6
(a) Porphyrins	7
(b) Phthalocyanines	7
(c) Polymers	10
2.1.2 Inorganic materials	11
(a) Metal oxides	11
(b) Catalytic metals	13
2.2 Deposition methods	14
2.2.1 Langmuir-Blodgett films	14
2.2.2 Thermal evaporation	16
2.2.3 Spin-coating	17
2.3 Optical gas sensing devices	18
2.3.1 Surface plasmon resonance	18
2.3.2 Fibre optical devices	19

2.3.3 Infra-red absorption devices	20
2.3.4 Chemiluminescence devices	20
2.4 Electrochemical gas sensing devices	21
2.4.1 Potentiometric sensors	21
2.4.2 Amperometric sensors	22
2.4.3 Conductimetric sensors	23
2.5 Mass gas sensing devices	23
2.5.1 Piezoelectric sensors	24
2.5.2 Surface acoustic wave sensors	24
2.6 Thermal gas sensing devices	26
2.6.1 Pyroelectric sensors	27
2.6.2 Catalytic sensors	27
2.7 Gas sensor arrays	28
2.8 Summary	30
References	31
Chapter Three	38
Materials	38
3.0 Preface	38
3.1 Phthalocyanines	38
3.1.1 Chemical structure	39
3.1.2 Thermal and chemical stability	40
3.1.3 LB film deposition	41
3.1.4 Optical properties	42
(a) UV/Visible spectroscopy	42

(b) Surface plasmon resonance _____	42
3.2 Polysiloxanes _____	43
3.2.1 Chemical structure _____	44
3.2.2 Thermal and chemical stability _____	45
3.2.3 LB film deposition _____	46
3.2.4 Optical properties _____	47
(a) UV/Visible spectroscopy _____	47
(b) Surface plasmon resonance _____	47
3.3 Co-ordination polymers _____	48
3.3.1 Chemical structure _____	48
3.3.2 Thermal and chemical stability _____	49
3.3.3 LB deposition _____	50
3.3.4 Optical properties _____	51
(a) UV/Visible spectroscopy _____	51
3.4 Conclusion _____	51
References _____	52
Chapter Four _____	54
Experimental Methods _____	54
4.0 Preface _____	54
4.1 Langmuir-Blodgett technique _____	54
4.2 Optical and structural characterisation _____	57
4.2.1 Surface plasmon resonance _____	57
4.2.2 Ellipsometry _____	62
4.2.3 Low angle X-ray diffraction _____	64

4.2.4 Electron spin resonance	71
4.2.5 Brewster angle microscopy	74
4.2.6 UV/Visible spectroscopy	76
4.2.7 Surface profiling	76
4.3 Data processing	77
4.3.1 Neural networks	77
References	82
Chapter Five	84
Vapour Sensing Methods	84
5.0 Preface	84
5.1 Design of vapour generation system	84
5.2 Calibration of vapour generation system	87
5.2.1 Clausius-Clapeyron data for vapours	87
5.3 Gas sensing using surface plasmon resonance	88
5.3.1 Photodiode detector	88
(a) Design of gas sensing system	89
5.4 CCD camera detector	90
References	92
Chapter Six	93
Results and Discussion: Film Characterisation	93
6.0 Preface	93
6.1 Langmuir layer characterisation of MBSH	93
6.1.1 Brewster angle microscopy	94

6.1.2 Langmuir-Blodgett technique	94
(a) Surface pressure versus area isotherms	94
(b) Langmuir-Blodgett deposition	95
6.2 Structural characterisation of MBSH	96
6.2.1 Surface plasmon resonance	96
6.2.2 Ellipsometry	97
6.2.3 UV/Visible spectroscopy	98
6.2.4 Alpha-step measurements	98
6.2.5 Low-angle X-ray diffraction	100
6.2.6 Structural orientation of MBSH/TA	102
6.3 Langmuir layer characterisation of poly(CuMBSH)	103
6.3.1 Complex formation	103
6.3.2 Brewster angle microscopy	103
6.3.3 Langmuir-Blodgett technique	104
(a) Surface pressure versus area isotherms	104
(b) Langmuir-Blodgett deposition	105
6.4 Structural characterisation of poly(CuMBSH)	105
6.4.1 Surface plasmon resonance	105
6.4.2 Ellipsometry	107
6.4.3 UV/Visible spectroscopy	108
6.4.4 Alpha-step measurements	108
6.4.5 Low angle X-ray diffraction	109
6.4.6 Electron spin resonance	110
6.4.7 Structural orientation of poly(CuMBSH)	112

6.5 Summary	113
References	115
Chapter Seven	116
Results and Discussion: Vapour Sensing	116
7.0 Preface	116
7.1 Comparison of materials to saturated vapour concentrations	116
7.2 Background response of silver layer	117
7.3 Comparison of materials to controlled vapour concentrations	119
7.3.1 Copper 5,5'-methylenebis (N-hexadecylsalicylideneamine): effect of film thickness	120
7.3.2 Copper 5,5'-methylenebis (N-hexadecylsalicylideneamine): effect of different vapours	122
7.3.3 Copper phthalocyanine	124
7.3.4 Polysiloxane	126
7.3.5 Mathematical modelling of response characteristics	128
7.4 The effect of water vapour	130
7.5 Vapour sensing mechanism in LB films	132
7.5.1 Changes in the SPR curve of poly(CuMBSH)	132
7.5.2 Proposed sensing mechanism	133
7.6 Summary	134
References	136

Chapter Eight	137
Results and Discussion: Pattern Recognition Techniques	137
8.0 Preface	137
8.1 Zinc phthalocyanine exposed to NO _x	137
8.2 Polysiloxane exposed to toluene vapour	139
8.3 Poly(CuMBSH) exposed to benzene and water vapour using a neural network	141
8.4 Design of neural network	141
8.4.2 Data capture and processing	142
8.4.3 Testing the neural network	143
8.5 Summary	146
References	148
Chapter Nine	149
Conclusions and Suggestions for Future Work	149
9.1 Conclusions	149
9.2 Suggestions for further work	151
References	154
Appendix A	155
Computer Programs	155
Appendix B	163
Publications	163

Chapter One

Introduction

Over the last forty years the research dedicated to the development of reliable gas sensors has significantly increased. There is now an increased need for low power, sensitive and selective gas sensors. This is partially a result of increased levels of pollution, especially from environmentally dangerous gases such as SO₂, NO_x, and health threatening vapours such as toluene and benzene. Many industrial processes require the use of chemicals, of which there are about 100,000 on the European Inventory of Existing Chemical Substances. Exposure to some of these substances may pose a risk to the health of the workers involved. In the UK, EU and the USA, regulations and directives relating to the health and safety of workers outline ways in which these health risks may be assessed and exposure limited.^{1,2}

Gas	8 Hour Exposure Limit [ppm]²	15 Minutes Exposure Limit [ppm]
benzene	5	N/A
toluene	50	150
ethanol	1000	N/A

Table 1.1: Safe exposure limits in parts per million (ppm) for the toxic gases used in this work. (Source: EH40/97 Occupational Exposure Limits 1997).

For example, the Health and Safety Executive in the UK recommends that the maximum long term (8 hours continuous exposure) and short term (15 minutes exposure) exposure limits for benzene, toluene and ethanol vapours are as shown in table 1.1. Currently new legislation is being drafted in the USA further reducing the legal limits of benzene exposure. This new law states that no employee may enter a room with airborne levels of benzene vapour above 100 parts per million. The Agency for Toxic Substances and Disease Registry in the USA note that long-term low-level exposure (200 ppm for over 1 year) to toluene can cause damage to kidneys, memory loss and nausea. High levels of toluene (600 ppm for over 1 year) can cause permanent damage to the brain, and continuous exposure may even result in death. At present there are no portable devices that can reliably detect these low concentrations of aromatic hydrocarbons. Gas sensors have also been developed to monitor the freshness of food stuffs, such as canned meats, vegetables and fruits. A further application is the use of gas sensor arrays in the brewing industry to ensure consistency and quality in the flavour of beers and whiskies.

Practical difficulties encountered with many sensors include poor sensitivity and selectivity to low gas concentrations, and sensor poisoning when exposed to high concentrations. Fluctuations in the operating temperature and humidity level can also affect the response of a sensor. One approach to overcome these problems is to use an array of gas sensing devices. By coating each sensing element with a different material, the response to a particular gas or vapour will vary over the array.³ This pattern of responses can then be used in conjunction with pattern recognition software or a neural

network to produce a sensing system that eliminates the problems due to temperature and humidity.

In this work, a gas sensor has been fabricated exploiting the phenomenon of surface plasmon resonance (SPR). Over recent years, the interest in SPR gas sensing has increased⁴ with much of the research focused on the sensing of NO_x.⁵ One advantage of this approach is that optical systems are low power techniques, ideal for use in the most hazardous of environments. The gas sensitive materials used in this work are ultra thin organic films deposited by the Langmuir-Blodgett (LB) technique.

A summary of existing research in the field of chemical sensing can be found in Chapter Two. In the first part, the various materials that have been used for gas sensing are described. This is followed by a review of device structures and the optical parameters measured in the sensing process.

Chapter Three introduces the organic materials used: polysiloxane (AMCR23), substituted phthalocyanines with copper and zinc as the central metals (CuPcBC and ZnPcBC), and a co-ordination polymer (poly(CuMBSH)). A discussion of the basic physical properties of the materials is presented. Detailed descriptions of the experimental techniques used in this work are contained in Chapter Four. This also includes the material characterisation and deposition processes. Chapter Five contains the optical theory for surface plasmon resonance and the design and operation of the gas sensing systems.

The results presented in Chapter Six were obtained from a detailed investigation of the properties of the co-ordination polymer in both its monomer and polymer forms. Chapters Seven and Eight present the results obtained from the gas sensing systems, with a discussion of their implications. The former chapter is concerned with the response from an SPR gas sensing system using a silicon photodiode as detector, whereas the latter examines the response of an SPR system using a charge coupled device (CCD) camera as detector. LB films of poly(CuMBSH) were exposed to concentrations of benzene and water vapour and the results were presented to a neural network for analysis. Conclusions from the whole thesis, including suggestions for further work, can be found in Chapter Nine.

References

- 1 P.T. Walsh, *Measurement and Control*, 29, **1996**, 5-12.
- 2 Health and Safety Executive EH40/97, “**Occupational Exposure Limits**”, *HSE Books*, Suffolk (UK), **1997**.
- 3 P.S. Barker, J.R. Chen, N.E. Agbor, A.P. Monkman, P. Mars, M.C. Petty, *Sensors and Actuators B*, 17, **1994**, 143-147.
- 4 C. Nylander, B. Liedberg, T. Lind, *Sensors and Actuators B*, 3, **1982/3**, 79-88.
- 5 J.P. LLOYD, C. Pearson, M.C. Petty, *Thin Solid Films*, 160, **1988**, 431-443.

Chapter Two

Gas Sensing Review: Materials and Techniques

2.0 Preface

There are two distinct elements that make up a gas sensing system, the gas sensing material and the system within which it is incorporated. The gas sensing materials can be subdivided into two main groups: inorganic compounds, such as metal oxides; and organic compounds, such as phthalocyanines and polymers. This chapter reviews the different materials that can be used and the structures to which they can be applied.

2.1 Materials

2.1.1 Organic materials

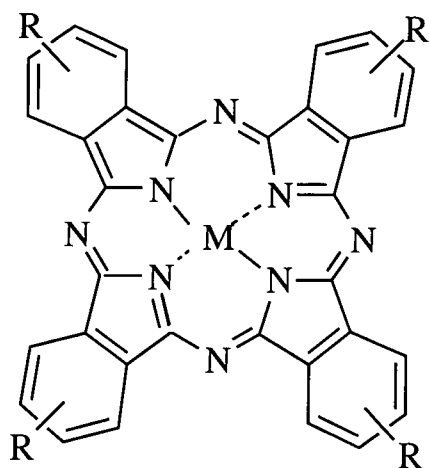
Over recent years organic materials have been widely used for gas sensing. This is due to their low temperature (room temperature) operation characteristics; their high sensitivity to many different gases; their ability to be deposited as ultra thin films (molecular dimensions); and their increased commercial availability. One major advantage of organic compounds is that they are easy to modify chemically, to enhance both the sensitivity and selectivity. Three major groups of organics have been widely studied: porphyrins, phthalocyanines and polymers. Each of these is discussed in turn.

(a) Porphyrins

Porphyrins are synthetic compounds very similar to some biological gas sensing molecules such as haemin and chlorophyll.^{1,2} They comprise a hydrocarbon (benzene) ring structure with a central metal ion and substituted organic groups on the periphery. Porphyrins have not been as widely used in sensing systems as other organics, partly because of their lower melting points (*ca* 200°C).³ On exposure to certain gases (electron-accepting or donating) there is a relatively large change in their electrical conductivity. Studies undertaken on these materials have shown that the sensitivity is dependent upon the electronegativity of the central metal ion.⁴ It has also been demonstrated that the response of porphyrins as gas sensing materials is dependent upon the thickness and the peripheral substituents of the porphyrin ring.⁴ Langmuir-Blodgett films (39 layers) of symmetrically substituted cobalt porphyrin have been exposed to 5 ppm NO₂. Changes in the film due to the gas were monitored using electrical conductivity changes. The response and recovery times were found to be 10 mins and 1 hour respectively.⁵

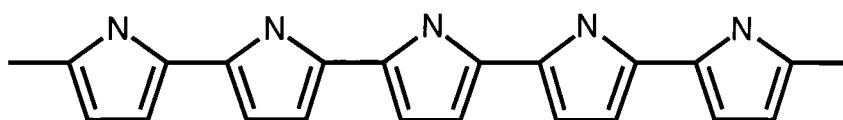
(b) Phthalocyanines

Phthalocyanines are similar to porphyrins and are both thermally stable (up to 200°C) and chemically stable (resistant to weak acids, bleaches and stable under UV illumination) enabling them to be used in a variety of environments.⁶ Figure 2.1 shows the structure of a typical phthalocyanine molecule. The central ion can either be two ions of hydrogen (metal-free phthalocyanine, represented by H₂), metals, such as Cu²⁺, Zn²⁺, Ni²⁺, or other suitable metals of oxidation states 0 to 6 (represented by M). The R,

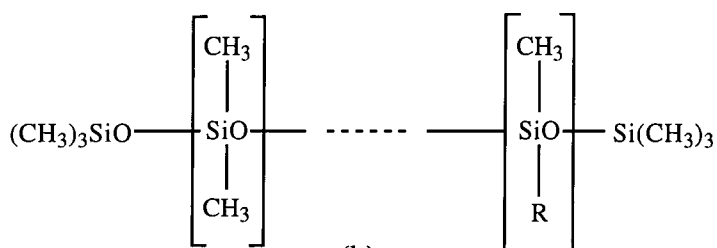


M : Cu ; Ni ; Zn

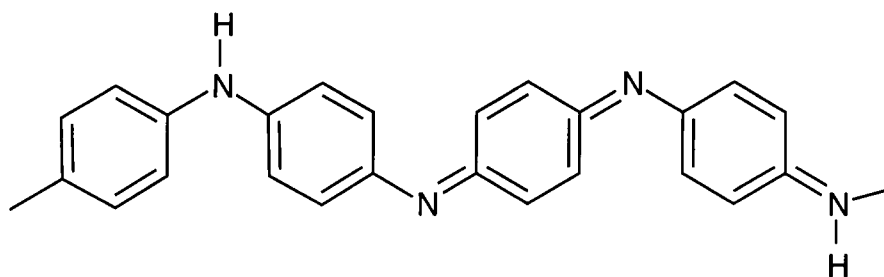
Figure 2.1: Structure of substituted phthalocyanine (R denotes the position of the substituent) with either Cu, Ni, Zn as the central metal.



(a)



(b)

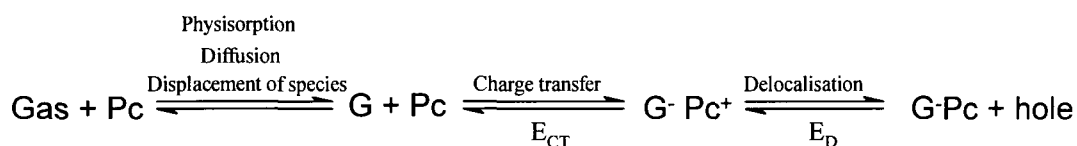


(c)

Figure 2.2: Structures showing (a) a section of the polypyrrole backbone (b) part of a polysiloxane backbone, R denotes position of substituent (c) part of a polyaniline backbone (PANi).

in figure 2.1, denotes the substituted organic side chain. Relatively long side chains (C_8 to C_{18}) are undesirable for good quality LB films. This is probably due to their tendency to overlap and interact.⁷ In contrast short side chains (C_4 to C_7) lead to highly anisotropic multilayers. By varying the side chains or the central metal the response to a specific gas can be changed.

It has been suggested that the gas sensing mechanism for phthalocyanine films is a three stage process.⁸ The first step is due to surface adsorption of the gas molecules (this is a fast effect). The second is a slow diffusion of the gas molecules into the bulk of the film. This process can be speeded up by elevating the sensing temperature or by reducing the film thickness. The third relies on the creation/removal of mobile charge carriers to enhance/reduce the conductivity. This process can be represented below for phthalocyanines with p-type semiconductor characteristics, where G is a molecule of the gas/vapour interacting with the phthalocyanine (Pc) film, G^- is the ionised gas molecule, E_{CT} is the energy involved in the charge transfer between the two species and E_D is the energy required to free the charge (ie, create a mobile hole).¹¹



[2.1]

The process involves the absorption of the gas molecule (G) into the bulk of the phthalocyanine film. A charge transfer then occurs between the phthalocyanine molecules, and the absorbed gas molecule (oxidation).

Electrical conductivities of phthalocyanines, deposited by a variety of techniques, have been shown to be sensitive to gases such as oxides of nitrogen, NH_3 , O_2 , I_2 and some aromatic hydrocarbons (such as toluene).⁹⁻¹² The conductivities of these systems can change over several orders of magnitude for low concentrations (with sensitivities down to the parts per billion (ppb) level).⁹ Although phthalocyanines operate well at low temperatures, raising the temperature of the sensing element to between 100 and 160°C greatly improves their response characteristics.⁹ However, this does increase the power consumption of the sensing system and may limit its portability.

The optical properties (refractive index, film thickness) of phthalocyanines have also been shown to be sensitive to a variety of gases, such as NO_2 ^{13,14} and some aromatic hydrocarbons.¹⁵ Surface plasmon resonance has often been used to detect these changes (a description of this technique is included in section 2.3.1). The advantage of optical techniques is that they are low power, and most research has focused on ultra thin phthalocyanine sensitive layers operating at room temperature.

Phthalocyanine films can be deposited in a variety of ways: vacuum sublimation,^{2,9} spin-coating or the Langmuir-Blodgett (LB) technique. The last method is an elegant means of accurately depositing ultra-thin well-ordered films.^{12,16-18} Thin films have the advantage of a high surface to volume ratio (ie, large surface area to small film thickness) which allows quicker diffusion of gas molecules into the bulk.¹⁹ The reduction in film thickness also eliminates the need for the sensor to operate at elevated

temperatures (above room temperature). A more detailed discussion of the chemical and physical properties of phthalocyanines will be presented in Chapter Three.

(c) Polymers

Organic conductive polymers are a relatively new class of materials that have attracted considerable interest for gas sensing. Materials such as polypyrrole,²⁰ polysiloxane²¹ and polyaniline^{4,22} (see figure 2.2) have all been investigated as active gas sensing layers. The electrical conductivity can be affected by exposure to various organic and inorganic gases.¹⁹ A large number of polymeric materials are commercially available. Polymers offer considerable potential to be chemically modified or doped, to optimise the selectivity and sensitivity. These materials have been exploited in a variety of sensing systems: conductivity devices,²³ quartz microbalance oscillators,^{24,25} bulk and surface acoustic waves;²⁶ and optical techniques,^{27,28} including surface plasmon resonance.²⁹

A common method of obtaining a polymeric thin film is by electrochemical growth across electrodes,^{3,12} though films have also been deposited using spin-coating,³⁰ thermal evaporation³¹ and the LB technique.³² The last method has been used to deposit polymers formed at the air/water interface.^{26,33} The synthesis and structure of these materials will be discussed in more detail in Chapter Three.

2.1.2 Inorganic materials

Early research into gas and vapour sensitive materials concentrated on inorganic materials, such as metal oxides. This work has proved successful, with a number of systems commercially available to detect NO_2 , CH_4 , NH_3 , Cl_2 and other gases. The most commonly used materials are the semiconductor oxides and catalytic transition elements.

(a) Metal oxides

It has long been known that the absorption of a gas or vapour onto the surface of a semiconducting material generates or modifies existing surface states, thus influencing the electrical properties (eg conductivity) of the sensing material.³⁴ Metal oxide films such as ZnO ³⁵, Fe_2O_3 ³⁶ and SnO_2 ³⁷ have been used as gas sensing layers.

Practical sensors are most commonly based on changes in the surface conductivity of thin films, where gases adsorb at internal grain surfaces. Metal oxide films have been doped with a number of materials: Pt for CO detection; Al for NO_2 detection; Pd for chlorinated and amino volatile organic compounds (VOC); and SO_2 annealing has been used to improve response to aromatic VOCs.³⁸ Figure 2.3 shows a band diagram illustrating the interaction between gas molecules and a semiconductor surface.³⁹ There is a limited density of electron donors (for absorbed hydrogen) or acceptors (for absorbed oxygen) bound to the surface of a wide band gap semiconductor, such as SnO_2 or ZnO . These are in the form of surface states that can exchange charge with the interior of the semiconductor. The position (in energy) of the surface state relative to the

Fermi level of the semiconductor depends on its affinity to electrons. If its affinity is low, it will lie below the Fermi level and donate electrons (reducing agent) to the space charge region. If it is an acceptor, it will be positioned above the Fermi level and extract electrons (oxidising agent) from the space charge region. By changing the surface concentration of the donors/acceptors the conductivity of the material is modulated.

Metal oxides have been used to detect a number of gases and vapours such as aromatic hydrocarbons (toluene and benzene),³⁵ natural gases, petrol vapours,³⁶ CO and NO₂.³⁷ Research has now progressed away from single element metal oxide sensors to sensor arrays (see section 2.7).

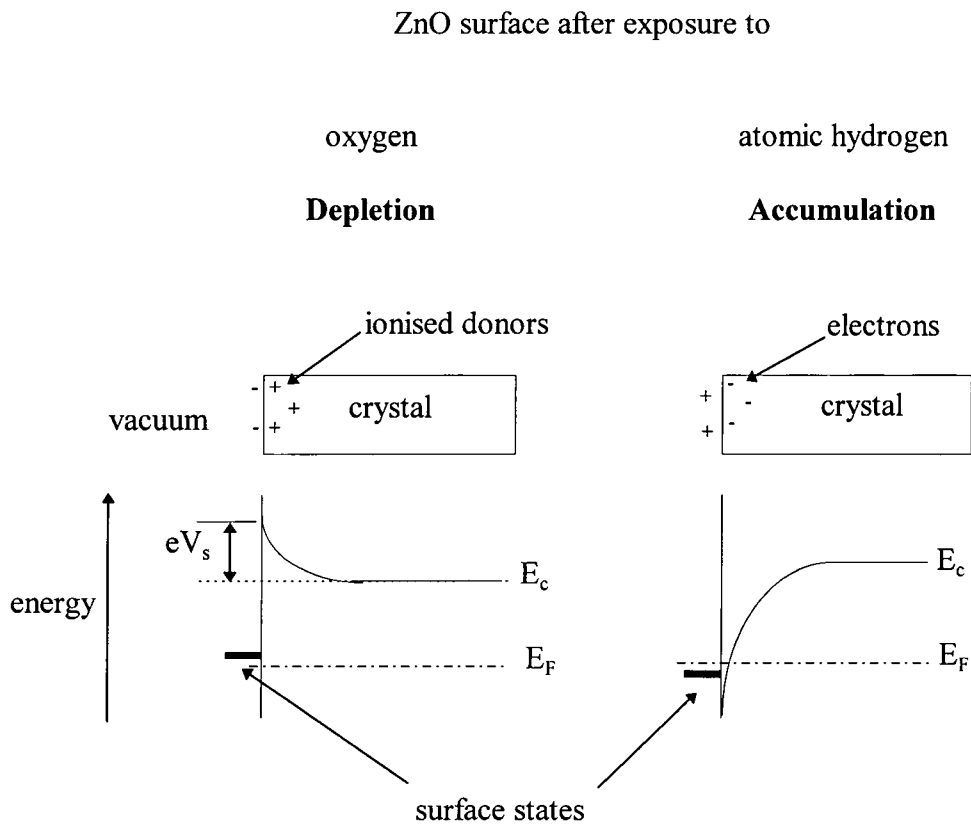


Figure 2.3: Space-charge modulation by absorption in a semiconducting n-type oxide sensor [reproduced from reference 39].

These consist of a number of discrete sensing elements. It is hoped that increasing the number of sensing elements will add some selectivity and reduce the background drift exhibited by some metal oxide sensors.^{37,38,40,41}

(b) Catalytic metals

The functions of catalytic metals in metal-oxide-semiconductive sensors can be divided into three distinct roles. The first is that the metal dissociates the incoming gas (eg, hydrogen) through its catalytic action; the second is that it transports the atoms to the metal/oxide (usually Si) interface; and finally it absorbs the atoms (at the metal/oxide boundary) as detectable dipoles.⁴² The dipole layer that is formed will be detected by a change in the semiconductor's surface field, which will constitute a change in the metal work function.

Gas sensitive devices utilising catalytic metals have been used, in many instances, as gates on field effect devices such as MOSFETs (Metal Oxide Semiconductor Field Effect Transistors). The first commercial device appeared 10 years ago and was a leakage detector based on the hydrogen sensitive palladium gate field effect transistor.⁴³ Amongst the metallic elements that have been used are palladium,⁴⁴ gold,⁴⁵ platinum⁴⁶ and nickel.⁴⁷

There are a number of systems that have been investigated using an array of sensors made from catalytic metals. The basic idea is that the sensors are trained (via a neural network, see section 2.7) to recognise a pattern unique (sensor response) to each

gas/vapour. The systems use a number of different sensors, fabricated from either different metals or different metal thicknesses. For example, Lunderström *et al*, used conductivity changes in an eight sensor array of iridium (Ir), palladium (Pd) and platinum (Pt) of different thicknesses to detect concentrations of methanol, ethanol, propan-1-ol and propan-2-ol.^{48,49} This system was able to detect and discriminate between the four gases down to about 100 parts per million (ppm). The system itself had to be operated at 800°C to catalytically decompose the hydrocarbons (usually only 300°C is required). This high temperature is a problem and limits the potential application in portable devices.

2.2 Deposition methods

There are a number of techniques used to deposit organic thin films on device structures. Three of the most common methods are: Langmuir-Blodgett deposition; thermal evaporation and spin coating. An overview of these techniques is given below.

2.2.1 Langmuir-Blodgett films

Langmuir-Blodgett (LB) films derive their name from Irving Langmuir and Katherine Blodgett (the principle workers in the field). LB films are highly ordered ultra thin monolayers and multilayers of organic compounds deposited onto solid substrates. The LB technique usually uses materials that consist of amphiphilic long chain molecules (the 'classic' compounds are fatty acids and fatty acid salts).

LB films are produced by first taking a small quantity of material dissolved in a suitable solvent (eg chloroform, toluene, ethyl acetate etc...), and applying it to a clean subphase (usually water) surface. As the solvent evaporates from the floating film, the material spreads out to form a monomolecular layer. Slowly compressing the film causes the molecules to undergo a transition from the expanded (gas) phase, through a liquid-like region to an ordered condensed phase. The different phases exhibited on the subphase surface are shown in figure 2.4 for an idealised long chain organic molecule; this type of plot is known as a pressure versus area isotherm. From the isotherm plot, the area per molecule (a) can be calculated by extrapolating from the condensed phase to the line of zero pressure (total film area = A), provided the concentration (C), volume (V) and molecular weight (M) of the molecule are known.⁵⁰

$$a = \frac{AM}{CN_A V} \quad [2.2]$$

By comparing this value with those estimated by space filling models, it is possible to speculate on the orientation of the molecule on the subphase surface.

The compressed monolayer (ie, in the condensed phase) can then be transferred to a solid substrate; this involves moving the substrate through the air/subphase interface. The resultant films can take three different forms, depending on how the substrate moves through the subphase surface and on the monolayer-substrate and monolayer-monomolayer interactions. Figure 2.5 details the different structures; Y-type deposition refers to the situation in which a substrate picks up material from the subphase on every downstroke and upstroke; X-type deposition is when the substrate only picks up on the downstroke; and Z-type deposition is when the substrate only picks up on the upstroke.

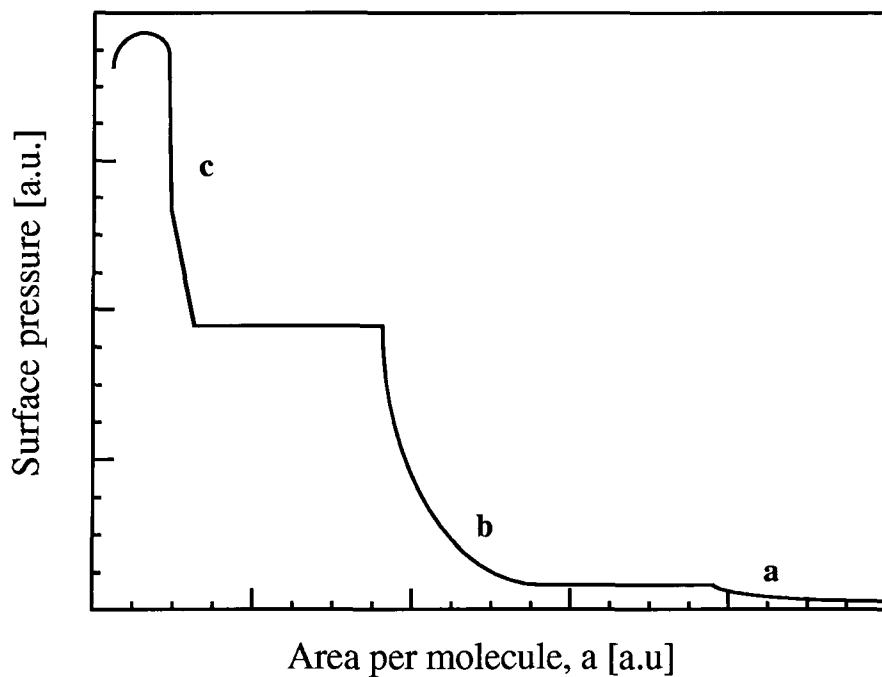


Figure 2.4: Idealised surface pressure versus area per molecule isotherm for a long chain organic compound **a**) is the gaseous phase **b**) represents the liquid phase **c**) is the condensed (solid) phases.

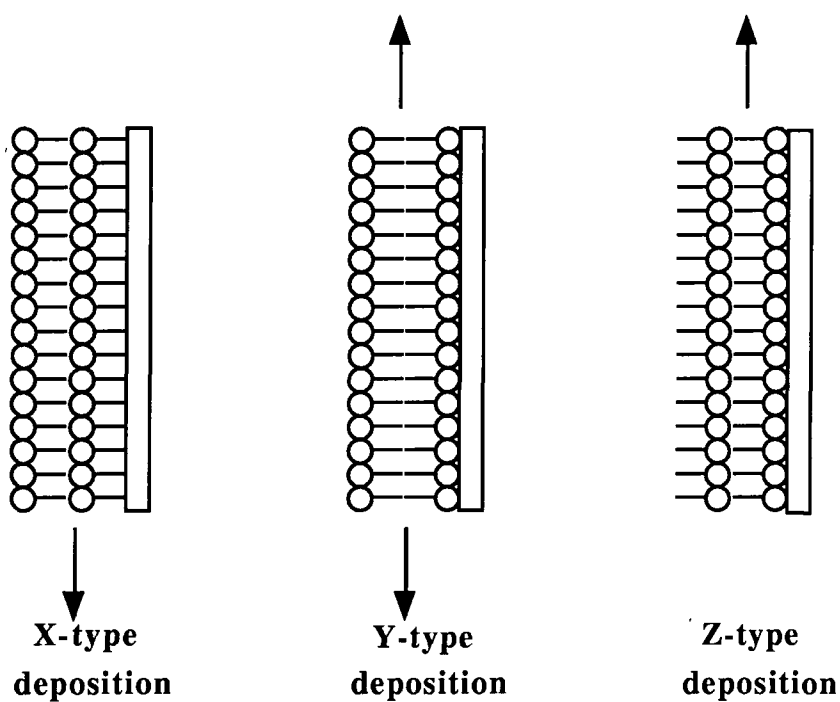


Figure 2.5: Langmuir-Blodgett deposition methods and structures, arrows indicate the direction in which the film is transferred.

A more detailed description of the Langmuir-Blodgett technique can be found in reference 50.

Since the reaction between a gas/vapour and a film is believed to be a surface phenomenon, layers fabricated from the LB technique should produce fast response and recovery times. The LB technique is also a room temperature process. This avoids any damage to the film produced from techniques that use high energy bombardment of substrates (eg, thermal evaporation).⁵¹ LB films have been used in a number of systems as the gas sensitive layers. Common materials are phthalocyanines^{15,22,52,53} and polysiloxanes.^{13,21,28}

2.2.2 Thermal evaporation

The deposition of thin films by thermal evaporation usually takes place at reduced pressure, typically 10^{-4} mbar or lower. This is a non-equilibrium process, involving a series of steps: evaporation; transfer of material to the substrate; condensation of material on the substrate; and nucleation and film growth on the substrate.

The conversion of the solid to the vapour phase sometimes takes place at temperatures below the solid's melting point, through sublimation. In the vapour phase the molecules travel at high velocities making frequent collisions with others in the vacuum system. The average distance a molecule will travel before colliding with another is called the mean-free path, λ , given from simple kinetic theory by

$$\lambda = \frac{kT}{\sqrt{2\pi\sigma^2 p}} \quad [2.3]$$

where σ is the diameter of the molecule, k is Boltzmann's constant, T is the absolute temperature and p is the vapour pressure of the evaporant. From the above equation it is evident that the mean-free path is increased as the vapour pressure is reduced.

As material evaporates, the vapour pressure of the evaporant above the source increases. When this becomes greater than the equilibrium vapour pressure of the evaporant (at the substrate temperature) condensation occurs. The condensed molecules coalesce to form stable nucleation sites and subsequently act as centres for film growth. The monolayer grows to form a film covering the entire substrate. The film may not be continuous until many monolayers thick. This contrasts to the LB technique in which complete coverage of the substrate can be achieved by a single monolayer.

2.2.3 Spin-coating

Regarded as one of the simplest and quickest means of depositing thin films, spin coating has been extensively used in the microelectronics industry. Spinning has also been used to deposit films of polyaniline⁵⁴ and polysiloxane^{55,56} compounds. The materials used in spinning must first be dissolved in a suitable solvent, then filtered to remove any particulate contamination. The cleaned substrate is held in place on a rotating platform by a vacuum. The spinning process comprises: the deposition and spreading of the material; generation of the thin film; and complete evaporation of the solvent. The speed and duration of the deposition and spreading of the material is

crucial in determining the thickness of the resulting film. Materials deposited by spin-coating do not need to be amphiphilic as for LB films. Moreover for organic materials there are reduced possibilities of material decomposition than for thermal evaporation. The quality of films can also be controlled by adjusting either the substrate temperature during spinning, the spin speed and the spin duration.

2.3 Optical gas sensing devices

Optical techniques such as optical fibres and waveguides transmit light over long distances (with relatively low attenuation). This has led to the development of remote optical sensors, which have the advantage over their electrical counterparts in being usable in hazardous locations. The sensors can exploit a variety of physical phenomenon: surface plasmon resonance; evanescent fields; infra-red absorption and chemiluminescence. These are detailed below.

2.3.1 Surface plasmon resonance

The excitation of surface plasmons has been studied both theoretically and experimentally.^{57,58} The phenomenon can be described as a collective oscillation in the free electron plasma at a metal boundary.⁵⁹ The oscillations are usually excited using an electromagnetic field. However surface plasmons cannot be directly excited at the metal dielectric interface (ie, by incident photons) because energy and momentum conservation cannot be simultaneously obtained. This problem can be overcome using a prism to focus light onto the metallic layer. A system schematic can be seen in figure 2.6, this arrangement is known as the Kretschmann configuration.

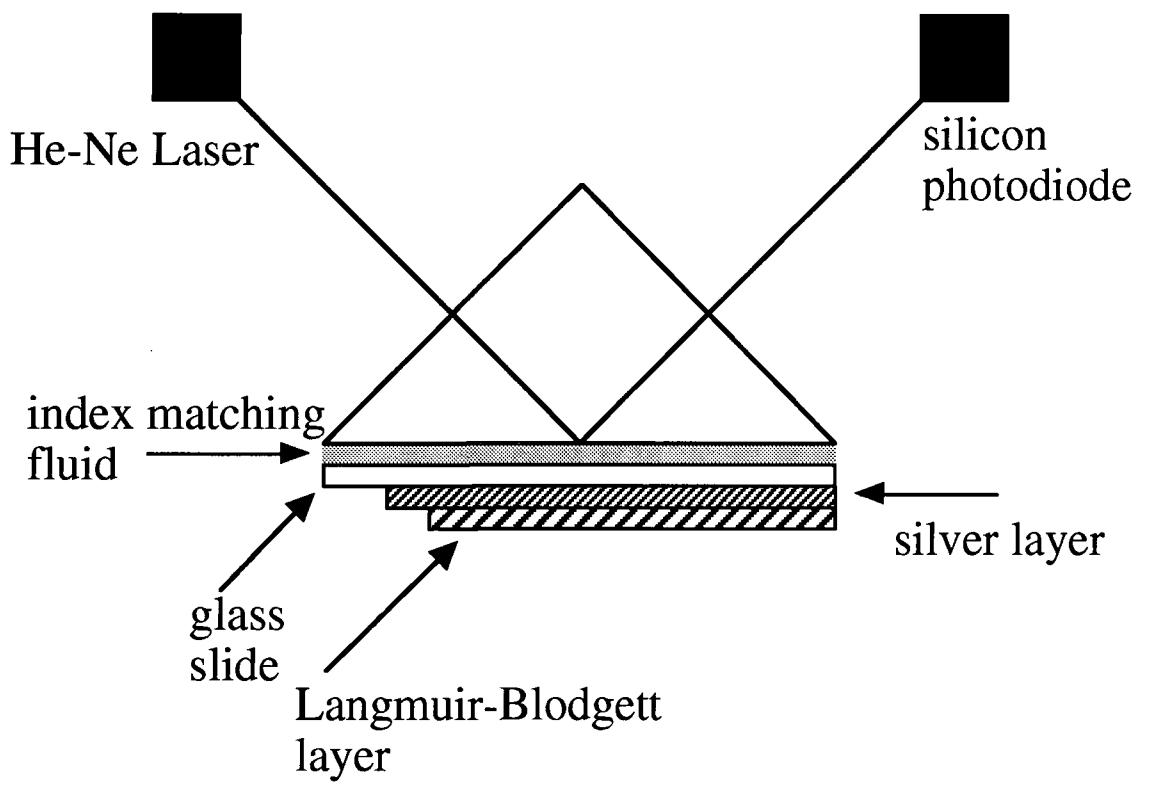


Figure 2.6: Kretschmann-Rather arrangement for SPR investigations.

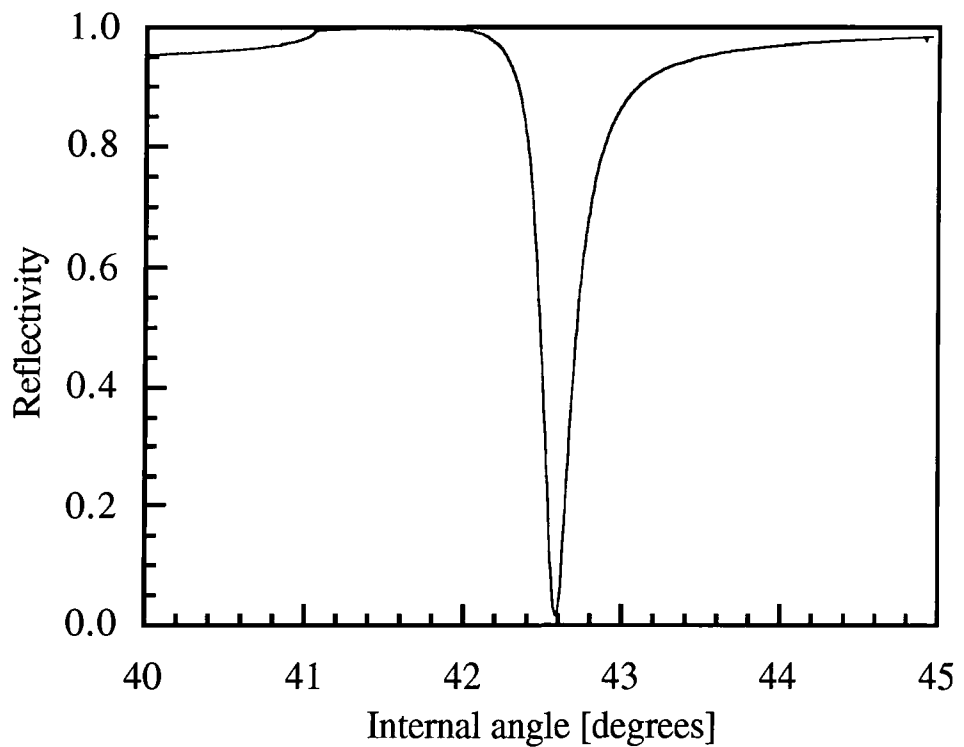


Figure 2.7: SPR profile for a 50 nm silver layer evaporated onto a quartz glass slide ($\lambda = 632.8$ nm)

Lasers are used to interrogate the surface of metal/dielectric system because they are non dispersive, monochromatic light sources. The monochromatic light is arranged so that it is incident at the critical angle of the prism. The intensity of the reflected beam from the prism/metal surface is recorded (usually via a photodiode). At a certain angle the parallel component of the light wavevector will match that for surface plasmons at the opposite surface of the metallic film and be attenuated (see Chapter Four). Scanning the laser through a range of angles (above the critical angle) and plotting the intensity of the reflected light against incident angle produces a profile unique to the metallic layer, and any overlayer, see figure 2.7. It should be noted that the surface plasmons are Transverse Magnetic (TM) waves and can therefore only be excited by p-polarised light. Using the fact that surface plasmons are very sensitive to the boundary conditions (eg, to anything deposited on top of the metallic layer), it is possible to determine the properties (thickness and permittivity) of deposited films. Exploiting this sensitivity to the boundary conditions, it is possible to use the SPR technique for gas sensing, see Chapters Four and Five.

SPR and LB films have been combined to detect a range of gases and vapours. For example, LB layers of phthalocyanine have been used to detect gases such as oxides of nitrogen,^{13,60} and organic hydrocarbons such as toluene.¹⁵

2.3.2 Fibre optical devices

Fibre optical sensors are normally based on the evanescent wave principle. If focused light is directed into a glass fibre (core) which is encased in a material of a lower

refractive index (cladding), part of the beam will be transmitted to the end of the fibre by total internal reflection at the core/cladding interface. The resulting standing wave in the fibre core will penetrate a small distance into the cladding. The absorption or dispersion of energy within the cladding is determined by the optical constants of the cladding material. Thus any optical changes in the cladding, due to a gas or vapour, will change the amount of light transmitted down the fibre. The absorption of light at a range of frequencies in unclad fibres have been recorded on exposure to acetone, ethyl alcohol and sulphuric acid.⁶¹ Optical fibres have also been used to detect pollutants in water, eg, polydimethylsiloxane clad fibres to detect trichloroethene, dichloromethane and chlorobenzene.⁶²

2.3.3 Infra-red absorption devices

Infra-red sensors exploit the fact that any compound with covalent bonds, or a net dipole moment, will interact with infra-red radiation at a characteristic frequency. The result may be the formation of new, or suppression of old, absorption bands. Sensitivity in this type of system is high and the selectivity may be increased by the use of narrow band optical filters, sources and detectors. Infra-red gas sensors have been used to detect CO, CH₄, CO₂ and NO_x.^{63,64}

2.3.4 Chemiluminescence devices

This method involves the coating of the tip of an optical fibre with gas/vapour sensitive materials, entrapped in a polymer matrix. The fibre guides a light beam to the sensing tip and the wavelength of the emitted light is recorded. Interactions between

gases/vapours and the coated tip change the wavelength and intensity of the emitted light. These types of sensors have been used for medical applications and in-vivo blood analysis. In one case, the tip of a fibre optic cable was coated with oxygen and carbon dioxide sensitive materials. The two gases were detected and differentiated by the two distinct emission bands generated by the excitation of the sensitive materials.⁶⁵

2.4 Electrochemical gas sensing devices

There are three main types of electrochemical sensors, each being categorised by the physical parameter being measured. These include: potentiometric sensors, in which a potential is induced at the sensor terminals due to the interaction of a gas/vapour; amperometric sensors, in which a change in current is detected at the sensor head; and conductimetric sensors, in which a change in conductance is detected.

2.4.1 Potentiometric sensors

Potentiometric sensors operate under conditions of zero current. The potential change is obtained from the interaction of electrically neutral gas molecules with the sensor. To produce a potential difference at the sensor head requires a mechanism linking the interaction of the gas molecules to the generation of either ions or electrons at the interface within the sensor. Commercial potentiometric sensors are based on the absorption of a gas into an electrolyte (solid or liquid) via the porous metal electrode, where it is hydrolysed. This reaction induces a variation in the local ion activity, the result of which is a change in the measured potential between the sensing and reference electrodes. Selectivity can be achieved by coating the electrode with a semi-permeable

membrane. A suspended gate field effect transistor (SGFET) has been used as a device to detect concentrations of nitrobenzene, nitrotoluene and methanol gases. The principle operation of the device is based on the chemical modification of the electron work function of a chemically sensitive layer.⁶⁶

2.4.2 Amperometric sensors

Amperometric sensors use changes in current, induced by a gas or vapour, to determine the concentration or type of gas/vapour present. Depending on whether electrons are being added or withdrawn (by the ambient gas/vapour), the sensing electrode can be either a cathode or anode. Similar to other types of gas sensors, these devices are used with semi-permeable membranes through which the gas/vapour can diffuse into the electrolyte. The gas/vapour is then either oxidised or reduced resulting in a change in the steady state current over a scanned potential range.

Amperometric sensors have been used to detect concentrations of CO₂ in pure nitrogen. The structure of one reported thin film microelectrode device consisted of three coplanar electrodes deposited on SiO₂/Si wafer substrate.⁶⁷ The working electrode was a disk shaped Pt electrode, with two outer electrodes: a Pt counter electrode; and a Ag/AgCl reference electrode. The device showed a linear response over the range 0 to 100% concentration of CO₂ with a 90% response time of 30s.

2.4.3 Conductimetric sensors

Conductimetric sensors are generally referred to as chemiresistors and are one of the simplest types of sensors available. A chemiresistor comprises two electrodes for measurement of the input/output signals and a gas sensitive layer on the surface of the electrodes. A number of materials have been used as the active sensing layer including metal oxides,⁶⁸ conducting polymers²³ and phthalocyanines.^{11,69}

When a voltage is applied to the electrodes, conduction electrons and holes are able to travel through the thin film from one electrode to the other. On exposure to a gas/vapour, a reaction takes place, either increasing or decreasing the number of available charge carriers. This affects the conductivity of the film. Variations in the conductivity may be due to surface and/or bulk reactions which should be reversible for a practical sensor. Factors affecting the response of these devices include the quality and thickness of the sensitive material as well as the geometry of the electrode structure.

2.5 Mass gas sensing devices

Changes in mass can be viewed as a general feature of the interaction between a sensor and a gas/vapour. Although macroscopic scales and balances are not considered as sensors, microbalances (such as piezoelectric crystals) are. This is due to their small size, high sensitivity and stability. The advantages of mass sensors are their simplicity of construction and operation, plus their low power consumption and light weight. There are two main types of mass sensors which will be discussed. The first is the piezoelectric crystal and the second is the surface acoustic wave (SAW) device.

2.5.1 Piezoelectric sensors

There are several materials that exhibit the piezoelectric effect, yet the most prevalent is quartz because it is relatively inexpensive and has a high piezoelectric constant. In 1959 Sauerbrey showed that the change in the resonant frequency of a crystal due to the deposition of a uniform film would be equal to a layer of quartz of the same mass.⁷⁰

Thus

$$\Delta f = \frac{\Delta M_s F^2}{A \rho N} \quad [2.4]$$

where A is the area of the quartz crystal, F is the fundamental frequency of the crystal, ΔM_s is the mass of any film deposited onto the crystal surface, ρ is the density of the quartz crystal and N is the frequency constant of the crystal. In gas sensing, the crystal is made the frequency determining element in a circuit, so that any mass changes experienced by the crystal are measured by a change in circuit frequency. The analyser circuitry can be made compact, so the whole unit is portable. The sensitivity of this type of system is excellent with detection limits of the order of 10^{-12} g.⁶⁷ Piezoelectric crystals have been used to detect a range of gases, especially aromatic hydrocarbons such as toluene,⁷¹ benzene⁷² and toluene diisocyanate.⁷³

2.5.2 Surface acoustic wave sensors

In 1885 Lord Rayleigh predicted that surface acoustic waves (SAW) could propagate along the surface of a solid in contact with a medium of low density (such as air). These waves, which are sometimes known as Rayleigh waves, have considerable importance in areas such as structural testing, telecommunications, signal processing and sensing. A

surface acoustic device is a transmission (delay) line in which a mechanical (acoustic) wave is piezoelectrically generated in one oscillator transmitted along the surface of the substrate, then transformed back into an electrical signal at the receiver. The transmitter and receiver are a series of interdigitated fingers, connected by the deposited sensing layer. The substrate of the SAW device is a piezoelectric crystal, which mechanically deforms under an applied voltage to produce the propagated wave. The wave is detected by the interdigitated fingers in the receiver that convert the mechanical wave back to an electrical signal. A schematic representation of the device can be seen in figure 2.8.⁷⁴ Most sensors employ a dual arrangement, with one sensor exposed to the gas/vapour and the other used as a reference. The analytical information is obtained from the interaction of the gas/vapour with the travelling wave moving through the delay line (sensing material). Interactions between the gas/vapour and the sensing material lead to an increase in the layer's mass, which has the effect of modulating the travelling wave. This is detected at the receiver as either a variation in the wave amplitude (ΔA), a shift in the frequency (Δf) or a phase shift in the wave $\Delta\phi$. The most common technique uses changes in the frequency of the transmitted wave Δf to detect a gas or vapour.

The selectivity of a SAW device is determined by the choice of the chemically sensitive layer (delay line). Thin phthalocyanine films have been used as sensing layers to detect concentrations of benzene, chloroform, diethyl ether and trichloroethylene vapour.⁷⁵ The main problems with SAW devices are their susceptibility to moisture, and temperature dependence. Some of these problems may be overcome, with sophisticated signal processing.

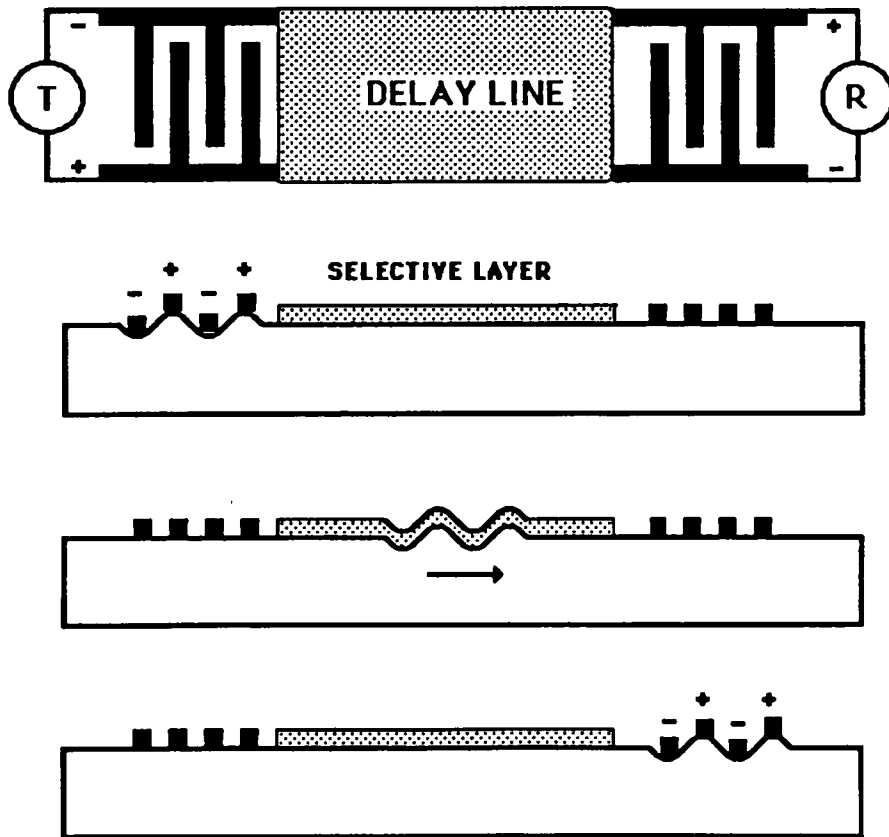


Figure 2.8: Diagram of a SAW sensor with transmitter T, receiver R and the chemically selective layer deposited on a delay line [reproduced from reference 71].

2.6 Thermal gas sensing devices

The first law of thermodynamics states that any process involving a change in internal energy also absorbs or generates heat or work. Thus during an interfacial reaction between a gas/vapour and sensing layer there must be a change in enthalpy which can be monitored. In a closed system the change in temperature ΔT is given by

$$\Delta T = \frac{\Delta H}{C_p} \quad [2.5]$$

where ΔH is the change in enthalpy and C_p is the heat capacity of the system at constant pressure. The two main types of sensors that exploit temperature changes are pyroelectric and catalytic sensors.

2.6.1 Pyroelectric sensors

The pyroelectric effect is the ability of certain materials (certain crystals, ceramics and polymeric materials) to acquire different charges on opposite faces when heated. Gas sensors have been fabricated from lithium tantalate (LiTaO_3) with two evaporated NiCr electrodes with gold contacts. One of the electrodes has a layer of the sensitive material, the second is used as a reference. Heat loss, or gain, associated with the interaction of an ambient gas and the sensing layer is recorded by a change in the electrical response of the device. One practical application for this type of device is using charcoal as the active sensing layer to monitor the residual gases in a conventional oil pumped vacuum system at a total pressure of 10^{-5} torr.⁷⁶

2.6.2 Catalytic sensors

Catalytic gas sensors (also called pellistors) are designed specifically for the detection of flammable gases within air, mainly for the use in mining operations. The structure of catalytic sensors is one of the simplest on the market. The devices usually contain a platinum coil imbedded in $\text{ThO}_2/\text{Al}_2\text{O}_3$ coated with either a porous catalytic metal, palladium or platinum. The coil acts as both a heating coil and a resistance thermometer. The sensors operate at elevated temperatures (over 200°C) to allow catalytic combustion of the gas. When a flammable gas reacts with the sensing material ($\text{ThO}_2/\text{Al}_2\text{O}_3$) heat is

evolved causing an increase in temperature of the platinum coil, thus increasing its resistance. If the sensor is placed within a Wheatstone bridge configuration, any changes in resistance are easily monitored. Since catalytic sensors operate at elevated temperatures these devices have a large operating power requirement (~ 1 W), limiting portability. To try and overcome the problem of power consumption, catalytic sensors have been produced using Si micromachining technology to create small scale sensors. The small area of the sensors reduces the power (~ 40 mW) needed to heat the surface to a temperature at which the catalytic process can occur.⁷⁷ These sensors have detected concentrations of hydrogen and carbon dioxide gases, at a sensing temperature of 220°C .

2.7 Gas sensor arrays

In the previous sections a number of gas sensing systems have been described, yet these techniques only detect one gas or vapour. Commercial systems, though, need sensors which can discriminate between a number of gases or vapours simultaneously. Thus there has been increased research on systems which utilise a number of sensor coatings or types to add some degree of discrimination, these are known as sensor arrays or electronic noses. To recognise a range of gases or vapours the sensor outputs are usually grouped into a set of patterns, these are then analysed on computer by pattern recognition techniques.⁷⁸ The only drawback is that these methods require output signals which do not significantly vary over time (drift) and repeatable changes in output signal when exposed to a target gas or vapour.

Polysiloxanes have been used in sensor arrays to detect organic vapours.^{26,79} An array of piezoelectric sensors have been connected together and the outputs monitored by a neural network. The number of inputs to the neural network corresponded to the number of sensors in the array with a partially connected hidden layer. The output layer was set up to detect toluene and n-octane. The sensor array was able to discriminate between the two vapours over a range of concentrations (100 to 800 ppm). The system was found to be stable, with no need for calibration over a 10 month period. Furthermore, the reaction to humidity up to 70 % was found to be low.

Neural networks and gas sensing array techniques have been applied to tin oxide sensors, discriminating between CO, ethanol and methanol.⁸⁰ Six tin oxide sensors were used as sensor inputs. A three layer (input, hidden and output) neural network was used which had 13 inputs, two for each sensor and one for biasing and 3 outputs, one for each gas. The network was able to distinguish between the three gases, with the response showing some proportionality to vapour concentration. The network showed response to humidity with concentrations above 800 ppm being greatly affected. Some additional information was added into the training process of the network, to try and eliminate the effect of humidity. However, the only effect was to increase the training time so much that this modification had to be removed.

At present, there are a number commercial systems available utilising artificial nose technology. One is produced by Neotronics Ltd and uses polymer sensor arrays, during test stages it was trained to detect the difference between 'Coke and Pepsi' and is being

used by different beer producers to detect the quality of the product during the fermentation process. Others electronic noses are marketed by Aroma-Scan and Bloodhound.

2.8 Summary

A review of gas sensitive materials, deposition techniques and sensing devices has been presented. Organic materials often offer advantages over inorganic compounds, because of their simpler processibility, ease of tailoring the molecule and improved sensitivity and selectivity. The Langmuir-Blodgett technique has been used to produce thin gas sensitive layers on a number of different substrates. Thin films, produced in this way, allow gases or vapours to diffuse in and out of the layers making more responsive systems.

A variety of sensors has been described, with each type having its own advantages and disadvantages, depending on operating environment. Optical sensors have the advantage that they are low power techniques, enhancing their portability and can be used in hostile environments.

References

- 1 J. Travis, A.K. Ray, S.C. Thorpe, M.J. Cook, S.A. James, *Materials Science Technology*, 6, **1995**, 988-994.
- 2 S. Dogo, J.P. Germain, C. Maleysson, A. Pauly, *Thin Solid Films*, 219, **1992**, 244-250.
- 3 R.H. Tredgold, M.C. Young, P. Hodge, A. Hoofar, *IEE Proceedings*, 132, **1985**, 151-156.
- 4 M.M. Catalano, M.J. Crossley, M.M. Harding, L.G. King, *J. Chem. Soc., Chem. Commun.*, **1984**, 1535-1536.
- 5 L. Sun, C. Gu, K. Wen, X. Chao, T. Li, G. Hu, J. Sun, *Thin Solid Films*, 210, **1992**, 486-488.
- 6 C.C. Lenznof, A.B.P. Lever, “**Phthalocyanines, Properties and Applications**” *VCH Publishers (UK)*, Cambridge, **1993**, 1-20.
- 7 C. Granito, L.M. Goldenberg, M.R. Bryce, A.P. Monkman, L. Troisi, L. Pasimeni, M.C. Petty, *American Chemical Society*, 12, **1996**, 472-476.
- 8 H.Y. Wang, J.B. Lando, *Langmuir*, 10, **1994**, 790-796.
- 9 T.A. Jones, B. Bott, S.C. Thorpe, *Sensors and Actuators B*, 17, **1989**, 467-474.
- 10 C. Gu, L. Sun, T. Zhang, T. Li, M. Hirata, *Thin Solid Films*, 244, **1994**, 909-912.
- 11 M. Passard, C. Maleysson, A. Pauly, S. Dogo, J.P. Germain, J.P. Blanc, *Sensors and Actuators B*, 18-19, **1994**, 489-492.

-
- 12 S. Mukhopadhyay, C.A. Hogarth, *Adv. Mater.*, 6, **1994**, 162-164.
 - 13 J.P. Lloyd, C. Pearson, M.C. Petty, *Thin Solid Films*, 160, **1988**, 431-443.
 - 14 J.D. Wright, A. Cado, S.J. Peacock, V. Rivalle, A.M. Smith, *Sensors and Actuators B*, 29, **1995**, 108-114.
 - 15 C. Granito, J.N. Wilde, M.C. Petty, S. Houghton, P.J. Iredale, *Thin Solid Films*, 284-285, **1996**, 98-101.
 - 16 D. Crouch, S.C. Thorpe, M.J. Cook, I. Chambrier, A.K. Ray, *Sensors and Actuators B*, 18-19, **1994**, 411-414.
 - 17 J. Travis, A.K. Ray, S.C. Thorpe, M.J. Cook, S.A. James, *Measurement Science and Technology*, 6, **1995**, 988-994.
 - 18 A. Lu, L. Zhang, D. Jiang, Y. Li, Y. Fan, *Thin Solid Films*, 244, **1994**, 955-957.
 - 19 M.C. Petty, *Biosensors and Bioelectronics*, 10, **1995**, 129-134.
 - 20 J.W. Gardner, P.N. Bartlett, K.F.E. Pratt, *IEE Proc. Circuits Devices Syst.*, 142 (5), **1995**, 321-333.
 - 21 L.S. Miller, A.M. McRoberts, D.J. Walton, D.A. Parry, A.L. Newton, *Materials Science & Engineering C*, 3 (3-4), **1995**, 257-262.
 - 22 N.V. Lavrik, D.De Rossi, Z.I. Kazantseva, A.V. Nabok, B.A. Nesterenko, S.A. Piletsky, V.I. Kalchenko, A.N. Shivaniuk, L.N. Markovskil, *Nanotechnology*, 7, **1996**, 315-319.

-
- 23 P.N. Bartlett, S.K. Ling-Chung, *Sensors and Actuators B*, 20, **1989**, 287-292.
- 24 R. Zhou, U. Weimar, K.D. Schierbaum, K.E. Geckeler, W. Gopel, *Sensors and Actuators B*, 26-27, **1995**, 121-125.
- 25 G. Kraus, A. Hierlemann, G. Gauglitz, W. Gopel, *Transducers '95-Eurosensors IX*, **1995**, 675-682.
- 26 A. Hierlemann, U. Weimar, G. Kraus, M. Schweizer-Berberich, W. Gopel, *Sensors and Actuators B*, 26-27, **1995**, 126-134.
- 27 K. Spaeth, G. Kraus, G. Gauglitz, *Fresenius Journal of Analytical Chemistry*, 357 (3), **1997**, 292-296.
- 28 H. He, R.J. Fraatz, M.J.P. Leiner, M.M. Rehn, J.K. Tusa, *Sensors and Actuators B*, 29, **1995**, 246-250.
- 29 N. Kalita, J.P. Cresswell, M.C. Petty, A. McRoberts, D. Lacey, G. Gray, M.J. Goodwin, N. Carr, *Optical Materials*, 1, **1992**, 259-265.
- 30 K.D. Schierbaum, *Sensors and Actuators B*, 18-19, **1994**, 71-76.
- 31 S. Nakagomi, T. Yamamoto, *Sensors and Actuators B*, 14, **1993**, 617-618.
- 32 J. Nagel, U. Oertel, *Polymer*, 36 (2), **1995**, 381-386.
- 33 A.K. Dey, *J. Indian Chem. Soc.*, 63, **1986**, 357-370.
- 34 A.M. Azad, S.A. Akbar, S.G. Mhaisalkar, L.D. Birkefield, K.S. Goto, *J. Electrochem. Soc.*, 139 (12), **1992**, 3690-3704.

-
- 35 T. Seiyama, A. Kato, K. Fujiishi, M. Nagatani, *Analytical Chemistry*, 34 (11), **1962**, 1502-1503.
- 36 A.S. Poghossian, H.V. Abovian, V.M. Aroutiounian, *Sensors and Actuators B*, 18-19, **1994**, 155-157.
- 37 J. Mizsei, V. Lantto, *Sensors and Actuators B*, 6, **1992**, 223-227.
- 38 J. Getino, J. Gutiérrez, L. Arés, J.I. Robla, M.C. Horrillo, I. Sayago, J.A. Agapito, *Sensors and Actuators B*, 33, **1996**, 128-133.
- 39 J. Janata, "**Principles of Chemical Sensors**", *Plenum Press*, London, **1989**, 221.
- 40 J.W. Gardner, A.Pike, N.F. de Rooij, M. Koudelka-Hep, P.A. Clerc, A. Heirlemann, W. Göpel, *Sensors and Actuators B*, 26-27, **1995**, 135-139.
- 41 J.W. Gardner, *Sensors and Actuators B*, 26-27, **1995**, 261-266.
- 42 J. Janata, R.J. Huber, "**Solid State Chemical Sensors**", *Academic Press Inc.*, London, **1985**, 31-32.
- 43 I. Lunderström, *Sensors and Actuators A*, 56, **1996**, 75-82.
- 44 D. Xinfang, Y. Haiming, J. Hen, *Sensors and Actuators B*, 12, **1992**, 1-4.
- 45 L. Ping, P.K. Dasgupta, *Anal. Chem.*, 61, **1989**, 1230-1235.
- 46 P. Norberg, U. Ackelid, I. Lunderström, L.G. Peterson, *J. Appl. Phys.*, 81 (5), **1997**, 2094-2100.
- 47 T.L. Poteat, B. Lalevic, *IEEE Trans. Electron Devices*, vol 29, 123-129.

-
- 48 I. Lunderström, T. Ederth, H. Kariis, H. Sundgren, A. Spetz, F. Winquist, *Sensors and Actuators B*, 23, **1995**, 127-133.
- 49 M. Holmberg, F. Winquist, I. Lunderström, F. Davide, C. DiNatale, A.D'Amico, *Sensors and Actuators B*, 35-36, **1996**, 528-535.
- 50 M.C. Petty, "**Langmuir-Blodgett Films: An Introduction**", *Cambridge University Press*, (UK), **1996**, 12-63.
- 51 S. Mukhopadhyay, C.A. Hogarth, S.C. Thorpe, M.J. Cook, *Journal of Materials Science: Materials in Electronics*, 5, **1994**, 312-323.
- 52 H. Perez, A. Barraud, *Synthetic Metals*, 61, **1993**, 23-29.
- 53 Y. Gorbunova, M.L. Rodríguez-Méndez, J. Souto, L. Tomilova, J.A. de Saja, *Chem. Mater.*, **1995**, 7, 1443-1447.
- 54 C. Di Bartidomo, P.S. Barker, M.C. Petty, P. Adams, A.P. Monkman, *Advanced Materials for Optics and Electronics*, 2, **1993**, 233-236.
- 55 K. D. Schierbaum, W. Göpel, *Synthetic Metals*, 61, **1993**, 37-45.
- 56 M. Haug, K.D. Schierbaum, G. Gauglitz, W. Göpel, *Sensors and Actuators*, B, 11, **1993**, 383-391.
- 57 A. Otto, *Phys. Stat. Sol.*, 42, **1970**, K37-K39.
- 58 E. Kretschmann, H. Raether, *Z. Naturforsch*, 23a, **1968**, 2135-2136.
- 59 C.Nylander, B. Liedberg, T. Lind, *Sensors and Actuators*, 3, **1982/83**, 79-88.
- 60 D.G. Zhu, M.C. Petty, *Sensors and Actuators*, B, 2, **1990**, 265-269.

-
- 61 J. Heo, M. Rodrigues, S.J. Saggese, G.H. Sigel, *Applied Optics*, 30 (27), **1991**, 3944-3951.
- 62 J. Bürck, J-P. Conzen, B. Becknaus, H-J. Ache, *Sensors and Actuators*, B, 18-19, **1994**, 291-295.
- 63 T. Hanawa, S. Kuwabata, H. Hashimoto, H. Yoneyama, *Synthetic Metals*, 30, **1989**, 173-181.
- 64 J.P. Li, R.H. Tredgold, R. Jones, *Thin Solid Films*, 160, **1990**, 167-176.
- 65 O.S. Wolfbeis, L.J. Weis, M.J.P. Leiner, W.E. Ziegler, *Anal. Chem.*, 60, **1988**, 2028-2030.
- 66 M. Josowicz, J. Janata, K. Ashley, S. Pons, *Anal. Chem.*, 59, **1987**, 253-258.
- 67 Z-B. Zhou, Q-H. Wu, C-C. Liu, *Sensors and Actuators*, B, 21, **1994**, 101-108.
- 68 S-S. Park, H. Zheng, J.D. Mackenzie, *Materials Letters*, 17, **1993**, 346-352.
- 69 C. Gu, L. Sun, T. Zhang, *Thin Solid Films*, 244, **1994**, 909-912.
- 70 J.F. Alder, C.A. Isaac, *Analytica Chimica Acta*, 129, **1981**, 163-174.
- 71 M.H. Ho, G.G. Gauilbault, *Anal Chem*, 52, **1980**, 1489-1492.
- 72 C.S.I. Lai, G.J. Moody, J.D. Ronald-Thomas, D.C. Mulligan, J.F. Stoddart, R. Zarzycki, *Chem. Soc. Perkin. Trans. II*, **1988**, 319-324.
- 73 J.F. Alder, C.A. Isaac, *Analytica Chimica Acta.*, 129, **1981**, 175-188.
- 74 J. Janata, "**Principles of Chemical Sensors**", *Plenum Press*, London, **1989**, 70.

-
- 75 M. Urbanczyk, W. Jakubik, S. Kochowski, *Sensors and Actuators*, B, 22, **1994**, 133-137.
- 76 J. Janata, R.J. Huber, "**Solid State Chemical Sensors**", *Academic Press Inc.*, London, **1985**, 197-203.
- 77 M. Gall, *Sensors and Actuators*, B, 4, **1991**, 533-538.
- 78 M.Holmberg, F. Winqvist, I. Lunderstöm, F. Davide, C. DiNatale, A. D'Amico, *Sensors and Actuators B*, 35-36, **1996**, 528-535.
- 79 A. Heirlemann, U. Weimar, G Kraus, M. Schweizer-Berberich, W. Göpel, *Sensors and Actuators B*, 26-27, **1995**, 126-134.
- 80 D. Vlachos, J. Avaritsiotis, *Sensors and Actuators B*, 33, **1996**, 77-82.

Chapter Three

Materials

3.0 Preface

Three distinct materials were used in this work: phthalocyanines, which are classified as molecular crystals; polysiloxanes; and a co-ordination polymer. Each of these reveals a change in optical behaviour upon exposure to a gas, organic vapour or water. This chapter summarises the important chemical and physical characteristics of each material. The data contained within this chapter are from either work undertaken during this project or from other sources.

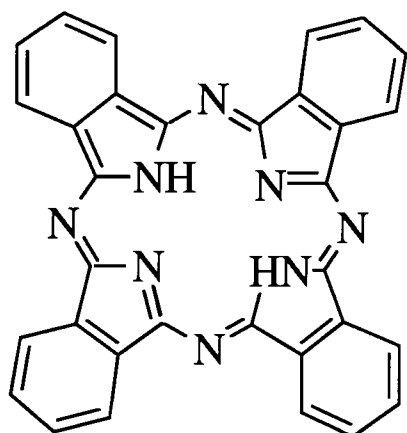
3.1 Phthalocyanines

The first synthesis of a phthalocyanine was recorded in 1907 when Braun and Tcherniac heated *o*-cyanobenzamide to a high temperature. However, the structure of this metal-free, unsubstituted phthalocyanine was only determined a quarter of a century later.¹ Phthalocyanines have now established themselves as blue and green dyestuffs and are an important industrial commodity, used primarily as colourings in inks, plastics and metal surfaces. Recently their use as the photoconducting agent in photocopying machines has rekindled research interest. Possible application areas currently under study include: chemical sensors; electrochromic displays; electrocatalysis for fuel cell applications; and liquid crystal colour display applications.¹

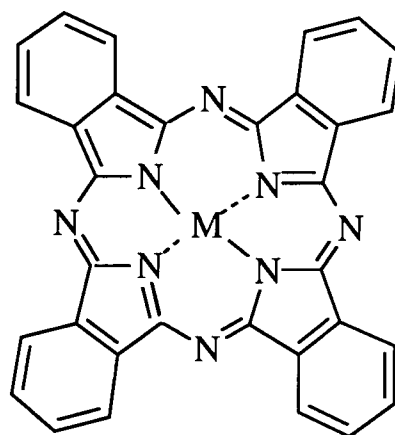
3.1.1 Chemical structure

There are three main types of phthalocyanine commercially available: the first is the metal free phthalocyanine, shown in figure 3.1 (a); then there is the metallophthalocyanine (in this work Cu and Zn were used), shown in figure 3.1 (b); and finally the substituted phthalocyanine, which can be either tetra, octa or hexadecasubstituted, in this work only tetrasubstituted was used, shown in figure 3.1 (c). M denotes the position of the metal in the metallophthalocyanine and R denotes the position of the substituent. The use of peripheral substitution is to enhance the solubility of phthalocyanines which are, in general, rather insoluble in organic solvents, but also to moderate their structural and physical properties.

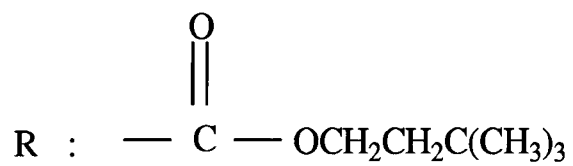
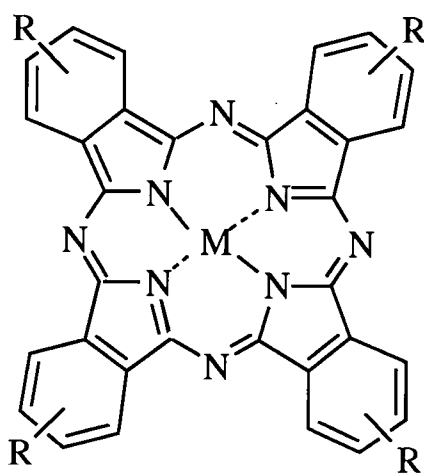
Copper and zinc phthalocyanines were prepared by L. Pasimini *et al* using a two step reaction.² The first stage is the production of the base phthalocyanine, Cu(II) [tetracarboxy] phthalocyanine. This was accomplished by refluxing a mixture of trimellitic anhydride (10g, 0.05 mol), urea (30g, 0.5 mol), CuCl₂ + 2H₂O (5.1g, 0.03 mol), ammoniummolybdate (1g, 8 x 10⁻⁴ mol) and nitrobenzene (150 ml) for 4 hours. The resulting solid was filtered, heated and washed to produce Cu(II) [tetracarboxy] phthalocyanine. The second step was the preparation of the final compound, Cu(II) [tetrakis(3,3-dimethyl-1-butoxycarbonyl)] phthalocyanine (CuPcBC). This was achieved by refluxing Cu(II) [tetracarboxy] phthalocyanine (3g, 4 mmol) with thionyl chloride (20 ml), N,N-dimethylformamide (1g, 0.01 mol) for 24 hours.² The resulting compounds CuPcBC (or ZnPcBC, synthesised by substituting Cu with Zn in the above



(a)



(b)



M = Cu or Zn

(c)

Figure 3.1: (a) Metal-free phthalocyanine, (b) metallophthalocyanine, (c) tetrasubstituted metallophthalocyanine used in this work.

processes) were supplied by Dr L. Valli, University of Lecce. A full description of the synthesis can be found in reference 2, and those contained therein.

Sublimed films of phthalocyanines are strongly dependent upon the sublimation conditions. There are two distinct phases of phthalocyanines, α and β , that can be formed using this method. The α -phase is formed, after sublimation, by annealing the sample over the temperature range 60 to 140°C. An α to β transition occurs at annealing temperatures over 210°C.³ The α crystalline form differs from the β by a smaller tilt angle between the axis of stack and the normal of the phthalocyanine film. This results in a considerably shorter metal-metal distance in the β phase and a longer interstack distance. The morphology of the films is very important for gas sensing applications, with the α phase being more sensitive to the presence of oxygen.⁴

3.1.2 Thermal and chemical stability

It is well known that phthalocyanines have excellent thermal and chemical stability, with some phthalocyanines known to sublime at 400°C or above in nitrogen.⁵ The thermal stability can be affected by the substituents and the central metal ions, shown in table 3.1.⁶ The majority of conductive phthalocyanine gas sensors operate at elevated temperatures, to aid reversibility of the sorption-desorption process.

Sample	Temperature for 5 wt % loss [°C]			Temperature for 10 wt % loss [°C]		
	N ₂	Dry air	Humid air	N ₂	Dry air	Humid air
CuPc	551	416	423	573	443	443
ZnPc	530	485	500	550	515	520

Table 3.1: Characteristic temperatures for 5 and 10 wt % weight loss for purified samples [reproduced from reference 6].

3.1.3 LB film deposition

Phthalocyanine compounds that sublime are generally not sufficiently soluble to be deposited by the LB technique. However, there are exceptions. A variety of peripherally substituted phthalocyanine compounds have now been synthesised and formed into LB films. The film morphologies of LB deposited films are quite different to sublimed films, as are the vapour response characteristics. LB films are generally regarded as more reproducible and have better vapour responses.⁷

Floating layers can be transferred to glass, single crystal silicon and ITO substrates using the LB technique (see Chapter Four). Optimum film transfer was achieved at a deposition surface pressure of 15 mN m⁻¹ for CuPcBC and 20 mN m⁻¹ for ZnPcBC and a substrate dipping speed of between 2 and 10 mm min⁻¹. Under these conditions, Y-type deposition was observed with film transfer ratios between 0.9 and 1.0.^{7,8} The pressure versus area isotherms can be seen in figure 3.2 for CuPcBC and figure 3.3 for ZnPcBC. There are discrepancies in the area per molecule for each phthalocyanine, with

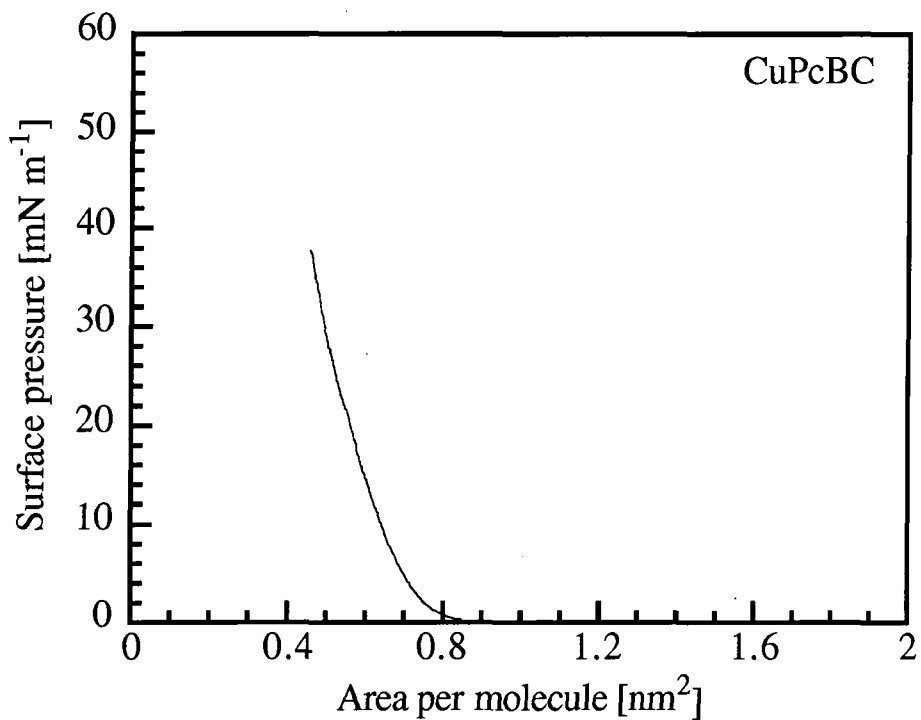


Figure 3.2: Surface pressure versus area isotherm for CuPcBC spread on a subphase of pure water (temperature = 18 ± 2 °C, pH = 5.8 ± 0.2 , compression rate 1×10^{-2} nm² molecules⁻¹ s⁻¹) [reproduced from reference 5].

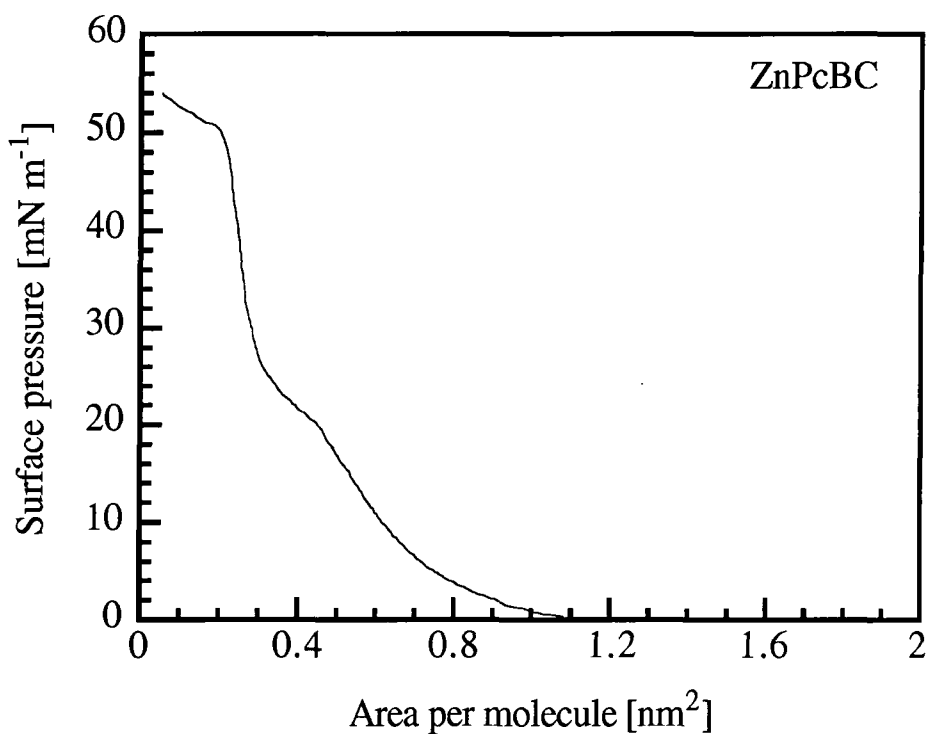


Figure 3.3: Surface pressure versus area isotherm for ZnPcBC on a pure water subphase (temperature = 18 ± 2 °C, pH = 5.8 ± 0.2 , compression rate = 1×10^{-2} nm² molecules⁻¹ s⁻¹) [reproduced from reference 6]

CuPcBC having a considerable greater area per molecule. This was explained by different molecular arrangements on the subphase.⁸

3.1.4 Optical properties

(a) UV/Visible spectroscopy

The visible spectrum for various concentrations of CuPcBC in ethyl acetate is shown in figure 3.4. There are 2 bands of interest, Q_I (λ ca 600 nm) and Q_{II} (λ ca 680 nm). The Q_I absorption is associated with monomeric phthalocyanine while the Q_{II} band is thought due to aggregated molecules.²

Both phthalocyanine compounds produced LB films that appeared homogenous on visual inspection. The optical absorption spectrum for 40 layers of CuPcBC deposited onto quartz glass slides (20 layers deposited on each side) is shown in figure 3.5. This is very similar to that measured in solution, in figure 3.4, with a Q_I band at 615 nm.⁷

(b) Surface plasmon resonance

Surface plasmon resonance (SPR) measurements can yield the permittivity and thickness of phthalocyanine LB layers. In each case, LB layers were deposited onto a 50 nm silver layer evaporated onto a quartz glass slide. Substrates were mounted in the computer-controlled SPR system described in Chapter Four. Figure 3.6 shows the SPR curves for the 50 nm silver layer and 1 LB layer of CuPcBC. The addition of the monolayer causes the SPR curve to broaden and the point of minimum intensity to shift

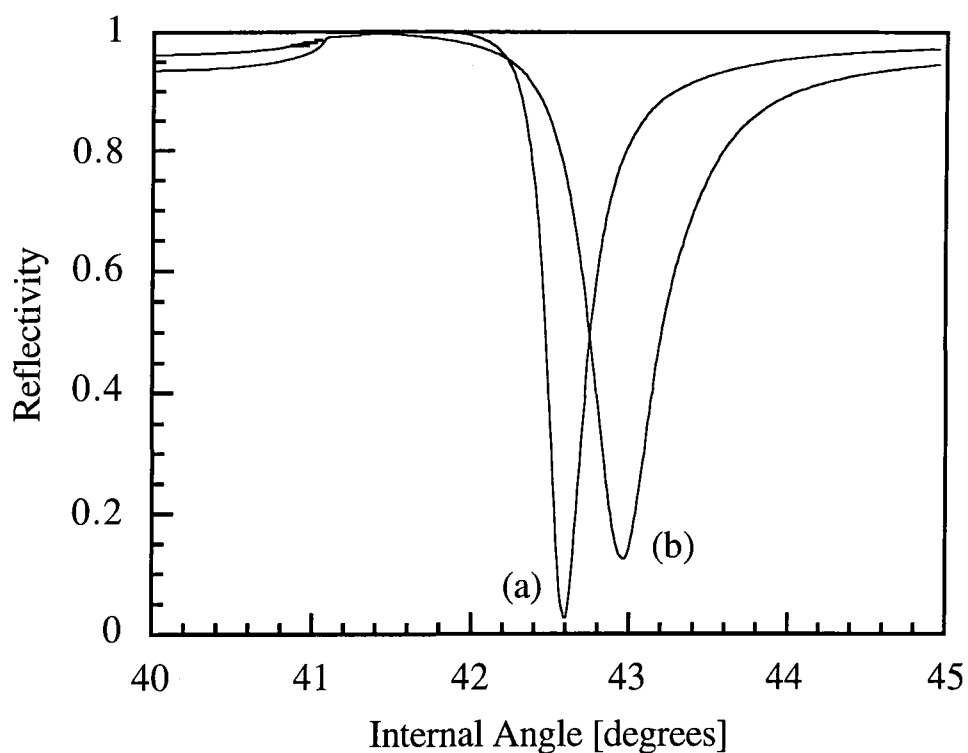


Figure 3.6: Surface plasmon resonance curves ($\lambda = 632.8$ nm) for (a) 50 nm silver layer (b) one LB layer of CuPcBC deposited on the Ag.

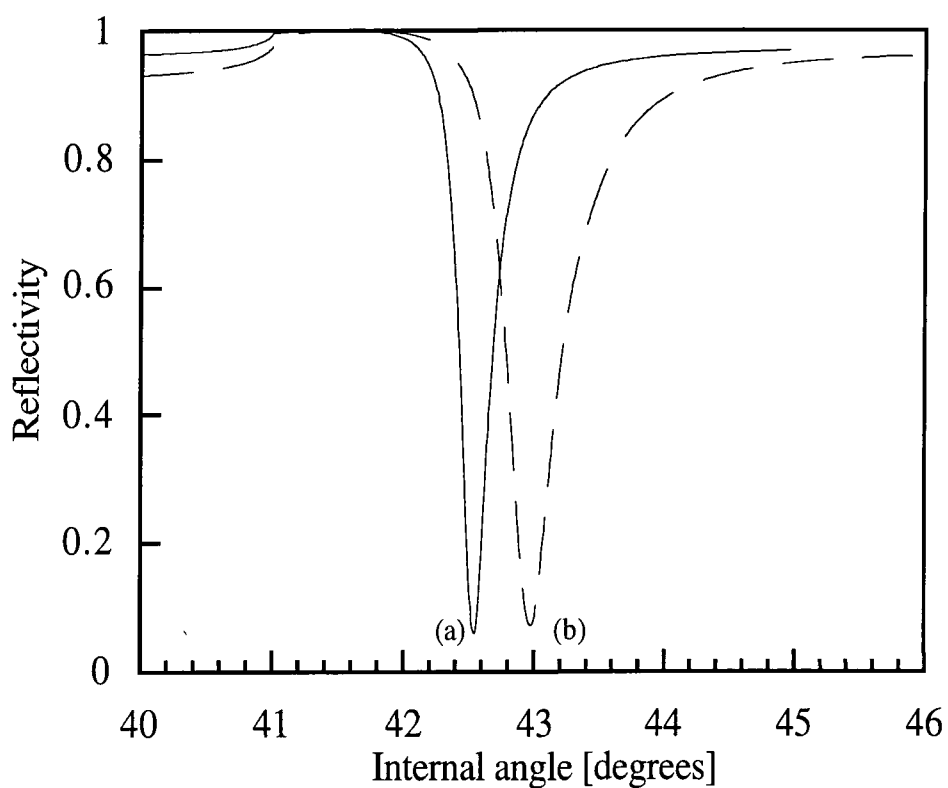


Figure 3.7: Surface plasmon resonance curves ($\lambda = 632.8$ nm) for (a) 50 nm silver layer (b) one LB layer of ZnPcBC deposited on the Ag [reproduced from reference 6].

to higher angles. The decrease in resonance depth can be attributed to absorption by the film, since the absorption peak for CuPcBC is close to the wavelength of the incident laser beam.⁹ Figure 3.7 shows the SPR curve for the 50 nm silver layer and 1 LB layer ZnPcBC. The addition of the organic film has produced a shift in the resonance curve to higher angles by approximately 0.5° , an increase in the resonance width and a very small decrease in the depth of resonance. In each case, the SPR curves were modelled on computer to give values for permittivity ($\lambda = 632.8$ nm) and LB film thickness (see Chapter Four), these are shown in table 3.1.⁸

Material	Permittivity	Layer thickness [nm]
CuPcBC ⁷	$(2.81 \pm 0.28) + i(1.05 \pm 0.1)$	1.87 ± 0.51
ZnPcBC ⁶	$(2.69 \pm 0.27) + i(0.76 \pm 0.1)$	3.49 ± 0.35

Table 3.2: Comparison between the permittivity and layer thickness measurements for Cu and Zn substituted metallophthalocyanines, from SPR ($\lambda = 632.8$ nm) [reproduced from reference 9].

3.2 Polysiloxanes

The first synthesis of an organosilicon (tetraethylsilane) compound dates back to 1863 by Friedel and Crafts, 27 similar compounds had been synthesised by the turn of the century. By 1931, high polymer silicones were set for commercial applications in the USA. These were mainly manufactured for glass fibre fabrics and high temperature electrical insulators. As by-products to this work, a number of fluids such as poly(dimethylsiloxane) were developed in the pre-war period. These met the needs of

the military and by 1942 were being used as heat resistant organosiloxane resins and fluids.

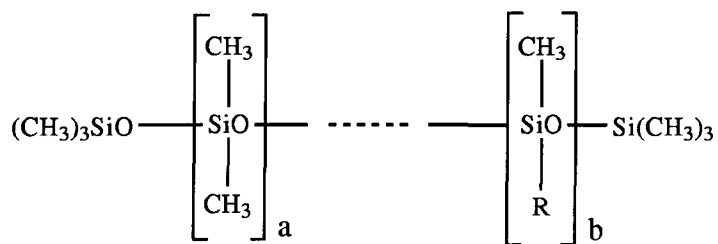
The chemical make-up of silicones can be represented by the general polymer formula



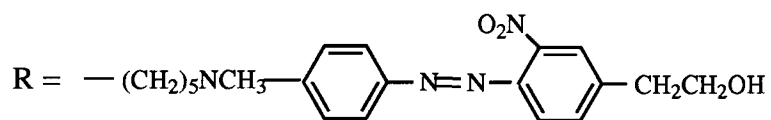
where R is a substituent, n is large and a can be varied from 0 to 4. These materials can possess both 'inorganic' characteristics, due to the high percentage of ionic character in the Si-O bonds and 'organic' characteristics due to the substituent groups. Thus the physical properties of any organopolysiloxane are governed by the type and number of organic groups substituted to the silicon backbone, as well as by the way the siloxane backbone is linked together. A range of organic moieties have been used as substituents such as: methyl, phenyl, and ethyl. The substitution of methyl groups promotes fluidity, low viscosity-temperature index, low melting point and high liquid compressibility, whereas phenyl groups produce opposite effects.¹⁰

3.2.1 Chemical structure

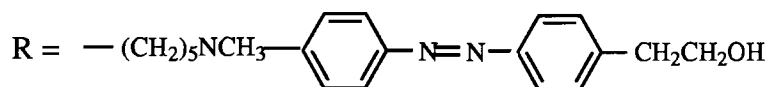
This research has concentrated on organopolysiloxanes, in particular two compounds synthesised by Dr. A. McRoberts, University Hull. Figure 3.8 shows the structure of the materials used, AMCR22 and AMCR23. The initial siloxane backbone consists of poly(dimethylsiloxane) and poly(methylsiloxane) units. The reactive hydrogen in the backbone is used to incorporate the chromophoric side groups. The polymer was



$$a:b = 1:1; \quad a+b = 16$$



AMCR22



AMCR23

Figure 3.8: Structure of the polysiloxanes used in this work.

dissolved in chloromethane, then methanol was added to precipitate the polymer. The precipitate was then collected by centrifugation (5000 rpm) and then dried.¹¹

The polymer spine renders the molecule insoluble in water and acts as a substitute to the hydrocarbon chain. The alcohol head groups tend to improve the monolayer orientation while the methylene spacer units, between the dye moiety and the backbone, permit the chromophores some degree of movement. The latter consist of donors (nitromethyl and ether oxygen groups) separated by a conjugated aromatic ring from acceptor (azophenyl groups) groups.¹²

3.2.2 Thermal and chemical stability

Organopolysiloxanes are characterised by combinations of chemical, mechanical and electrical properties not common to any other class of polymers. Polysiloxanes containing methyl and phenyl groups are known to: have high thermal and oxidative stability; be insoluble in water; possess a relative inertness to many ionic reagents; to exhibit high dielectric strength and low power loss. Moreover, polysiloxanes show good thermal stability, with materials able to withstand temperatures up to 400°C (under a vacuum and in an inert atmosphere). The ionic character of the silicon oxygen bond also adds to the materials' thermal stability. Unfortunately, this property renders polysiloxanes susceptible to attack by certain chemicals. Acids such as sulfuric, phosphoric and hydrochloric all cause depolymerisation. This also occurs with water under extreme heat and pressure. Solid salts such as aluminium and ferric chlorides cleave both siloxane and silicon-carbon bonds, causing an increase in viscosity. With

the exceptions already noted, polysiloxanes are relatively inert to most chemicals. In general, aqueous solutions of any kind (dilute acids, metal salts, alcohols, chlorinated solvents and hydrocarbons) have little effect on polysiloxanes.¹⁰

3.2.3 LB film deposition

The Langmuir and LB deposition properties of AMCR22 and AMCR23 were investigated by N. Kalita *et al.*¹² Initially each compound was dissolved in chloroform (1g l^{-1}) and spread onto a pure water subphase. Pressure versus area isotherms, shown in figure 3.9 were similar for both compounds (only AMCR23 shown) and show two distinct regions. The first is an expanded region at large molecular areas, there was then a plateau at surface pressure of *ca* 25 mN N^{-1} . In the plateau region, there was no sign that the monolayer had collapsed on the water surface. It was therefore suggested that, in this region, molecules of AMCR22 and AMCR23 undergo some sort of molecular rearrangement.¹³ Due to the shape of the isotherms it was not useful to derive values for area per molecule, yet due to the similarity to the molecule shown in reference 12 it was possible to suggest that AMCR22 and AMCR23 were orientated with the polymer backbone in a parallel to the subphase surface.

Both polysiloxanes could be transferred to a variety of substrates (hydrophobic glass, single crystal silicon and evaporated silver) using the LB technique. For deposition, the surface pressure was held at *ca* 20 mN m^{-1} . The transfer ratio was *ca* 1.0 for Z type deposition.¹³

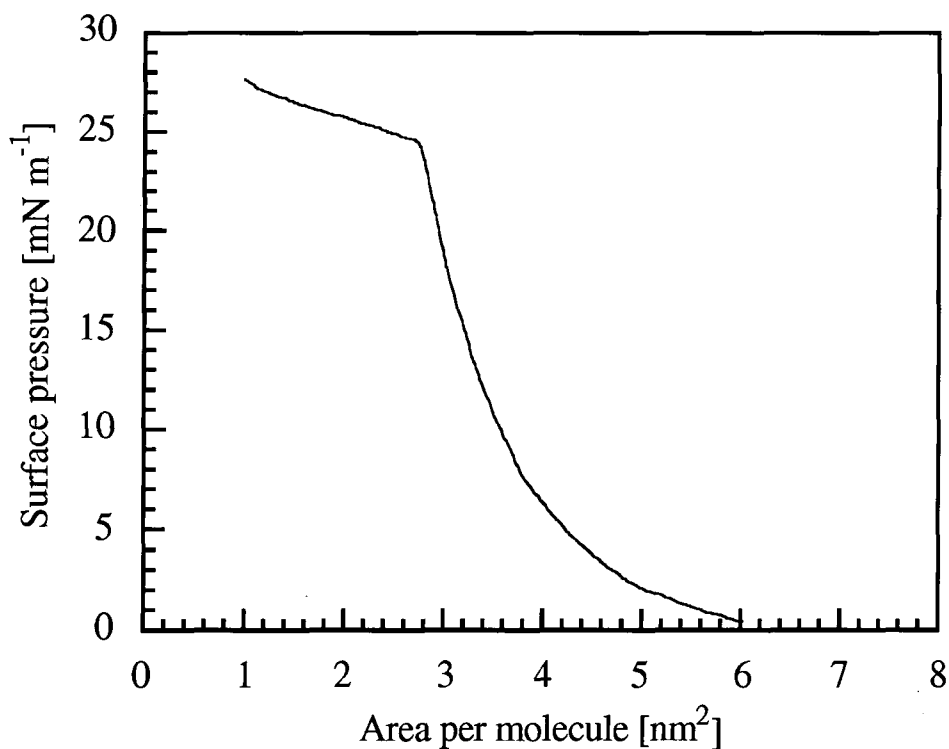


Figure 3.9: Surface pressure versus area isotherms for AMCR23 spread on a subphase of pure water (temperature = 18 ± 2 °C, pH = 5.6 ± 0.2 , compression rate = 1×10^{-3} nm² molecules⁻¹ s⁻¹) [reproduced from reference 13].

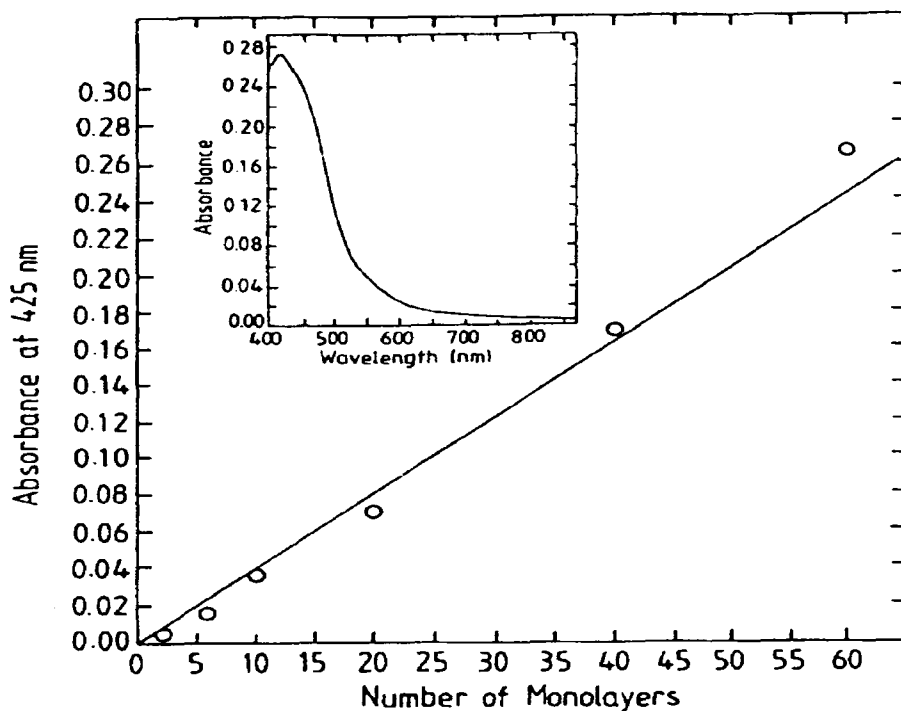


Figure 3.10: Optical absorption at 430 nm versus number of monolayers for Z-type LB films of AMCR23. The full absorption spectrum is given inset [reproduced from reference 13].

3.2.4 Optical properties

(a) UV/Visible spectroscopy

The optical absorption ($\lambda = 430$ nm) for a series of LB layers of AMCR23 is shown in figure 3.10. As can be seen, there is a linear increase in absorption with film thickness, indicating reproducible LB dipping characteristics. The full spectrum is shown inset to figure 3.10 and indicates that AMCR23 exhibits a broad absorption in the blue/green region of the visible spectrum, giving the layers a characteristic yellow/brown appearance.¹³

(b) Surface plasmon resonance

Surface plasmon resonance studies were performed on LB layers of AMCR22 and AMCR23. Figure 3.11 shows the SPR curve for a monolayer of AMCR23 deposited onto *ca* 50 nm silver layer, the curves were modelled on computer to give values for permittivity and layer thickness.

Material	Permittivity	Thickness [nm]
AMCR22	1.99 + i0.038	1.7
AMCR23	3.11 + i0.120	1.7

Table 3.3: Comparison between the permittivity and layer thickness measurements for AMCR22 and AMCR23, from SPR ($\lambda = 632.8$ nm).

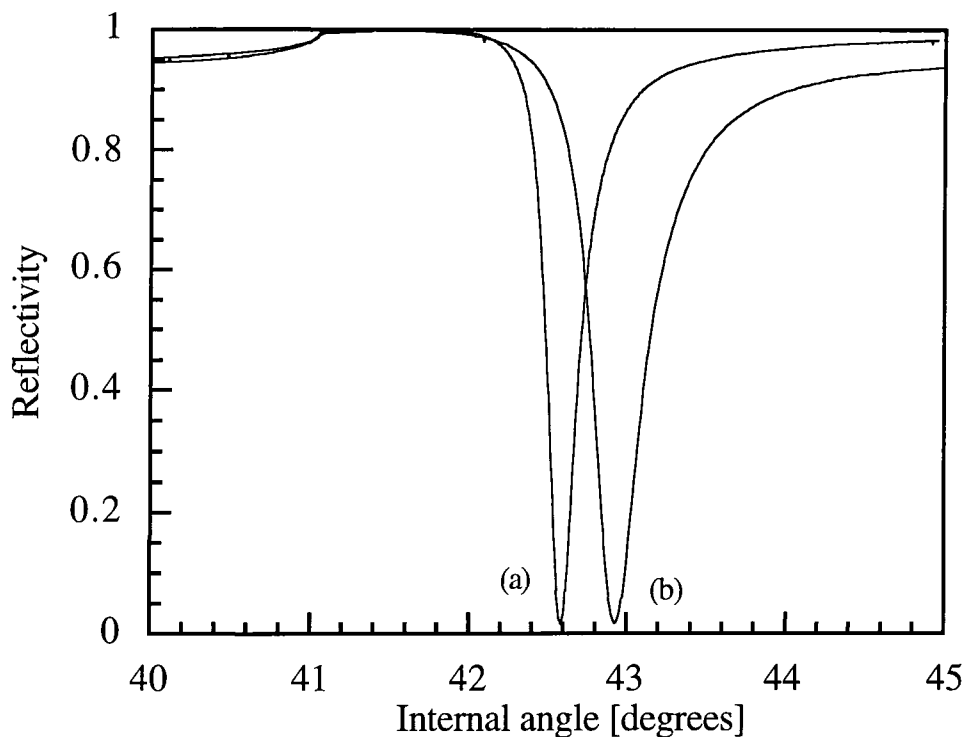


Figure 3.11: Surface plasmon resonance curves ($\lambda = 632.8$ nm) for (a) 50 nm silver layer (b) 1 LB layer AMCR23 deposited onto the Ag layer.

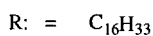
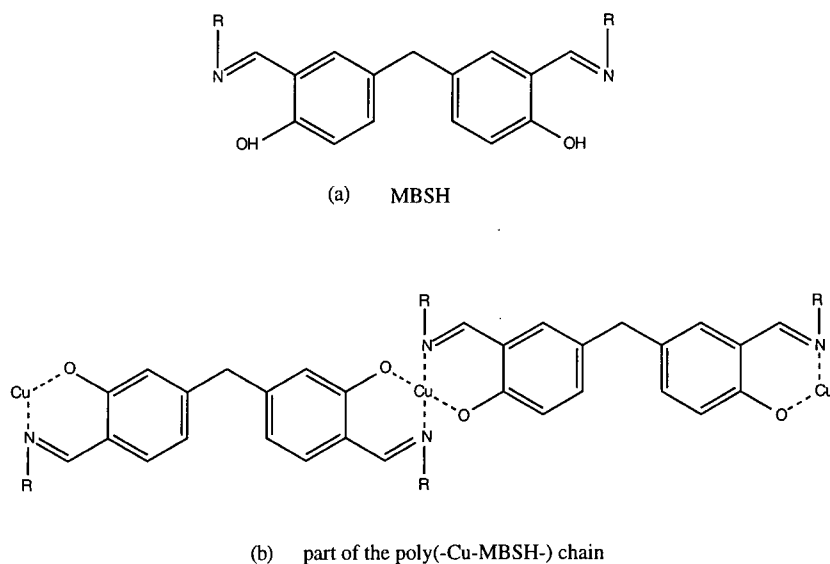


Figure 3.12: Structure of 5,5' methylenebis (N-hexadecylsalicylideneamine) as deposited from (a) a subphase of ultra pure water (MBSH) (b) a subphase containing copper acetate (poly(CuMBSH)).

From molecular models, the thickness values imply a tilt angle with respect to the substrate normal of 47° for AMCR22 and 41° for AMCR23.¹³

3.3 Co-ordination polymers

The term “co-ordination polymer” has been used to describe a great number of materials. In its broadest sense this can be applied to any macromolecular entity that contains co-ordinate covalent bonds.¹⁴ This work is only concerned with co-ordination polymers in which a metallic element is involved in the co-ordinate covalent bond. There are two main categories of co-ordination polymers. The first is where the metallic element is an integral part of the backbone, and the second is where the metallic element is co-ordinated to polymer repeat units containing donor groups. The synthesis of a co-ordination polymer is usually achieved by one of the following techniques: the metal complex combining with favourable donor groups present in the ligand; the ligand itself being a polymer to which the metallic element can combine; or the metal may co-ordinate with the ligand and the resulting monomer may react with another compound to form a polymer.¹⁵

3.3.1 Chemical structure

In this work, a monomer of 5,5'-methylenebis(N-hexadecylsalicylideneamine) (MBSH) was reacted with copper (II) acetate to form Cu(II) 5,5'-methylenebis(N-hexadecylsalicylideneamine) poly(CuMBSH).¹⁶ The structure of MBSH and the resulting polymer poly(CuMBSH) are shown in figure 3.12. Though most of the

characterisation on this complex was undertaken as part of this work (Chapter Six) some of the properties, from other sources, are given below.^{17,18}

The synthesis of the monomer (MBSH) was undertaken by Dr J. Nagel at the Institut für Polymerforschung Dresden. The material was prepared by boiling 0.1 mol hexadecylamine and 100 ml ethanol. After resolution, 0.05 mol methylene-bis-salicylaldehyde (MBS) in 100 ml ethanol was added to the hexadecylamine solution, whilst maintaining the solution at boiling point. This mixture was heated for 1 hour, then, after cooling to room temperature, a yellow solid was filtered off, recrystallised in ethanol and dried at 60°C to produce MBSH.¹⁶

3.3.2 Thermal and chemical stability

Compounds related to the MBSH monomer have been investigated for their thermal stability after reaction with a metal. 5,5' methylene-bis-salicylaldehyde (the initial compound used to synthesis MBSH) was reacted with both Cu and Zn to form a coordination polymer. These compounds were then heated at 250°C for 3 hours, with the percentage weight loss recorded every hour. The results from this experiment are shown in table 3.4.¹⁹ The data show that over the three hour period the Zn compound is more stable than the copper, with only 0.5% weight loss over the 3 hour period. All the samples were heated for a total of 28 hours at 250°C after this time the samples were completely destroyed.

Metal	Percentage weight loss		
	1 hour	2 hours	3 hours
Cu	0	0.5	0.5
Zn	3.5	4.5	5.0

Table 3.4: Temperature stability of poly(ZnMBS) and poly(CuMBS) after heating at 250°C over a three hour period [reproduced from reference 19].

3.3.3 LB deposition

The co-ordination of MBSH was formed by reacting the monomer with metal (II) ions dissolved in the subphase. Figure 3.13 shows the isotherms for MBSH spread on a subphase containing different quantities of copper (II) acetate. As the concentration of copper in the subphase increases, the collapse area of the floating film is shifted towards higher values. The highest value for collapse area was *ca* 0.9 nm² (with a copper (II) acetate concentration of 10⁻⁵ mol), which is close to the area of the MBSH monomer parallel to the subphase surface (obtained from molecular models). Monolayers of poly(CuMBSH) could be transferred to a variety of substrates using the LB technique.¹⁷ Optimum film transfer (Y-type deposition) was obtained at a surface pressure of 25 mN m⁻¹ and a substrate dipping speed of between 6 and 8 mm min⁻¹ yielding a deposition ratio of 1.0 ± 0.1.¹⁹ Pure MBSH could not be transferred easily to substrates, though a monolayer sample was produced using the horizontal lifting method.^{16,20}

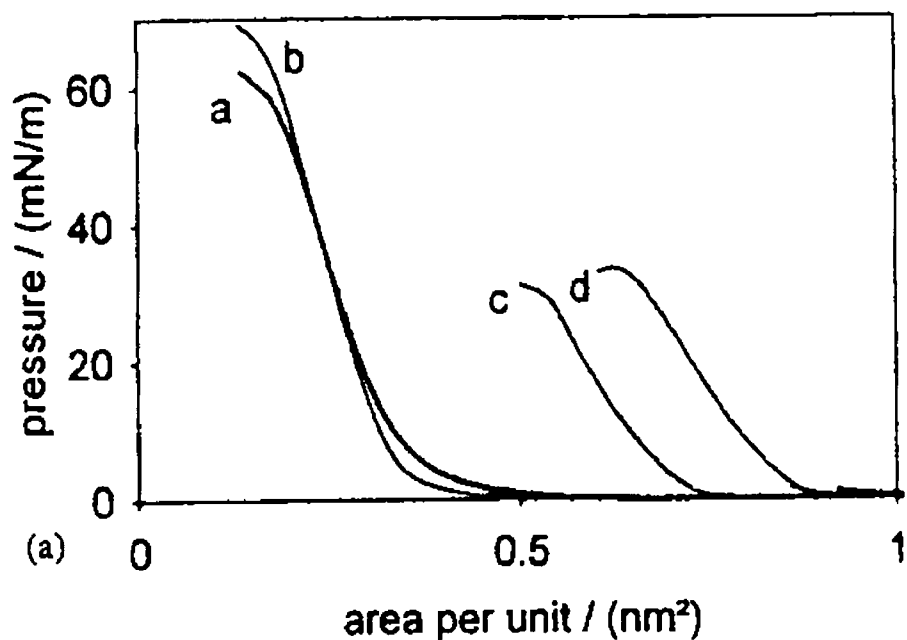


Figure 3.13: Surface pressure versus area isotherms for MBSH spread on a subphase containing (a) pure water (b) pure water and copper acetate (10^{-7} M) (c) pure water and copper acetate (10^{-6} M) (d) pure water and copper acetate (3×10^{-6} M) [reproduced from reference 17].

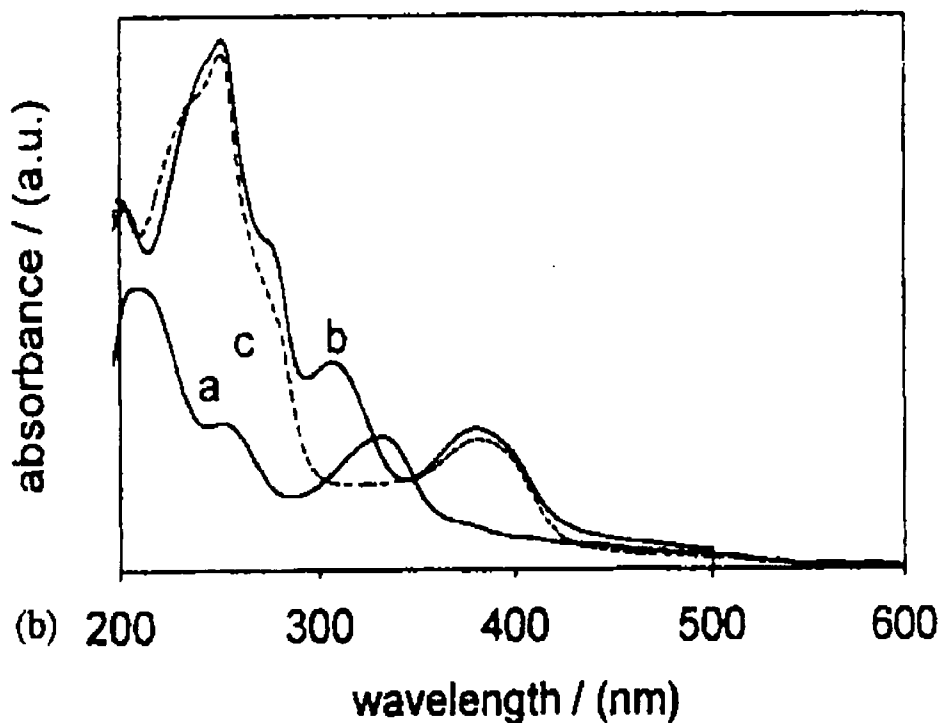


Figure 3.14: Optical absorption spectrum for (a) 1 LB layer MBSH (b) 10 LB layers poly(CuMBSH) (c) 10 LB layers poly(ZnCuMBSH), not used in this work [reproduced from reference 17].

3.3.4 Optical properties

(a) UV/Visible spectroscopy

The UV/Visible spectra for MBSH monomers, in the pure form and incorporating copper and zinc metal ions are shown in figure 3.14. Samples were prepared by depositing 10 LB layers onto quartz glass slides (monolayer in the case of MBSH). The spectra for poly(CuMBSH) and poly(ZnMBSH) were different from that of the monomer indicating that a complex formation (MBSH reacting with the metal dissolved in the subphase) took place at the air/subphase interface.¹⁶

3.4 Conclusion

A brief discussion of the chemical and physical properties of the three materials used has been presented. This included their ability to form floating layers and subsequent Langmuir-Blodgett deposition characteristics. The optical absorption spectrum for each material, along with permittivity and layer thickness data (obtained using surface plasmon resonance), has also been reported. The syntheses of the compounds have also been briefly explained.

References

- 1 C.C. Leznoff, A.B.P. Lever, "**Phthalocyanine: Properties and Applications**", *VCH Publishers*, Cambridge (UK), **1989**, 5.
- 2 L. Pasimeni, M. Meneghetti, R. Rella, L. Valli, C. Granito, L. Troisi, *Thin Solid Films*, **265**, **1995**, 58-65.
- 3 R.D. Gould, *Co-ordination Chemistry Reviews*, **156**, **1996**, 237-274.
- 4 C.C. Leznoff, A.B.P. Lever, "**Phthalocyanine: Properties and Applications**", *VCH Publishers*, Cambridge (UK), **1989**, 362-378.
- 5 Y. Sadaoka, W. Göpel, B. Suhr, A. Rager, *Journal of Materials Science Letters*, **9**, **1990**, 1481-1483.
- 6 Y.Q. Liu, D.B. Zhu, T. Wada, H. Sasabe, *Synthetic Metals*, **71**, **1995**, 2283-2284.
- 7 C. Granito, L.M. Goldenberg, M.R. Bryce, A.P. Monkman, L. Troisi, L. Pasimeni, M.C. Petty, *Langmuir*, **12** (2), **1996**, 472-476.
- 8 J.N. Wilde, M.C. Petty, J. Saffell, A. Tempore, L. Valli, *Measurement and Control*, **30**, **1997**, 269-273.
- 9 C. Granito, J.N. Wilde, M.C. Petty, S. Houghton, P.J. Iredale, *Thin Solid Films*, **284-285**, **1996**, 98-101.
- 10 F.G.A. Stone, W.A.G. Graham, "**Inorganic Polymers**" *Academic Press*, London, **1962**, 189-307.

-
- 11 N. Carr, M.J. Goodwin, A.M. McRoberts, G.W. Gray, R. Marsden, R.M. Scrowston, *Makromol. Chem., Rapid Commun.*, **8**, **1987**, 487-493.
 - 12 N. Kalita, J.P. Cresswell, M.C. Petty, A. McRoberts, D. Lacey, G. Gray, M.J. Goodwin, N. Carr, *Optical Materials*, **1**, **1992**, 259-265.
 - 13 N. Kalita, *PhD Thesis*, University of Durham, **1991**.
 - 14 F.G.A. Stone, W.A.G. Graham, "**Inorganic Polymers**" *Academic Press*, London, **1962**, 447-522.
 - 15 A.K. Dey, *J. Indian Chem. Soc.*, **63**, **1986**, 357-370.
 - 16 U. Öertel, J. Nagel, *Thin Solid Films*, 284-285, **1996**, 313-316.
 - 17 J.N. Wilde, A.J. Wigman, J. Nagel, A. Beeby, B. Tanner, M.C. Petty, *Acta Polymer.*, **49**, **1998**, 294-300.
 - 18 J.N. Wilde, J. Nagel, M.C. Petty, *Thin Solid Films*, in press.
 - 19 C.S. Marvel, N. Tarköy, *J. Am. Chem. Soc.*, **79**, **1957**, 6000-6002.
 - 20 M.C. Petty, "**Langmuir Blodgett Films: an Introduction**", *Cambridge University Press*, UK, **1996**, 60-61.

Chapter Four

Experimental Methods

4.0 Preface

This chapter is concerned with the experimental techniques used in the course of this work. The equipment and methods used in the deposition and characterisation of thin organic films have been detailed. Film deposition was undertaken using the Langmuir-Blodgett technique and film characterisation was performed using surface plasmon resonance, ellipsometry, low angle X-ray diffraction, electron spin resonance, UV/Visible spectroscopy, Brewster angle microscopy and surface profiling.

4.1 Langmuir-Blodgett technique

Surface pressure versus area measurements and Langmuir-Blodgett (LB) deposition studies were carried out in a class 10,000 clean room using constant perimeter LB troughs designed at the University of Durham. Figure 4.1 shows a schematic diagram of the constant perimeter LB deposition system. The barrier tape fabricated from glass fibre coated with polytetrafluoroethylene (PTFE) was mounted on 6 PTFE rollers. Two rollers were fixed and the other four were attached to movable metal arms driven by a variable speed dc motor and toothed belt system. The insets to figure 4.1 (a) and (b) show the maximum and minimum areas the system could attain with the movable metal

arm. The final positions of the metal arms were controlled by microswitches connected to control electronics.

The subphase consisted of ultra pure water, derived from filtered tap water. The water was purified by pre-filtering, reverse osmosis, carbon filtration, two stages of de-ionisation, UV sterilisation and finally 0.2 μm particulate filtration. Water quality was monitored using a Anatel Total Organic Carbon (TOC) analyser which indicated a resistivity of $> 17.5 \text{ M}\Omega \text{ cm}$. The trough was constructed from either glass or PTFE and mounted on a hand operated mechanical jack. This allowed the trough to be lowered below the level of the barrier tape to aid cleaning, or raised to adjust the water level relative to the barrier tape. Troughs were removed and cleaned in a fume cupboard with chloroform and rinsed in ultra pure water. The barrier tapes and rollers were also removed and cleaned with chloroform and rinsed in ultra pure water. The surface pressure was measured by a Wilhelmy plate.¹ This consisted of a piece of chromatography paper (3 cm long by 1 cm wide) partially immersed in the subphase linked to a microbalance by a thread. Changes in the force on the plate due to variations in surface tension were measured by the balance (via the Wilhelmy plate sensor) and converted into an electrical signal. This signal was used to adjust the position of the barrier tape so a desired surface pressure could be maintained. To determine the surface pressure, it is important to know the forces acting on the sensor, these are gravity and surface tension (downward forces), and buoyancy, due to displaced water (upward force). For a rectangular plate of density ρ_m length l , width w and thickness t immersed depth h in a subphase of density ρ_s , the net downward force is shown in equation 4.1.

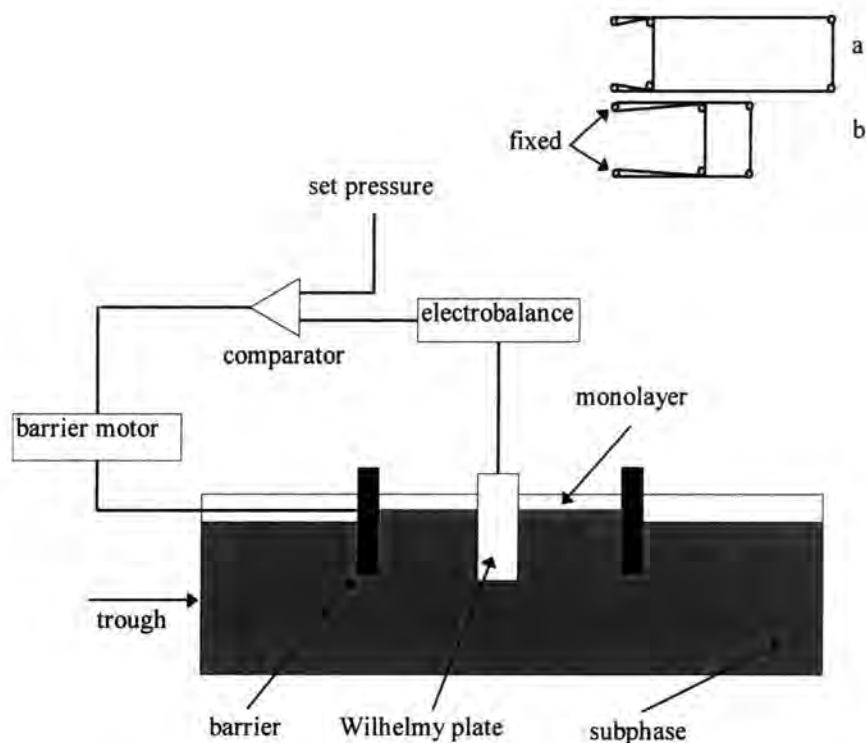


Figure 4.1: Schematic diagram of the feedback system used to allow the control of monolayer surface pressure. The constant perimeter barrier system is shown inset.

$$F = \rho_m g l w t + 2\gamma(t + w) \cos\theta - \rho_s g t w h \quad [4.1]$$

where γ is the surface tension of the liquid and θ is the contact angle on the solid plate and g is the gravitational constant. For a completely wetted plate ($\theta = 0$) and the thickness (t) of the sensor being very much smaller than the width (w), the change in force due to a change in surface tension is given by

$$\Delta\gamma = \frac{\Delta F}{2w} \quad [4.2]$$

The dipping head consisted of a variable dc motor driving a micrometer screw. Samples were clamped into a suitable holder which could be fitted on to the front of the dipping head. The position of the barriers and the dipping head were monitored using high

precision linear potentiometers. This allowed precise control of the dipping process giving the user the ability to control the upper and lower deposition limits and thus the area of substrate to be covered.

4.2 Optical and structural characterisation

4.2.1 Surface plasmon resonance

The theory of surface plasmons was generated from Maxwell's equations applied to a plasma (the free electrons in a metal, which are treated as an electron liquid of high density). Density changes on the surface of this so called liquid are called surface plasmons or polaritons.² The excitation of these plasmons is not possible by direct illumination of a metallic surface, so a special arrangement is needed. Two approaches have been explored and are in wide use. The first is known as the Kretschmann-Rather configuration⁶, where a metallic layer is deposited onto the base of a prism (figure 4.2)

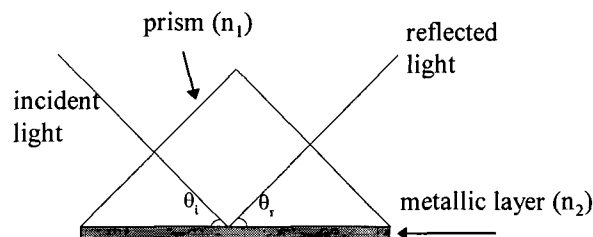


Figure 4.2: Kretschmann-Rather configuration used to excite surface plasmons.

The second arrangement is known as the Otto configuration³, in this case the metallic layer is separated from the base of a prism by a distance d , comparable to the wavelength of the illumination light in air, see figure 4.3. In practice, it can be difficult to place a metallic layer so close to the base of the prism (less than $1 \mu\text{m}$). In this work

the Kretschmann-Rather geometry was used and mathematical explanations will reflect this experimental setup.

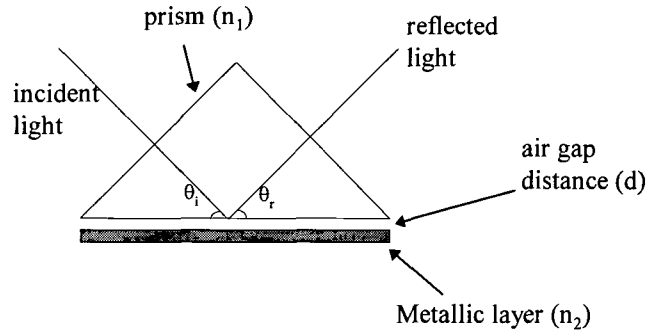


Figure 4.3: Otto geometry used to excite surface plasmon, where $n_1 > n_2$.

The incident angle of the excitation light has to be above the critical angle θ_c for the prism, given by a modified version of Snell's law

$$\sin \theta_c = \frac{n_0}{n_1} \quad [4.3]$$

where n_0 is the refractive index of the material around the prism (usually air ($n=1$)) and n_1 is the refractive index of the prism. At θ_c the light undergoes total internal reflection. As a result, an evanescent wave is created which propagates along the interface between the metal and the prism. This electromagnetic wave will penetrate a small distance into the metallic film d_p .⁴

$$d_p = \frac{\lambda}{2\pi n_1} \left[\sin^2 \theta_i - \left(\frac{n_2}{n_1} \right)^2 \right]^{-\frac{1}{2}} \quad [4.4]$$

where λ is the wavelength of the impinging light, n_1 is the refractive index of the prism, n_2 is the refractive index of the metallic layer and θ_i is the internal angle the light makes

with the metallic surface (ie angle of incidence ($\theta_i > \theta_c$)). In certain circumstances, the evanescent wave can couple with free electrons in the metallic layer. In doing so it excites the surface plasmons at the interface between the metallic layer and a dielectric (material deposited onto the metallic layer or air). This situation is similar to a mechanical resonance and, as a result, this phenomenon is known as surface plasmon resonance (SPR). The transfer of energy from the evanescent wave to the surface plasmons causes an attenuation in the intensity of the reflected light. One of the properties of surface plasmons is that they require the impinging light to have its electric field orientated normal to the metal/dielectric interface.⁵ If the media are isotropic then the only way this can be achieved is with p-polarised light (TM).

Conventional studies of surface plasmons use visible radiation, typically from a He-Ne laser, with a silicon photodiode to record the intensity of the reflected light. In general silver or gold are chosen as metallic layers because they have suitable dielectric constants at this wavelength and they produce sharpest resonances. Scanning the angle of the incident laser light over a range (above θ_c) and monitoring the reflected light intensity, via the silicon photodiode, it is possible to generate a plot unique to the metallic layer. Figure 4.4 shows a typical SPR curve. The first rise on the plot (at $\theta \approx 41^\circ$) corresponds to the critical angle of the prism. As the laser scans through angles above θ_c there is a rapid fall off in reflectivity (normalised intensity of reflected light). This is due to the excitation of surface plasmons in the metallic/dielectric interface. At $\theta = 42.6^\circ$, the reflect intensity reaches a minimum. At this point most of the impinging light is used to excite the surface plasmons, this is therefore known as the “SPR point”.

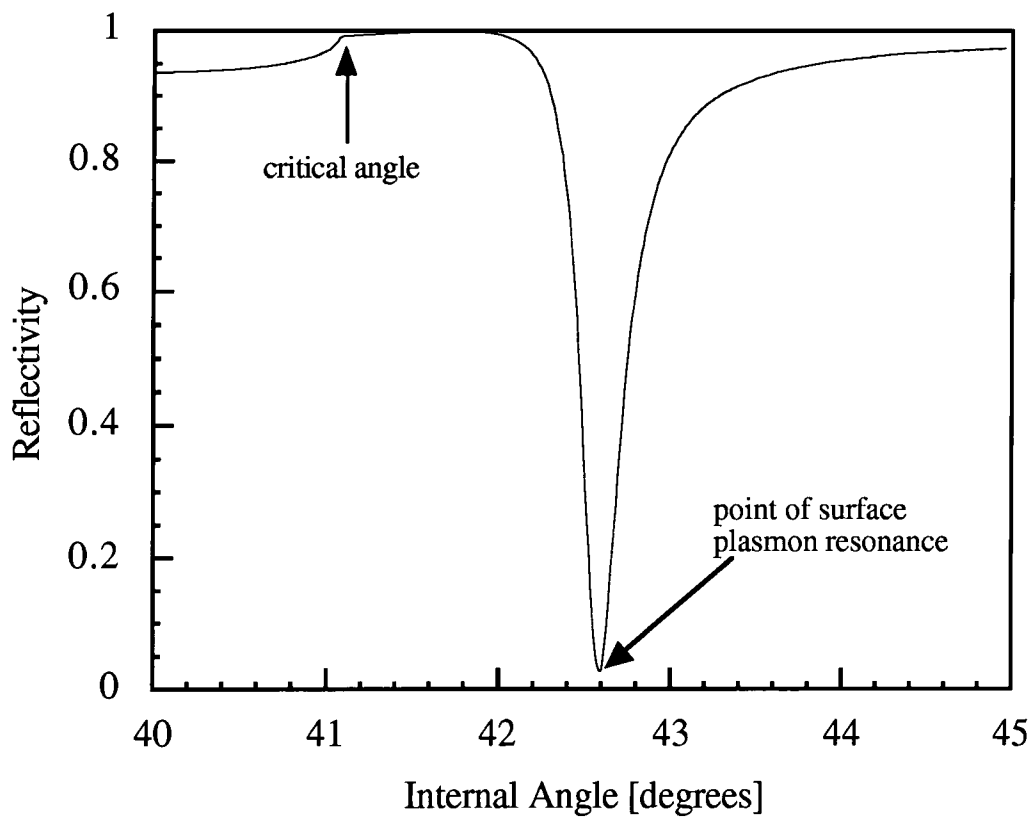


Figure 4.4: Surface plasmon resonance curve for 50 nm silver layer deposited on a quartz glass slide ($\lambda = 632.8$ nm)

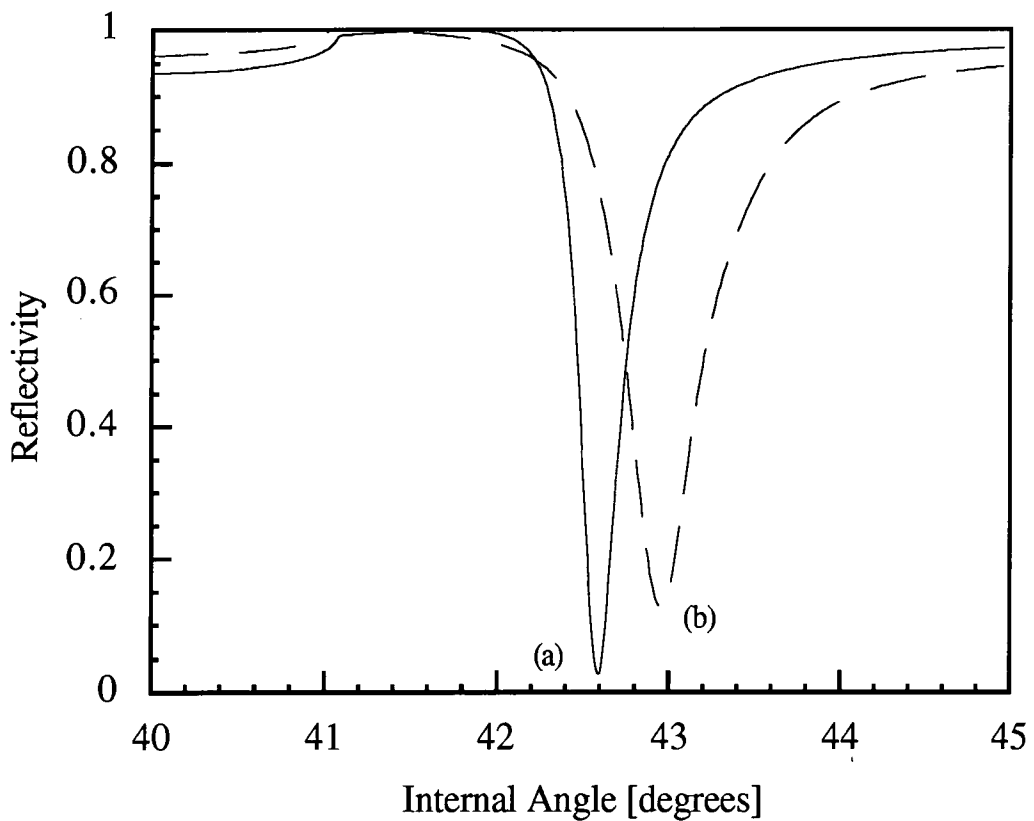


Figure 4.5: Surface plasmon resonance curve for (a) 50 nm silver layer, (b) 1 LB layer deposited on the silver layer ($\lambda = 632.8$ nm).

At angles beyond this, less of the reflected light is used to excite the surface plasmons and so the reflected intensity returns to its initial value.

As stated previously, the electromagnetic energy penetrates a distance into the metallic layer (d_p). If the metal layer is thinner than d_p , this evanescent wave will penetrate through to the metal/air interface. If a layer is deposited onto the metallic layer, via the Langmuir-Blodgett technique (or others such as spinning, evaporation or spraying), this will change the shape and angular position of the SPR minimum. This is shown in figure 4.5, for 1 LB layer of copper phthalocyanine deposited onto a 50 nm thick layer of silver. The addition of this new layer has caused the SPR curve to move to higher angles and reduce in intensity. This change is related to the optical properties of the new film. Knowing the optical constants for the metallic layer, it is possible to derive values not only for the thickness of this new layer, but also its permittivity. The parallel component (x -direction) of the wave vector K_x of the incident light on the metallic layer is given by

$$K_x = \frac{\omega}{c} \sqrt{\epsilon_0} \sin \theta_i \quad [4.5]$$

where ϵ_0 is the dielectric constant of the prism, θ_i is the internal angle of the incident radiation, $\omega = 2\pi f$ (f is the frequency of excitation radiation) and c is the speed of light in a vacuum. The wave vector of the surface plasmons K_{sp} is^{4,6}

$$K_{sp} = \frac{\omega}{c} \left[\frac{\epsilon_1 \epsilon_2}{\epsilon_1 + \epsilon_2} \right]^{\frac{1}{2}} \quad [4.6]$$

where ϵ_1 and ϵ_2 are the dielectric constants of the metal and any overlayer, respectively. At resonance, when $K_{sp} = K_x$ and $\theta_i = \theta_{sp}$, the angle of SPR minimum, the dielectric constant of an over layer (ϵ_2) is given as

$$\epsilon_2 = \frac{\epsilon_1 \epsilon_0 \sin^2 \theta_{sp}}{\epsilon_1 - \epsilon_0 \sin^2 \theta_{sp}} \quad [4.7]$$

The dielectric constants of the metal and the overlayer are of the form

$$\epsilon = \epsilon' + i\epsilon'' \quad [4.8]$$

This is a generalised case, since it has been assumed that both the prism and dielectric are lossless. However the situation is different in practice. For a detailed mathematical analysis of this situation the reader is directed to a number of research papers.⁷⁻⁹

The experimental setup used to generate SPR curves is shown in figure 4.6. The laser is plane polarised and is adjusted to give p-polarisation by rotation within its mount. The prism is of refractive index 1.52 and mounted on a motorised rotation stage with a minimum step size of 0.004 degrees. Silvered glass slides are mounted onto the base of the prism using index matching fluid ($n = 1.52$ at 25°C) to form a good optical contact. The reflected light is monitored by a silicon photodiode mounted on a separate rotation stage linked to the main stage by a gear system of ratio 1:2 (ie, prism moves through θ , detector moves through 2θ). The system is controlled by a 486 PC with data from the Si photodiode passed via a voltmeter and IEEE interface card to the computer.

To derive the optical constants of the LB layer from the SPR curves, it is essential to know the permittivity and thickness of the metallic layer. These values can be obtained in a number of ways, the most useful is to measure the properties of the silver layer before the deposition of LB film. The values for permittivity and refractive index were modelled on a UNIX workstation using a computer programme developed at the University of Durham.¹⁰

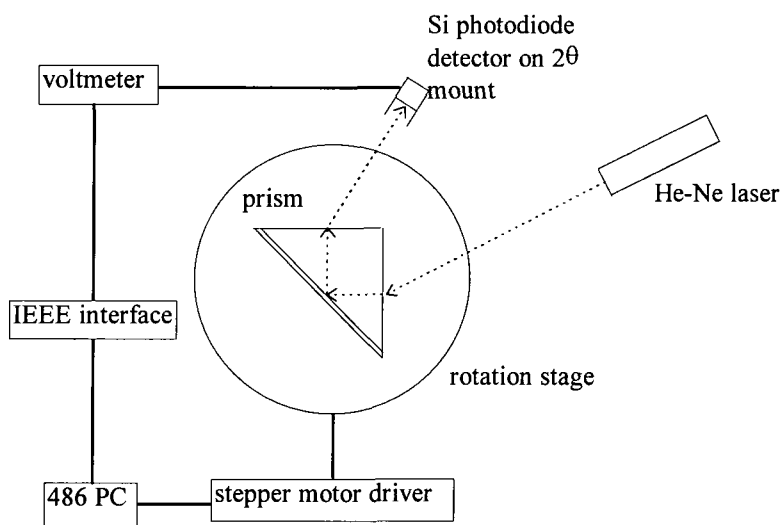


Figure 4.6: Experimental setup for computer controlled surface plasmon resonance measurements.

4.2.2 Ellipsometry

Ellipsometry has been used to determine the thickness and optical constants of many thin layers, including LB films. When a light beam with a known polarisation is reflected from a surface, the amplitude and phase of the parallel and perpendicular components of the electric field are modified. If a thin film is deposited onto a known substrate, the change in the polarisation state of the light beam can be used to determine the thickness and permittivity of the additional layer. In this work, the thickness and

permittivities of LB films deposited onto silicon substrates were measured using ellipsometry.

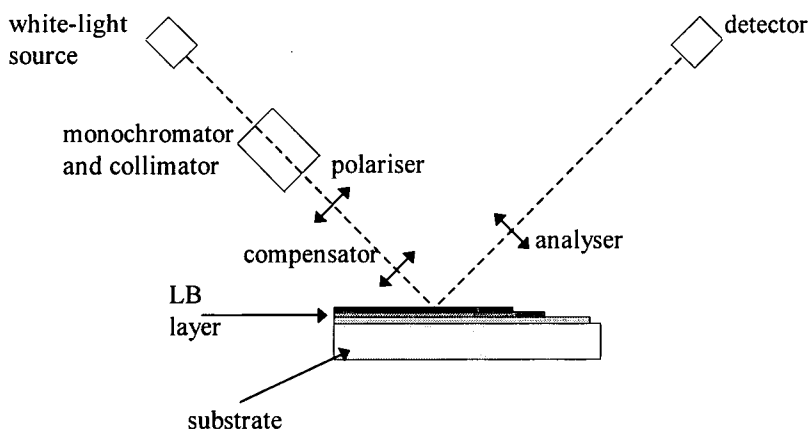


Figure 4.7: Optical system of Rudolph AutoEl-IV ellipsometer.

Figure 4.7 shows the optical arrangement of the Rudolph AutoEl-IV ellipsometer used in this work. The source is a white light which is filtered and collimated to give monochromatic unpolarised light, this is then passed through a rotatable prism polariser. The resulting linearly polarised light is then passed through a compensator, the output of which is elliptically polarised light. The light is reflected from the sample and passed through an analyser, this is a second polariser. Finally the intensity of the reflected light is monitored by a photomultiplier tube (PMT).

The ellipsometer was capable of operating at three different wavelengths: 405.0; 546.1; and 632.8 nm. The equipment had a built-in microprocessor to control the measurements and perform calculations. These assumed that the LB films were non-absorbing and isotropic. This is not the case in practice, but studies on fatty acid films

have shown that values derived from this simple model do not deviate significantly from those obtained using anisotropic models.¹¹

For the ellipsometric measurement of LB layers, silicon substrates were cleaned with pure water and placed in an ultrasonic bath in a 2% solution of dimethyldichlorosilane ((CH₃)₂SiCl₂) in 1,1,1-trichloroethane. This solution creates a hydrophobic surface on silicon which improves the LB film transfer. On removal from the ultrasonic bath, the substrates were rinsed with ultrapure water to remove any traces of the (CH₃)₂SiCl₂ before being dried in a stream of nitrogen. A stepped LB film structure, e.g. 20, 40, 60 LB layers, was deposited, leaving part of the silicon substrate uncoated. It was necessary to determine the optical constants for the silicon layer and subsequently input these values into the ellipsometer. The results obtained are cyclic, with many possible thickness, thus each sample was measured at two wavelengths 546.1 and 632.8 nm. The thickness of the LB layer was independent of wavelength and by comparing the possible thicknesses at both wavelengths, the program could select any results which matched.

4.2.3 Low angle X-ray diffraction

Low angle X-ray diffraction is a powerful tool for the determination of crystal structures. For example, it is possible to determine total thickness, distance between layers or crystal planes and degree of film roughness. X-rays were discovered in 1895 by William Roentgen, who bombarded metals with high energy electrons. From diffraction experiments performed in 1899, it was suggested that X-rays were electromagnetic radiation with wavelengths around 0.1 nm. In 1912, Max von Laude

scattered X-rays from solids and, since the wavelength of X-rays was about the same as the distance between atoms in crystals (NaCl), diffraction effects were observed. It is from these experiments that modern X-ray crystallography developed. A schematic diagram of an X-ray spectrometer can be seen in figure 4.8.¹² Applying a voltage to the filament gives the electrons enough energy so that they are ejected from it. The electrons bombard the anode plate changing the state of its atomic electrons (ie, promoting them to higher orbitals), the resultant release of energy is in the form of X-rays (as seen by Roentgen). The X-rays are initially collimated by the two polarisers placed in their path. The beam is then scattered by the sample, producing a unique diffraction pattern. A moveable detector records the X-ray intensity as a function of θ to determine where constructive interference occurs. The point at which constructive interference occurs is known as the Bragg peak. This situation arises because of the way X-rays are reflected from adjacent layers (within LB films) or atomic planes.

LB films are made up of a series of layers deposited on top of each other. X-rays penetrate the film and are reflected from different layers. If the separation between layers is d , then for constructive interference to occur the difference in path lengths has to be $2d(\sin\theta)$, where θ is measured from the film surface.

This model of X-ray diffraction from adjacent layers can be seen in figure 4.9. For constructive interference

$$\lambda = \frac{2d}{n} \sin \theta \quad \text{where } n = 1, 2, 3 \dots \quad [4.9]$$

where d is the interplanar spacing, θ is the incident angle of the X-rays, λ is their wavelength and n is the order of constructive interference. This is known as Bragg's law.

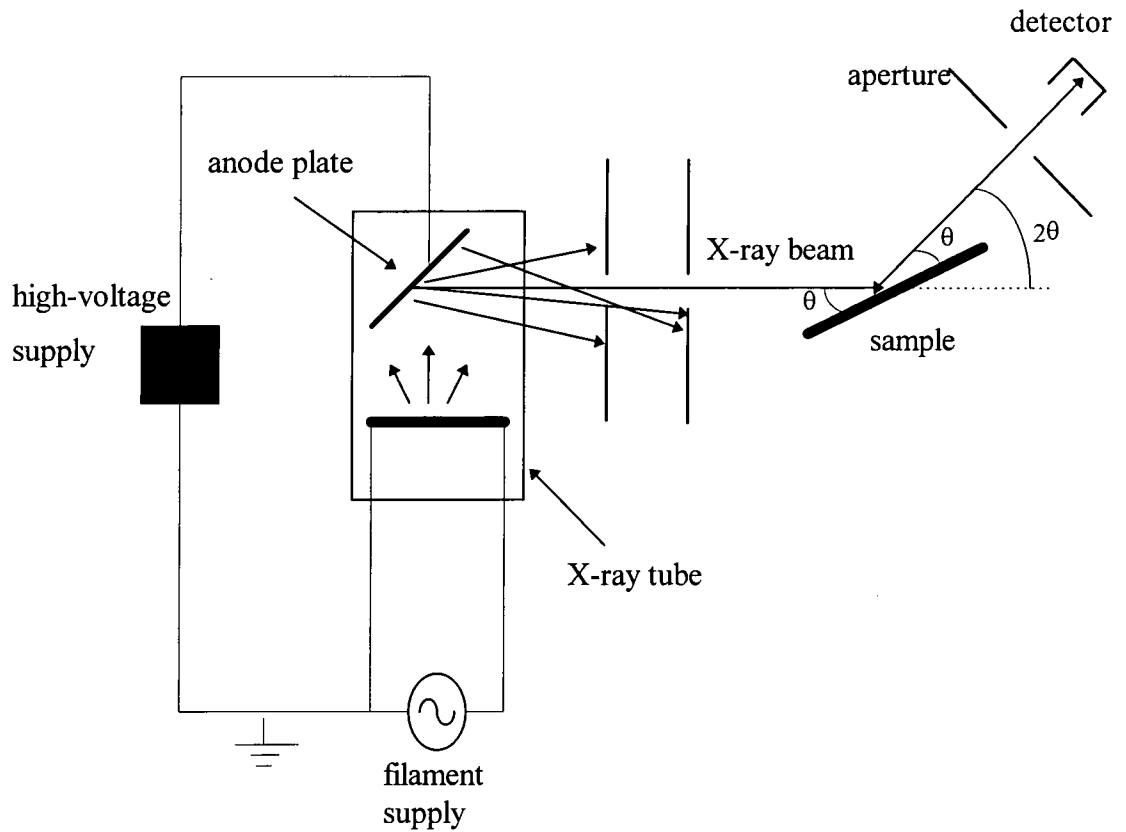


Figure 4.8: Schematic diagram of an X-ray spectrometer used to determine the properties of crystals and other materials. [reproduced from reference 12]

There are also reflections from the top and bottom of the multilayer film. This was first noted by Kiessig and forms one of the most accurate methods to determine the total thickness of a film. As before, the equation for total film thickness is determined by the path distance between the top and bottom of the film

$$t = \frac{n\lambda}{2 \sin \theta} \quad n = 1,2,3\dots \quad [4.10]$$

With most X-ray diffraction traces (shown in figure 4.10) there are a number of Kiessig fringes.

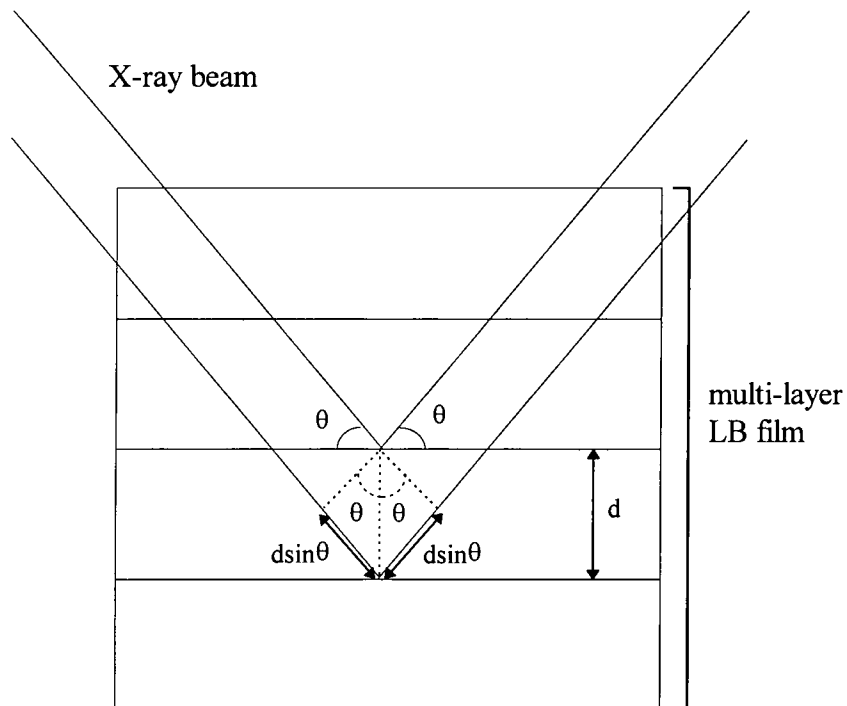


Figure 4.9: The geometry of X-ray diffraction between adjacent LB layers.

The most accurate way of determining the total thickness is to take an average over all of the fringes, thus equation 4.10 becomes

$$t = \frac{\lambda}{2 \sin(\theta_{\max} - \theta_{\min})} \quad [4.11]$$

where θ_{\max} is the position of the last Kiessig fringe and θ_{\min} is the position of the first fringe.¹³

Using the experimental arrangement depicted in figure 4.8, there are three different measurements which can be recorded: the specular; off-specular and the transverse-

diffuse reflections. The only difference between the plots is the orientation of the substrate relative to the incident X-ray beam, figure 4.10.

The specular component. In this situation the detector is placed so that the angle of the incident beam equals the angle of reflected beam. The sample and detector are then scanned through a range of angles, producing the plot shown in figure 4.10 (a). This gives the strongest signal, showing reflections from the internal structure of the film. In figure 4.10 (a) the Kiessig fringes are shown as the series of 'bumps' at the far left of the plot and the Bragg peak is at about 1° . It is possible to determine the quality of LB layer packing, known as the radius of correlation (R_c). The width of the Bragg peak at half-height is used to determine this (see Chapter Six).

The off-specular component. This case is shown in figure 4.10 (b). There are no evident Kiessig fringes, yet there is a Bragg peak (as before) and the intensity (number of counts per second) of the reflected beam has reduced. This is due to the angle of the detector being 0.1° off the angle of incidence. This scan eliminates any effects from the substrate or equipment (ie, a control). It is usual to plot a graph of (the specular component) - (the off-specular component), this gives a plot representative of the sample itself.

The transverse-diffuse plot. This measurement is generated by moving the incident angle to the position of a Bragg peak, then moving the sample through a range of angles either side of this. The plot in figure 4.10 (c) is for the first Bragg peak shown in the

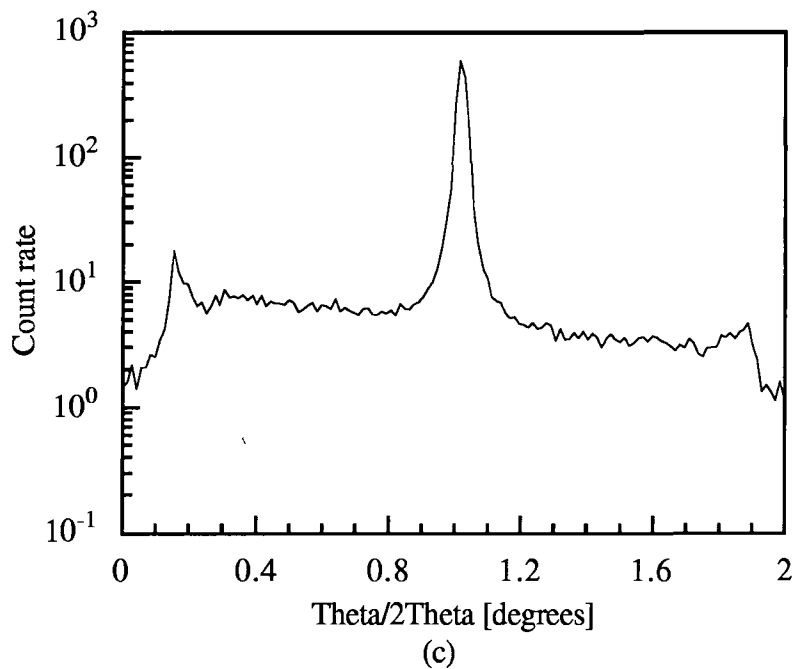
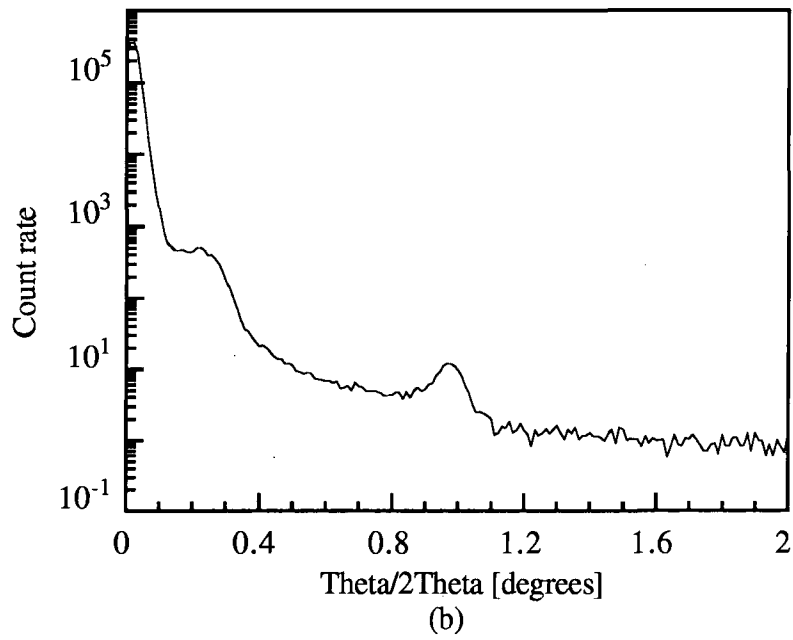
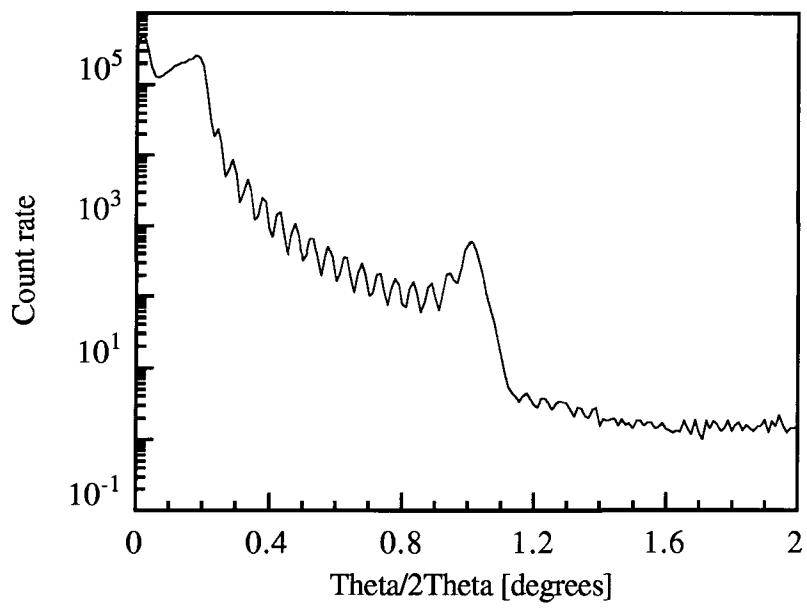


Figure 4.10: Low angle X-ray diffraction plots for an LB film deposited on single crystal silicon (a) Specular plot. (b) Off-Specular plot (c) Transverse-diffuse plot.

previous two plots. A large spike is generated when the incident angle of the X-ray beam equals the angle of reflection (ie, return to the specular condition). It is possible to determine the degree of roughness within the film. The total interfacial roughness can be split into two parts: the correlated roughness (similar to a perfect 3d crystal); and the uncorrelated roughness (deviations from this model), shown in figure 4.11.¹⁴

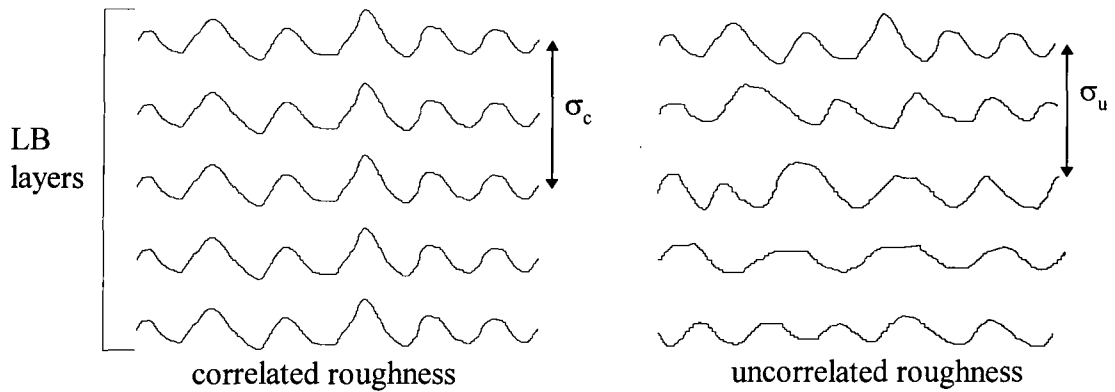


Figure 4.11: A schematic view of the correlated and uncorrelated interfacial roughness.

Multilayer films have vertical and horizontal roughness. The scattering of the X-ray beam will be increased as the interlayer roughness increases (either correlated or uncorrelated). It is possible to determine the roughness in the z-plane (vertical) of a film, but in doing so the roughness of the other planes (x and y) are ignored, for simplicity.

$$I_{diff} = I_o \exp(-S_z^2 \sigma_u^2) \times \left[1 - \exp(-S_z^2 \sigma_c^2) \right] \quad [4.12]$$

$$I_{spec} = I_o \exp\left[-S_z^2 (\sigma_u^2 + \sigma_c^2)\right] \quad [4.13]$$

where I_o is the reflected intensity from an ideal mirror, σ_c is the correlated roughness, σ_u is the uncorrelated roughness and S_z is

$$S_z = \frac{4\pi \sin\left(\frac{\theta}{2}\right)}{\lambda} \quad [4.14]$$

Taking the ratio of the specular component to the diffuse it is possible to derive an expression for σ_c .

$$\sigma_c = \frac{\sqrt{\ln\left(\frac{I_{diff}}{I_{spec}} + 1\right)}}{S_z} \quad [4.15]$$

Values for I_{diff} and I_{spec} can be determined from figure 4.10 (c) by finding the area under the first order Bragg peak (I_{spec}) and the area under the rest of the curve (I_{diff}). This is because S_z will be maximum at the Bragg peaks, due to the uncorrelated or correlated roughness of the film. To derive a value for the uncorrelated roughness of the film, it is essential to know a value for I_0 . This can be calculated from theory and is the reflected intensity of the X-ray beam from an ideal mirror. In the case of this work, I_0 was unknown for the machine used and, as a result, values for σ_u were not derived.

On their own these data only provide an estimation of the roughness of the film in the z-direction. To obtain accurate information on the magnitude of roughness it would be necessary to model the shape of the first order Bragg peak, which was not done in this work.

4.2.4 Electron spin resonance

Electron spin resonance (ESR) spectroscopy is a powerful technique that provides information on molecular orientation, distribution of paramagnetic centres and the extent of disorder within thin films. Some atoms or molecules contain electrons with unpaired spins (ie, free atoms, free radicals or compounds of transition metals with unfilled electron shells) and it is from these materials that ESR spectra are expected. Materials with unpaired electrons also show some degree of paramagnetism and therefore ESR is also known as electron paramagnetic resonance (EPR). ESR spectra arise from mechanisms by which the spin of a particle can interact with a beam of electromagnetic radiation. If the incoming radiation has the same frequency as the particle of interest, it interacts coherently and energy is exchanged. At any other frequency there will be no interaction. There are four important characteristics of ESR spectra, these are, intensity, width, position and multiplet structure.

The intensity of ESR spectra is proportional to the number of free radicals and paramagnetic centres present within films. This technique provides an estimation of the number of the free radicals down to 10^{-13} mole.¹⁵

The width of resonance depends strongly on the relaxation time of the electronic spin state. Electron spin relaxation times of the order 10^{-7} seconds, with line widths of 10 MHz (*ca* 10^{-4} tesla), are detectable.

The position of absorption varies directly with the applied field and since different instruments use different fields it is convenient to quote the position of absorption in terms of its g value. The g value, or Landé splitting factor, is a numerical factor which depends upon the state of the electrons within the atom. The g value for most materials does not deviate much from 2 (representative of a free electron), though some values between 0.2 and 8 have been reported for ionic crystals. The reason for this is that in free radicals, electrons are not confined to a localised orbit, but can move over an orbit encompassing the whole molecule. This is very similar to an electron in free space. Unpaired electrons in ionic crystals though are bound to another atom (usually a transition metal). Thus the electron is localised in a particular orbit and gives a greater g value than free radicals.

The multiplet structure refers to the spectral features formed by more than two closely spaced lines. There are two types of multiplet structure. The first is the fine structure which only occurs in ionic crystals. The second is the hyperfine structure seen in both crystals and free radicals. Fine structure arises when there is more than one unpaired electron, whilst the hyperfine arises through the coupling of the unpaired electron and a neighbouring nuclei.

It is also possible from ESR spectra to determine the orientation of molecules on a substrate. The effective g value of ion radicals such as Cu^{2+} can be characterised by changing the angle of the substrate relative to the applied magnetic field. This is done by mounting the substrate in a chamber that can be rotated about a central axis. As the

observed g values change from a maximum to a minimum, due to interaction between the applied field and the electron spin, a minimum indicates that the applied field is orientated normal to the main molecular axis.¹⁵

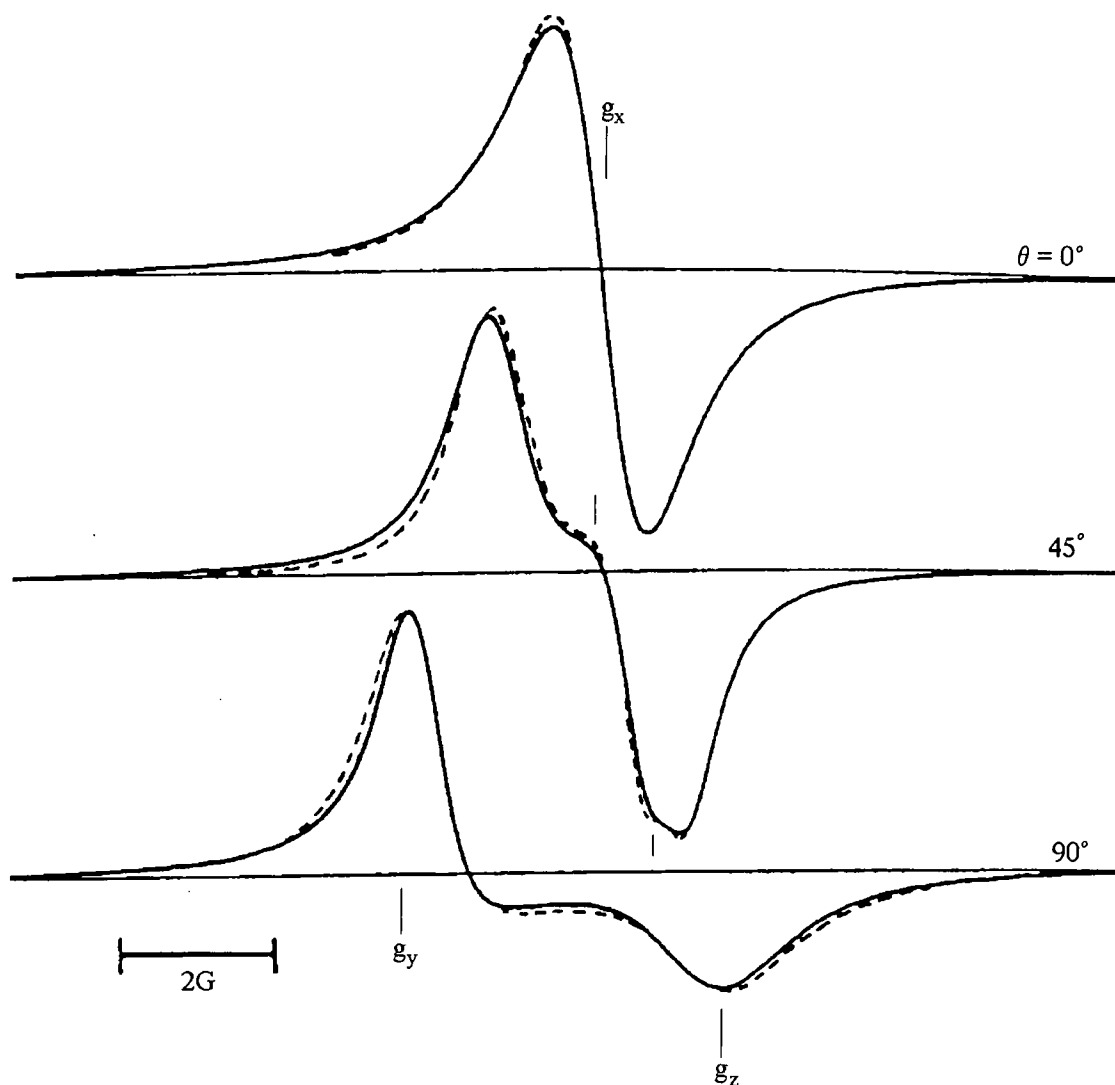


Figure 4.12: Electron spin resonance spectra for an LB film of C₂₂PT at the K band at 300K for $\theta = 0^\circ$, 45° and 90° . Where θ is the angle between the external magnetic field and the plane normal. [reproduced from reference 14]

Figure 4.12 shows ESR spectra for LB layers of $C_{22}PT$ at 0° , 45° and 90° to the dipping plane. The position of the g -factor due to the x component, is shown in the first curve and g due to the y and z components are indicated in the third curve; the position of the linewidth minimum is shown in the second curve.¹⁵

4.2.5 Brewster angle microscopy

Brewster angle microscopy relies on the fact that electromagnetic radiation is plane polarised when reflected from a surface (eg, water). When unpolarised light is incident upon a material surface, the light with its polarisation vector perpendicular to the plane of incidence is preferentially reflected.

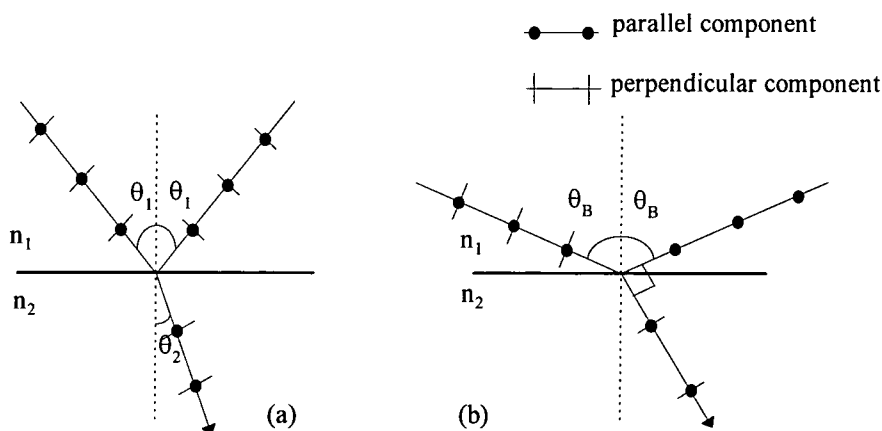


Figure 4.13: In (a) light reflected from the interface between two media of refractive index n_1 and n_2 is partially plane polarised (less of the parallel component than the perpendicular component), while in (b) for the Brewster angle.

Changing the angle of incidence of the light changes the intensity of parallel and perpendicular components of the reflected light. At a particular angle θ_B the parallel component of the reflected light falls to zero (ie, it is all transmitted through the material). This angle is known as the Brewster angle, shown in figure 4.13 (b).¹⁶

For Brewster angle microscopy measurements, a p-polarised light source (usually a He-Ne ($\lambda=632.8$ nm)) is used. When p-polarised light is incident at the interface between materials of different refractive indices ($n_2>n_1$), at the Brewster angle no visible light is reflected. For the air/water interface n_1 (air) = 1 and n_2 (water) = 1.333, at $\lambda = 632.8$ nm the Brewster angle is

$$\tan \theta_B = \frac{n_2}{n_1} \quad [4.16]$$

Using equation 4.16, the Brewster angle is 53.1° , for the air/water interface. The intensity of reflected light shows a minimum at the Brewster angle, but does not totally vanish as stated by the theory. This is because there is no sharp optical boundary between the two media and the surface of the water is not perfectly planar.¹⁷

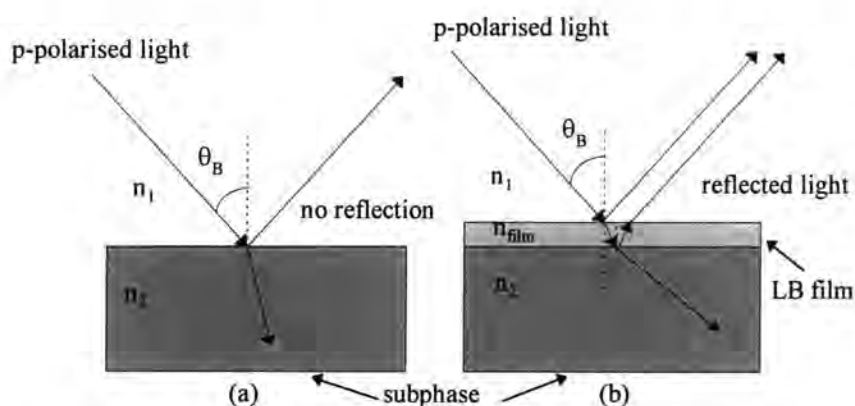


Figure 4.14: Schematic of light incident at (a) an air/water interface, (b) the interface of air and an LB film spread on a subphase of pure water.

If a layer of amphiphilic molecules is introduced at the air/water interface to form a new interface, θ_B no longer corresponds to the Brewster angle for this interface. Under these conditions, light is reflected and may be observed with a microscope situated at the Brewster angle, as shown in figure 4.14.

Brewster angle microscopy measurements were undertaken in the Department of Chemistry of Durham using a 8 mW He-Ne laser with the beam expanded to a diameter of 5mm. The reflected beam was passed via a Glan-Thompson polariser to a COHU 4910 series CCD (charge coupled device) camera (resolution of 520 x 350 lines) fitted with an Optem zoom lens (focal range 75-85 mm; resolution 2 μm per pixel). The laser and camera were each mounted on rotation stages (Ealing Electro-Optics) which allowed small adjustments ($\pm 0.00025^\circ$) to be made.¹⁸

4.2.6 UV/Visible spectroscopy

Absorption spectra of multilayer LB films deposited onto quartz slides were measured over the range 200 to 900 nm in 1 nm steps using a Perkin-Elmer Lambda 19 UV-VIS-NIR dual beam spectrophotometer. A baseline was recorded with two identical slides as samples, one in the path of each beam. One of these slides was then removed and replaced by one with an LB coating. The other slide remained in place as a reference sample as the spectra were recorded.

4.2.7 Surface profiling

Surface profiling is a technique which has been used to measure the thickness of cadmium-stearate LB layers.¹⁹ This involves moving a stylus across the surface of a sample under test. The upward force on the stylus, due to the thickness of the sample, can then be measured electronically against stylus position. Since the profilometer detects changes in height, a step must be formed in the film. In this work, this was achieved by carefully wiping away a portion of the film using a tissue soaked in a

suitable organic solvent, usually chloroform. To prevent the stylus from damaging the surface of the film, a layer of aluminium *ca* 150 nm thick was then deposited by thermal evaporation over the step between the film and the area of cleaned substrate. The stylus profilometer used was a Tencor Instruments Alpha-step 200. A stylus force of 8 ± 1 mg was used, together with a scan length of 1 - 2 mm and a sample frequency of 1 reading per micron.

4.3 Data processing

4.3.1 Neural networks

There has been great interest in using neural networks in conjunction with gas sensitive devices over recent years. This is partially to add an extra dimension of discernability to materials, or systems that show partial recognition to certain gases or vapours. The only limitation of using neural networks is that they will not improve systems that produce indeterminate responses between vapours.

Neural networks consist of a number of discrete elements called neurons, which act as processors of the data. Most systems consist of a three layer network, two layers that can be seen, called the input and output layers and one that cannot, called the hidden layer. The first work on modelling neurons, dating back to the 1940s, was undertaken by McCulloch and Pitts.²⁰

“... a synthetic neuron forms a weighted sum of the action potentials which arrive at it (each one of these potentials is a numeric value which represents the state of the neuron

which has emitted it) and then activates itself depending on the value of the weighted sum. If this sum exceeds a certain threshold, the neuron is activated and transmits a response (in the form of an action potential) of which the value is the value of its activation. If the neuron is not activated, it transmits nothing.” [Reproduced from reference 20]

The schematic of a basic three-layer neural network is shown in figure 4.15

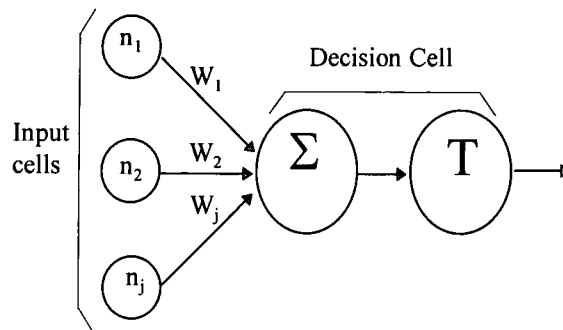


Figure 4.15: j input neural network with one hidden layer

The j input neurons each hold a specific numerical value, these are fed to the hidden (processing) layer plus a numerical value W_j (called a weight). The hidden layer sums up the values of all the input neurons

$$\sum_{j=1}^j n_j W_j \quad [4.17]$$

and passes this value onto the output layer. The output layer has a transfer function, T, that will determine the output value of the network, for linear networks the function is shown in figure 4.16. If equation 4.17 is greater than or equal to a threshold value (W_0) then the network output will be a 1, otherwise the output will be a 0. Thus, if we encode

some inputs to a neural network and have a desired output, we can train the network (adjust the weights) to recognise set input patterns.

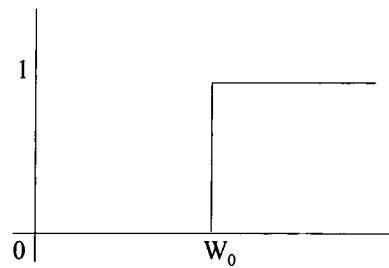


Figure 4.16: Linear transfer function for a neural network.

This type of network has little scope in determining unknown input patterns, so some degree of mathematical freedom has to be built into a network for it to exhibit free learning. The technique that most networks use to produce learning is called 'Back-propagation'. The principle is to replace the simple threshold function (figure 4.16), with a differentiable function, such as the sigmoid shown in figure 4.17

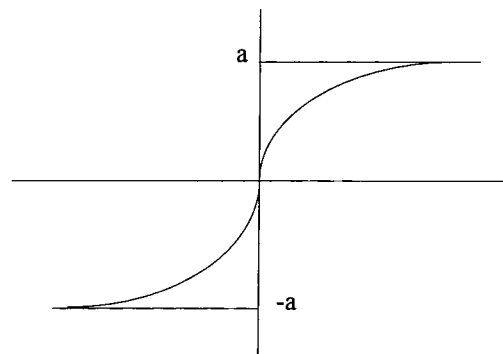


Figure 4.17: Sigmoid function for a neural network.

These types of networks contain both input and output layers, but possibly multiple hidden layers. Each neuron in each layer is connected to every other neuron in the next

layer by connections whose weights are given by real numbers. The back-propagation network works by moving an error signal from the output neuron backwards through intermediate layers towards the network input. This movement of the signal is similar to the way data is passed from the input via hidden layers to the output. There are three methods a neural network can learn to recognise data, they are, supervised learning, unsupervised learning and reinforcement learning.

Supervised learning. Each pattern received at the input neurons is specified an output value. The weights are systematically altered so that the size of the error reduces with each learning step.

Unsupervised learning involves the clustering of data from a given set. The neural network tries to distinguish patterns between data from the same training set (ie, all given the same output value). In this case, the weights and output values converge to values that represent the statistical regularities of the inputted data.

Reinforcement learning involves changing the networks weights on the action of a teacher (ie, computer operator). The difference between this and the supervised learning technique is that the teacher only says when the weights need changing (rather than specifying the answer). It is analogous to a teacher facilitating learning, rather than didactically giving the answers to problems (data sets).

For the data presented within this thesis, a back propagation network was used, simulated on a Pentium computer using 'NeuroShell 2.0'. Data were presented to a 66 input neural network with two output nodes. The output nodes were used to indicate whether either benzene or water vapour was present. There was one hidden layer with 41 neurons, this figure was determined automatically by the computer programme. The experimental setup for data collection is detailed in Chapter Five, whilst experimental results generated by the network are contained in Chapter Eight.

References

- 1 M.C. Petty, “**Langmuir-Blodgett films: an Introduction**”, Cambridge University press, Cambridge (UK), **1996**, 53-54.
- 2 J.W. Sadowski, I.K.J. Korhonen, J.P.K. Peltonen, *Optical Engineering*, 34 (9), **1995**, 2581-2586.
- 3 A. Otto, *Phys. Stat. Sol.*, 42, **1970**, K37.
- 4 J. Wilson, J.F.B. Hawkes, “**Optoelectronics: an Introduction**”, 2nd ed. Prentice Hall, London (UK), **1989**, 306-310.
- 5 J.R. Sambles, R.A. Innes, “**Proceedings of the Surface Plasmon Polariton Workshop**”, IOP Publishing, Bristol (UK), **1988**, 121-138.
- 6 E. Kretschmann, H. Raether, *Z. Naturforsch*, 23a, **1968**, 2135-2136.
- 7 E.M. Yeatman, *Biosensors and Bioelectronics*, 11, **1996**, 635-649.
- 8 H.E deBruijn, B.S.F. Altenburg, R.P.H. Kooyman, J. Greve, *Optics Communications*, 82 (5,6), **1991**, 425-432.
- 9 E.M. Yeatman, E.A. Ash, *Proc. SPIE*, 1028, **1988**.
- 10 J.P. Cresswell, *PhD Thesis*, University of Durham, **1992**.
- 11 M.C. Petty, “**Langmuir-Blodgett films: an Introduction**”, Cambridge University Press, Cambridge (UK), **1996**, 169-170.
- 12 P.M. Fishbane, S. Gasiorowicz, S.T. Thornton, “**Physics for Scientists and Engineers**”, Prentice Hall, New Jersey, **1996**, 1063-1067.

-
- 13 M.C. Petty, "**Langmuir-Blodgett films: an Introduction**", Cambridge University press, Cambridge (UK), **1996**, 98-104.
 - 14 D.E. Savage, J. Kleiner, N. Schimke, Y.H. Phang, T. Jankowski, J. Jacobs, R. Kariotis, M.G. Lagally, *J. Appl. Phys*, 69 (3), **1991**, 1411-1424.
 - 15 S-I Kuroda, *Colloids and Surfaces A: Physicochemical and Engineering Aspects*, 72, **1993**, 127-141.
 - 16 J. Wilson, J.F.B. Hawkes, "**Optoelectronics: an Introduction**", 2nd ed. Prentice Hall, London (UK), **1989**, 7-10.
 - 17 T. Kaercher, D. Hönig, D. Möbius, *International Ophthalmology*, 17, **1993**, 341-348.
 - 18 J.N. Wilde, A.J. Wigman, J. Nagel, A. Beeby, B. Tanner, M.C. Petty, *Acta. Polymer.*, 49, **1998**, 294-300.
 - 19 L.M. Walpita, C.W. Pitt, *Electronic Letters*, 13 (7), **1977**, 210-212.
 - 20 E. Davalo, P. Naïm - translated by A. Rawsthorne, "**Neural Networks**", Macmillian Education Ltd, London, **1991**, 19.

Chapter Five

Vapour Sensing Methods

5.0 Preface

This chapter deals with the design and operation of the gas sensing equipment used throughout this work. Concentrations of benzene, toluene, ethanol and water vapours were generated using diffusion techniques. Vapour sensing utilised surface plasmon resonance, initially with a silicon photodiode as detector, then using a charge coupled device (CCD) camera. Data collected via the CCD camera were then passed to a neural network to be identified.

5.1 Design of vapour generation system

Vapours were generated using the diffusion cell shown in figure 5.1. This consisted of a reservoir (containing the desired vapour as a liquid) immersed in a temperature-controlled water bath and an upper cell where nitrogen and vapour mixed.¹ The design of the capillary tube was essential since this determined the operating temperature of the water bath and, thereby, the concentration of vapour.² Vapours have the property of diffusing through tubes at a uniform rate if the temperature, concentration and tube geometry remain unchanged. The concentration of vapour generated then rely upon the amount of vapour diffusing through the capillary tube and the flow rate of the nitrogen

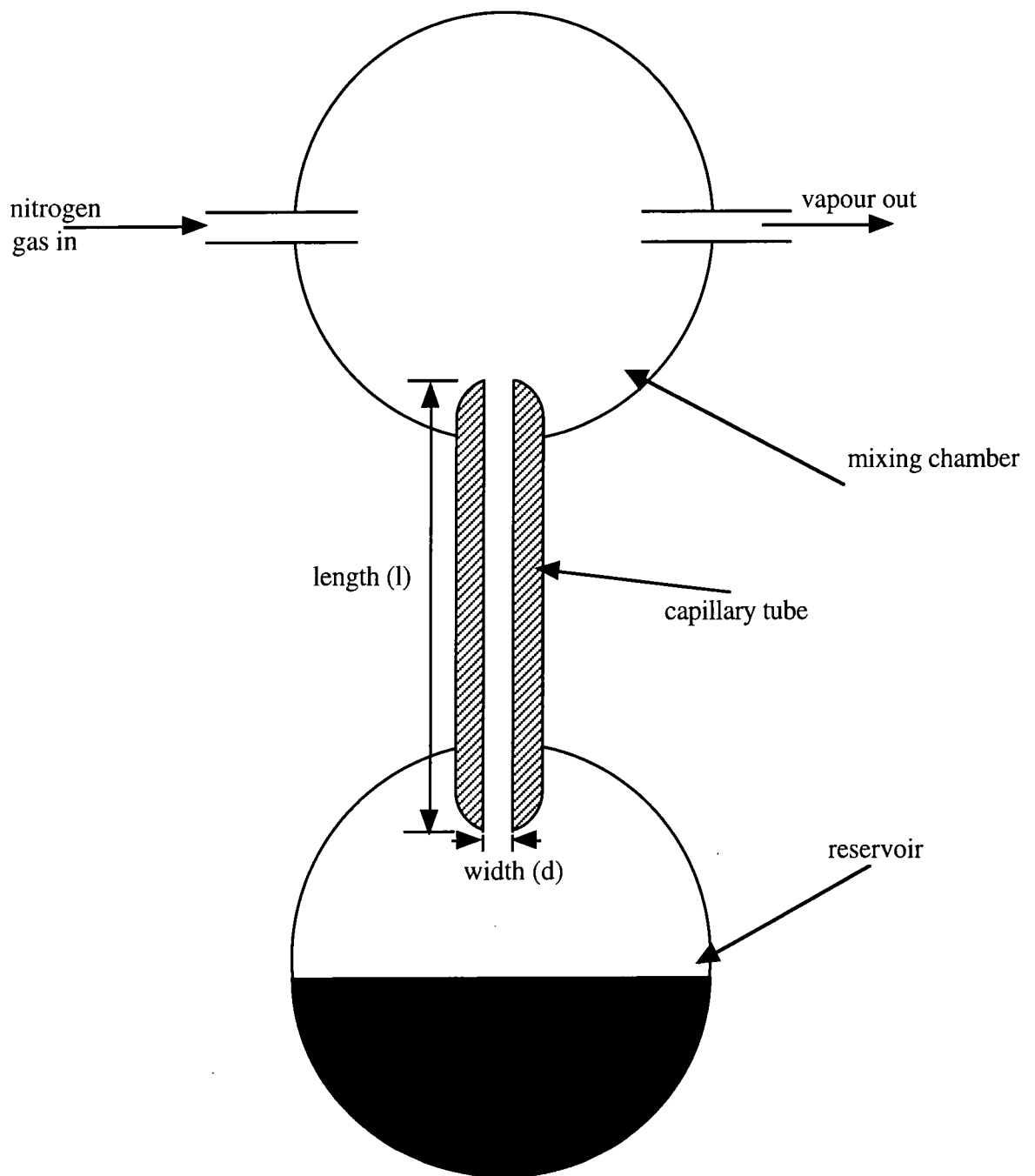


Figure 5.1: Schematic of vapour diffusion cell.

stream. A fast rate produces a low concentration (for a given diffusion rate) and a slow flow rate a high concentration.

Capillary tubes should be between 2 and 20 mm in diameter as diameters less than 2 mm make tube filling difficult and ones greater than 20 mm lead to excess turbulence. It is also advantageous to have a large reservoir as the diffusion system can be given ample time to equilibrate, and prolonged runs with the calibrated mixture can be made. The accuracy of the temperature controlled bath is of great importance, since a change in temperature can affect the diffusion rate by 5 to 10 % (temperature should be within a 0.4°C range to obtain accuracy of ±1 %).³ It is possible to predict the diffusion rate of a solvent and thereby the concentration of vapour produced at a constant flow rate

$$r = \frac{DPmA}{RTL} \ln\left(\frac{P}{P-\rho}\right) \quad [5.1]$$

$$D = D_0 \left(\frac{T}{T_0}\right)^2 \left(\frac{P_0}{P}\right) \quad [5.2]$$

where r is the diffusion rate, M is the molecular weight of the vapour, P is the total system pressure (for an open system this is 1 atm or 720 mm Hg), P_0 is 1 atm, A is the cross sectional area of the capillary tube, L is the length of the capillary tube, T is the absolute temperature of the system, T_0 is 273K, R is the gas constant, D is the diffusion coefficient at temperature T and pressure P , D_0 is the diffusion coefficient at 0°C and 1 atm, ρ is the vapour pressure of the solvent. Substituting equation 5.1 into 5.2 generates an equation involving the diffusion coefficients at 0°C and 1 atm (quoted in most reference texts).

$$r = \left(\frac{D_o P_o MA}{RT_o^2 L} \right) T \ln \left(\frac{P}{P - \rho} \right) \quad [5.3]$$

From equation 5.4 it is then possible to calculate the concentration of vapour generated in vapour parts per million (vpm), C_{vpm}

$$C_{vpm} = \frac{10^2 r}{Q} \quad [5.4]$$

where r is the diffusion coefficient [ml min^{-1}] and Q is the nitrogen flow rate [ml min^{-1}].

Four vapours were generated, benzene, toluene, ethanol and water vapours. Due to different diffusion coefficients, each vapour had a different working range (ie, range of vapour produced). The diffusion coefficient and working range are shown in table 5.1.⁴

Vapour	Diffusion coefficient [3] [$\text{cm}^2 \text{s}^{-1}$]	Minimum vapour concentration generated [vpm]	Maximum vapour concentration generated [vpm]
toluene	0.0709	100	3000
benzene	0.0770	100	10000
ethanol	0.1020	630	17000
water	0.2200	630	40000

Table 5.1: Comparison of diffusion coefficients of vapours used in this work and the maximum and minimum vapour concentration generated.

5.2 Calibration of vapour generation system

The diffusion rate for each of the vapours was calculated over a 4 day period. Each of the samples was initially weighed before being placed in the vapour generating system. The reservoir of solvent (benzene, toluene and ethanol) were then weighed regularly over the period. After exposure, the decrease in weight of the solvent (due to evaporation) was averaged and a diffusion rate was calculated, the units of which were g min^{-1} . This experiment was repeated for each vapour and at 4 different temperatures. It was subsequently possible to calculate the vapour pressure of each solvent at each temperature (substituting D_0 in equation 5.3 into equation 5.2)

$$\rho = P \left(1 - \exp \left(- \frac{r}{MT} \right) \right) \quad [5.5]$$

These values could then be used to check and calibrate the system, by comparing the figures to those obtained using the Clausius-Clapeyron equation.

5.2.1 Clausius-Clapeyron data for vapours

The Clausius-Clapeyron equation is an important relation that describes how pressure (in particular, vapour pressure) of a two phase system varies with temperature. The two phase system in question is one in which a liquid and its vapour are in equilibrium. The standard form of the Clausius-Clapeyron equation is⁵

$$\ln \rho = - \frac{l_{23}}{RT} + \ln C \quad [5.6]$$

where ρ is the vapour pressure, l_{23} is the latent heat of transformation, R is the gas constant, T is the temperature of the system and C is a constant of integration. This

equation can be used to calculate the vapour pressure of a substance at any temperature. The only problem is obtaining the value of the constant of integration from experimental measurements. In the case of this work, data for the vapour pressures of benzene, toluene and ethanol vapour were taken from reference 6, which quoted values in mm Hg for 6 different temperatures.⁶ Data for the vapour pressure of benzene, toluene and ethanol were computed using equation 5.5 and then compared graphically to values from reference 6, shown in figure 5.2. As can be seen for the three plots (vapour pressure data were not generated for water vapour), the values obtained experimentally match those from reference 6. There is some deviation, but this can be attributed to experimental inaccuracies, the purity of solvent used and inaccuracy in temperature bath measurements.

The data derived from the vapour pressure of benzene, toluene and ethanol vapour indicate that the experimental system for generating vapours works and followed basic vapour pressure laws.

5.3 Gas sensing using surface plasmon resonance

5.3.1 Photodiode detector

Surface plasmon resonance (SPR) gas sensing was performed on a manual SPR system. This consisted of a class IIb He-Ne ($\lambda = 632.8$ nm) laser (p-polarised, beam intensity 5mW), and a silicon photodiode to record the reflected intensity of the beam, shown in figure 5.3. The beam was passed initially through a neutral density filter, to cut down the beam intensity and so reduce any localised heating effects in the sample and to avoid

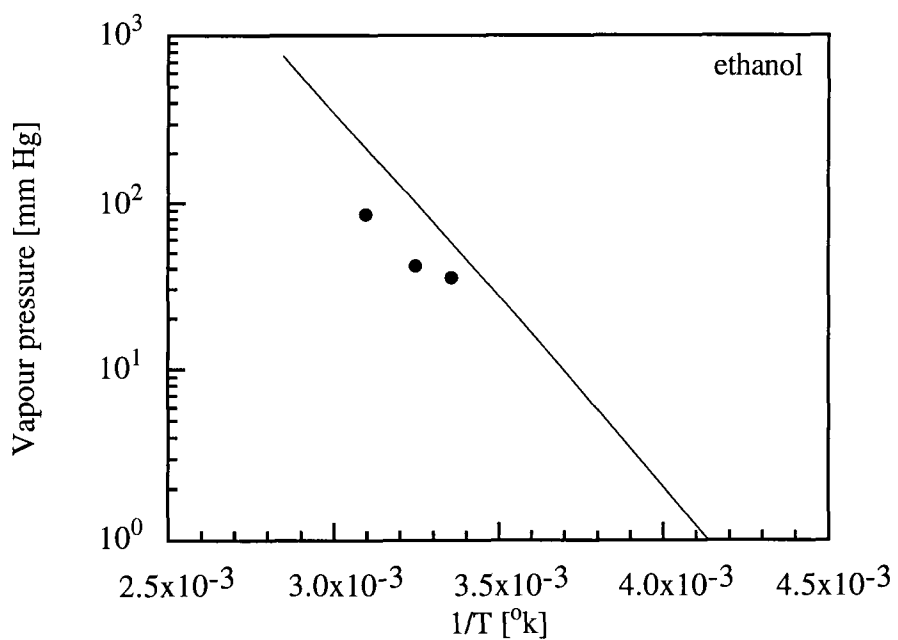
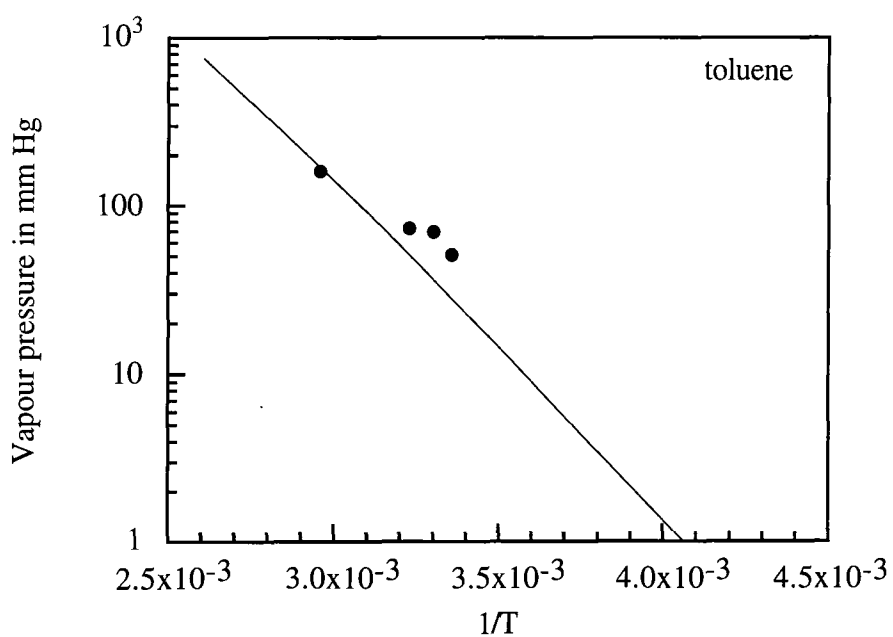
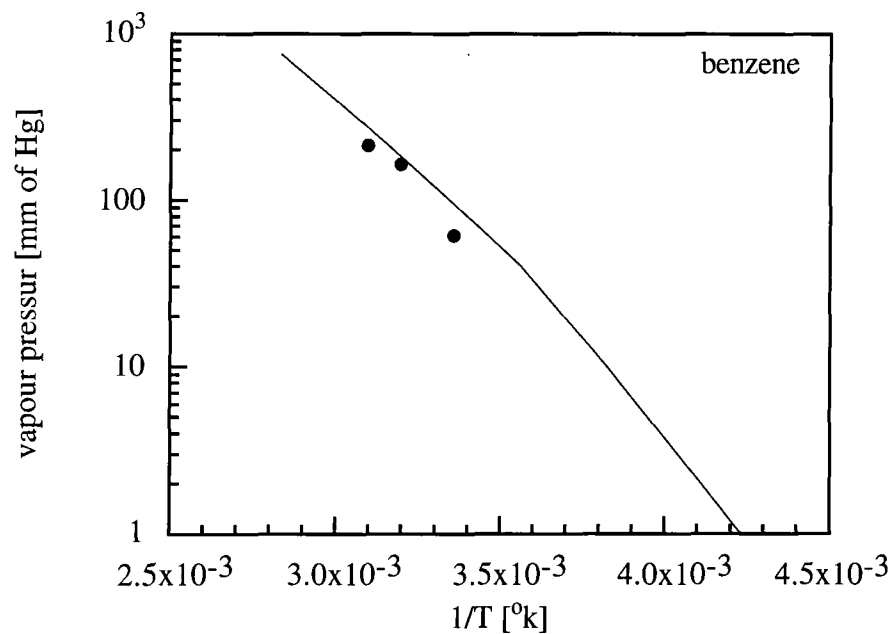


Figure 5.2: Clausius-Clapeyron graphs for benzene, toluene and ethanol vapours. Straight line represents theoretical data points and the dots are experimental.

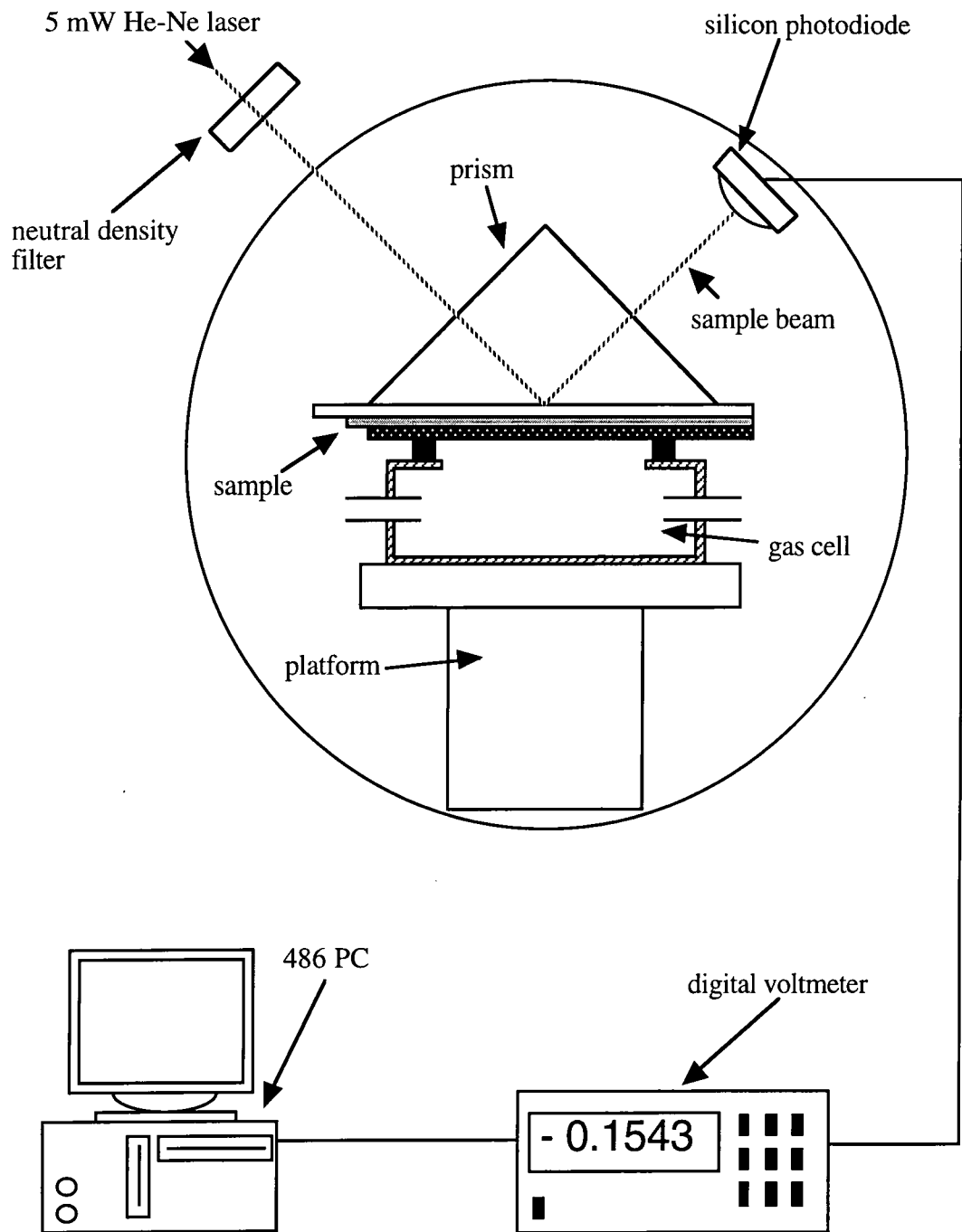


Figure 5.3: Schematic of the silicon photodiode equipment used in this work.

saturating the photodiode. In the centre of the system was a 45°, 45°, 90° prism supported on the gas sensing cell. The cell consisted of inlet and outlet pipes and was sealed to the substrate via an o-ring. Light reflected from the prism base was measured using a large area silicon photodiode, the output of which was fed to a voltmeter. A program was written in Turbo Pascal to allow the computer to interface with the voltmeter via an IEEE interface card. This program, listed in appendix A, allowed the user to define the operating time and sampling rate of the gas sensing experiment. The program would then capture data throughout this time and display a graphic record of the sensing trace on the screen whilst saving the data to disk for retrieval at a later date.

(a) Design of gas sensing system

The gas sensing system, shown in figure 5.4, was used to expose samples to concentrations of benzene, toluene, ethanol and water vapour. Samples were mounted initially in the SPR rig using the Kretschmann-Raether configuration. The SPR profile of the sample was manually recorded to find the position of the SPR minimum (a 5° range was used sampling rate 0.1°). The laser was then fixed at the angle, on the low side of resonance, at the point of steepest gradient. This point was chosen so that a small change in the SPR curve would produce the biggest possible change in reflected beam intensity (ie, photodiode output). The voltage output of the SPR system, as monitored by the silicon photodiode, was then passed to the PC. Changes in reflectivity, were displayed as variations in voltage against time.

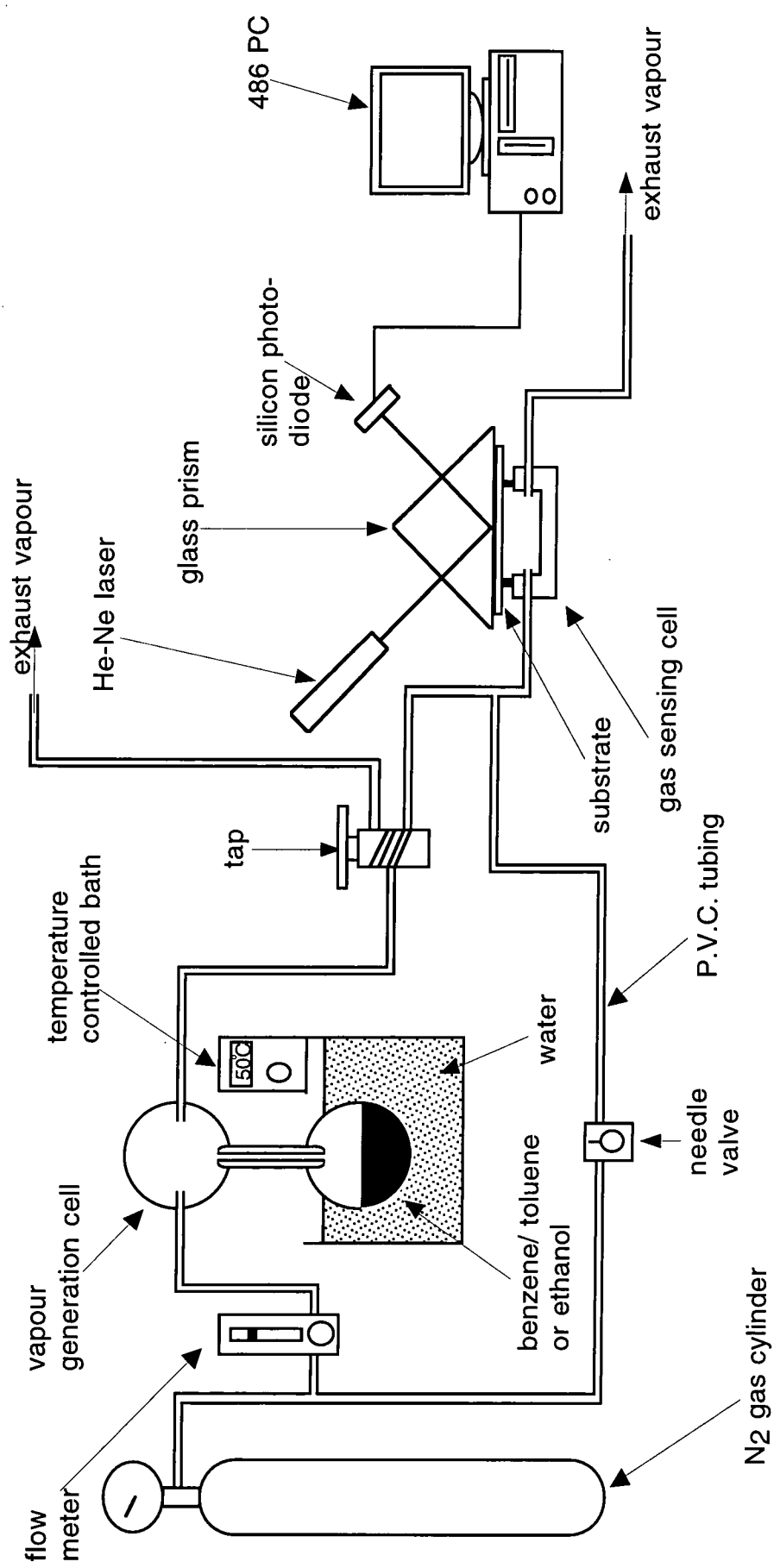


Figure 5.4: Surface plasmon resonance vapour sensing system as used in this work.

Vapours were generated in the diffusion cell, described in section 5.1. Samples were exposed initially to 100 cc min^{-1} of pure nitrogen (BOC Ltd), this was to stabilise the sample in a known atmosphere. Sensing layers were exposed to nitrogen until their output had settled, thus the exposure time for each sample (to N_2) varied. Once the output had settled, vapour was introduced in a stream of nitrogen (carrier gas). A constant flow of vapour was maintained throughout the experiment, even when the sample was exposed to pure nitrogen. In the latter case, the vapour generated was vented to a fume cupboard. Vapour was constantly generated to avoid any variations in concentration.

5.4 CCD camera detector

The SPR system used for image processing is shown in figure 5.5. The light source was a 3 mW He-Ne laser diode ($\lambda = 632.8 \text{ nm}$) expanded to a diameter of 10 mm. This provided approximately a 5° span of angles. A CCD (charge coupled device) camera served as the detector. An image processing package (PC Image) running on a 486 PC was used to display data from individual pixels (pixel size $19.6 \mu\text{m} \times 16 \mu\text{m}$). For further details on data processing and reduction, see Chapter Eight.

A wealth of information is available from any change in an SPR curve following the interaction of the active film with a gas or vapour.⁷ For example, the angle of the SPR minimum, the resonance depth and the width of the resonance curve can all vary. A change in the film thickness or refractive index will result in a shift in both the resonance angle and the width of the resonance curve, while increased adsorption or

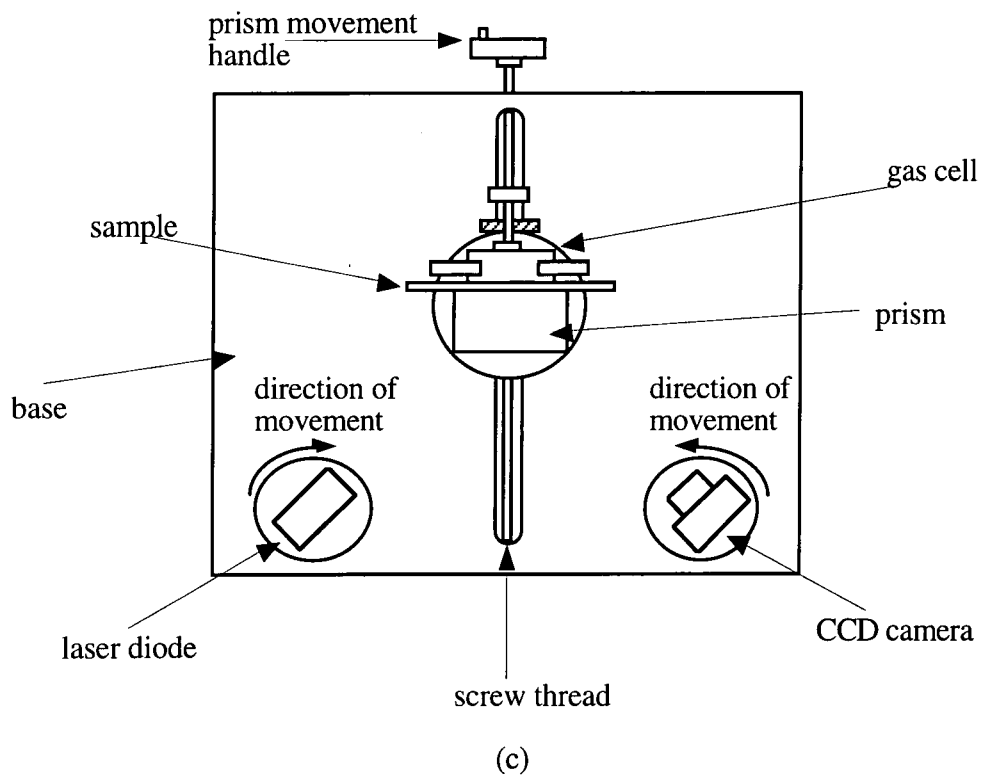
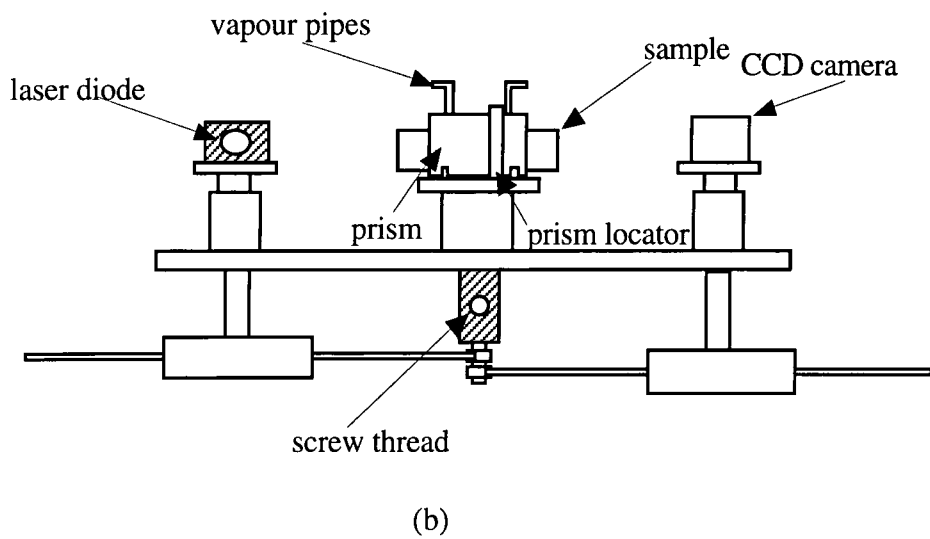
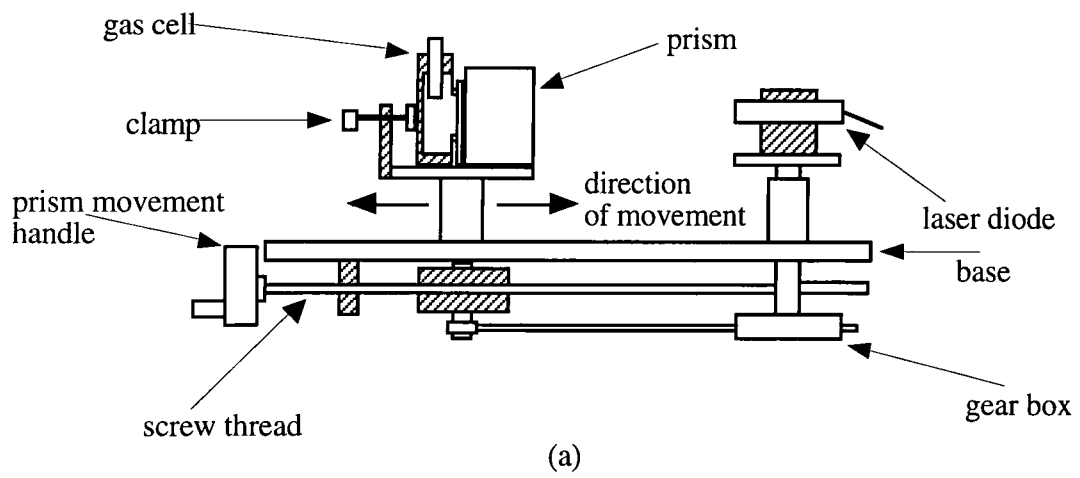
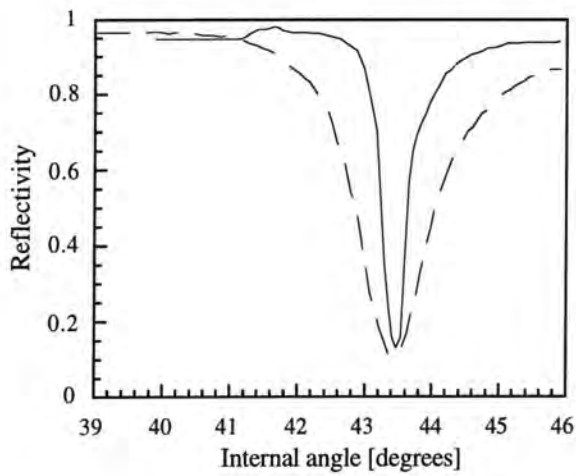


Figure 5.5: Schematic of CCD camera SPR equipment (a) Side elevation. (b) Front elevation. (c) Top elevation.

scattering in the overlayer film will produce a change in the depth of resonance. If, as a result of an interaction of the active film with a gas, the SPR curve shifts to a higher angle, reduces in intensity (decrease of resonance depth) or narrows, then the output voltage will increase (assuming the incident angle of the laser is fixed on the low angle side of resonance). In contrast, a decrease in the output voltage could correspond to a shift in the SPR curve to a smaller angle, a broadening or to an increase in the resonance depth. This measurement arrangement is simple, but, because only one parameter is monitored, the selectivity is poor. For example two different overlayers may interact differently to the same gaseous species (eg, the refractive index of one may change while the film thickness may be affected in the second case), but the change in reflectivity could be the same.

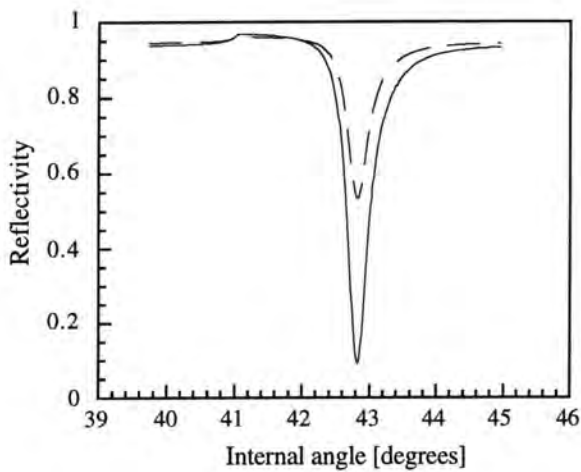
Figure 5.6 illustrates how theoretical changes in the SPR curves can provide more detailed information as CCD images. In each case, the change to the SPR curve is shown on the left and the corresponding CCD image of the pixels on the right. An SPR curve corresponding to a single LB layer on a metallised substrate is shown in figure 5.6a (i). The dark line in the centre of the SPR image (figure 5.6a (ii)) corresponds to the points where the incident light excites surface plasmons and is absorbed (the resonance minimum in figure 5.6a (i)). If the SPR curve moves to higher angles (shown by the dashed (theoretical) line in figure 5.6b (i)), the corresponding CCD image (figure 5.6b (ii)) will also move to the right (ie higher angles). Figure 5.6c illustrates the effect of a broadening in the SPR curve, while figure 5.6d shows the effect of the SPR curve becoming less defined (loss of resonance).



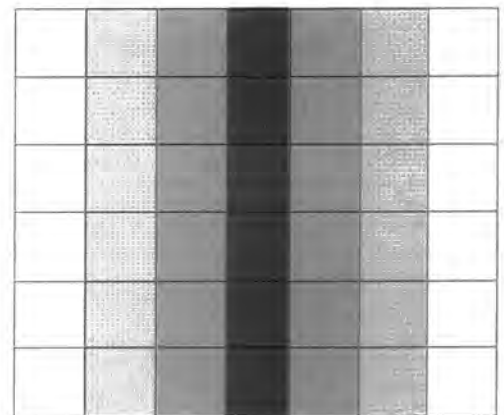
c (i)



c (ii)



d (i)



d (ii)

Figure 5.6: Theoretical SPR curves and CCD images showing the effect of changes to the SPR curve on the pixels in the CCD image (a) Single LB layer deposited on Ag. (b) Effect of a shift in the SPR curve to higher angles (dashed curve). (c) Effect of broadening in the SPR curve (dashed curve). (d) Effect of loss in depth of resonance (dashed curve).

References

- 1 J.M. Mckelvey, H.E. Hoelscher, *Anal. Chem.*, 29, **1957**, 123.
- 2 C. Granito, J.N. Wilde, M.C. Petty, S. Houghton, P.J. Iredale, *Thin Solid Films*, 284-285, **1996**, 98-101.
- 3 G.O. Nelson, "**Gas Mixtures: Preparation and Control**", Lewis Publishers Ltd, Chelsea UK, **1992**, 137-146.
- 4 "**International Critical Tables**", Vol V, McGraw-Hill, New York USA, 1929.
- 5 F.W. Sears, G.L. Salinger, "**Thermodynamics, Kinetic Theory, and Statistical Thermodynamics**", 3rd ed., Addison Wesley Publishing, London UK, **1975**, 193-196.
- 6 R.C. West, M.J. Astile, "**CRC Handbook of Chemistry and Physics**", *CRC Press Ltd-Florida*, 59, **1978**, D241 - D257.
- 7 J.N. Wilde, M.C. Petty, J. Saffell, A. Tempore, L. Valli, *Measurement and Control*, 30, **1997**, 259-265.

Chapter Six

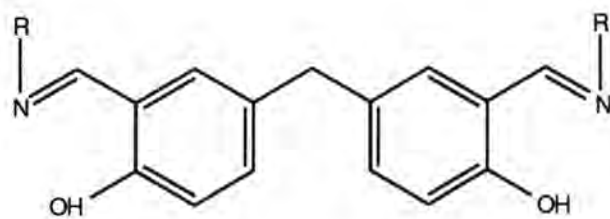
Results and Discussion: Film Characterisation

6.0 Preface

In this chapter, the structural and optical properties of a Schiff base co-ordination polymer (5,5'-methylenebis (N-hexadecylsalicylideneamine)) are discussed. Material was spread on two distinct subphases: the first contained de-ionised water (MBSH); the second contained a solution of the pure water and copper(II) acetate tetrahydrate (at a known concentration) (poly(CuMBSH)). The resulting Langmuir layer was investigated using Brewster angle microscopy and surface pressure versus area isotherms. The structural properties of Langmuir-Blodgett films, deposited from these subphases, were studied using surface plasmon resonance, low-angle X-ray diffraction, ellipsometry, UV/visible spectroscopy, electron spin resonance and Alpha-step measurements.

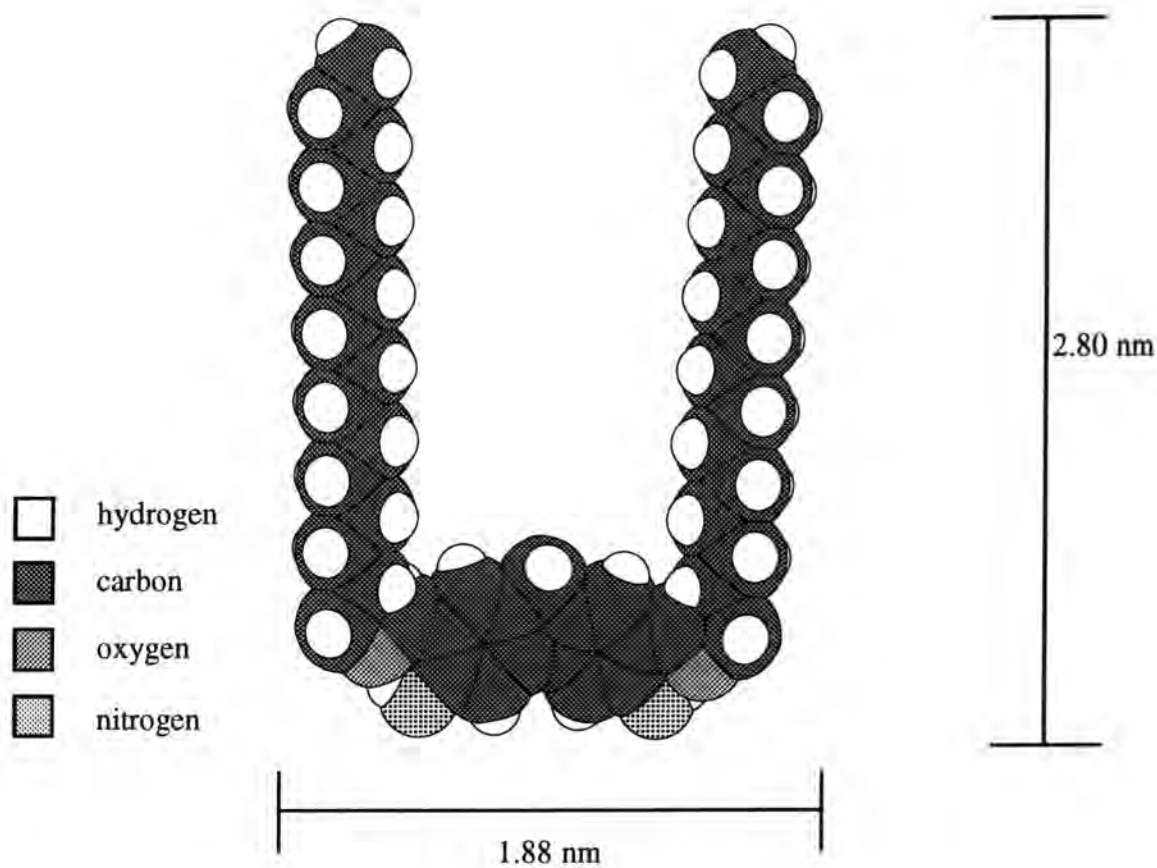
6.1 Langmuir layer characterisation of MBSH

The chemical structure and space filling model of the MBSH monomer is shown in figure 6.1. MBSH was dissolved in chloroform at a concentration of 1 g l^{-1} . The solution was placed in an ultrasonic bath for 10 minutes to ensure all the MBSH had dissolved. A suitable amount (30 - 100 μl) was distributed over the surface (maximum area 416 cm^2) of a pure water subphase using a micro syringe. This material was left



(a)

$R = C_{16}H_{33}$



(b)

Figure 6.1: Structure of 5,5' methylenebis (N-hexadecylsalicylideneamine) (MBSH) used in this work (a) chemical structure (b) space filling model

uncompressed on the surface of the subphase for 15 mins to ensure all the solvent had evaporated from the film.

6.1.1 Brewster angle microscopy

Brewster angle microscopy (BAM) images were recorded for 30 μl of MBSH spread on a subphase (maximum surface area 416 cm^2) of pure water at zero surface pressure. Figure 6.2 shows the growth of domains as the surface area is reduced. These begin to coalesce at very low surface pressures. The first two images (recorded at an area per molecule of 1.45 nm^2 and 1.10 nm^2 , respectively) show domains of increasing size. The third image (area per molecule of 0.83 nm^2) indicates that the domains are beginning to coalesce, forming a more uniform layer. The final picture was taken close to the dipping pressure (area per molecule 0.38 nm^2). This shows a uniform bright image from the subphase surface. The increase in specular reflection from the subphase surface depends upon the inhomogeneities, refractive index or density of the monolayer.¹ Therefore, it is likely that, at the deposition pressure (25 mN m^{-1}), MBSH forms an homogenous Langmuir layer.

6.1.2 Langmuir-Blodgett technique

(a) Surface pressure versus area isotherms

Isotherms were obtained for a solution of MBSH spread on a subphase containing pure water. Pressure versus area isotherms were recorded at a compression speed 1.6×10^{-2} $\text{nm}^2 \text{ molecule}^{-1} \text{ s}^{-1}$. Figure 6.3 shows isotherms for 100 μl MBSH. These were recorded

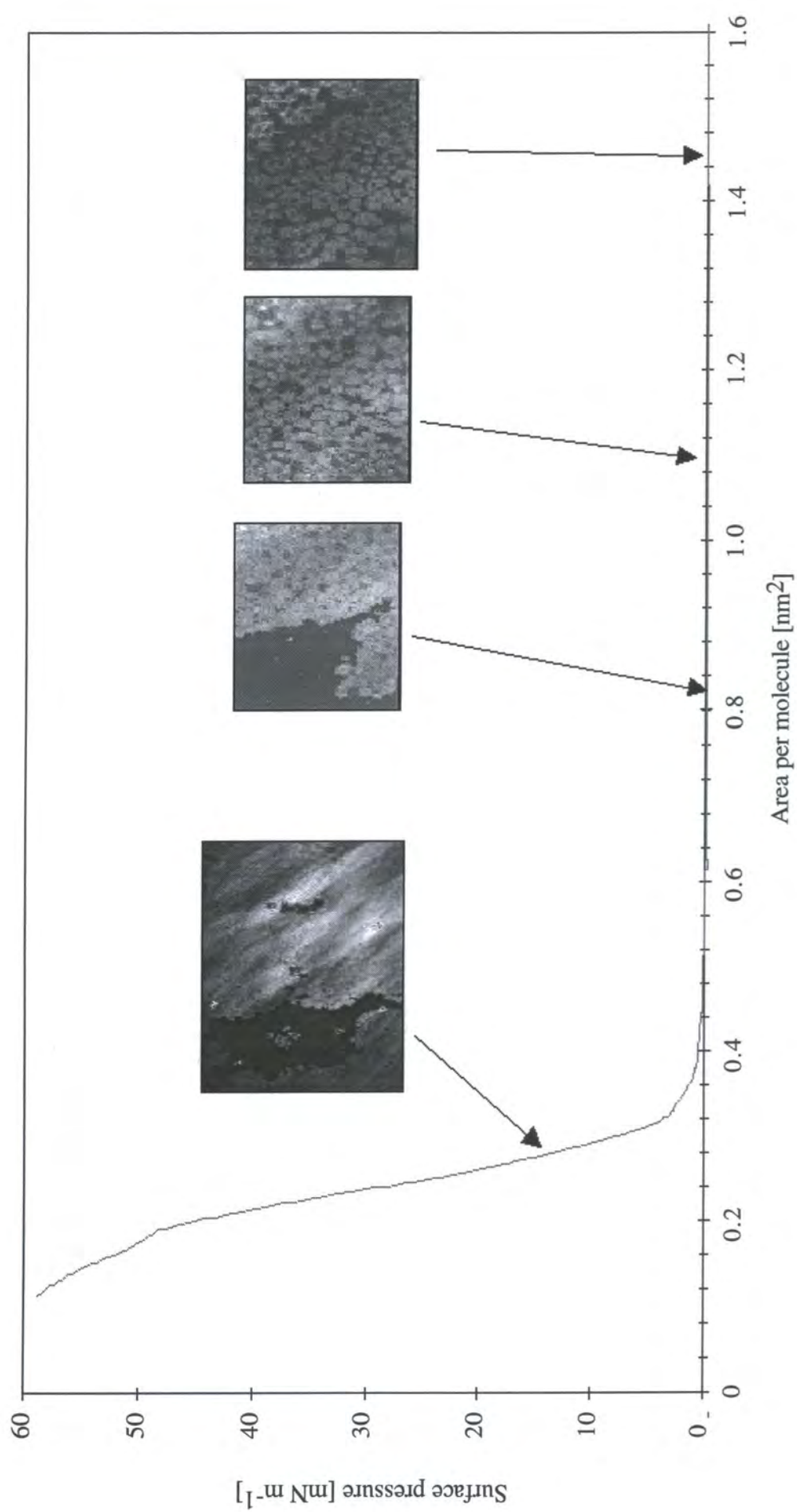


Figure 6.2: Brewster angle microscopy images superimposed on an isotherm for 50 μl MBSH spread on a subphase of pure water.

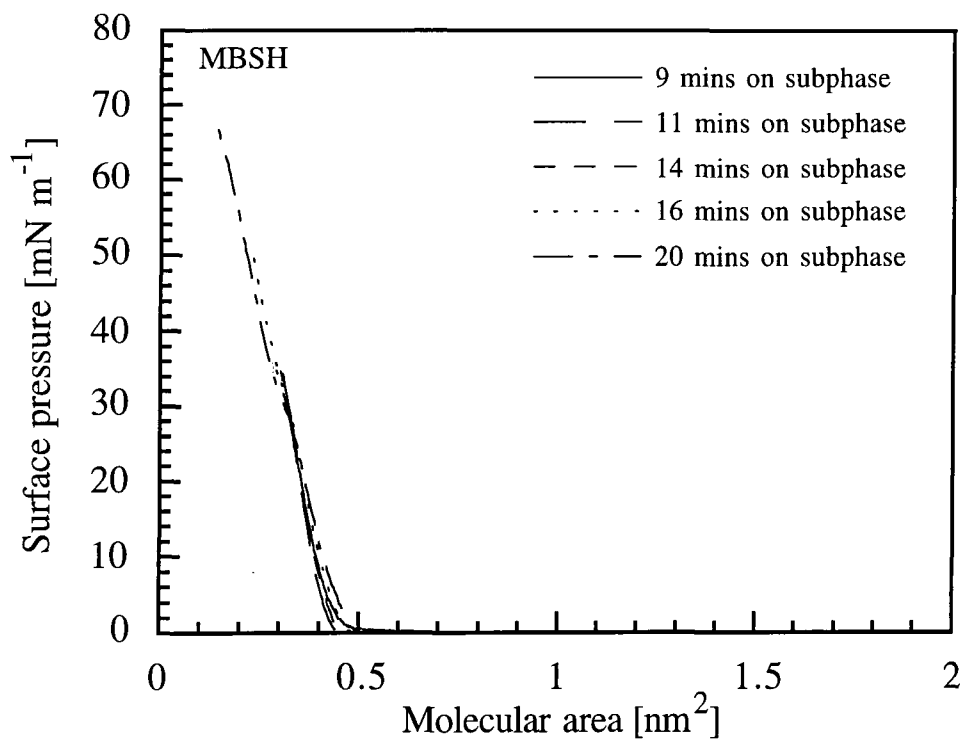


Figure 6.3: Surface pressure versus area isotherms for 100 μl MBSH spread on a subphase of pure water ($\text{pH } 5.8 \pm 0.2$ at 20 ± 2 $^{\circ}\text{C}$). The isotherms were recorded at various times after the solution had been applied to the subphase surface.

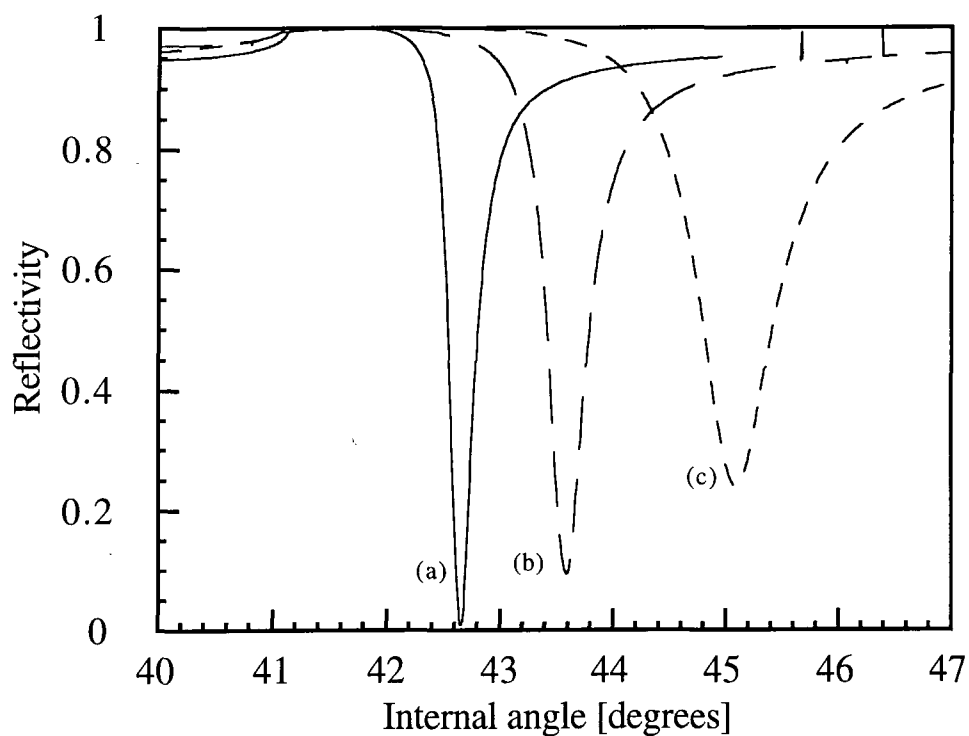


Figure 6.4: Surface plasmon resonance ($\lambda = 632.8$ nm) curves for (a) 50 nm silver layer (b) silver + 2 LB layers MBSH (c) silver + 4 LB layers MBSH.

at various times after the solution had been applied to the subphase surface. The shape of the isotherm was found to be independent of this time. The area occupied by the molecules in the Langmuir layer (obtained by extrapolating the steeply rising part of the curve to zero surface pressure) was calculated as $0.41 \pm 0.1 \text{ nm}^2$. From space filling molecular models, the dimensions of the MBSH monomer were found to be $(1.88 \pm 0.1) \times (2.80 \pm 0.1) \times (0.4 \pm 0.1) \text{ nm}$. Thus, the maximum area per complex (assuming it is orientated with the hydrophobic branches almost perpendicular to the subphase surface) is *ca* 0.8 nm^2 ($1.88 \times 0.4 \text{ nm}$). This figure is almost twice the measured value and suggests that MBSH could form a layer that is more than one molecule in thickness at the air/water interface. A proposed model for the arrangement of the molecules, on the subphase and substrate, will be discussed in section 6.2.6.

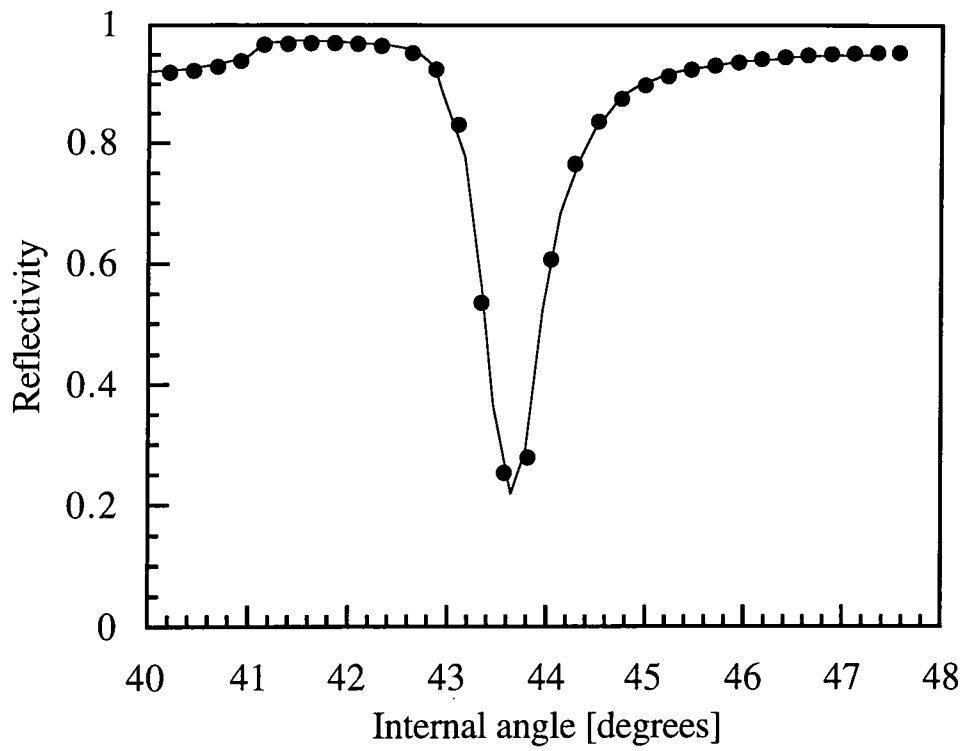
(b) Langmuir-Blodgett deposition

Floating layers of pure MBSH could not be transferred to substrates using the LB technique. However the addition of tricosanoic acid (TA) to a solution of MBSH aided deposition, the optimum concentration being 38% TA to 62% MBSH by volume (molar ratio 1 (MBSH): 1.7 (TA)). Film transfer was obtained at a surface pressure of 25 mN m^{-1} and a substrate dipping speed of between 2 and 4 mm min^{-1} . The substrates used were hydrophobic glass, single crystal silicon slides (orientation (100)) and silvered glass slides. The deposition ratio was reproducible (over a number of layers), with the first down stroke giving a ratio of 0.6 ± 0.1 and all other passes through the subphase surface giving 1.0 ± 0.1 .

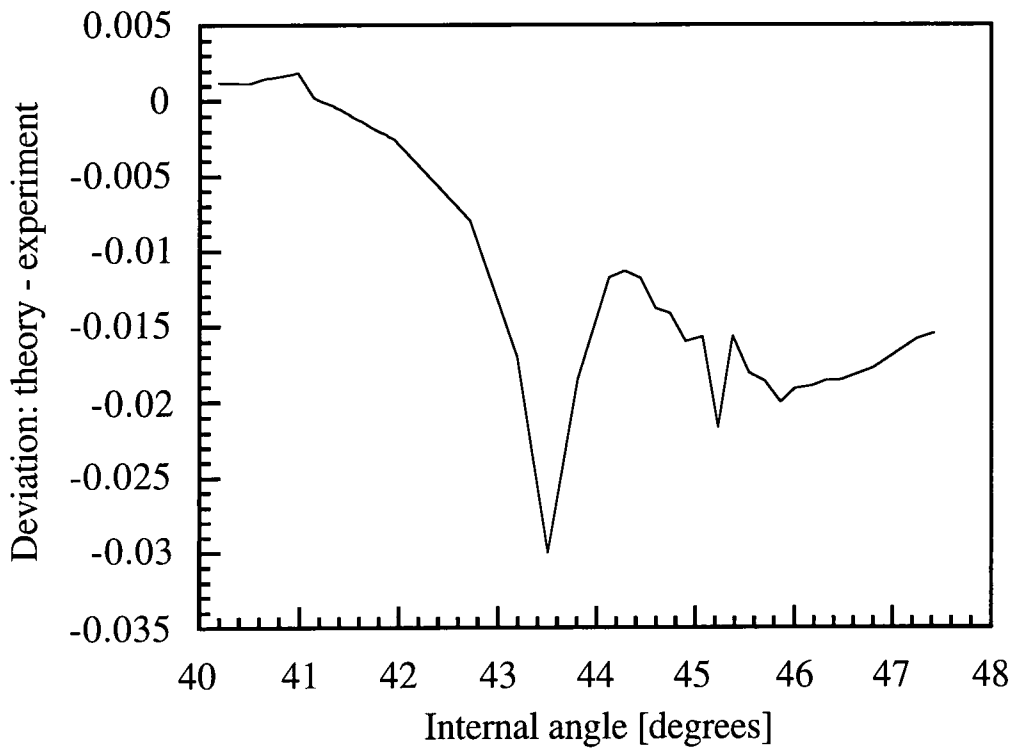
6.2 Structural characterisation of MBSH

6.2.1 Surface plasmon resonance

Surface plasmon resonance curves were generated for 2 and 4 LB layer samples of MBSH/TA on silvered (50 nm) glass slides. The curves are shown in figure 6.4, with the first curve (a) being the uncoated 50 nm silver profile and curves (b) 2 LB layers MBSH/TA and (c) 4 LB layers MBSH/TA. As the number of LB layers increase the point of resonance moves to higher angles, the profile begins to broaden and the depth of resonance minimum decreases. This is due to the increasing thickness and absorption (at the laser wavelength $\lambda = 632.8$ nm) of the LB film. The data for the SPR curves shown in figure 6.4 can be modelled on computer, to give the permittivity of each film. Figure 6.5 (a) shows a fit for a new 2 LB layer film of MBSH/TA deposited on a 50 nm silver layer. The correlation between the theoretical data (solid line) and the experimental (dots) is good over most of the curve, with an average error of 0.02. The only deviation is at the point of resonance, where the theoretical data predict a shallower minimum, shown in figure 6.5 (b). The values for refractive index were approximated by taking the square root of the real part of the permittivity (making the assumption that the substrate and LB layer are isotropic and lossless) and are shown in table 6.1.² From these data, the average layer thickness for MBSH/TA is 4.98 ± 0.06 nm. This is in conflict with the molecular dimensions quoted in section 6.1.2(a), which give a smallest molecular length of 2.8 nm. One explanation for this discrepancy is that MBSH/TA could form a bilayer at the subphase surface.



(a)



(b)

Figure 6.5: (a) Surface plasmon resonance curve for 2 LB layers MBSH/TA on 50 nm silver; dots - experimental data; solid line - theoretical data, (b) deviation of theoretical SPR curve from the one obtained experimentally.

Number of LB layers	Permittivity	Refractive index	Film thickness [nm]
2	2.32 + 0.38i	1.52	9.85
4	2.38 + 0.17i	1.54	20.2

Table 6.1: SPR data for 2 and 4 LB layers MBSH/TA ($\lambda = 632.8$ nm).

6.2.2 Ellipsometry

Ellipsometry calculations ($\lambda = 632.8$ and 546.1 nm) were performed on LB films of the MBSH/TA mixture. A plot of thickness versus number of LB layers for MBSH/TA on hydrophobic silicon is shown in figure 6.6. Each value for the film's thickness was an average of five readings (at both wavelengths) on five different parts of the film. The data points in figure 6.6 lie on a straight line, confirming the reproducible nature of film transfer up to 59 LB layers. A straight line fit yields an average layer thickness of 5.38 ± 0.2 nm.

Ellipsometry was also used to determine a value for the refractive index of the MBSH/TA layer. The real part of the refractive index was measured at two wavelengths, $\lambda = 632.8$ nm and $\lambda = 546.1$ nm, with each value again being an average of five readings on two different 19-layer films. Table 6.2 shows a comparison of the refractive index of films deposited on silicon substrates. The change in refractive index between the two wavelengths is due to both films being more absorbing at the lower wavelength (see section 6.2.3). The data for both films are the same within experimental error, giving an

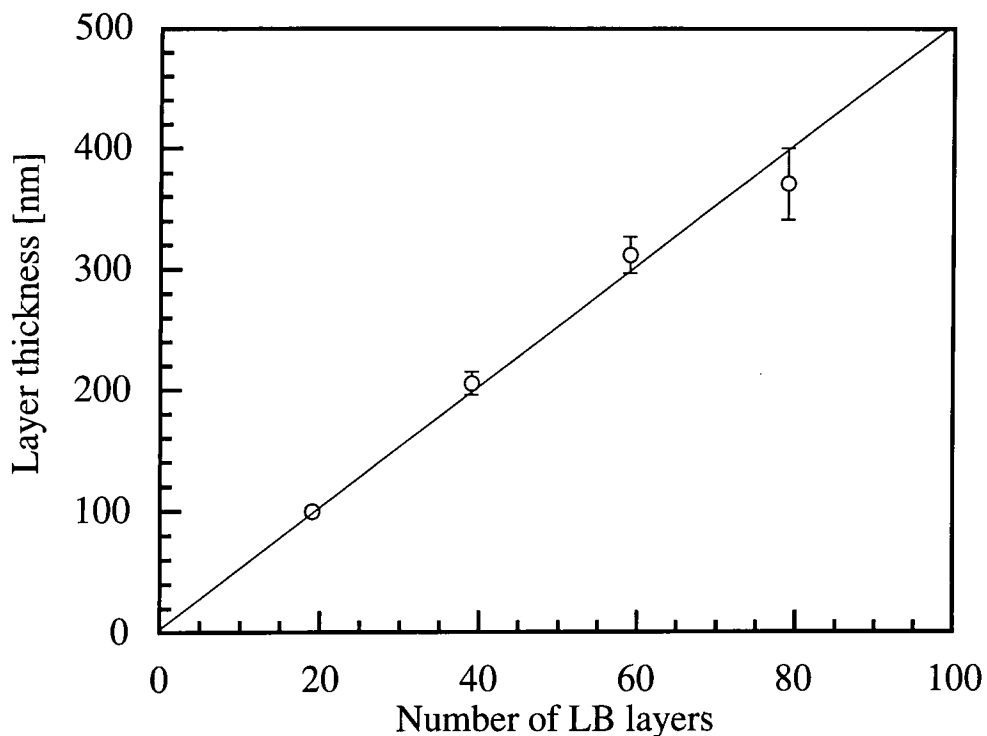


Figure 6.6: Film thickness versus number of LB layers measured using ellipsometry ($\lambda = 546.1$ and 632.8 nm). For LB layers of MBSH/TA as deposited onto single crystal silicon.

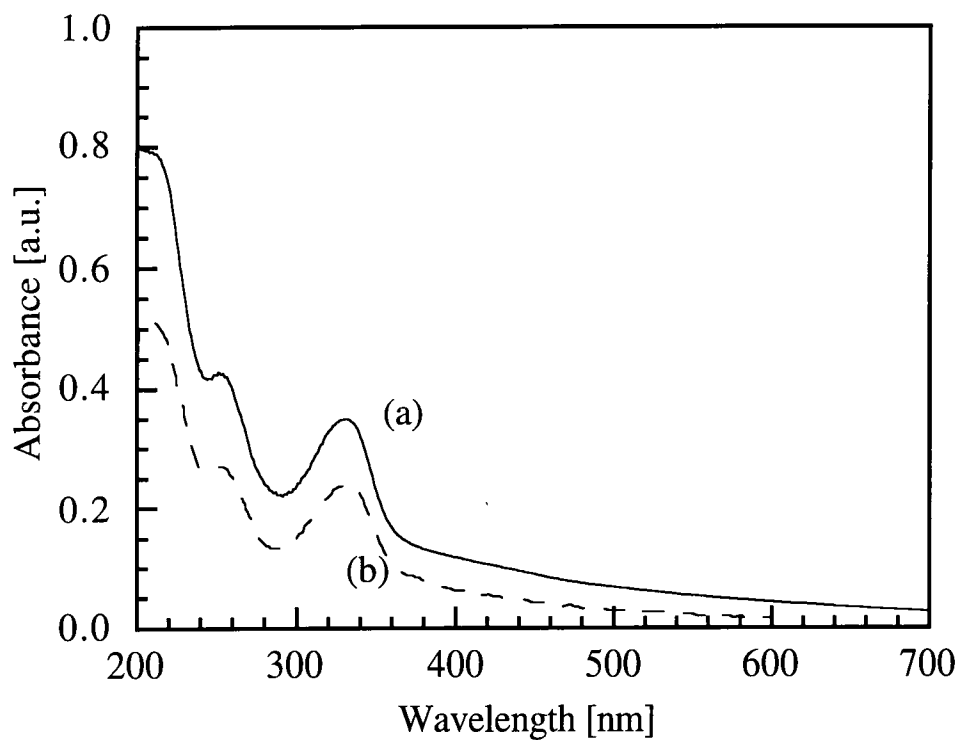


Figure 6.7: UV/visible spectra for (a) 29 LB layers MBSH/TA deposited onto a quartz substrate (b) 10 LB layers MBSH transferred by the horizontal touching technique [reproduced from reference 2].

average refractive index of 1.539 ± 0.01 at $\lambda = 546.1$ nm and 1.531 ± 0.006 at $\lambda = 632.8$ nm. The latter closely matches the average value obtained via SPR (at $\lambda = 632.8$ nm) of 1.530 ± 0.005 .

Number of LB layers	Refractive index	Refractive index
	$\lambda = 546.1$ nm	$\lambda = 632.8$ nm
19	1.547 ± 0.001	1.534 ± 0.001
19	1.534 ± 0.002	1.529 ± 0.003

Table 6.2: Refractive indices of MBSH/TA measured at $\lambda = 546.1$ and 632.6 nm

6.2.3 UV/Visible spectroscopy

MBSH/TA produced LB films that appeared homogenous on visual inspection. The optical absorption spectra for 10 LB layers of pure MBSH and 29 LB layers MBSH/TA deposited on quartz slides are shown in figure 6.7.³ Both spectra are almost identical, possessing absorption bands at 240 and 330 nm. These have been assigned to a $\sigma \rightarrow \pi^*$ transition, for the 240 nm band, and a $\pi \rightarrow \pi^*$ transition in the case of the 330 nm band.⁴

6.2.4 Alpha-step measurements

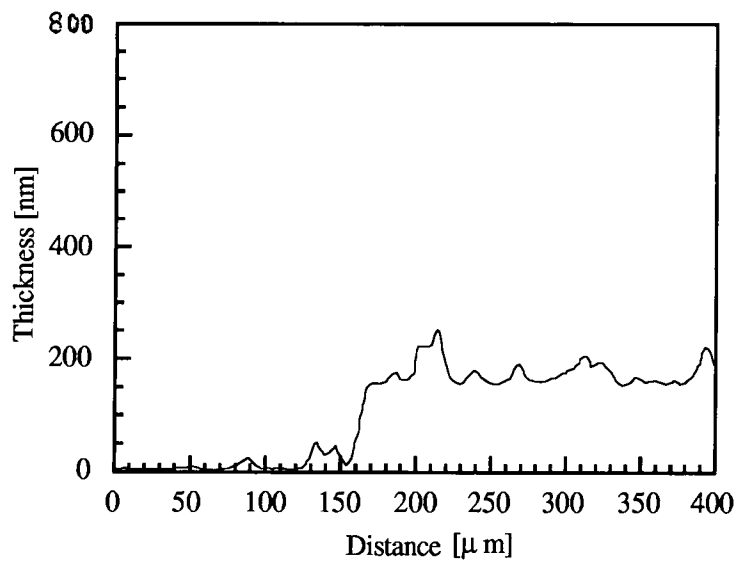
The thicknesses of multilayer films on hydrophobic silicon were measured using surface profiling (Alpha-step). A step between the silicon substrate and the LB film was formed by wiping a small area of material away with a tissue soaked in chloroform. Onto this

structure a thin layer of aluminium was evaporated to protect the film. The sample was then placed in the Alpha-step, where a stylus (weight *ca* 8 mg) was drawn over the metallised step. Three samples (19, 39 and 59 LB layers) deposited on single crystal silicon were examined. Figure 6.8 a,b and c show profiles of the metallised step, and the averaged size are given in table 6.3 below.

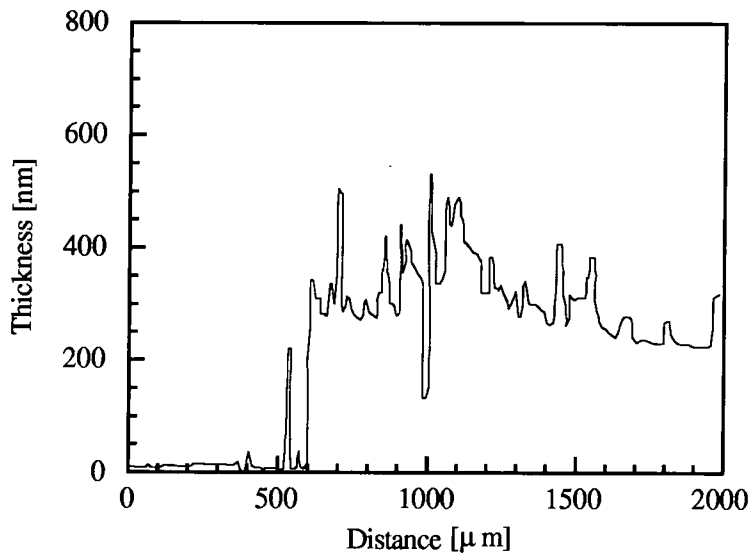
Number of LB layers	Step size [nm]	Average layer thickness [nm]
19	120.0 ± 19.7	6.3 ± 1.1
39	215.0 ± 15.3	5.5 ± 0.4
59	350.0 ± 9.9	5.9 ± 0.2

Table 6.3: Alpha-Step measurements on 19/39/59 layer LB films of MBSH/TA

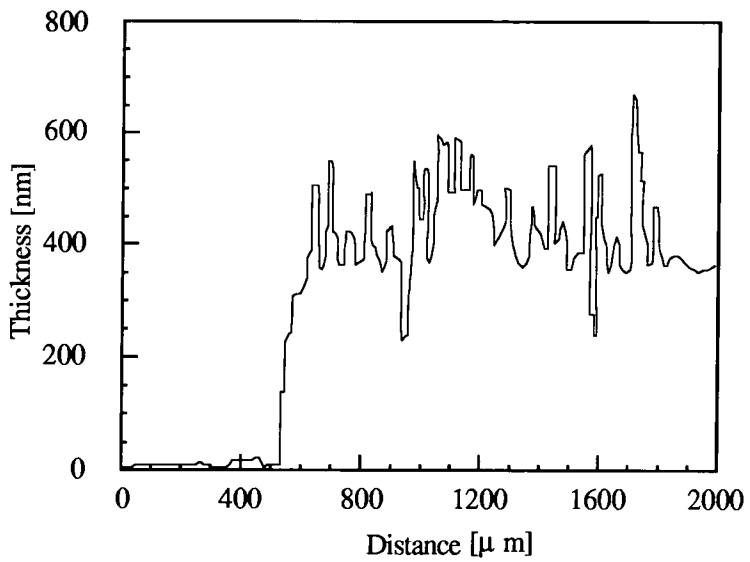
The surface of the films were uneven, revealing many surface defects. This indicates that LB films of MBSH/TA may not have good long range order between layers. There was a small increase in thickness close to edge of all the films, which was attributed to physical damage caused as the step was formed by wiping away a portion of the film. The relative step sizes confirm that reproducible dipping was achieved with a mixture of MBSH and TA, and that the average layer thickness was 5.9 ± 0.5 nm.



(a)



(b)



(c)

Figure 6.8: Alpha step profile for (a) 19 LB layers MBSH/TA (b) 38 LB layer MBSH/TA (c) 58 LB layers MBSH/TA deposited on single crystal silicon substrates.

6.2.5 Low-angle X-ray diffraction

Low-angle X-ray diffraction measurements were performed on 19/39/59 LB layer samples of MBSH/TA deposited on silicon substrates. Three measurements were taken for each sample: the specula component (incident angle equals angle of reflection); the off-specula (incident angle is 0.1° off the angle of reflection); and the transverse-diffuse component (profile of the Bragg peak). The off-specula component measures the scattering of the incident beam, due to the sample. Subtracting this from the specula component gives the scattering due to the LB film, shown in figure 6.9. A more detailed explanation of each technique has been provided in Chapter Four.

One diffraction peak was observed at a 2θ of 0.8° (for all the samples), corresponding to a first order Bragg reflection. From this it was possible to calculate the d-spacing (the repeat distance) of the MBSH/TA films to be 4.98 ± 0.1 nm. No Kiessig fringes were observed, thus it was not possible to calculate a total film thickness for the MBSH/TA film. From the other measurements, an average layer thickness of *ca* 5.0 nm has been derived. This contrasts to the expected repeat distance (usually bilayer thickness) of MBSH/TA. For Y-type LB films, the repeat distance is usually double the average layer thickness (ie, representative of a bilayer). With a repeat distance of 5.0 nm the expected average layer thickness would be 2.5 nm (*cf* average layer thickness for MBSH/TA of 5.0 nm). One explanation for this discrepancy is that both MBSH and MBSH/TA form a symmetrical bilayer at the air/water interface (see section 6.2.6).⁵



The lack of Kiessig fringes indicates that MBSH/TA may not form a well-ordered film on the substrate. The radius of correlation provides an indication of the long range order. This is defined as the number of layers needed before a stacking error of one half layer has built up⁶ and is calculated from the half-width of the diffraction peak. Figure 6.10 shows a linear plot of the Bragg peak for a 59 layer LB film of MBSH/TA, the half-width is indicated with its corresponding maximum and minimum angle values (θ_{\max} and θ_{\min}). These can then be put into a modified Bragg equation.⁷

$$R_c = \frac{n\lambda}{2 \sin(\theta_{\max} - \theta_{\min})} \quad [6-1]$$

where R_c is the radius of correlation, n is the Bragg peak order, and λ is the wavelength of the incident X-ray beam. The degree of long range order was calculated at 53.2 nm, which is equivalent to 5 bilayers of MBSH/TA stacking before half a layer of disorder is introduced. This is a relatively short distance, and substantiates the hypothesis that MBSH/TA forms LB films with little order (between layers).

The transverse-diffuse plot shown in figure 6.11 was generated by locating the sample at the first Bragg peak and holding the source and detector at the specula position ($\theta_i = \theta_r$). The sample was then tilted through a range of angles, the large spike in the centre of the plot is the first Bragg peak (ie, return to the specula position). From this plot it was possible to determine the surface roughness of the film. The average value for the correlated roughness (see section 4.2.4) of a sample can be deduced by taking the ratio of the specular component I_s (the area under the spike in figure 6.11) to the diffuse component I_d (area of the rest of the profile). The average value for the correlated roughness was calculated to be 1.27 ± 0.1 nm. This is large compared to the layer

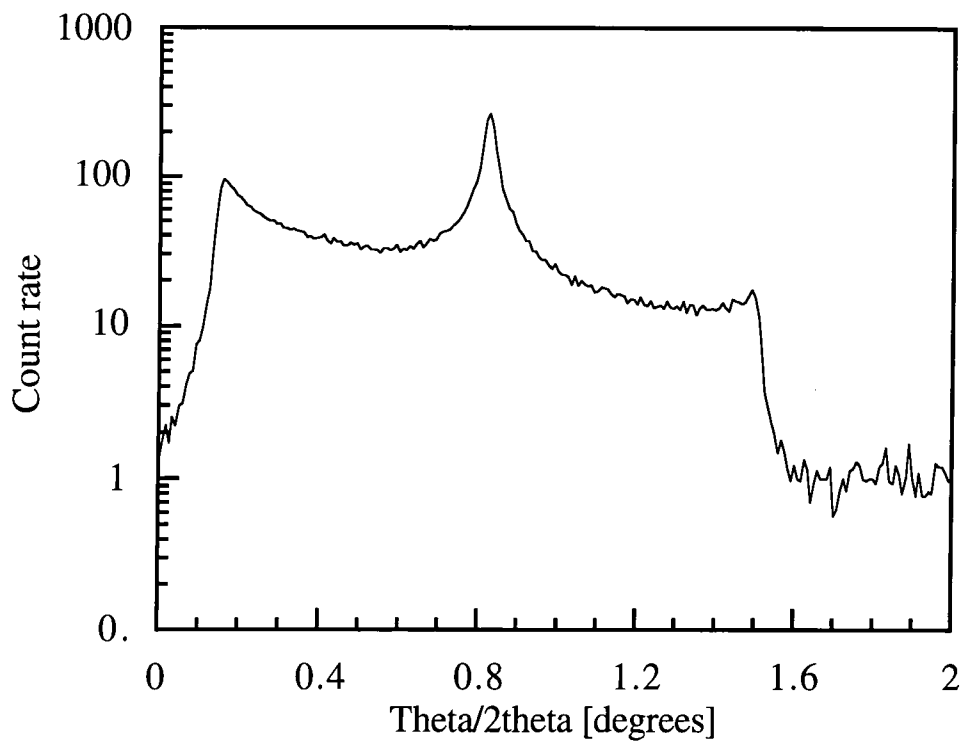


Figure 6.11: Transverse-diffuse plot for 59 LB layers MBSH/TA deposited on a single crystal silicon substrate.

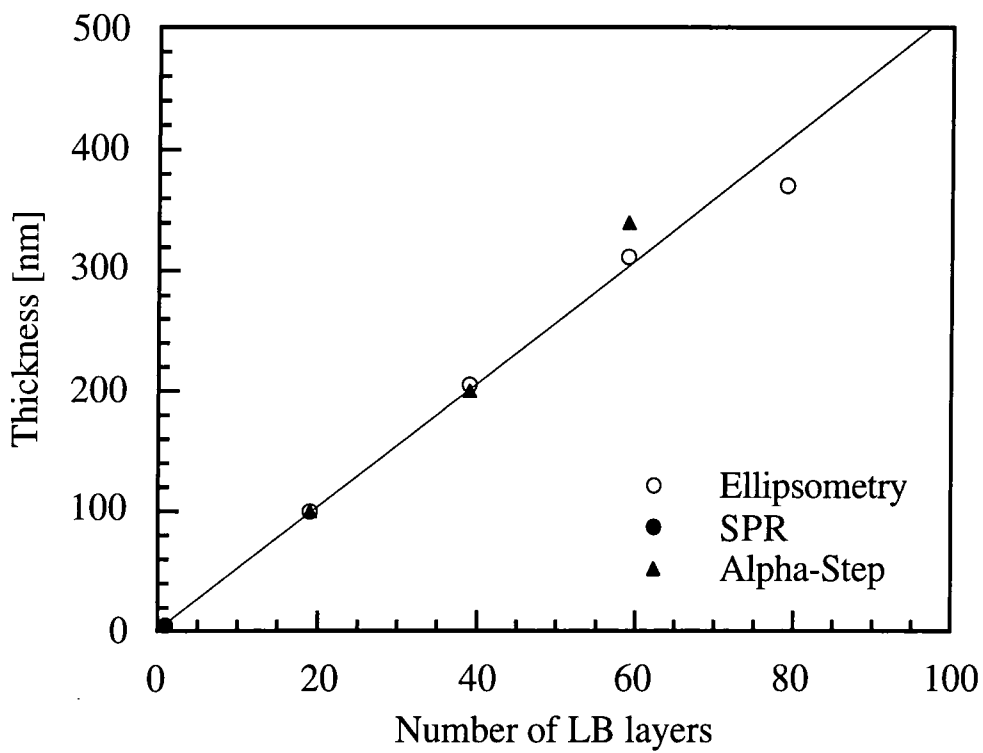


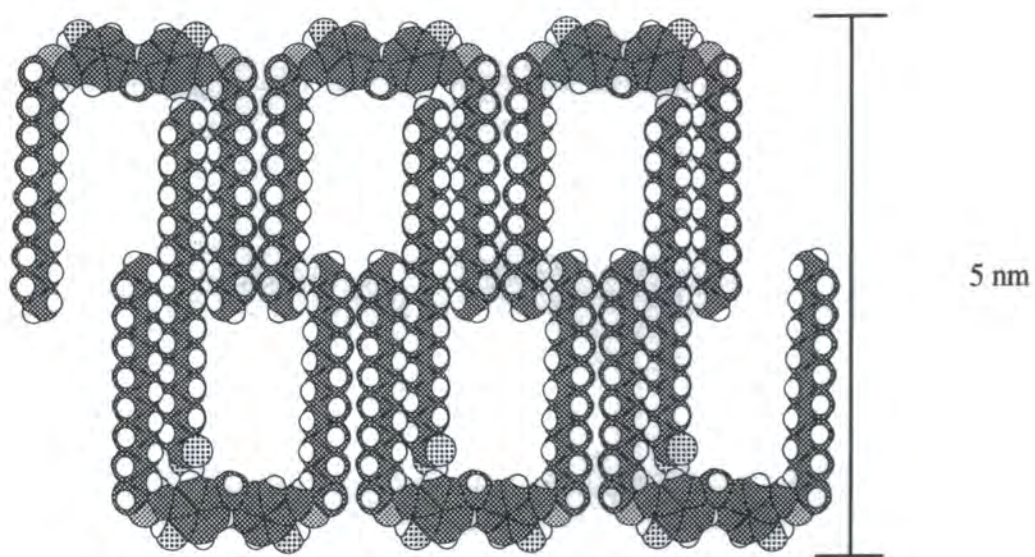
Figure 6.12: Film thickness versus number of LB layers of MBSH/TA deposited onto single crystal silicon.

thickness of MBSH/TA (*ca* 5.0 nm), again indicating that LB layers of MBSH/TA form relatively uneven layers on a substrate.

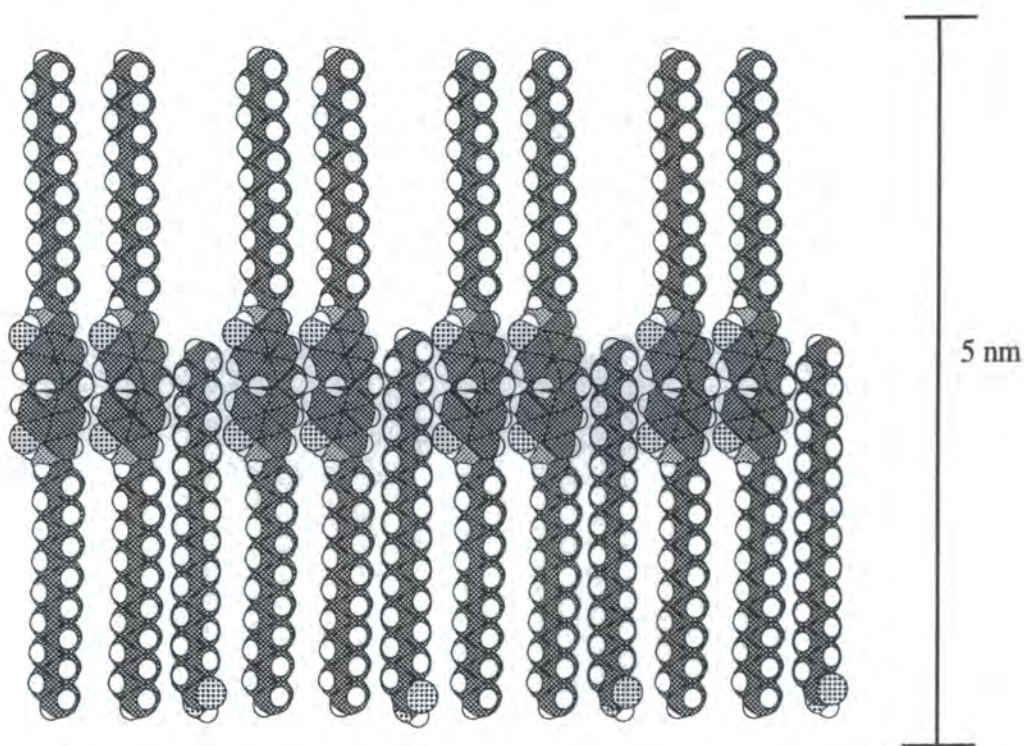
6.2.6 Structural orientation of MBSH/TA

The data shown in the previous sections indicate that LB films of MBSH/TA have a layer thickness of *ca* 5.0 nm. Figure 6.12 compares the total film thickness of MBSH/TA for each of the above techniques (SPR, ellipsometry, low angle X-ray diffraction and Alpha-step). The data lie on a straight line confirming that the films produce repeatable dipping characteristics, with the measurement techniques being in agreement (for layer thickness). A straight line fit to these data yields an average layer thickness of 5.01 ± 0.25 nm.

From molecular models, the largest length of MBSH is 2.8 nm (section 6.1.2(a)), and 3.0 nm for TA. The repeat distance of MBSH/TA from X-ray diffraction was *ca* 5.0 nm (ie the same length as our average layer thickness). There are a number of possible structures that could account for these discrepancies. For example, a complex of MBSH/TA could form in which the molecules form an interdigitated structure with the TA molecules sandwiched between two MBSH molecules (figure 6.13(a)). Another possibility is that the molecules of MBSH/TA are orientated so that one of the hydrophobic groups is adjacent to the subphase (figure 6.13(b)). This model has been suggested previously by Ashwell *et al* for second-harmonic generation in LB films.^{8,9} In both cases the structure, as deposited, would have a layer thickness of *ca* 5.0 nm, yet



(a)



(b)

hydrogen
 carbon
 oxygen
 nitrogen

Figure 6.13: The possible symmetrical orientations for MBSH/TA molecules deposited from a subphase of pure water.

due to the symmetrical shape of both conformations the d-spacing would also be *ca* 5.0 nm. The area per molecule of each system would also be 0.4 nm².

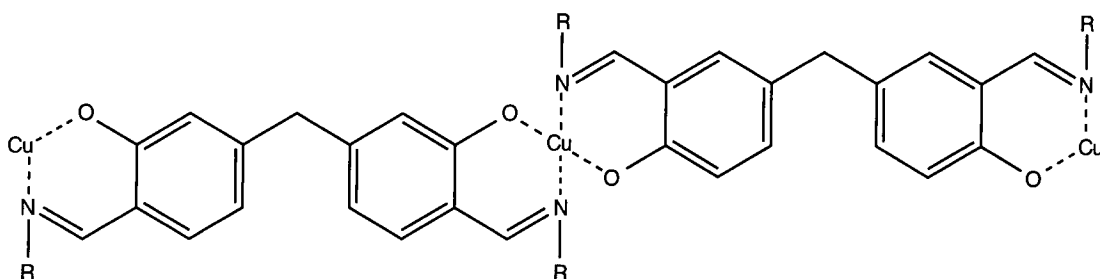
6.3 Langmuir layer characterisation of poly(CuMBSH)

6.3.1 Complex formation

On the addition of MBSH to the surface of a subphase containing copper(II) acetate tetrahydrate, an interfacial reaction occurs, linking the copper (II) ions (in the subphase) to two units of MBSH creating a linked chain (poly(CuMBSH)). This type of material is known as a Schiff base co-ordination polymer. Figure 6.14 shows the probable chemical structure.

6.3.2 Brewster angle microscopy

Brewster angle microscopy (BAM) pictures were recorded for 30 μl of MBSH spread on a subphase of pure water before and after the introduction of copper acetate (4 mg l⁻¹) into the subphase. Figure 6.15 shows images of the floating layer (a) before the introduction of copper acetate (b) 5 minutes after the introduction of copper acetate and (c) 50 minutes after the introduction of copper acetate. All the images were recorded at zero surface pressure, and an area per molecule of $0.52 \pm 0.05 \text{ nm}^2$. The floating layer undergoes two major changes in the time scale of the experiment. The first is the increase in domain size, from approximately 50 μm in diameter for figure 6.15(a), to an homogenous layer as shown in figure 6.15(c). The second change is the reduction in intensity of the domains, from very bright (almost saturation) in figure 6.15(a), through



part of the poly(CuMBSH) chain

_n

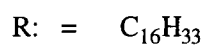
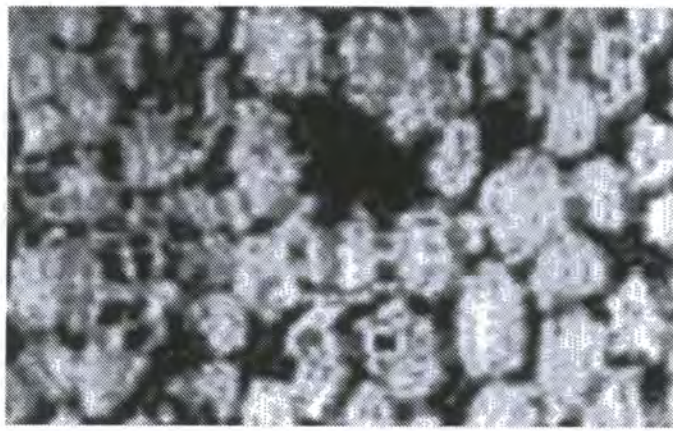


Figure 6.14: Structure of 5,5' methylenebis (N-hexadecylsalicylideneamine) as deposited from a subphase of pure water and copper acetate (4 mg l^{-1}).



(a)



(b)



(c)

Figure 6.15: Brewster angle microscopy images for 30 μl MBSH spread onto a subphase of (a) pure water (b) 5 minutes after copper acetate (4 mg l^{-1}) was added to the subphase (c) 50 minutes after copper acetate was added.

a transition stage in 6.15(b), to the less intense image in 6.15(c). The increase in domain size, from 50 μm to an homogenous layer, can be attributed to reorganisation on the Langmuir layer, as the copper in the subphase reacts with the MBSH monomer, forming poly(CuMBSH). The changes in image intensities are probably a consequence of the reduction in the thickness of the Langmuir layer (due to the Langmuir layer reorganisation). The intensity of reflected light from the subphase/Langmuir plane can depend upon the thickness, roughness or anisotropy of the Langmuir layer.^{1,10} Changes in both domain size and image intensity indicate that, during the polymerisation of the MBSH units by the Cu^{2+} ions (by a loss of two protons), the MBSH structure reorganises forming a thinner layer.

6.3.3 Langmuir-Blodgett technique

(a) Surface pressure versus area isotherms

Isotherms were obtained for a solution of MBSH spread on a subphase containing 4.0 mg l^{-1} copper acetate and pure water. Pressure versus area isotherms were recorded at a compression speed $3.2 \times 10^{-2} \text{ nm}^2 \text{ molecule}^{-1} \text{ s}^{-1}$. Figure 6.16 shows isotherms for 50 μl MBSH spread on the subphase. These were recorded at various times after the solution had been applied to the subphase surface. The shape of the isotherm was found to be independent of the time the material had spent on the subphase. The area occupied by the molecules in the Langmuir layer was calculated, the smallest area per molecule of poly(CuMBSH) being $0.82 \pm 0.1 \text{ nm}^2$. This figure compares well to that obtained from molecular models of *ca* 0.8 nm^2 and as published by Öertel *et* Nagel.² The area per molecule of poly(CuMBSH) is almost double that of MBSH (*cf* 6.1.2 (a)), suggesting

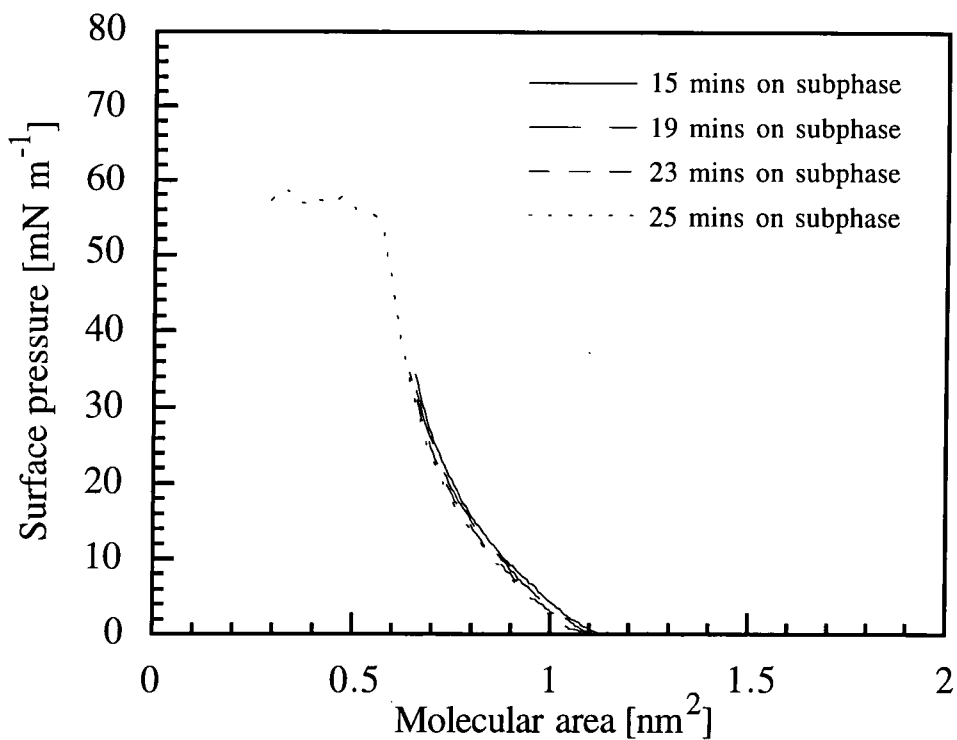


Figure 6.16: Surface pressure versus area isotherms for 50 μl MBSH spread on a subphase of pure water ($\text{pH} = 5.8 \pm 0.2$ at 20 ± 2 $^{\circ}\text{C}$) containing 4.0 mg l^{-1} copper acetate.

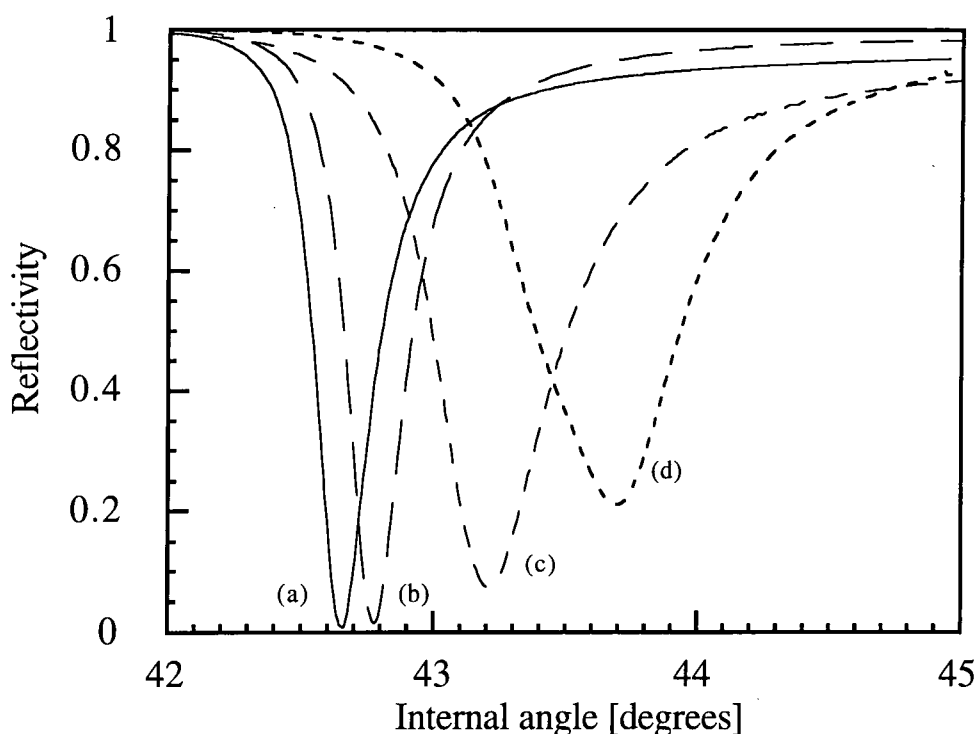


Figure 6.17: Surface plasmon resonance ($\lambda = 632.8 \text{ nm}$) curves for (a) 50 nm silver layer (b) silver + 1 LB layer poly(CuMBSH) (c) silver + 3 LB layer poly(CuMBSH) (d) silver + 5 LB layers poly(CuMBSH).

that MBSH reacts with the copper acetate in the subphase and rearranges on the subphase surface.

(b) Langmuir-Blodgett deposition

In contrast to pure MBSH (*cf* 6.1.2 (b)), poly(CuMBSH) could be easily transferred to glass, silvered glass, hydrophobic silicon and quartz substrates using the LB technique. Optimum film transfer (Y-type deposition) was obtained at a surface pressure of 25 mN m⁻¹ and a substrate dipping speed of between 6 and 8 mm min⁻¹. The deposition ratio was reproducible (over a number of layers), with the first down stroke giving a ratio of 0.5 ± 0.1 , all subsequent passes through the subphase surface gave a deposition ratio of 1.0 ± 0.1 .

6.4 Structural characterisation of poly(CuMBSH)

6.4.1 Surface plasmon resonance

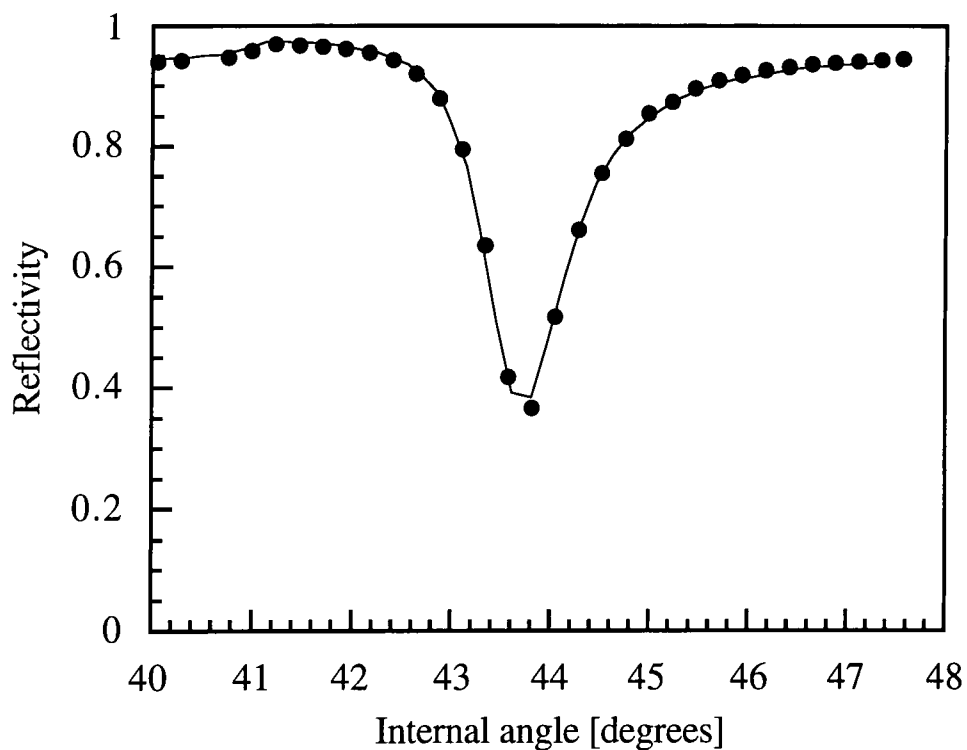
Surface plasmon resonance curves were generated for 1,2,3,4 and 5 LB layer samples of poly(CuMBSH) on silvered (50 nm) glass slides (Z-type deposition obtained using a dual area LB trough). The curves are shown in figure 6.17, with the first curve (a) being the uncoated 50 nm silver profile and curves (b) 1 LB layer poly(CuMBSH), (c) 3 LB layers of poly(CuMBSH) and (d) 5 LB layers poly(CuMBSH). The curves show that as the number of LB layers increase the point of resonance moves to higher angles, begins to broaden and the depth of resonance minimum decreases. The data for the SPR curves shown in figure 6.17 were modelled on computer, to give the permittivity and film

thickness for each film. The fitted data for a new sample (5 LB layers) of poly(CuMBSH) on 50 nm layer of silver are shown in figure 6.18 (a). In this case the fit is good, following the profile of the experimental data, with an average fitting error of 0.02. Figure 6.18 (b) shows the deviation from the theoretical results, as before the only part of the curve that does not fit perfectly is the depth of resonance minimum. The values for permittivity, thickness and refractive index are given in table 6.4 below.

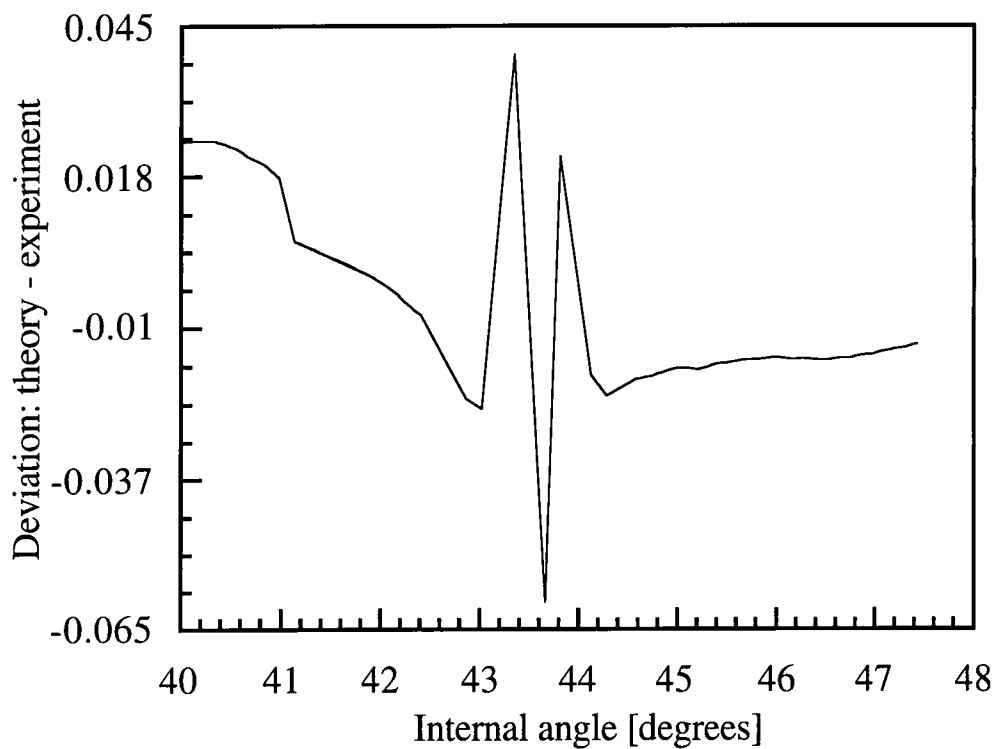
Number of LB layers	Permittivity	Refractive index	Film thickness [nm]
1	2.43 + 0.38i	1.56	2.13
2	2.41 + 0.43i	1.55	4.01
3	2.32 + 0.56i	1.52	5.91
4	2.45 + 0.10i	1.57	7.52
5	2.41 + 0.37i	1.55	9.38

Table 6.4: Permittivity and refractive index values for multilayer films of poly(CuMBSH) from SPR.

The values for refractive index were approximated, as before (*cf* 6.2.1), by taking the square root of the real part of the permittivity. The values for permittivity and refractive index for 1,2,3,4 and 5 LB layers give an average layer thickness of 1.97 ± 0.05 nm, which is a close match (within experimental error) with the value obtained via ellipsometry (section 6.4.2). The close match for the refractive index, and the linear



(a)



(b)

Figure 6.18: (a) Surface plasmon resonance curve for 5 LB layers poly(CuMBSH) on 50 nm silver; dots - experimental data; solid line - theoretical data, (b) deviation of theoretical SPR curve from the one obtained experimentally.

increase in film thickness with number of LB layers indicate that poly(CuMBSH) forms repeatable good quality LB layers even down to monolayer thickness.

6.4.2 Ellipsometry

Step structures of 19,39,59 and 72 LB layers of poly(CuMBSH) were deposited on hydrophobic silicon substrates. These were interrogated using ellipsometry (conditions as before, section 6.2.3) to obtain values for film thickness and refractive index. A plot of thickness versus number of LB layers for poly(CuMBSH) on hydrophobic silicon is shown in figure 6.19. The data points lie on a straight line, confirming the reproducible nature of film transfer. The straight line fit yields a layer thickness of 1.71 ± 0.25 nm. This is less than the minimum side chain lengths of the poly(CuMBSH) molecule indicating that the chains may not be perpendicular, but tilted through an angle from the vertical.

Ellipsometry was also used to determine the refractive index of the poly(CuMBSH) material. Measurements were undertaken on two films, the first 19 LB layers, and the second 39 LB layers. These data are presented in table 6.5. The values for refractive index at 632.8 nm are the same, within experimental error, yet those at 546.1 nm do not agree. These values for refractive index correspond to the shape of the UV/visible spectra with the film being more absorbing at 546.1 nm (*cf* shown in section 6.4.3). Poly(CuMBSH) has a greater refractive index than MBSH/TA, which could be a result of the reaction with the Cu^{2+} ions in the subphase.

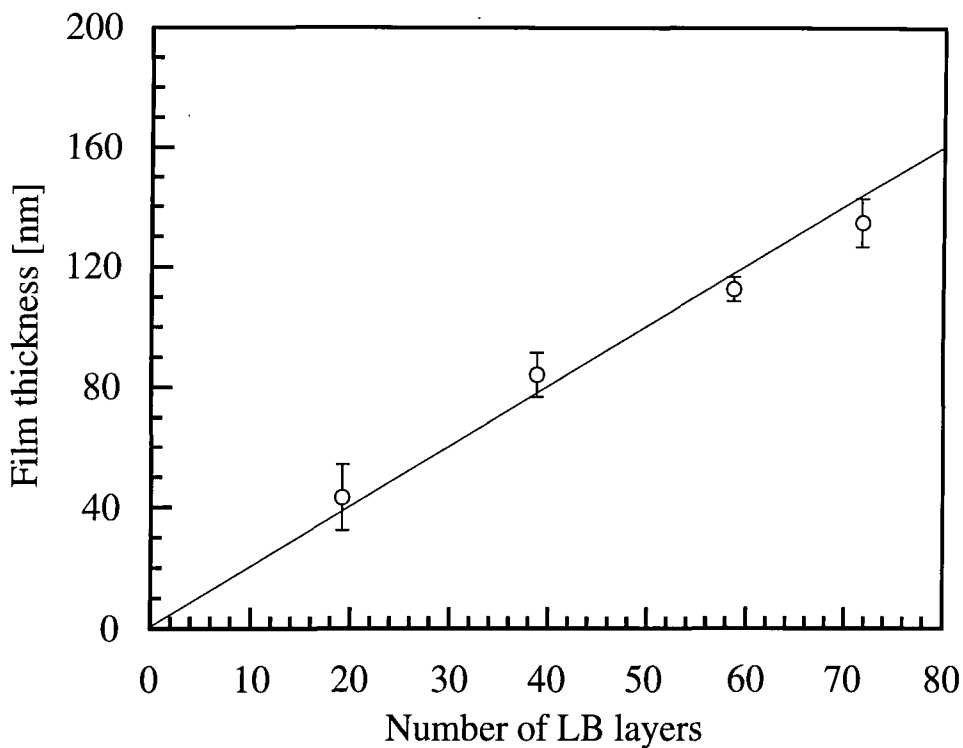


Figure 6.19: Film thickness versus number of LB layers measured using ellipsometry ($\lambda = 546.1$ and 632.8 nm). For LB layers of poly(CuMBSH) as deposited onto a single crystal silicon substrate.

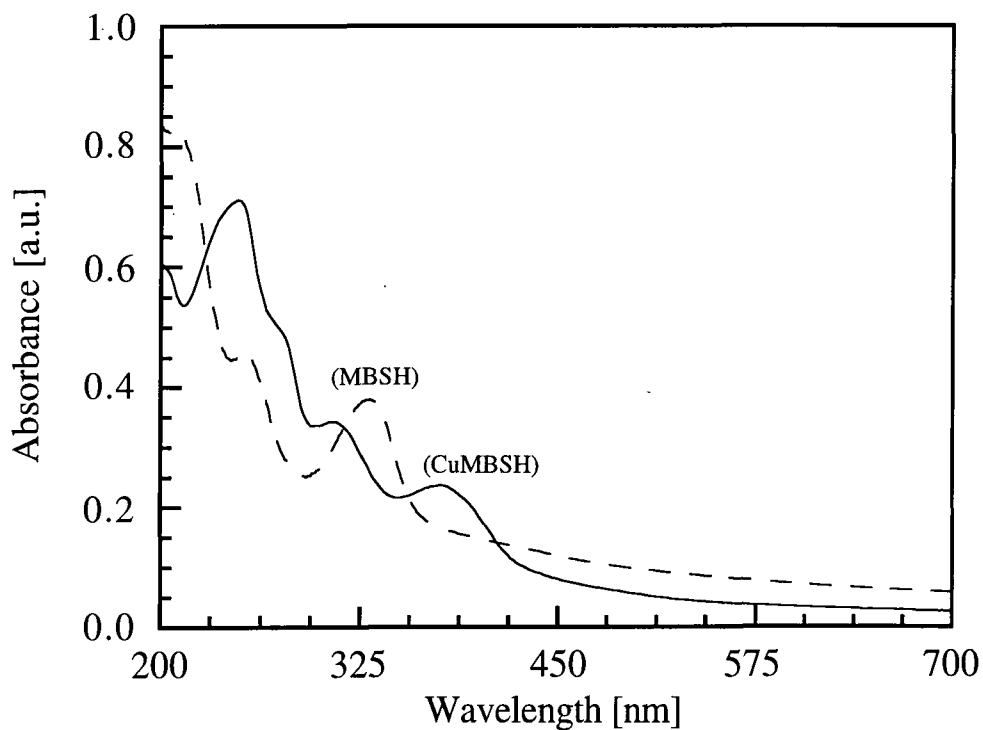


Figure 6.20: UV/visible spectra for 29 LB layers MBSH/TA and 29 LB layers poly(CuMBSH) deposited onto a quartz substrate.

Number of LB layers	Refractive index	
	$\lambda = 546.1 \text{ nm}$	$\lambda = 632.8 \text{ nm}$
19	1.542 ± 0.020	1.556 ± 0.004
39	1.594 ± 0.016	1.553 ± 0.010

Table 6.5: Refractive index of 19 and 39 LB layers of poly(CuMBSH)

6.4.3 UV/Visible spectroscopy

LB layers of poly(CuMBSH) appeared homogenous to the naked eye. The optical absorption spectra for 29 LB layers of MBSH/TA and poly(CuMBSH) deposited on quartz slides are contrasted in figure 6.20. Poly(CuMBSH) shows the same bands as MBSH/TA (*cf* 6.2.3), with a $\sigma \rightarrow \pi^*$ transition at 300 nm and a $\pi \rightarrow \pi^*$ transition at 380 nm. These absorptions are blue shifted (by *ca* 50 nm) in the poly(CuMBSH) spectrum, suggesting an interfacial reaction between MBSH and Cu^{2+} .

6.4.4 Alpha-step measurements

The thickness of a 72 LB layer film of poly(CuMBSH) on hydrophobic silicon was measured using an Alpha-step. Figure 6.21 shows the profile of the metallised step, with an average layer thickness of $2.03 \pm 0.6 \text{ nm}$. The surface of the film was continuous, showing few peaks. The profile for poly(CuMBSH) is much more regular than for MBSH/TA (*cf* 6.2.4) indicating that poly(CuMBSH) may form a film with greater long range order.

6.4.5 Low angle X-ray diffraction

X-ray diffraction measurements were performed on 19/39/59 LB layer samples of poly(CuMBSH) deposited on hydrophobic single crystal silicon substrates. Three measurements were taken for each sample (as before, see section 6.2.5): the specula; off- specula; and the transverse-diffuse component. Figure 6.22 shows one diffraction peak at a 2θ of 1° , which corresponds to the first order Bragg reflection. From this value it was possible to calculate the d-spacing (the repeat distance) for the poly(CuMBSH) film. The Kiessig fringes reveal the total film thickness due to interference between the top and bottom of each layer. A comparison of the d-spacing and total film thickness for each sample are given in table 6.6. The data indicate that the repeat distance of poly(CuMBSH) is 4.03 ± 0.03 nm, with a layer thickness of 2.26 ± 0.06 nm. Figure 6.23 is a linear plot of the Bragg peak for a 59 layer LB film of poly(CuMBSH), the half-width is indicated with its corresponding maximum and minimum angle values. This can then be put into the modified Bragg equation,⁷ to determine the radius of correlation (R_c). The degree of long range order was calculated at 99.76 nm, equivalent to 25 bilayers of poly(CuMBSH) stacking before half a layer of disorder. This figure is five times that for MBSH/TA confirming that LB films of poly(CuMBSH) are much more ordered.

As with LB films of MBSH/TA, we can calculate the correlated roughness (σ_c) of poly(CuMBSH) (*cf* section 6.2.5), using figure 6.24. This was calculated to be 0.32 ± 0.01 nm. The roughness of poly(CuMBSH) is thus much smaller than MBSH (1.27 ± 0.1

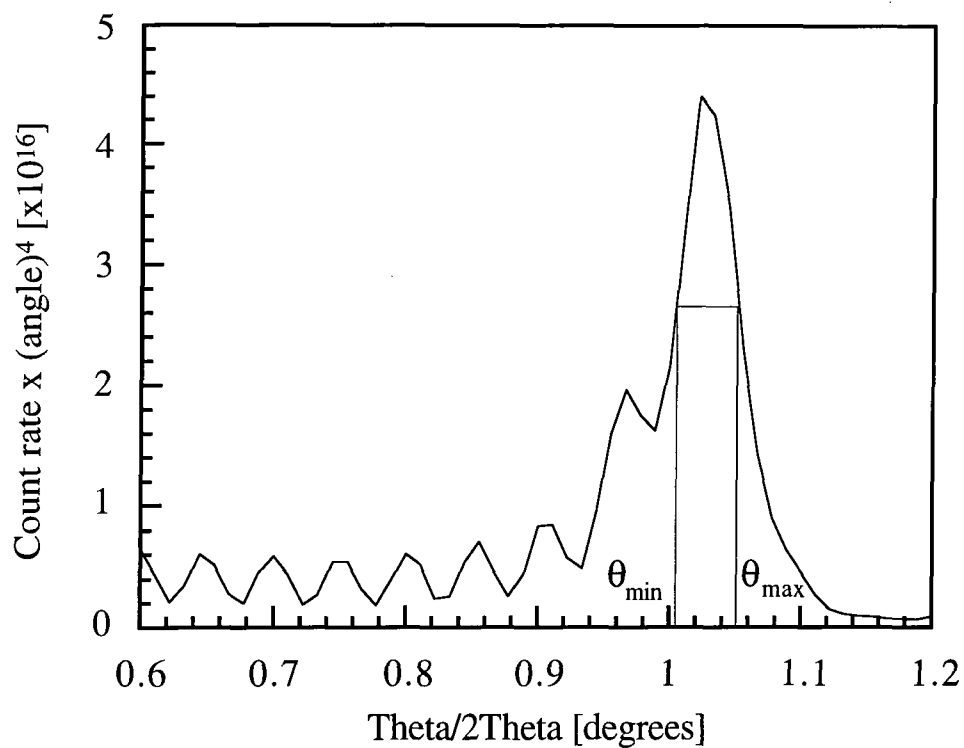


Figure 6.23: Linear plot of the first Bragg peak for 59 LB layers poly(CuMBSH) deposited on a single crystal silicon substrate.

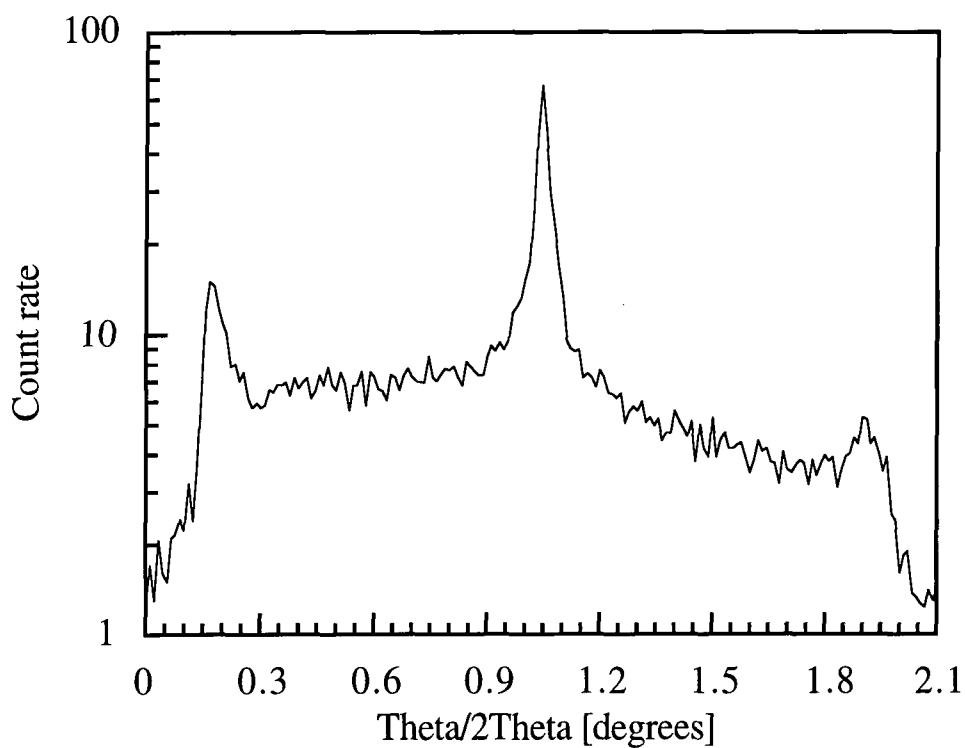


Figure 6.24: Transverse-diffuse plot for 59 LB layers poly(CuMBSH) deposited onto a single crystal silicon substrate.

nm) again supporting the view that LB films of poly(CuMBSH) have greater interlayer order.

Number of LB layers	d-spacing [nm]	Total film thickness [nm]
19	4.0 ± 0.1	47.8 ± 1.5
39	4.0 ± 0.1	82.9 ± 1.5
59	4.1 ± 0.1	127.5 ± 1.5

Table 6.6: Repeat distance and total film thickness of poly(CuMBSH)

6.4.6 Electron spin resonance

Electron spin resonance (ESR) spectroscopy was used to establish the orientation of as deposited poly(CuMBSH). Measurements to determine the orientation of the copper atoms within films of MBSH were undertaken at the Institute of Chemical Physics in Chernogolovka, Russia, by Dr. L.M. Goldenberg and Dr. V.I. Krinichnyi on samples prepared at the University of Durham.¹¹ 48 LB layers of poly(CuMBSH) were deposited onto polyethyleneterephthalate sheets. The coated sheets were cut into strips *ca* 5 mm wide and 20 mm long. These were then placed together to form sandwich structure (LB film-sheet-LB film-sheet etc) seven units thick. This approach was used to increase artificially the sample thickness, thus improving the signal strength. ESR measurements were performed on a commercial X-band PS-100X spectrometer with the polarising magnetic field modulated at 100 kHz. The samples were mounted so that the substrate

normal could be varied relative to the external magnetic field, the resulting linewidth ($g = 2.0544$) is shown in figure 6.25.

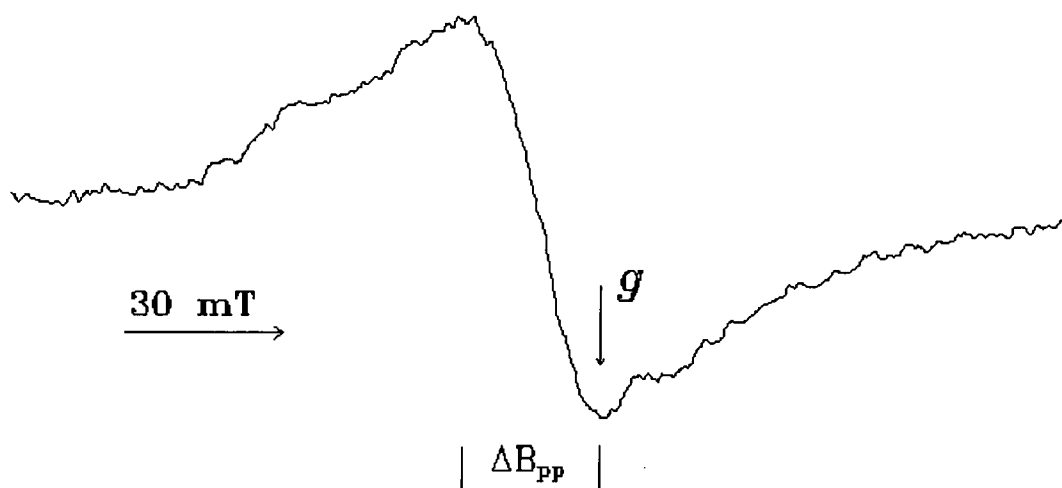


Figure 6.25: X-Band electron spin resonance spectra for LB films of poly(CuMBSH) at 313K, the position of the g-factor for free electrons is also shown.

The spectrum for poly(CuMBSH) is not well defined, leading to the conclusion that the orientation of Cu^{2+} ions are randomly distributed within the LB film. The g factor for poly(CuMBSH) is at a minimum when the applied magnetic field (B_0) is 120° to the substrate surface. This corresponds to the copper ions in the LB film being orientated at *ca* 30° to the substrate. A possible explanation for the tilt in the polymeric LB film may be due to the flexibility of the methylene group between the two benzene rings, the polymer chains could adopt a 'zig-zag' conformation in which Cu complex plane is effectively tilted, shown in figure 6.26.¹¹

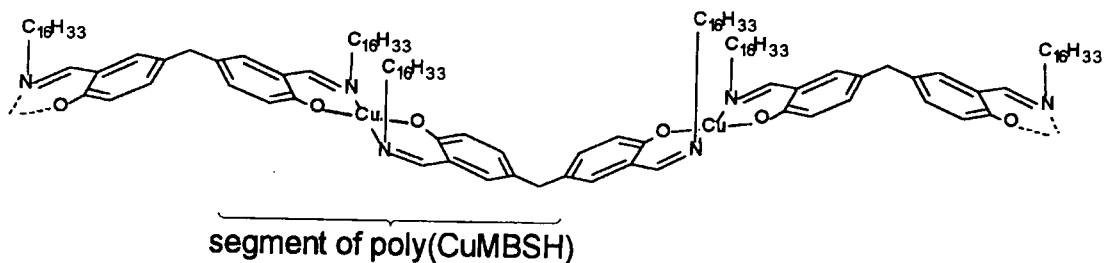


Figure 6.26: Possible orientation for a segment of the poly(CuMBSH) chain.

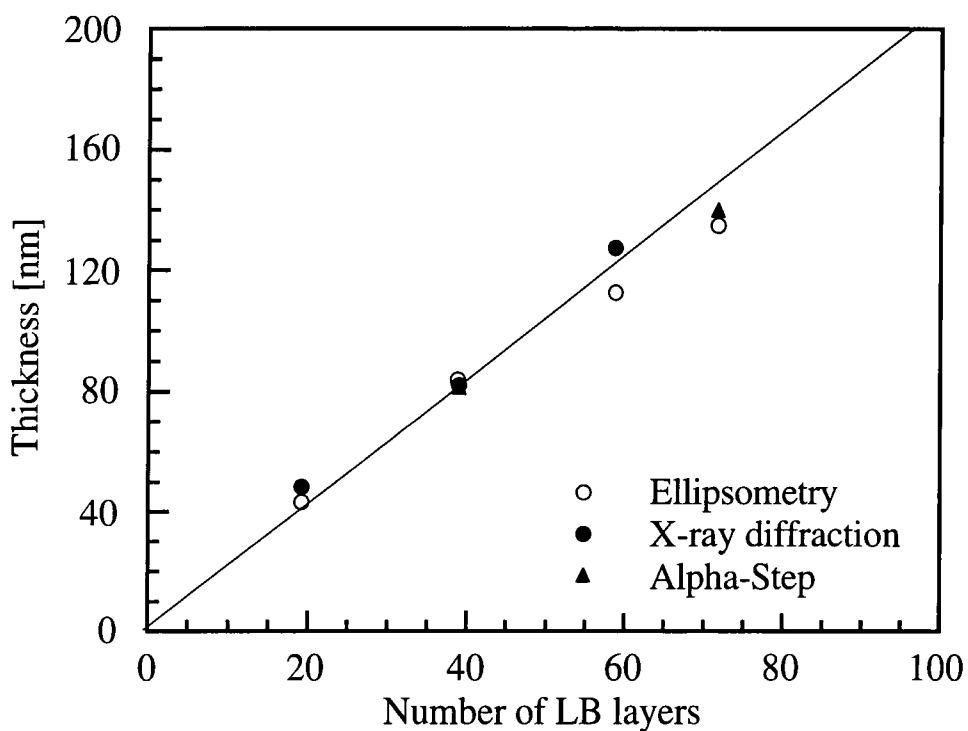


Figure 6.27: Film thickness versus number of LB layers of poly(CuMBSH) deposited onto single crystal silicon. X-ray data obtained from Kiessig fringes.

6.4.7 Structural orientation of poly(CuMBSH)

The data shown in the previous sections show that LB films of poly(CuMBSH) possess a layer thickness of *ca* 2.0 nm. Figure 6.27 compares the total film thickness of poly(CuMBSH) for each of the above techniques (SPR, ellipsometry, low angle X-ray diffraction, Alpha-step). The experimental points lie on a straight line indicating that the films possess repeatable dipping characteristics, with the measurement techniques being in agreement (for layer thickness). A straight line fit to these data yields an average layer thickness of 1.76 ± 0.25 nm.

The orientation of MBSH on a subphase of pure water and copper acetate, and the as deposited film, have also been investigated by Fourier transform infra-red spectroscopy (FTIR).¹² FTIR studies were undertaken by Dr J. Nagel at the Institut Für Polymerforschung, Germany. The experiments revealed that a complex formation took place between the azomethin N atom and the phenolic O atom of MBSH on the subphase surface. The degree of polymerisation could not be exactly determined, but it was assumed that a high degree of conversion of the MBSH unit had occurred.¹³

Computer modelling of the poly(CuMBSH) molecule was performed using HyperChem on a PC. This showed that each of the hydrophobic side branches of the poly(CuMBSH) molecule ($C_{16}H_{33}$) was approximately 2.8 nm long (ie, longer than the measured monolayer thickness). One possible explanation for this is that the side chains are not oriented perpendicular to the subphase, but tilted through 45° from the vertical, as indicated in figure 6.28 (for one repeat unit).

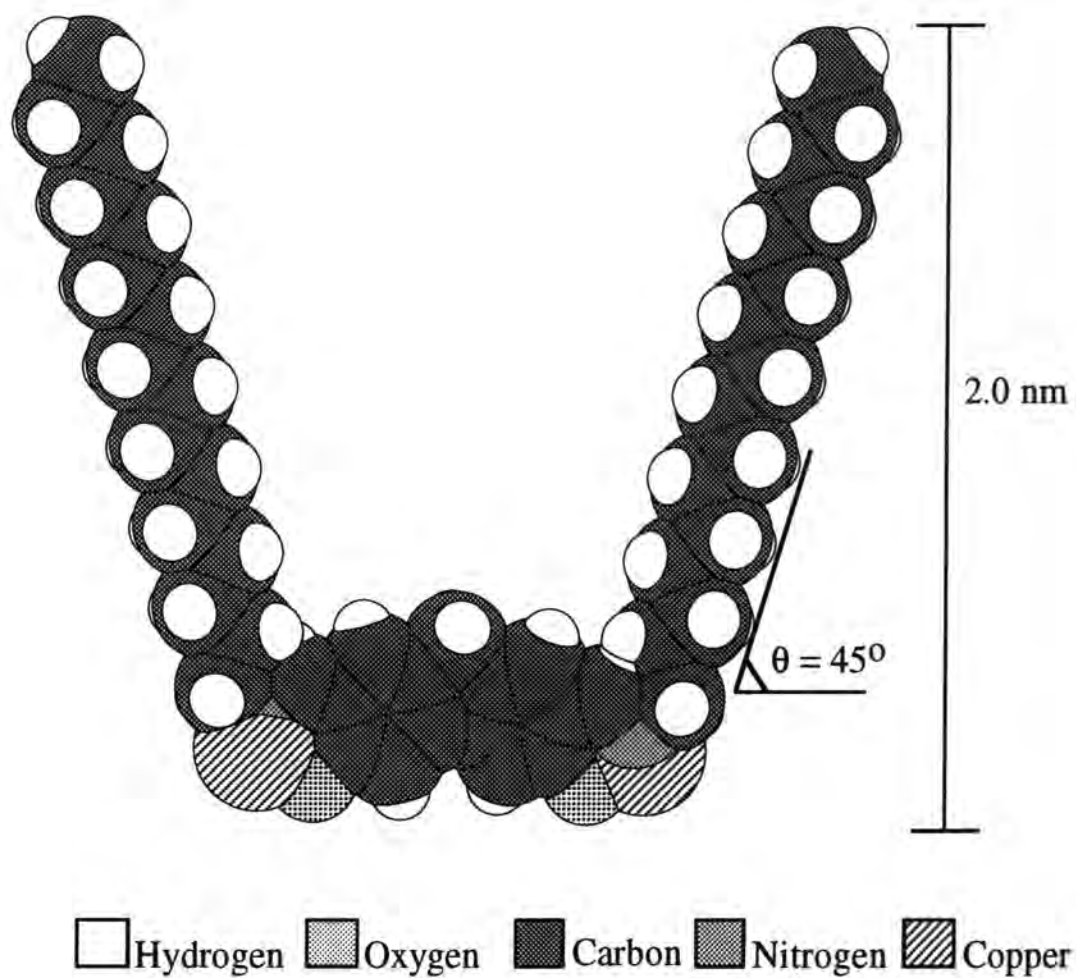


Figure 6.28: Possible orientation for one repeat unit of MBSH spread on a subphase of pure water containing 4 mg l^{-1} copper acetate (poly(CuMBSH))

6.5 Summary

The Langmuir layer and Langmuir-Blodgett deposition properties of 5,5'-methylenebis (N-hexadecylsalicylideneamine) deposited from a subphase of pure water have been described. The pure MBSH could not be deposited, but a mixture of MBSH and tricosanoic acid (38%TA to 62% MBSH by volume) produced repeatable LB deposition characteristics. The total film and layer thicknesses for MBSH/TA were measured by low angle X-ray diffraction, ellipsometry, SPR and using an Alpha-step. The average layer thickness from the above techniques was 5.01 ± 0.25 nm. Low angle X-ray diffraction gave a value of 5.00 ± 0.04 nm for the d-spacing of MBSH/TA. There are a number of possible structures that could account for this discrepancy, first, a complex of MBSH/TA in which the molecules form an interdigitated structure with the TA molecules sandwiched between two MBSH molecules. Secondly, the molecules of MBSH/TA may be orientated so that one of the hydrophobic groups is adjacent to the subphase. In both cases, the structure, as deposited, would have a layer thickness of *ca* 5.0 nm, yet due to the symmetrical shape of both conformations the d-spacing would also be *ca* 5.0 nm.

5,5'-methylenebis (N-hexadecylsalicylideneamine) was then deposited from a subphase containing water and 4.0 mg l^{-1} copper(II) acetate tetrahydrate. A reaction was found to occur between the copper (II) ions in the subphase, and the MBSH monomers. This formed a Langmuir layer of linked MBSH monomers (by the copper (II) ions). The average layer thickness was determined to be 1.76 ± 0.25 nm. Low angle X-ray diffraction gave a d-spacing (a bilayer thickness) of 4.0 nm, confirming that poly(CuMBSH) molecules are arranged in a Y-type manner in the deposited film. ESR

measurements indicated that the plane of copper atoms within the multilayer films were angled at 30° to the substrate surface. This angle can be accounted for by a rotation in the methylene group between the two benzene rings. The rotation forces the films of poly(CuMBSH) to adopt a 'zig-zag' conformation.

References

- 1 D. Honig, D. Möbius, *J. Phys. Chem.*, 95, **1991**, 4590-4592
- 2 J. Wilson, J.F.B. Hawkes, "**Optoelectronics, An Introduction**", 2nd Edition, *Prentice Hall International Ltd*, London, **1989**, (ISBN: 0-13-638461-7), 440-441.
- 3 U. Öertel, J. Nagel, *Thin Solid Films*, 284-285, **1996**, 313-316
- 4 J. Nagel, *Private Communication*.
- 5 Reference for materials that form a symmetrical monolayer structure.
- 6 L.A. Feigin, Yu.M. Lvov, V.I. Troitsky, *Soviet Scientific Reviews/ Section A*, 11 (4), **1989**, 285-377.
- 7 M.C. Petty, "**Langmuir-Blodgett films, An Introduction**", *Cambridge University Press*, Cambridge, **1996**, (ISBN: 0-521-42460-X), 98-104.
- 8 G.J. Ashwell, G. Jefferies, C.D. George, R. Ranjan, R.B. Charters, R.P. Tatam, *J. Mater Chem.*, 6, **1996**, 131-136.
- 9 G.J. Ashwell, P.D. Jackson, G. Jefferies, I.R. Gentle, C.H.L. Kennard, *J. Mater Chem.*, 6, **1996**, 137-141.
- 10 S. Henon, J. Meunier, *Rev. Sci. Instrumen.*, 62, **1991**, 936-939.
- 11 L.M. Goldenburg, J.N. Wilde, V.I. Krinichnyi, J. Nagel, M.C. Petty, *Thin Solid Films*, in preparation.
- 12 J. Nagel, U. Öertel, *Thin Solid Films*, in press.

Chapter Seven

Results and Discussion: Vapour Sensing

7.0 Preface

This chapter describes the results of experiments using sensing elements fabricated from LB films of phthalocyanines, polysiloxanes and a co-ordination polymer. The reaction of each element on exposure to concentrations of benzene, toluene, ethanol and water vapour was examined and the results obtained for the different materials are compared. The effect of each vapour on the underlying thin layers of silver (substrate coating) is also discussed.

7.1 Comparison of materials to saturated vapour concentrations

Initially a number of materials were exposed to saturated concentration of benzene, toluene and ethanol vapours. These data were recorded to give some indication of the most reactive sensing materials. LB layers of copper tetrakis-(3,3-dimethyl-1-butoxycarbonyl) phthalocyanine (CuPcBC), zinc tetrakis-(3,3-dimethyl-1-butoxycarbonyl) phthalocyanine (ZnPcBC), polysiloxane (AMCR23) and copper 5,5'-methylenebis (N-hexadecylsalicylideneamine) co-ordination polymer (poly(CuMBSH)) were all used. The chemical structures of these compounds can be found in Chapter Three.

Table 7.1 compares the change in photodiode output for each film on exposure to the various vapours. The response characteristics follow a basic trend; the magnitudes of the responses for benzene and toluene were similar while that for ethanol was lower. The turn-on characteristics for each material were similar with 90% response reached within 60 seconds. However, different recovery times were noted: poly(CuMBSH) and AMCR23 achieving full recovery within 60 minutes; CuPcBC and ZnPcBC did not recover fully, exhibiting some background drift in detector output, which was attributed to sensor ‘poisoning’. As the data indicate, poly(CuMBSH) is the most reactive on exposure to benzene, toluene and ethanol vapour. Three materials were chosen for further investigations. These were poly(CuMBSH), CuPcBC and AMCR23.

Vapour	poly(CuMBSH) [mV]	AMCR23 [mV]	CuPcBC [mV]	ZnPcBC [mV]
benzene	47	25	16	15
toluene	38	14	11	10
ethanol	20	6	4	5

Table 7.1: Response of different sensing materials to saturated concentrations of benzene, toluene and ethanol vapour.

7.2 Background response of silver layer

Silver was chosen as the substrate coating for all the gas sensing experiments in this chapter. The main consideration was that the SPR curve of silver is much sharper than that of gold. A sharper resonance means that a large change in photodiode output is

recorded for a small change in the shape/position of the SPR curve (ie, a more sensitive gas sensing system).

A 50 nm thick layer of silver on a quartz glass substrate, deposited by thermal evaporation, was first exposed to quantities of benzene, toluene and ethanol. This was to establish the effect on the underlying silver layer. For each vapour, a new substrate was prepared and its optical properties were examined by SPR. Figures 7.1, 7.2 and 7.3 show the change in reflectivity curves on exposure to 330 vapour parts per million (vpm) benzene, 300 vpm toluene and 629 vpm ethanol, respectively. On exposure to benzene and toluene (fig 7.1 and 7.2) there was a slow monotonic increase in the measured reflectivity. This could be attributed to a shift in the SPR curve to higher angles. A simple explanation for the similar response for both benzene and toluene is that their refractive indices are almost identical, benzene 1.498 and toluene 1.494.¹ On exposure to 629 vpm ethanol (lowest concentration that could be generated) the response of the silver layer was less dramatic. There was a slow upward drift in the photodiode output corresponding to a shift in the SPR curve to higher angles. This smaller drift in photodiode output may be due to the lower refractive index of ethanol vapour. For each experiment, there was no observed recovery (in the time scale of the experiment) when the vapour was replaced by dry nitrogen. This could be due to the force of attraction (Van der Waals force) between molecules of benzene, toluene or ethanol and the solid surface.³

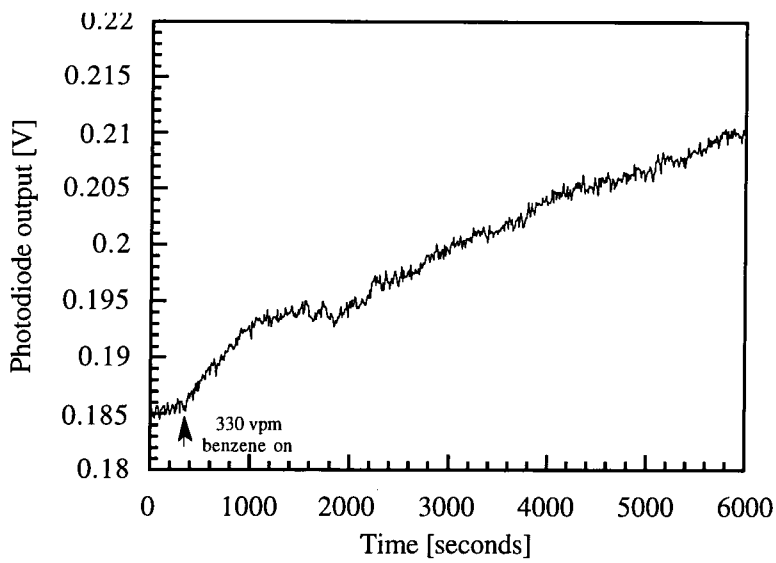


Figure 7.1: 50 nm silver layer exposed to 330 vpm benzene vapour

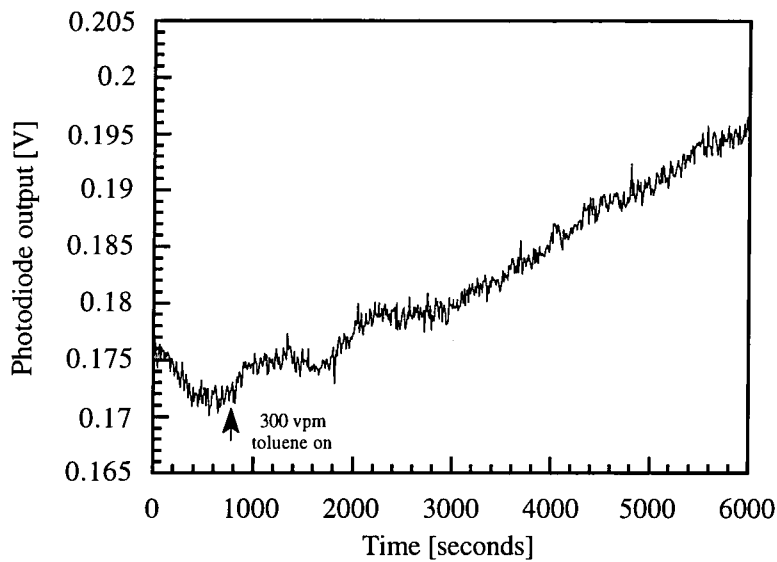


Figure 7.2: 50 nm silver layer exposed to 300 vpm toluene vapour

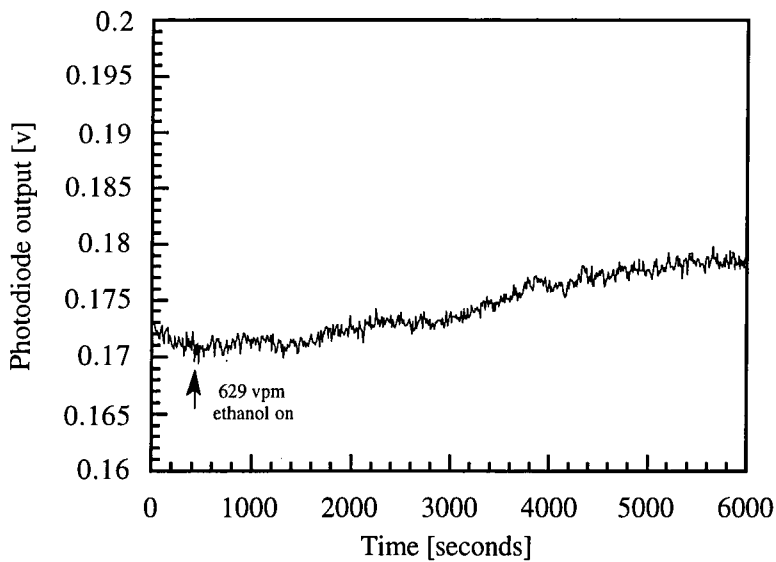


Figure 7.3: 50 nm silver layer exposed to 629 vpm ethanol vapour

This drift in photodiode output is almost certainly related to vapour condensing on the silver surface. The irreversibility could be due to the forces of attraction involved in this process. This effect has been documented for alkanes and other organic vapours on gold films.^{2,3} For example, Bradberry *et al* exposed gold layers to saturated vapour concentrations of methanol, n-heptane, n-heptane and ethanol, and the adsorption of vapours on the metallic surface was monitored by SPR.² The experiments indicated that the shift in the resonance curve (and so the change in film thickness) increased linearly with relative pressures (vapour concentration). For the vapours investigated, the film growth reached equilibrium after a relatively short time *ca* 70 minutes (for methanol, n-hexane and n-heptane). However, ethanol produced indefinite film growth. The data presented here for ethanol vapour supports this, with experiments run over 100 minutes and no film saturation observed within this time scale. The effect is also noted for vapours of benzene and toluene, which produced indefinite film growth, within the time scale of the experiment.

These data indicate that the drift in photodiode output is due to thin layers of vapour forming on the silver surface, changing either the refractive index or thickness of the system. Depositing LB layers onto the silver should inhibit this process, reducing the drift in photodiode output.

7.3 Comparison of materials to controlled vapour concentrations

Thin films of poly(CuMBSH), CuPcBC and AMCR23 were next exposed to varying concentrations of benzene (100 to 10000 vpm); toluene (100 to 3000 vpm); and ethanol

(629 to 17000 vpm). Data on the effect of water (630 to 40000 vpm) are presented in section 7.4.

7.3.1 Copper 5,5'-methylenebis (N-hexadecylsalicylideneamine): effect of film thickness

2,3,4 and 5 LB layer films of poly(CuMBSH) were exposed to 1000 vpm benzene to determine the optimum film thickness for the sensing system. Figures 7.4 and 7.5 show the change in photodiode output for 2 and 3 LB layer films of poly(CuMBSH). In each case, the magnitude of response was small at *ca* 2 mV. Both samples have fast response times, with almost complete recovery (return to the base line) within *ca* 60 seconds. When benzene vapour was replaced with pure nitrogen, the 2 LB layer film exhibited background drift, similar to that of benzene on bare silver. This was attributed to benzene vapour (during the original exposure) diffusing through the thin film and forming a layer on the silver surface. Within the time scale of the experiment this was non-reversible indicating that the sensor had been poisoned. This was also noticeable for 3 LB layers, although the drift was much smaller than for 2 LB layers. This reduction in drift could be due to the thicker LB layer inhibiting the diffusion of benzene through to the silver layer. It has been reported that the force of attraction between metallic films and liquid films (*ie* vapours) varies inversely as the square of the film thickness.² Thus a thicker LB film (such as poly(CuMBSH)) reduces this force of attraction and reduces the amount of vapour penetrating through the LB film causing background drift (*ie*, poisoning).

Concentrations of vapour used for poly(CuMBSH) were three times larger than those used for uncoated silver layers. In the latter case, exposure produced a slow monotonic drift in output voltage with no saturation and a change in output of *ca* 10 mV. The coated silver layer showed a reversible effect on exposure to benzene, with rapid turn on and off times. The sample also showed significantly reduced drift in photodiode output (even though the vapour concentration were greater). These are strong indications that the response is due to the interaction of the vapour with the LB film and not the silver substrate.

Figure 7.6 shows the change in photodiode output for 4 LB layers of poly(CuMBSH) deposited on 50 nm silver layer. The magnitude of response (*ca* 6mV) was much larger than 2 or 3 LB layers and there was no observable background drift (within the time scale of the experiment). Figure 7.7 shows the change in photodiode output for 5 LB layers exposed to 1000 vpm benzene. In this case, the response (*ca* 3mV) was smaller than for 4 LB layers. This reduction can be attributed to two factors: the first is that it would be more difficult for vapour to diffuse into the bulk of the thicker film; the second is that the SPR curve (see Chapter Six) for 5 LB layers is not as well-defined as for 4 LB layers, reducing the film's sensitivity. These data suggest that a system comprising of 4 LB layers poly(CuMBSH) on a 50 nm silver layer forms a good basis for further investigations

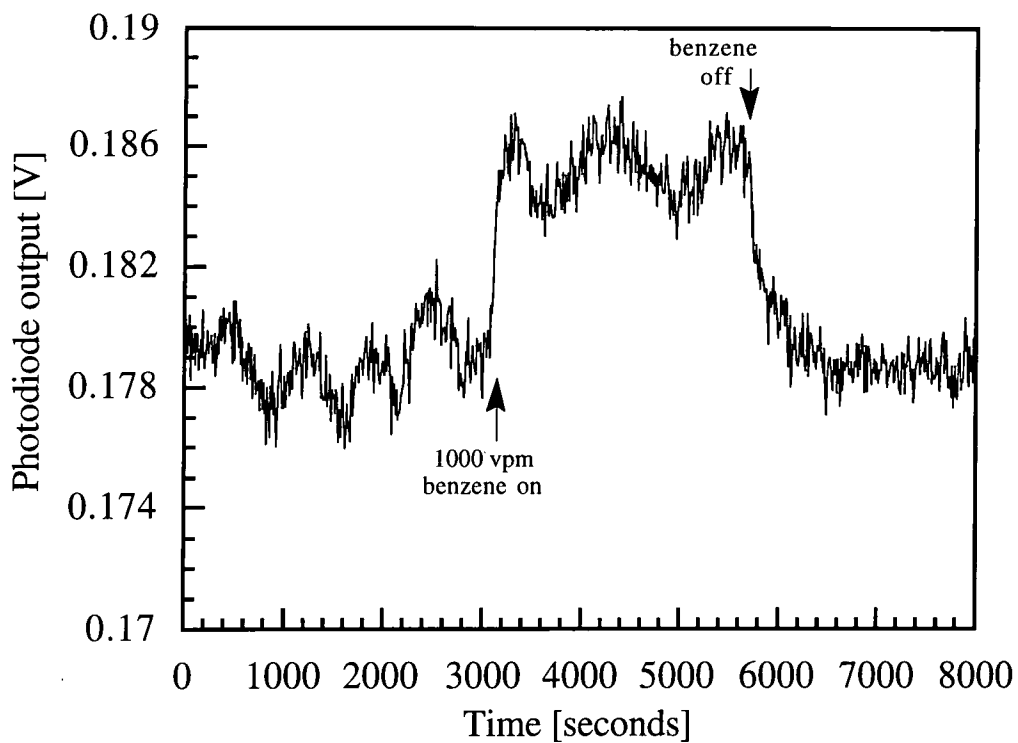


Figure 7.6: 4 LB layers poly(CuMBSH) exposed to 1000 vpm benzene vapour in a flow of pure nitrogen.

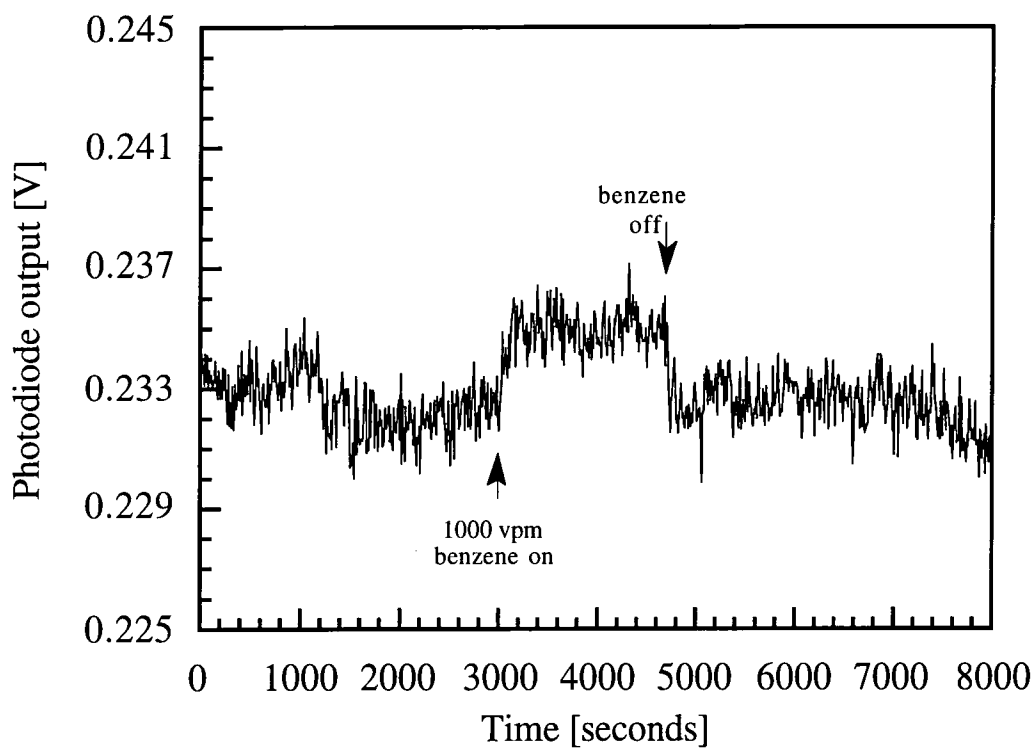


Figure 7.7: 5 LB layers poly(CuMBSH) exposed to 1000 vpm benzene vapour in a flow of pure nitrogen.

7.3.2 Copper 5,5'-methylenebis (N-hexadecylsalicylideneamine): effect of different vapours

For vapour sensing, 4 LB layers of poly(CuMBSH) were deposited onto a 50 nm silver layer evaporated onto a quartz substrate. The coated slides were mounted in the SPR system and the internal angle of the incident laser beam was chosen to be on the point of steepest gradient of the SPR curve, on the low angle side of resonance. The sample was initially exposed to dry nitrogen. After the output had settled (10 minutes), vapour was introduced via the diffusion cell. Films of poly(CuMBSH) were exposed to varying concentrations of benzene vapour, shown in figure 7.8. The results indicated that, on the introduction of benzene, there was a rapid rise in detector output (less than 60 seconds) and that this output was proportional to vapour concentration. When benzene was removed, the output returned to its base line value (*ca* 60 seconds) with no significant background drift. On exposure to toluene vapour, poly(CuMBSH) showed similar characteristics, with response and recovery times again *ca* 60 seconds, shown in figure 7.9. Poly(CuMBSH) was the most sensitive to benzene vapour, with a minimum detection limit *ca* 100 vpm. Toluene was slightly less responsive with a minimum detection limit of *ca* 300 vpm. 4 LB layers of poly (CuMBSH) were also exposed to concentrations of ethanol vapour, shown in figure 7.10. Once again, the response and recovery times were similar to those of benzene and toluene (*ca* 60 seconds in each case). However the detection threshold was *ca* 700 vpm.

Figure 7.11 shows the maximum response values (on exposure) for both benzene and ethanol, plotted against concentration. The error bars shown in figure 7.11 (and figures

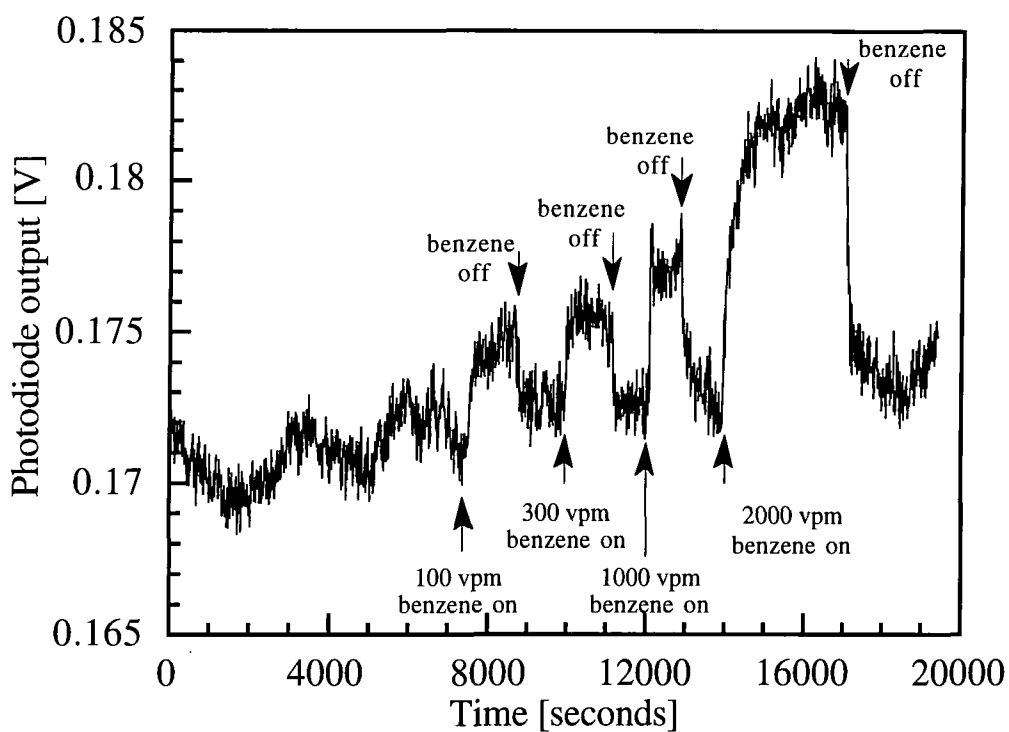


Figure 7.8: 4 LB layers poly(CuMBSH) exposed to 100/300/1000/2000 vpm benzene in a flow of pure nitrogen.

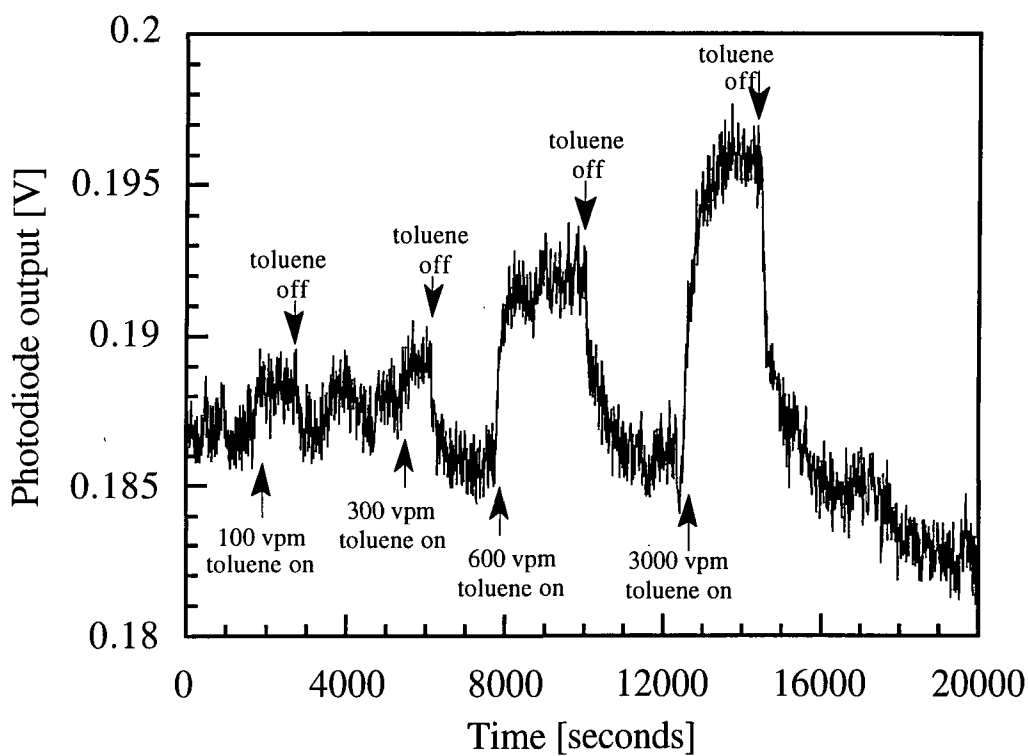


Figure 7.9: 4 LB layers Poly(CuMBSH) exposed to 100/300/600/3000 vpm toluene in a flow of pure nitrogen.

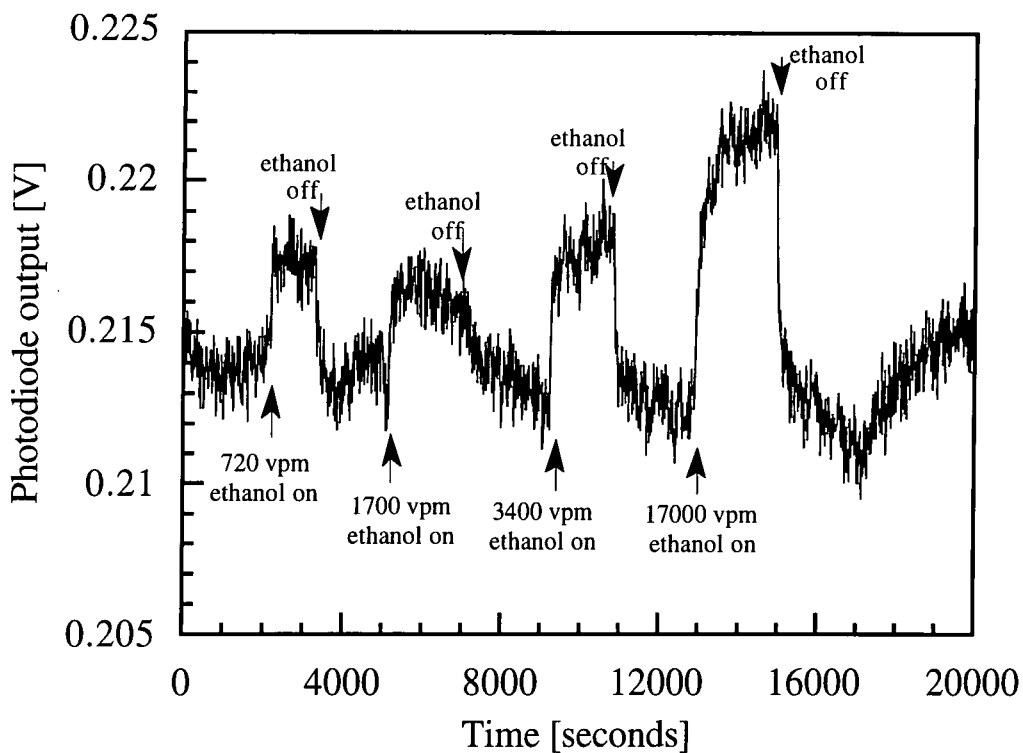


Figure 7.10: 4 LB layers poly(CuMBSH) exposed to 720/1700/3400/17000 vpm ethanol vapour in a flow of pure nitrogen.

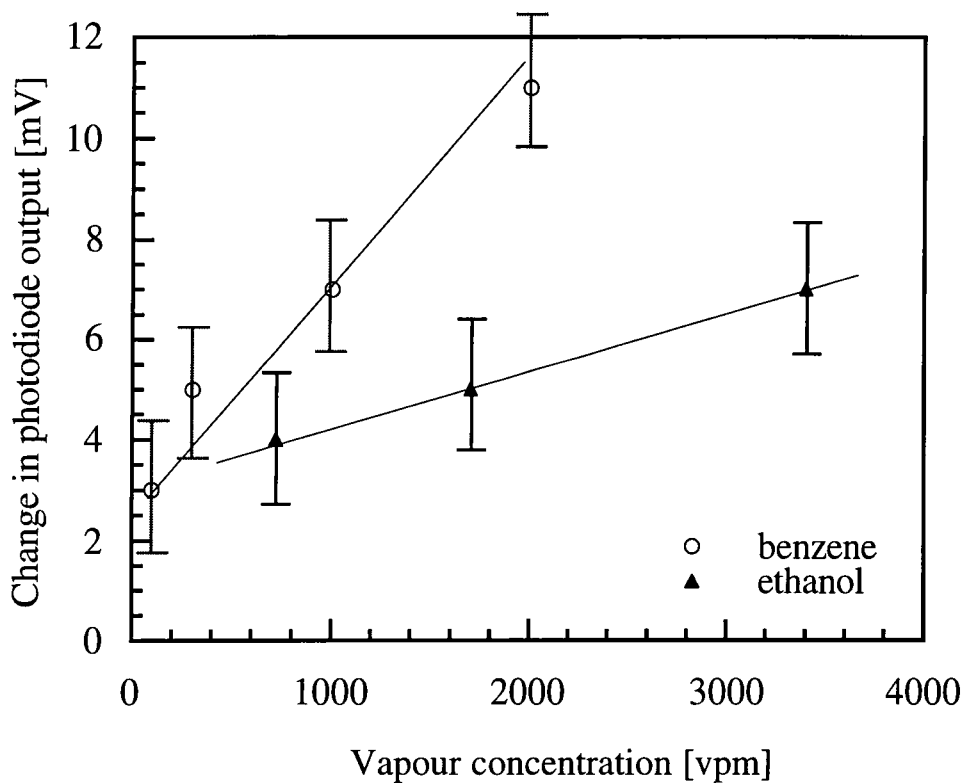


Figure 7.11: A plot of change in reflected voltage versus concentrations for 4 LB layers poly(CuMBSH) exposed to benzene and ethanol vapour.

7.15 and 7.19) were calculated from the maximum peak to peak noise before vapour was added (*ca* 1.2 mV) + maximum peak to peak noise after the response had saturated (*ca* 1.2 mV). As can be seen, the responses for both vapours exhibited linear characteristics with concentration, over the range investigated. However, the sensitivities (gradient of the line) for benzene and ethanol are different. Table 7.2 contrasts the sensitivity values for poly(CuMBSH) to the various vapours. The highest sensitivity is achieved with benzene, which has the smallest dipole moment and largest refractive index of all the vapours investigated. An explanation (as noted in section 7.1) is that the vapour is absorbed into the film, changing its refractive index or causing the film to swell. This will be discussed in more detail in section 7.5.

Vapour	Dipole moment [Debye] ⁴	Refractive index ¹	Minimum detectable concentration [vpm]	Sensitivity $\Delta(R/C)$ [$\mu V/vpm$]
benzene	0	1.498	100	4.2 ± 1.0
toluene	0.36	1.494	300	3.7 ± 1.0
ethanol	1.69	1.359	700	1.1 ± 1.0

Table 7.2: Sensing characteristics of 4 LB layers poly(CuMBSH) exposed to benzene/toluene and ethanol vapours. ΔR = change in photodiode output and ΔC = change in vapour concentration.

7.3.3 Copper phthalocyanine

Samples were initially exposed to dry nitrogen. After the output had settled (*ca* 10 minutes), vapour was added. Figure 7.12 shows the change in photodiode output against time after benzene vapour was added. CuPcBC showed very little response to concentrations below 300 vpm. The response and recovery times were also relatively slow at over 90 seconds (*cf* 60 seconds for poly(CuMBSH)). The magnitudes of response were low, *ca* 6 mV at 10000 vpm benzene (*cf* 1000 vpm on poly(CuMBSH) gave *ca* 8 mV). Within the time scale of our experiment, CuPcBC showed some drift in base line voltage. This was attributed to the thin (1 LB layer) covering of the silver layer. 1 LB layer of CuPcBC was used since it gave a sharp SPR curve, see Chapter Three. Figure 7.13 shows the response for 1 LB layer of CuPcBC exposed to concentrations of toluene vapour. Again, there was little reaction to concentrations less than 300 vpm. This could have been due to the noise on the output signal which was greater in magnitude than any change in sensor output. Concentrations above 600 vpm produced larger changes in photodiode output, yet the response and recovery times were slow (more than 150 seconds). Figure 7.14 shows the response of 1 LB layer of CuPcBC on exposure to varying concentrations of ethanol vapour. There was little reaction below *ca* 700 vpm, concentrations over 1700 vpm produce an observable change in the photodiode output, with rise and fall times of *ca* 90 seconds, though some background drift was observed. This was attributed, as before, to sensor poisoning with no recovery within the time scale of the experiment.

Figure 7.15 shows the maximum response values (on exposure) for benzene and toluene vapour plotted against concentration. As can be seen, the response of 1 LB layer

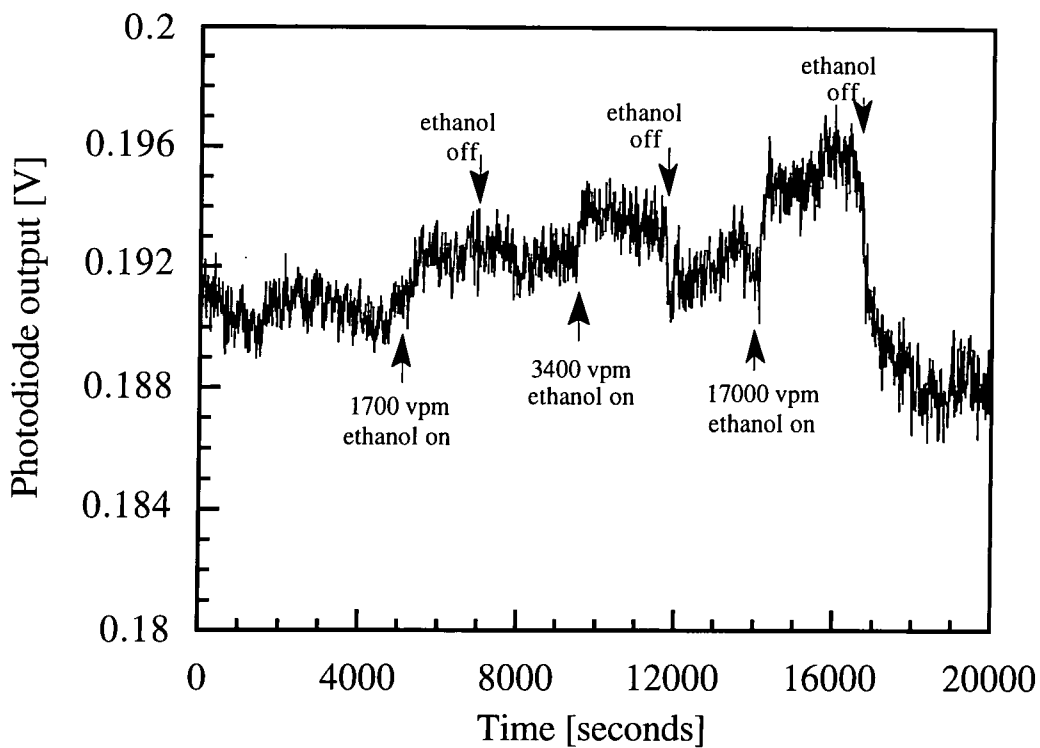


Figure 7.18: 1 LB layer AMCR23 exposed to 1700/3400/17000 vpm ethanol vapour in a flow of pure nitrogen.

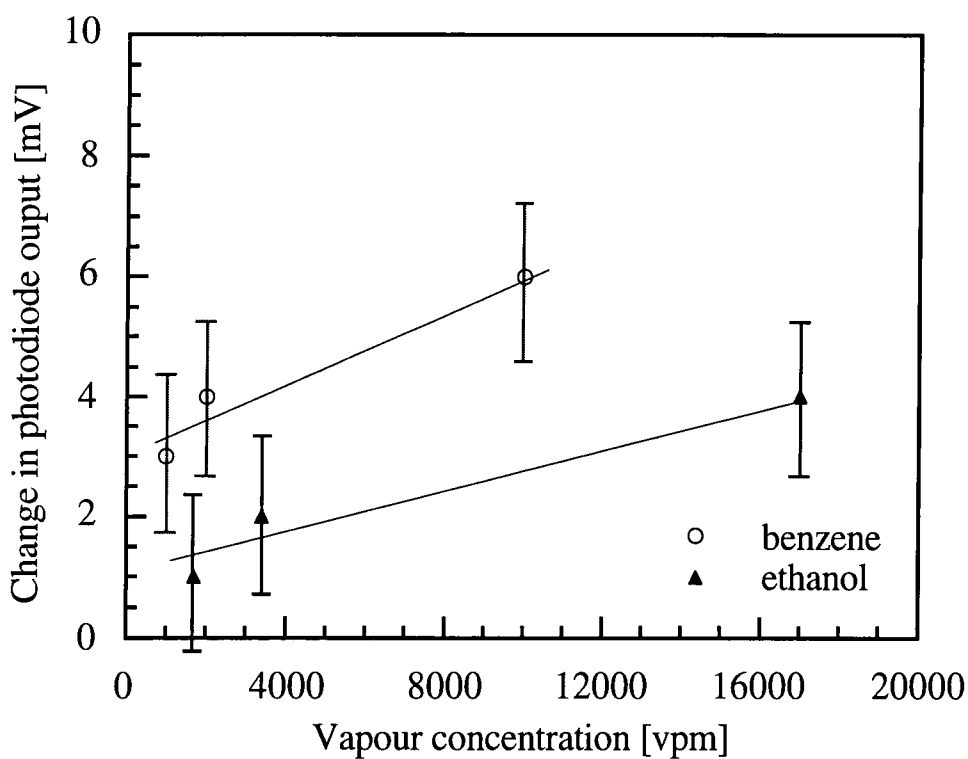


Figure 7.19: A plot of change in photodiode output versus concentration for 1 LB layer AMCR23 exposed to benzene and ethanol vapours.

CuPcBC is linear to low concentrations of each vapour. At a point (*ca* 1000 vpm for benzene, 600 vpm for toluene and 3400 vpm for ethanol) the response of CuPcBC to each vapour begins to saturate (*cf* poly(CuMBSH) linear over the range investigated). This could be due to the reaction sites (areas where ambient vapour can interact with the LB film) being full. Thus a change in vapour concentration produces no (or very little) change in the optical properties of the film.

Table 7.3 compares the sensitivity values for CuPcBC on exposure to benzene, toluene and ethanol. These were calculated, as before, by taking the gradient of line between 100 and 1000 vpm for benzene and 720 to 3400 vpm for ethanol (from figure 7.15).

Vapour	Dipole moment [Debye] ⁴	Refractive index ¹	Minimum detection concentration [vpm]	Sensitivity $\Delta(R/C)$ [$\mu\text{V}/\text{vpm}$]
benzene	0	1.498	300	6.0 ± 2.0
toluene	0.36	1.494	300	2.2 ± 1.0
ethanol	1.69	1.359	720	1.4 ± 1.0

Table 7.3: Sensing characteristics of 1 LB layer CuPcBC exposed to benzene, toluene and ethanol vapours. ΔR = change in photodiode output and ΔC = change in vapour concentration.

The values shown are for the sensitivity of CuPcBC to low concentrations of benzene, toluene and ethanol vapour (*ie*, below point of saturation). The data (shown in table 7.3)

indicate that benzene is the most reactive, then toluene and finally ethanol. The results suggest that CuPcBC is more responsive to benzene than poly(CuMBSH) ($6.0 \pm 2.0 \mu\text{V}/\text{vpm}$ for CuPcBC and $4.2 \pm 1.0 \mu\text{V}/\text{vpm}$ for poly(CuMBSH)). The sensitivity values for toluene and ethanol, though smaller than those for poly(CuMBSH) do not follow the same pattern (ie, benzene and toluene having similar refractive indices). This could be due to the different chemical structure and molecular orientation (CuPcBC forms a closely packed structure on the substrate)⁵ of CuPcBC inhibiting the diffusion of vapour into the bulk of the LB film, see section 7.5.2.

7.3.4 Polysiloxane

Figure 7.16 shows the change in photodiode output against time for 1 LB layer of AMCR23 exposed to varying quantities of benzene vapour. AMCR23 showed very little response to concentrations below 1000 vpm. The response and recovery times were also relatively slow at over 90 seconds (*cf* 60 seconds for poly(CuMBSH)). The magnitude of response was small, with only *ca* 5mV change in photodiode output recorded at a vapour concentration of 10000 vpm. The change in photodiode output for 1 LB layer of AMCR23 on exposure to varying concentrations of toluene vapour is shown in figure 7.17. There was little reaction to concentrations less than 600 vpm (*cf* 300 vpm for poly(CuMBSH) and CuPcBC), due to saturation by the background noise. Figure 7.18 shows the change in photodiode output for 1 LB layer of AMCR23 exposed to ethanol vapour. AMCR23 was unresponsive to concentrations of ethanol vapour below *ca* 3400 vpm. In these experiments, there was no observable drift in the photodiode output within the time scale of the experiment.

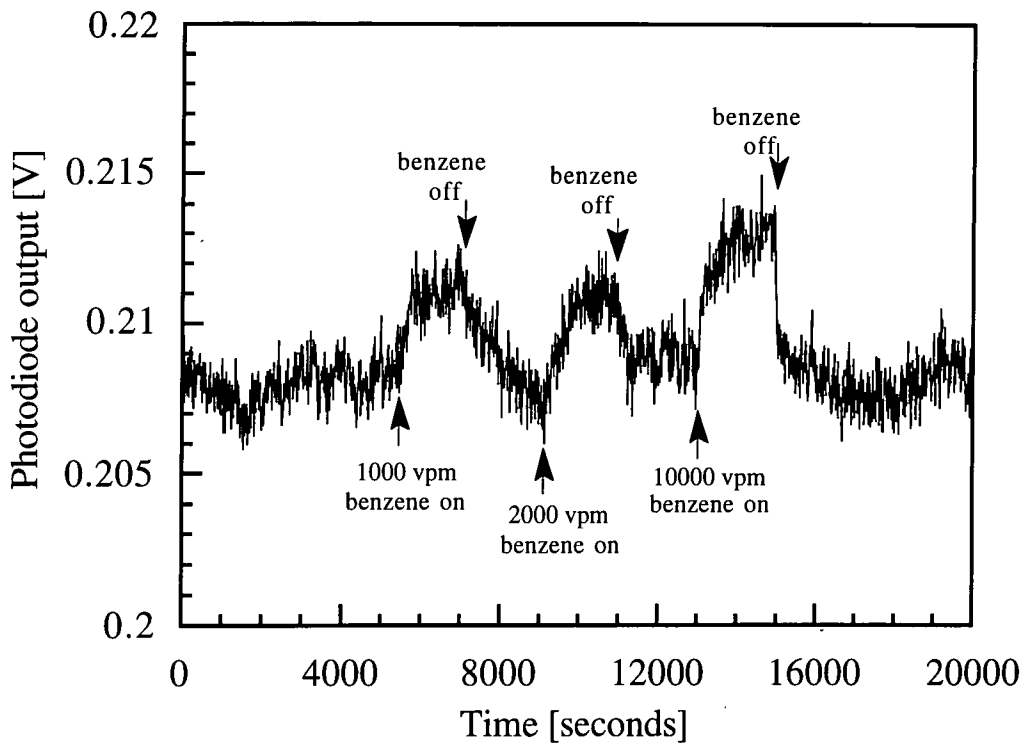


Figure 7.16: 1 LB layer AMCR23 exposed to 1000/2000/10000 vpm benzene vapour in a flow of pure nitrogen.

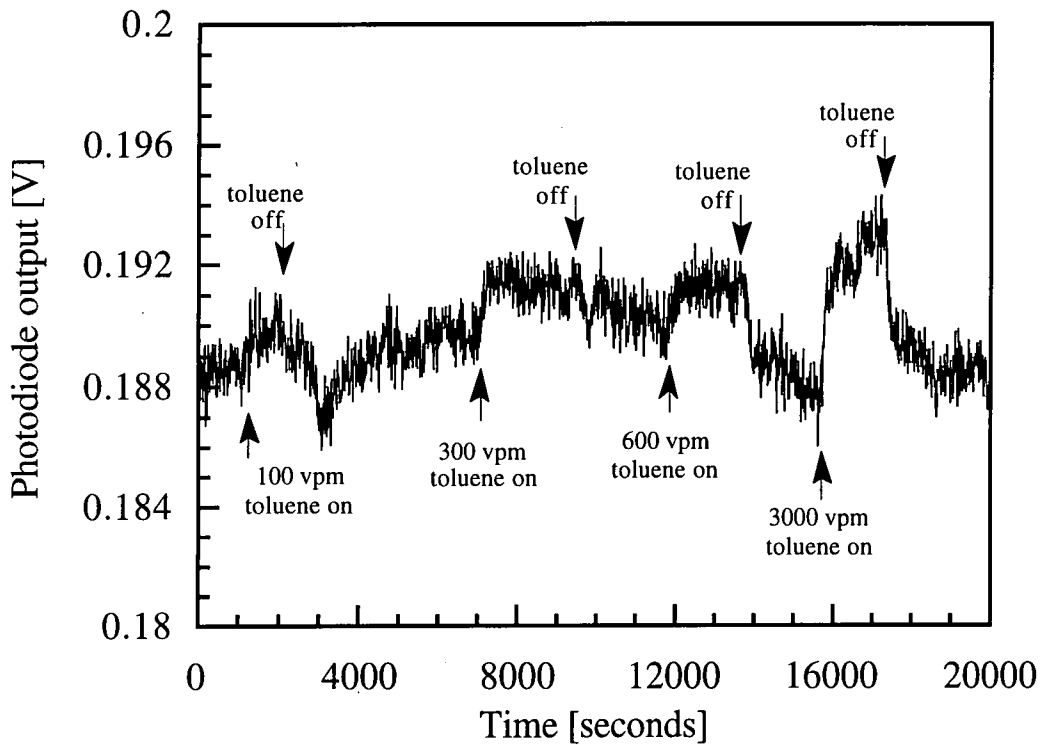


Figure 7.17: 1 LB layer AMCR23 exposed to 100/300/600/3000 vpm toluene vapour in a flow of pure nitrogen.

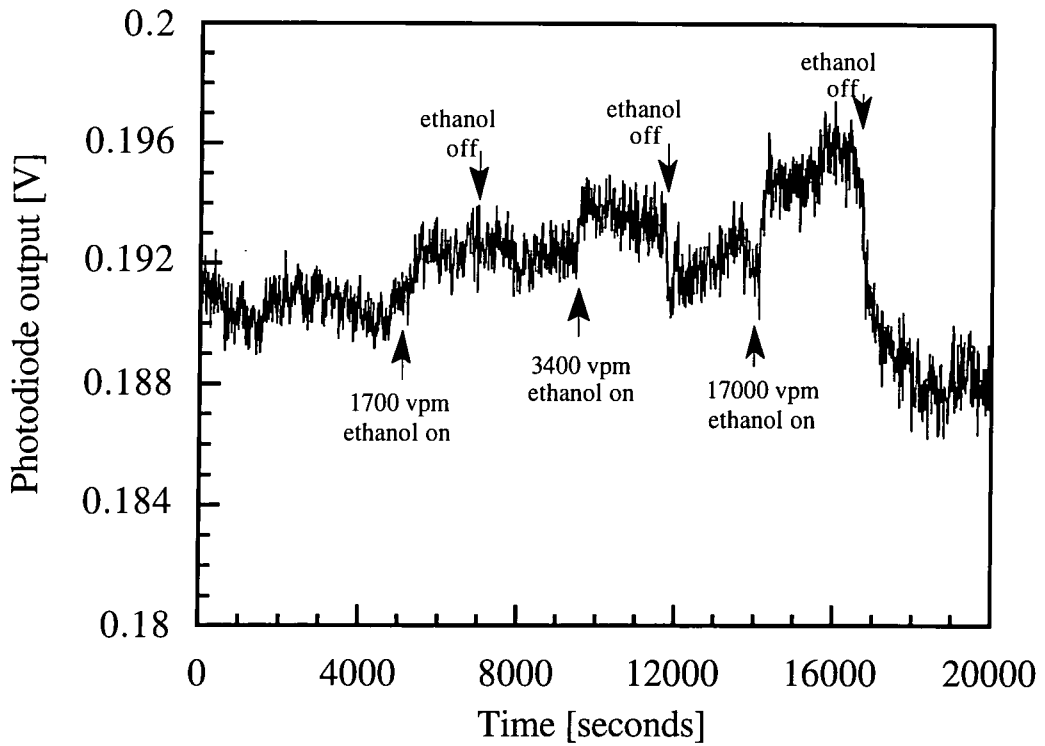


Figure 7.18: 1 LB layer AMCR23 exposed to 1700/3400/17000 vpm ethanol vapour in a flow of pure nitrogen.

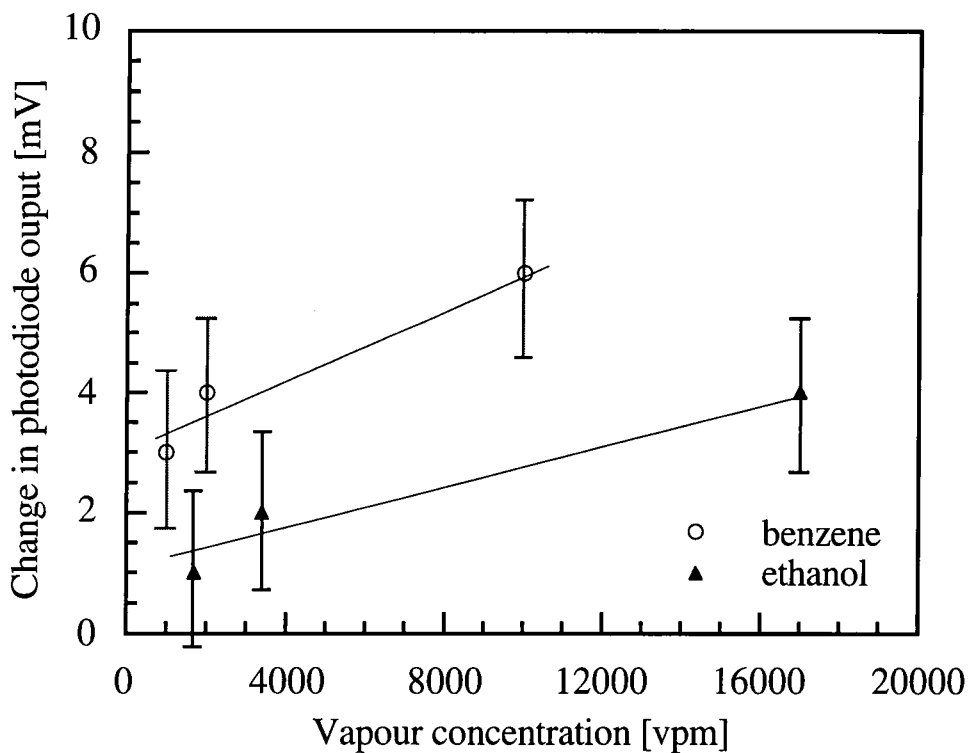


Figure 7.19: A plot of change in photodiode output versus concentration for 1 LB layer AMCR23 exposed to benzene and ethanol vapours.

Figure 7.19 shows the maximum response values (on exposure) for each of the three vapours, plotted against concentration. The responses of 1 LB layer of AMCR23 to concentrations of benzene and ethanol vapour show a degree of linearity with concentration (over the range investigated). Each of the vapours showed no saturation to higher concentrations, as seen for 1 LB layers of CuPcBC. This linear characteristics are similar to that obtained using poly(CuMBSH), indicating that the more open structures of both films may have a part to play in the gas/vapour sensing mechanism (see section 7.5.2).

Table 7.4 compares the sensitivity values for 1 LB layer of AMCR23 on exposure to benzene, toluene and ethanol vapours.

Vapours	Dipole moment [Debye] ⁴	Refractive index ¹	Minimum detection concentration [vpm]	Sensitivity $\Delta(R/C)$ [$\mu\text{V}/\text{vpm}$]
benzene	0	1.498	1000	0.3 ± 0.3
toluene	0.36	1.494	600	1.3 ± 1.0
ethanol	1.69	1.359	1700	0.2 ± 0.1

Table 7.4: Sensing characteristics of 1 LB layer AMCR23 exposed to benzene, toluene and ethanol vapours. ΔR = change in photodiode output and ΔC = change in vapour concentration.

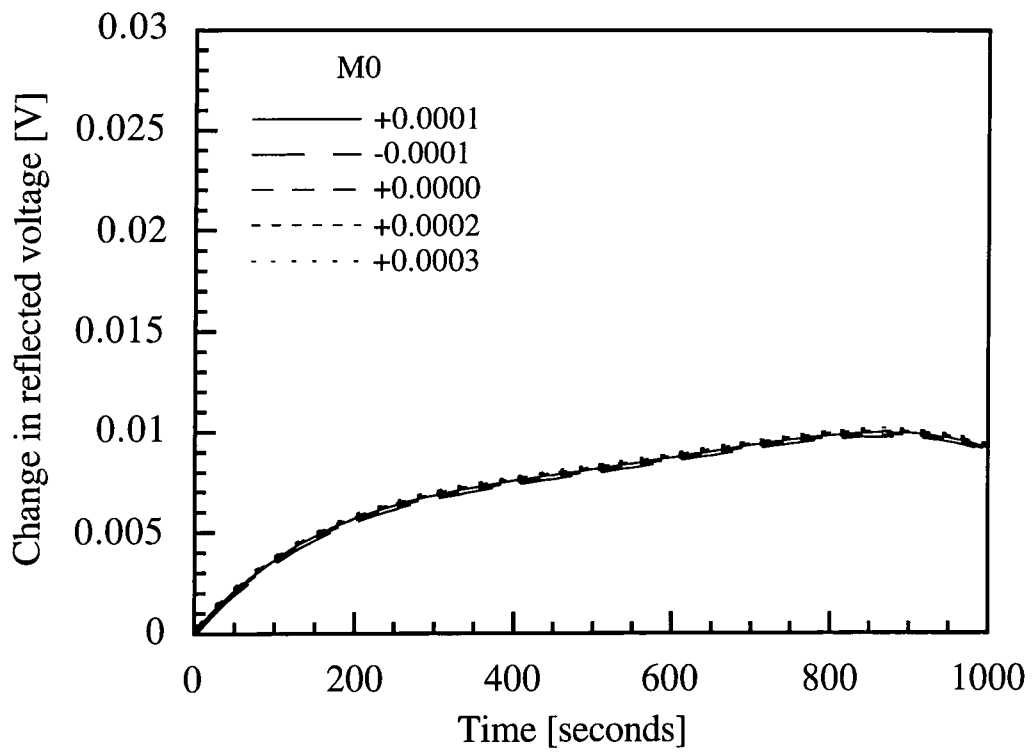
Table 7.4 indicates that AMCR23 shows the greatest sensitivity to toluene vapour. This is in contrast to results obtained from poly(CuMBSH) and CuPcBC. One possible explanation is that this could be due to the different chemical composition of the polysiloxane backbone. The backbone of polysiloxane comprises Si and O, whilst poly(CuMBSH) and CuPcBC comprises C and H. The sensitivity values for AMCR23 (see table 7.4) are much smaller than poly(CuMBSH) (see section 7.3.2). This reduction in sensitivity indicates that AMCR23 is not as reactive as either poly(CuMBSH) or CuPcBC. This could be due to the ability of poly(CuMBSH) to absorb vapour, as its relatively open structure allows diffusion. In contrast, LB layers of AMCR23 may be more densely packed making diffusion into/out of the bulk of the film difficult.

7.3.5 Mathematical modelling of response characteristics

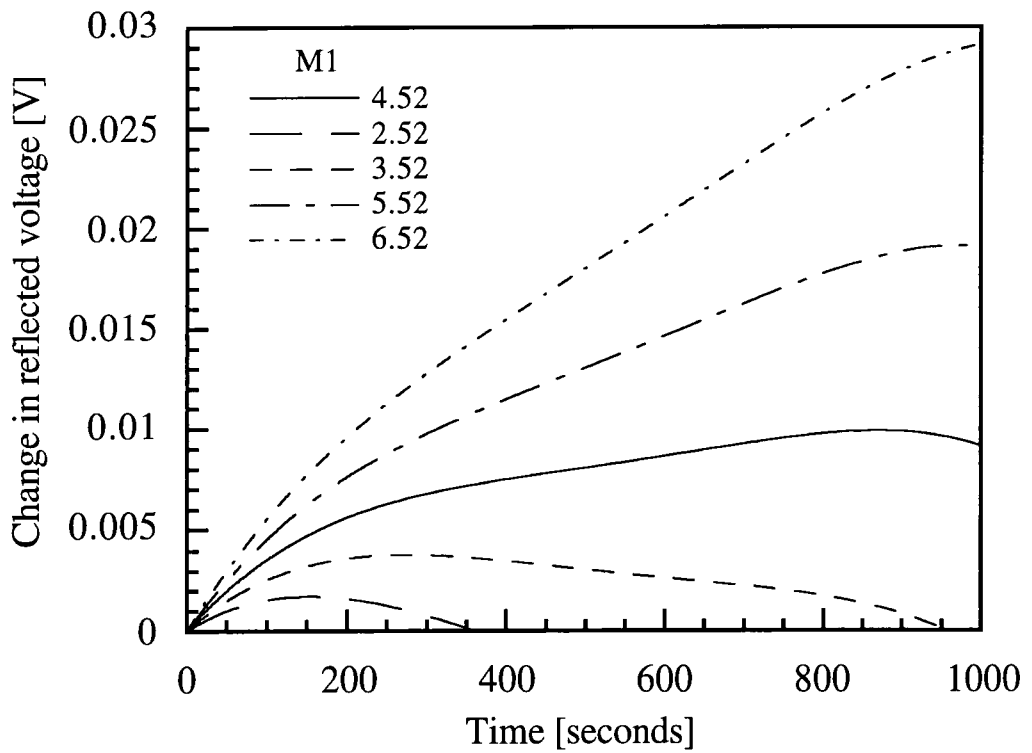
The response characteristics shown in the previous sections for poly(CuMBSH), AMCR23 and CuPcBC were modelled on computer to see if it was possible to derive a common mathematical expression for all the vapours and materials. Various methods of curve fit were tried (logarithmic and exponential), the only functions that were found to fit were polynomial expressions. To minimise errors, a polynomial of fourth order was used.

$$y = M0 + M1x + M2x^2 + M3x^3 + M4x^4 \quad [7.1]$$

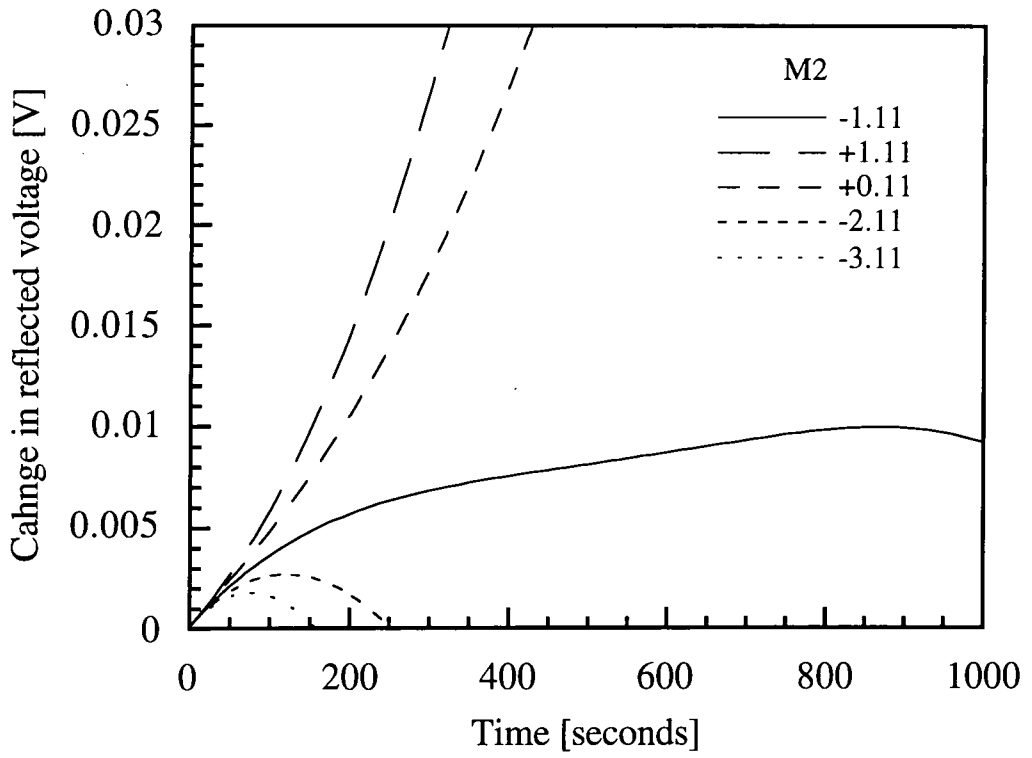
A set of curves were initially produced using the polynomial given in equation 7.1; these are shown in figure 7.20. The constants M0 to M4 were systematically changed



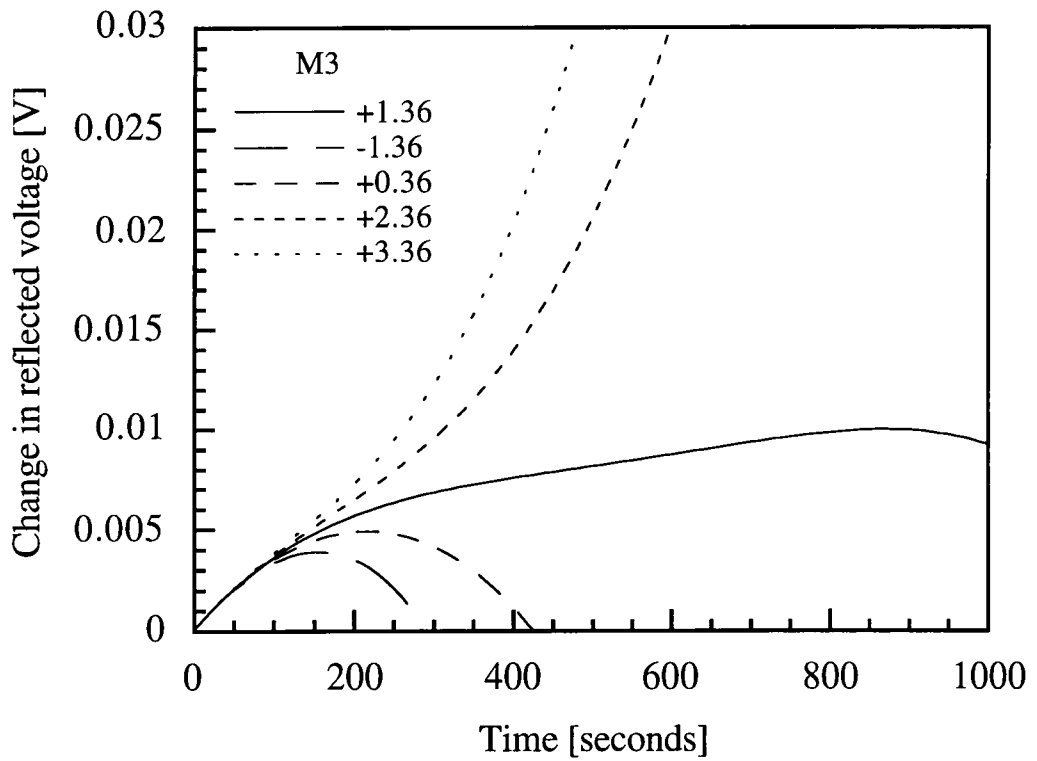
7.20 (a)



7.20(b)



7.20(c)



7.20(d)

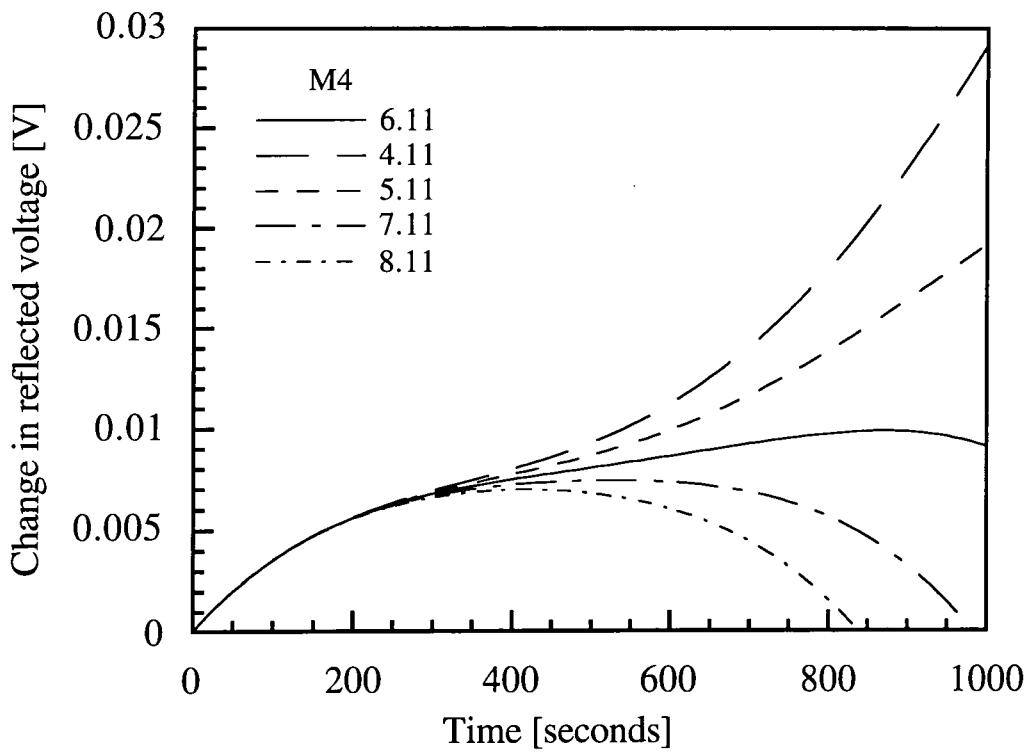
(one at a time, holding the others at their initial value) producing curves (a) to (e). The initial values that were used to produce these curves were.

$$y = 1.6 \times 10^{-4} + 4.53 \times 10^{-5} x - 1.12 \times 10^{-7} x^2 + 1.36 \times 10^{-10} x^3 - 6.11 \times 10^{-14} x^4 \quad [7.2]$$

Figure 7.20 (a) indicates that the effect of M0 is to change the intercept of the line with the y-axis, thus this has little effect on the shape of the response. Changing the value M1 and M2 in figures 7.20 (b) and (c) had a dramatic effect on the rise time of the curve. Increasing and decreasing the values of M3 and M4 only affected the shape of the curve once it had reached a steady state value, shown in figures 7.20 (d) and (e).

The curves shown in figure 7.21 are for the theoretical and experimental data obtained from 4 LB layers poly(CuMBSH) exposed to 2000 vpm benzene vapour. The correlation between the theoretical and experimental lines was good, with an average percentage fit of 96.7 %. Table 7.5 shows the values for M0 to M4 for all the materials exposed to all the vapours investigated. Values for M1 and M2 are the largest for poly(CuMBSH), indicating that it has the largest and fastest response times.

Though the data obtained for each of the vapours were mathematically modelled, the results are inconclusive. The only term of interest is M1 since this determines the rate and size of change in output voltage (on exposure to a vapour). The results indicate that poly(CuMBSH) was the most reactive and that there was little difference between AMCR23 and CuPcBC. These results only show that the reaction process was more complicated than initially thought, ie, it is not simply logarithmic or exponential.



7.20(e)

Figure 7.20: Theoretical curves generated using a fourth order polynomial (equation 7-2) to model gas sensing characteristics: (a) to (e) are for values of M0 to M4 varied respectively.

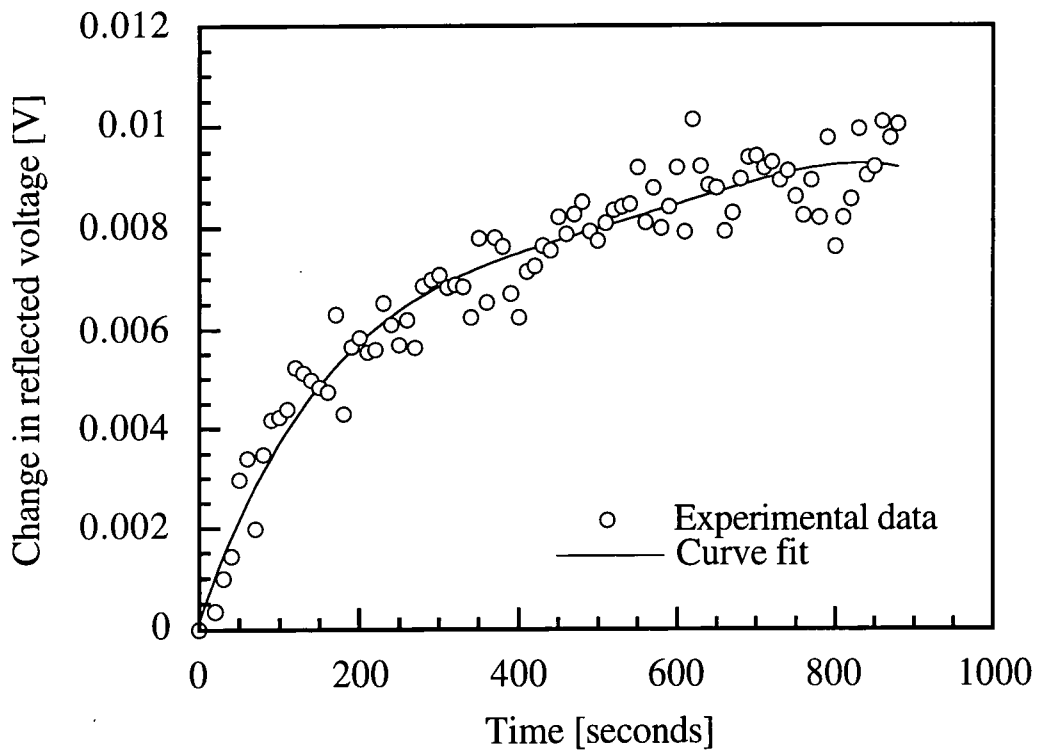


Figure 7.21: Comparison between experimental data for 4 LB layers poly(CuMBSH) exposed to 2000 vpm benzene vapour and a theoretical curve generated using a fourth order polynomial

Material and Vapour	M0	M1 [x10⁻⁵]	M2 [x10⁻⁷]	M3 [x10⁻¹⁰]	M4 [x10⁻¹⁴]	% Fit
Poly(CuMBSH)						
Benzene	0.00016	4.526	-1.117	1.355	-6.114	96.7
Toluene	-0.00054	4.220	-0.644	0.457	-1.210	97.7
Ethanol	-0.00011	2.730	-0.657	0.832	-4.186	91.2
AMCR23						
Benzene	0.00058	1.830	-0.486	0.580	-2.387	82.5
Toluene	-0.00005	1.382	-0.165	0.095	-0.192	95.1
Ethanol	-0.00039	1.765	-0.299	0.201	-0.457	77.1
CuPcBC						
Benzene	0.00051	1.210	-0.158	0.098	-0.215	93.6
Toluene	-0.00074	2.461	-0.361	-0.184	-0.181	93.9
Ethanol	-0.00130	1.23	-0.055	-0.042	0.293	95.7

Table 7.5: Values of M0 to M4 and percentage fit for poly(CuMBSH), AMCR23 and CuPcBC on exposure to benzene, toluene and ethanol vapours.

7.4 The effect of water vapour

Figure 7.22 shows the change in photodiode output for a 50 nm thick layer of silver on exposure to water (630 vpm). There was a slow monotonic rise in photodiode output on exposure to water vapour. When water was replaced by dry nitrogen there was no

observable recovery, within the time scale of the experiment. The rise in photodiode output was small, if compared to results obtained from benzene, toluene and ethanol vapours on silver (*cf* section 7.1). This could be due to the refractive index of water being the smallest of the tested vapours (1.330), or the dipole moment being the largest (1.69).¹ The film's lack of recovery could be due to the oxidation effect of water on thin silver layers. It was noticed that if silvered slides were left in a subphase of pure water, for more than 10 minutes, they became cloudy in appearance. This effect was not seen when samples were exposed to water vapour. This was probably due to the relatively low concentrations of water vapour used.

The change in photodiode output for 4 LB layers of poly(CuMBSH) exposed to varying quantities of water vapour is shown in figure 7.23. Poly(CuMBSH) was very reactive to water vapour of high concentrations, above 4000 vpm. This response was linear, with relatively fast turn on and off characteristics (*ca* 60 seconds in both cases).

Data for 1 LB layer AMCR23 exposed to concentrations of water vapour are shown in figure 7.24. There was no response to concentrations less than 4000 vpm with the response to concentration of 40000 vpm being low at *ca* 3 mV (*cf* 9 mV for poly(CuMBSH)). The turn-on and turn-off characteristics of AMCR23 to water vapour were rapid at *ca* 60 seconds in both instances. Within the time scale of the experiment, there was no observable drift in the photodiode output, indicating that there was no permanent damage to the film on exposure to water vapour (poisoning).

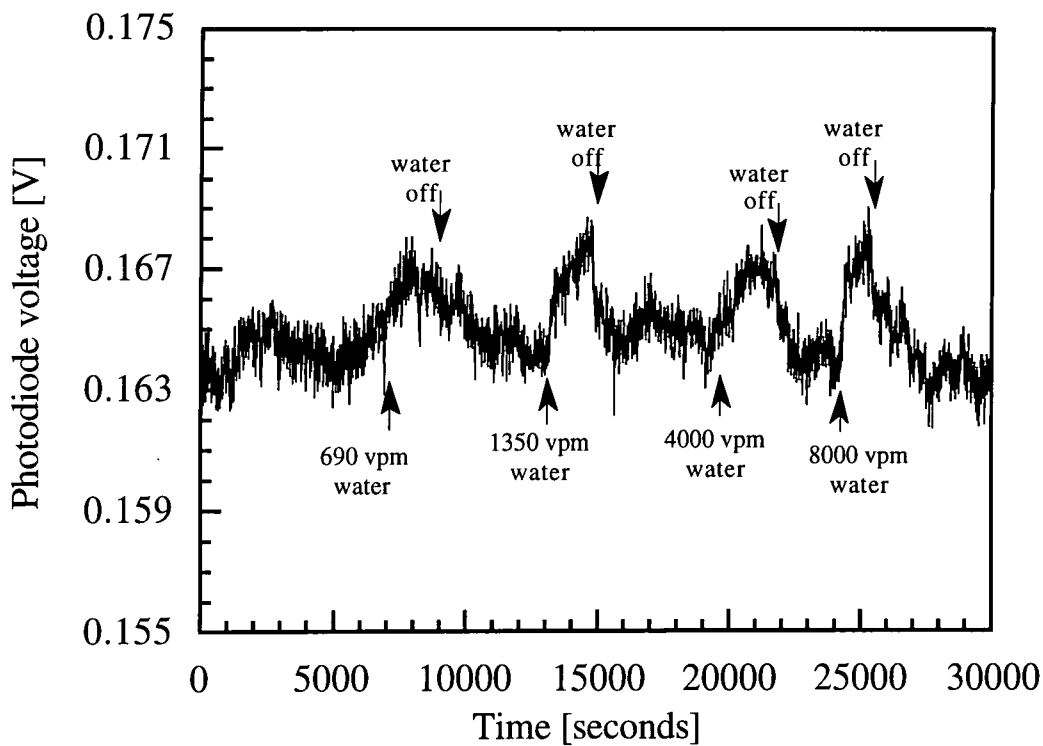


Figure 7.24: 1 LB layer AMCR23 exposed to 690/1350/4000/8000 vpm water vapour in a flow of pure nitrogen.

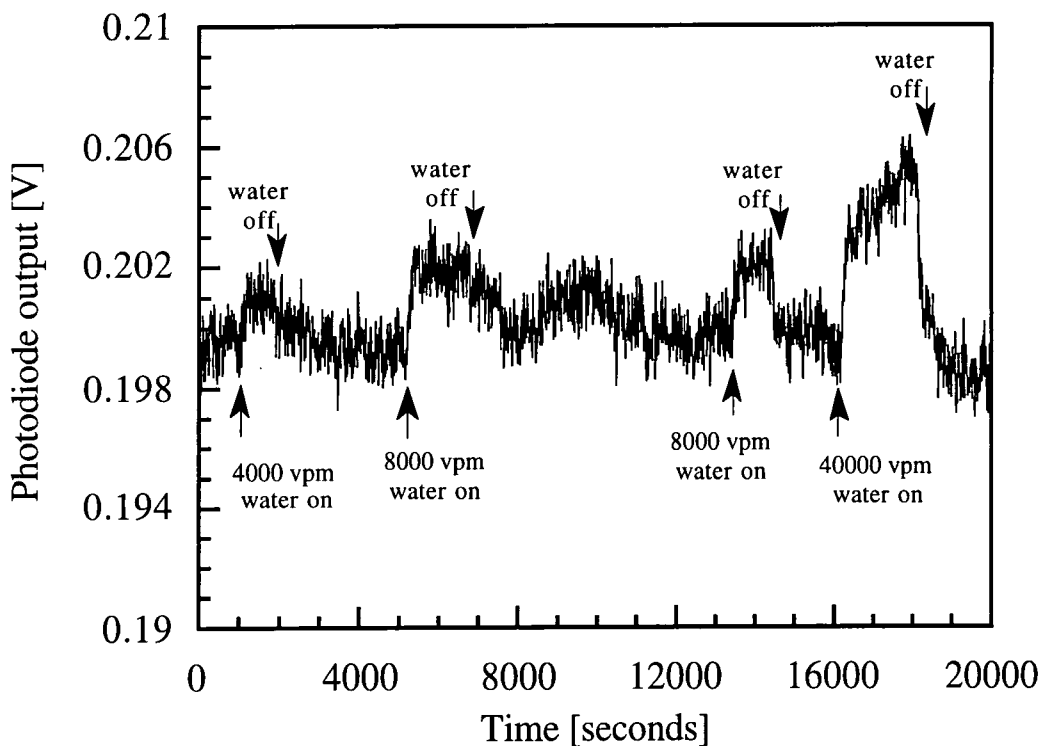


Figure 7.25: 1 LB layer CuPcBC exposed to 4000/8000/40000 vpm water vapour in a flow of pure nitrogen.

Figure 7.25 shows the change in photodiode output for 1 LB layer CuPcBC exposure to water vapour. CuPcBC was reactive to concentrations above 690 vpm water vapour, yet the response was saturated at *ca* 3 mV (ie, a change in concentration did not change the size of response). The turn-on and-off characteristics of CuPcBC were slow in comparison to the other materials, at *ca* 200 seconds (*cf* 60 seconds for poly(CuMBSH)). This corresponds to the slower turn-on and turn-off characteristics for CuPcBC on exposure to benzene, toluene and ethanol vapours (*ca* 150 seconds). There was no observable drift in the photodiode output within the time scale of the experiment.

7.5 Vapour sensing mechanism in LB films

LB layers of poly(CuMBSH) were exposed to quantities of benzene (1000 vpm), toluene (3000 vpm), ethanol (17000 vpm) and water vapour (40000 vpm). The full SPR curve of each film was then recorded in 100 cc min⁻¹ nitrogen, 30 minutes after exposure to either vapour, then after 30 minutes recovery in nitrogen.

7.5.1 Changes in the SPR curve of poly(CuMBSH)

SPR data for 4 LB layers of poly(CuMBSH) exposed to 1000 vpm benzene and 40000 vpm water vapour are shown in figures 7.26 and 7.27, respectively. The SPR curves were recorded at various intervals after the introduction of nitrogen gas (100 cc min⁻¹) and vapour. Figures 7.26 and 7.27 show that on the introduction of a vapour there is a very slight shift in the SPR curve to higher angles. This shift in the SPR supports the data shown in previous sections, where on exposure to all the vapours there was an

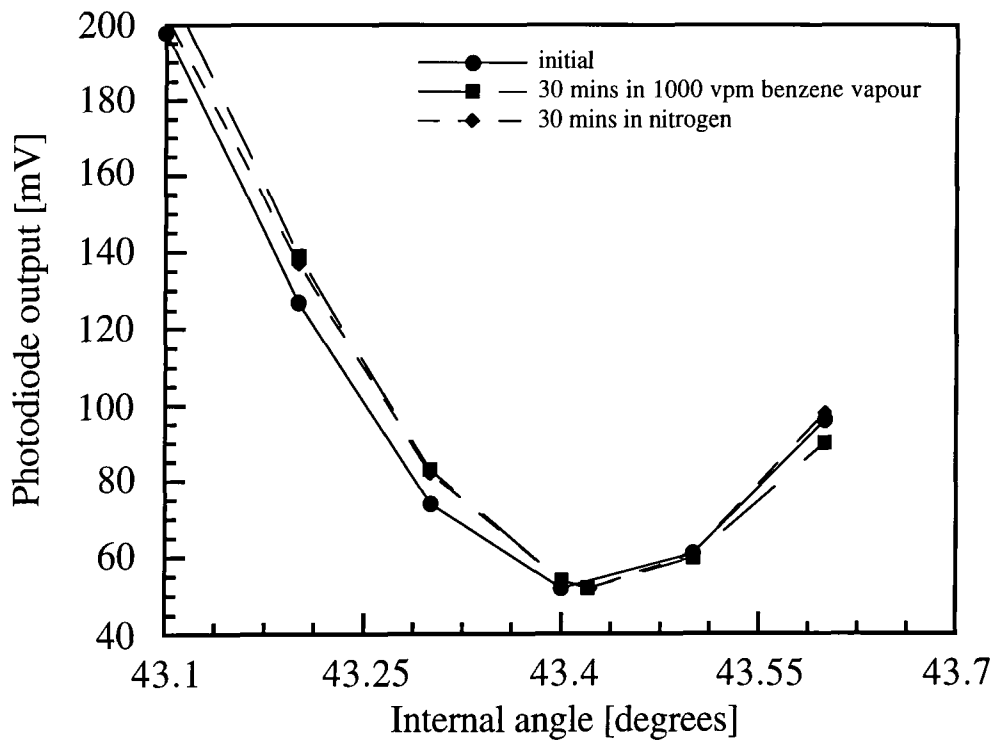


Figure 7.26: SPR curve for 4 LB layers poly(CuMBSH) initially exposed to pure nitrogen after 30 mins exposure to 1000 vpm benzene vapour, and finally after 30 mins exposure to pure nitrogen.

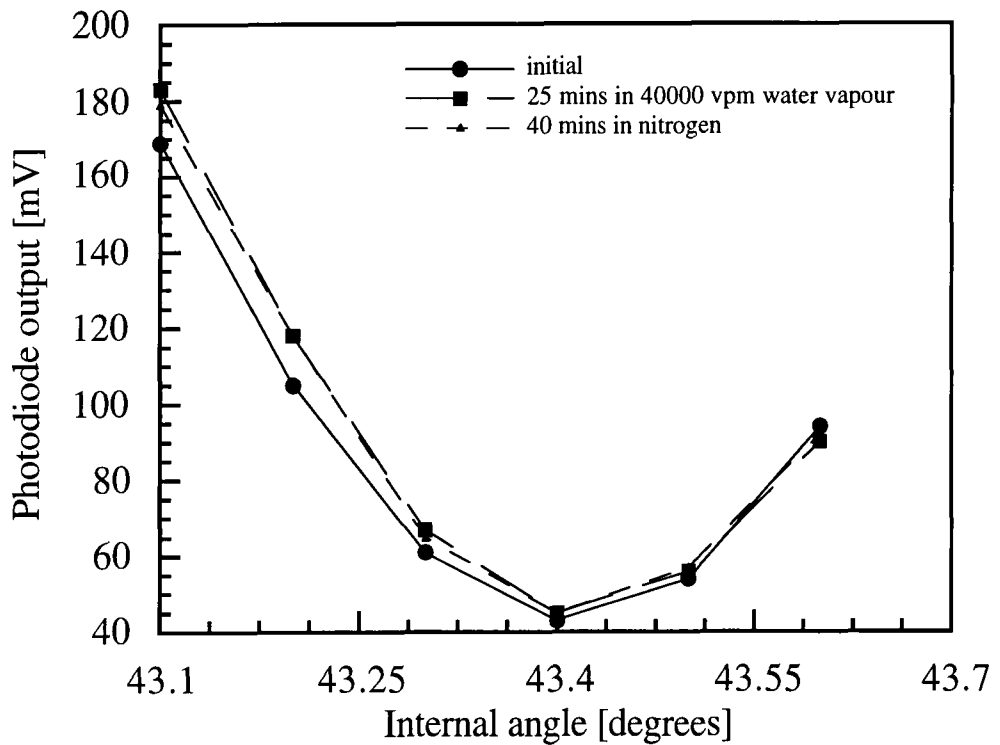


Figure 7.27: SPR curve for 4 LB layers poly(CuMBSH) initially exposed to pure nitrogen; after 25 mins exposure to 40000 vpm water vapour, and finally after 40 mins exposure to pure nitrogen.

increase in photodiode output. From the data shown it was not possible to deduce if there was any change in the shape of the SPR curve (narrowing/broadening). Further measurements are clearly needed to clarify this.

7.5.2 Proposed sensing mechanism

Multilayer LB films of poly(CuMBSH) showed repeatable response characteristics when exposed to benzene, toluene, ethanol and water vapour, the only differences being the sensitivity values (section 7.3.1). One explanation is that the sensitivity could be related to the refractive index or dipole moment of each vapour: benzene has the highest refractive index and lowest dipole moment and is the most reactive; toluene has a similar refractive index and dipole moment and has a slightly smaller sensitivity value; ethanol and water have much lower refractive indices and higher dipole moments and are less responsive.

The initial rapid response of all the films (shown in section 7.3) can be explained by the SPR curve shifting to higher angles. This shift could be due to vapour being trapped in the LB film causing either a change in refractive index, or a change in film thickness. Since the refractive indices of each LB layer (poly(CuMBSH) ≈ 1.554 , CuPcBC ≈ 1.60 ,⁵ AMCR23 ≈ 1.76 ,⁶ ZnPcBC ≈ 1.64 ⁷) are much greater than the refractive index of benzene, ($n = 1.498$), the addition of a thin layer of benzene (or any of the other vapours tested) onto the surface of each material would not cause a substantial change in its refractive index. Thus the dominant factor has to be the LB film swelling. It was assumed that poly(CuMBSH) was relatively non-polar and thus showed the greatest

affinity to gases which were non-polar (ie, benzene then toluene, ethanol and finally water vapour (seen in section 7.3.2)). CuPcBC, AMCR23 and ZnPcBC it was assumed were more polar than poly(CuMBSH) and thus exhibited less sensitivity to non-polar vapours. One explanation is that it is easier for vapours to be absorbed into LB films of similar polarity (ie, non-polar vapour and non-polar LB films). This hypothesis can be used to explain the result obtained for polysiloxane. AMCR23 was most sensitive to toluene vapour, because the LB film and vapour have a similar polarity.

When the vapour is replaced with dry nitrogen there is a rapid drying effect on the film (ie, the loss of the vapour formed on the surface of the LB film). This reduces the film's total thickness, forcing the SPR curve to return to its original position (ie a quick fall in photodiode output). Any vapour absorbed into the bulk of the LB film will take longer to diffuse out (if at all, ie, sensor poisoning). This was observed by the longer time for full recovery (*ca* 60 minutes). A schematic representation of the reaction process can be seen in figure 7.28. Figure 7.28 (a) depicts the substrate before any reaction has begun. Figure 7.28 (b) shows the formation of a thin condensed vapour film on the surface of the LB layer. Figure 7.28 (c) shows the result of the vapour diffusing through into the LB film causing swelling. The arrows in figures 7.28 (b) and (c) indicate that both processes are reversible, under ideal conditions.

7.6 Summary

Films of a 50 nm uncoated silver layer, copper tetrakis-(3,3-dimethyl-1-butoxycarbonyl) phthalocyanine (CuPcBC), zinc tetrakis-(3,3-dimethyl-1-butoxycarbonyl)

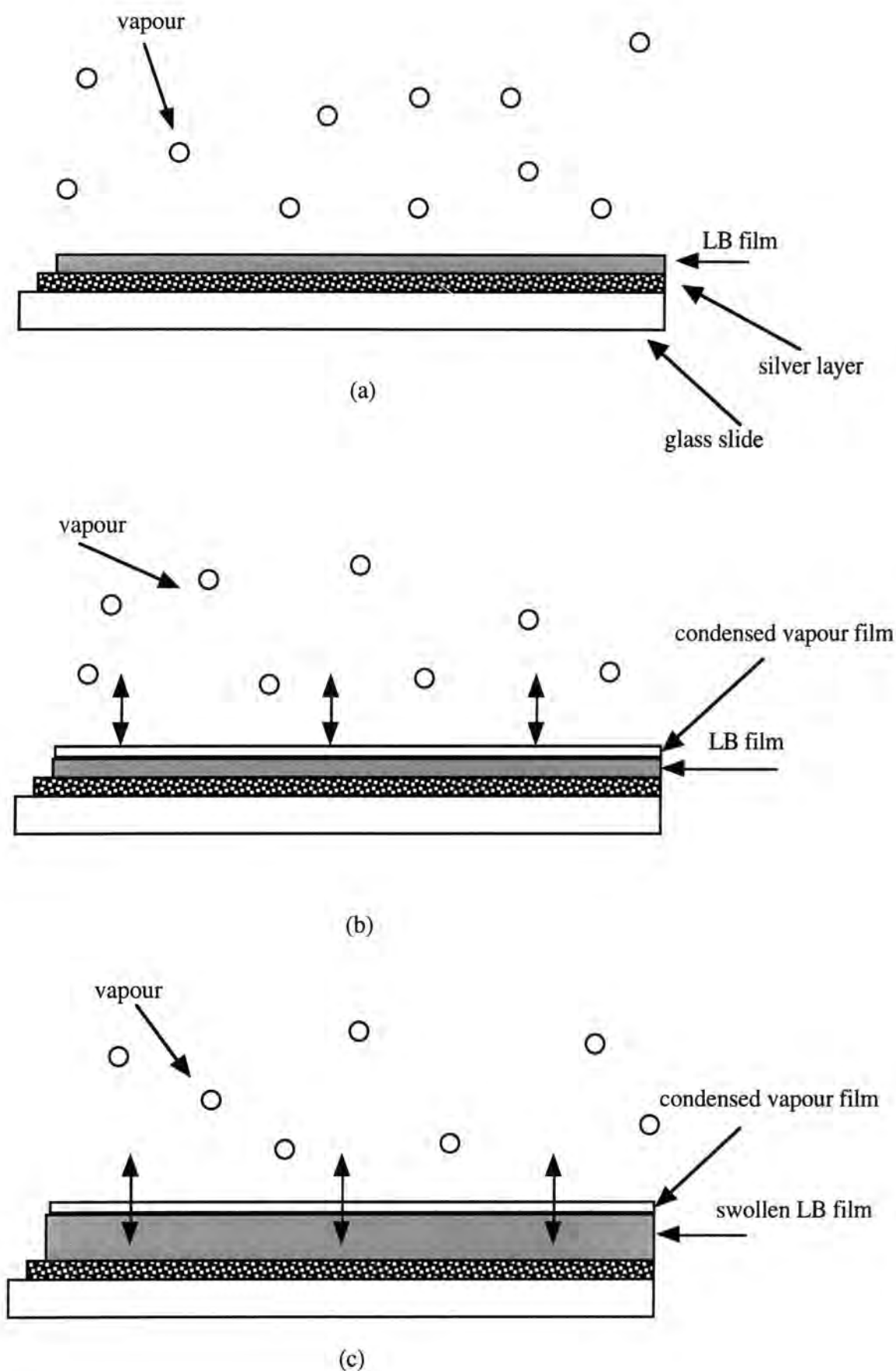


Figure 7.28: Schematic diagram illustrating the interaction between vapour molecules and LB layers: (a) LB layer before reaction; (b) adsorption of condensed vapour on the surface of the LB layer; and (c) diffusion of condensed vapour into the bulk of the LB film, causing swelling.

phthalocyanine (ZnPcBC), polysiloxane (AMCR23) and copper 5,5'-methylenebis (N-hexadecylsalicylideneamine) co-ordination polymer (poly(CuMBSH)) have been exposed to concentrations of benzene, toluene, ethanol and water vapour. Changes in the LB layers thickness were recorded, on exposure to vapours, using surface plasmon resonance.

The results indicate that 4 LB layers of poly(CuMBSH) were most reactive to all the vapours investigated. The response times were rapid (*ca* 60 seconds) with full recovery within 60 minutes. Poly(CuMBSH) showed a linear characteristics (over the range investigated) on exposure to increasing concentrations of vapours, with the response to benzene being the most reactive, then toluene, ethanol and finally water vapour. This was explained by it being easier for non-polar vapours to be absorbed into non-polar sensing layers.

The reaction process was explained as an initial absorption of vapour into vacant surface reaction sites. There is then some slower absorption of vapour into the bulk of the LB film, causing the film to swell, forcing the SPR curve to shift to higher angles and broaden (vapour dependent).

References

- 1 R.C. West, M.J. Astile, "CRC Handbook of Chemistry and Physics", *CRC Press Ltd-Florida*, 59, 1978, E-354 - E-355.
- 2 G.W. Bradberry, P.S. Vukusic, J.R. Sambles, *J. Chem. Phys.*, 98, 1, 1993, 651-653.
- 3 J.R. Sambles, J.D. Pollard, G.W. Bradberry, *Optics Communications*, 63, 5, 1987, 298-300.
- 4 R.C. West, M.J. Astile, "CRC Handbook of Chemistry and Physics", *CRC Press Ltd-Florida*, 59, 1978, E-63 - E-65.
- 5 C. Granito, J.N. Wilde, M.C. Petty, S. Houghton, P.J. Iredale, *Thin Solid Films*, 284-285, 1996, 98-101.
- 6 N. Kalita, J.P. Cresswell, M.C. Petty, A. McRoberts, D. Lacey. G. Gray, M.J. Goodwin, N. Carr, *Optical Materials*, 1, 1992, 259-265.
- 7 J.N. Wilde, M.C. Petty, A. Tempore, L. Valli, *Measurement and Control*, 30 (9), 1997, 269-273.

Chapter Eight

Results and Discussion: Pattern Recognition Techniques

8.0 Preface

This chapter presents data from experiments using a neural network to recognise different gases or vapours. Sensing elements fabricated from LB layers of polysiloxane, phthalocyanine and a co-ordination polymer were exposed to concentrations of NO_x , toluene, benzene and water vapour. These data were collected using a surface plasmon resonance system with a charge coupled device camera as detector. Images were captured and processed on computer. The results for benzene and water vapour were subsequently presented to a three layer neural network to be identified.

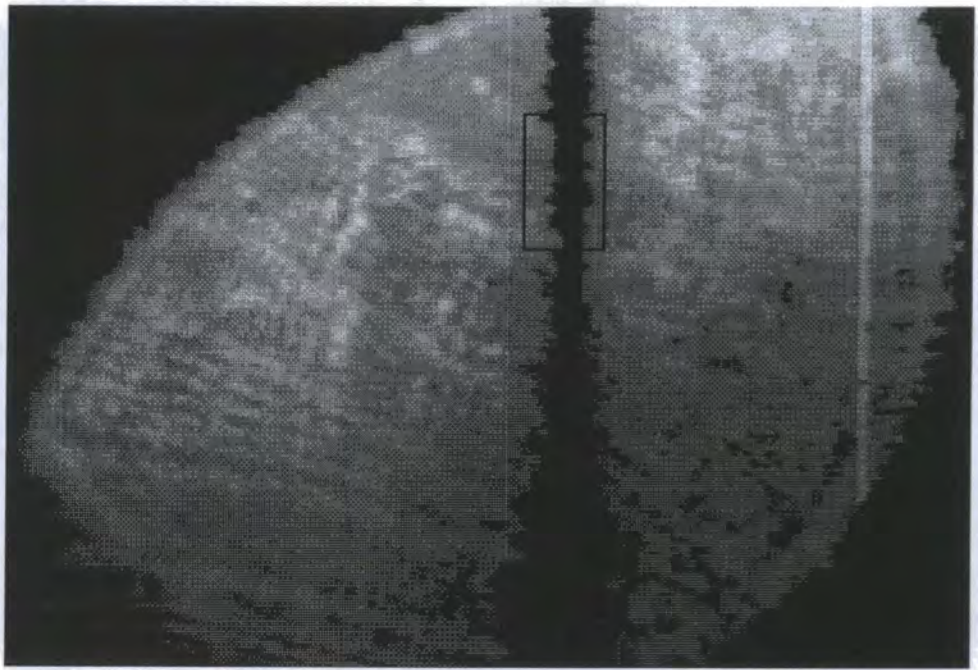
8.1 Zinc phthalocyanine exposed to NO_x

Layers of zinc substituted phthalocyanine (ZnPcBC) were deposited on silvered substrates using the Langmuir Blodgett (LB) technique.¹ These substrates were then mounted in a surface plasmon resonance (SPR) system where the detector was replaced by a charge coupled device (CCD) camera (the experimental design is detailed in Chapter Five). The samples were then exposed to 20 parts per million (ppm) NO_x and changes in the SPR profile were recorded by capturing images of the resonance point via the CCD camera.

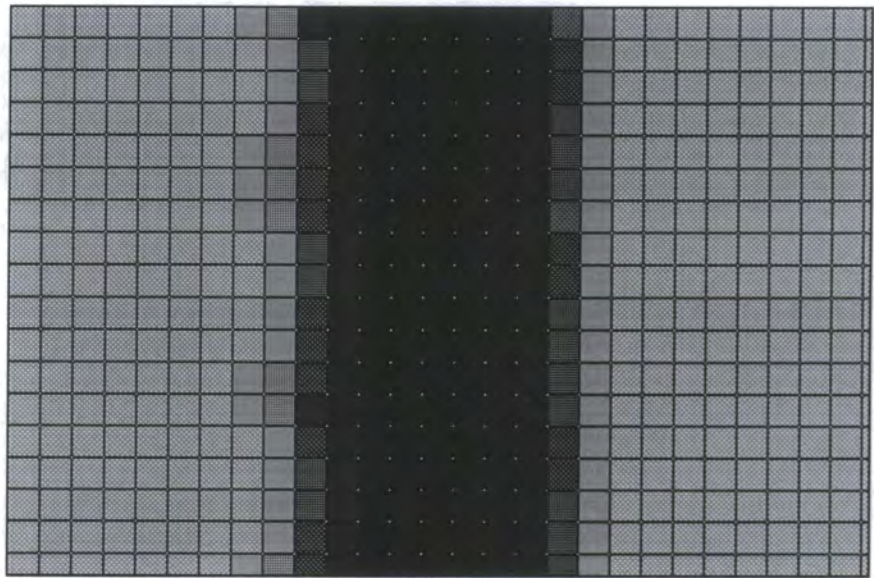
Figure 8.1 shows images (a) as captured by the CCD camera and those enhanced via image processing techniques on 'PC Image'. The image in figure 8.1 (a) shows the SPR point of ZnPcBC (indicated by the black line) and the box shows the region magnified to obtain figure 8.1 (b). The image in figure 8.1 (b) has been magnified 16 times to show the individual pixels and processed using brightness and contrast filters to accentuate any changes in the profile. In processing the picture some of the finer detail was lost. However, this was not significant enough to negate any results obtained.

As LB layers of ZnPcBC were exposed to NO_x , the shape and position of the SPR point should move depending on the interaction between the film and the ambient gas. Theoretical changes in the SPR profile are shown in Chapter Five, as the SPR profile moves to higher angles, broadens, narrows or becomes less defined (these changes are contrasted with those as seen by using a Si photodiode as detector).

Figure 8.2 shows the change in the SPR image for 1 LB layer ZnPcBC on exposure to 20 ppm NO_x and pure nitrogen. The individual pixels are evident in the CCD image of the as-deposited film following image processing (using contrast and brightness filters). The sample was first exposed to a flow of dry nitrogen at a rate of 600 cc min^{-1} , fig 8.2 (a). After 50 mins exposure, the SPR point (shown in figure 8.2 (b)) had shifted to higher angles by approximately 5 pixels and become less defined (loss of resonance). This effect was not reversible within the time scale of the experiment and was probably due to the removal of trapped water in the film (following LB deposition). The sample was then exposed to 20 ppm NO_x at the same flow rate. After 60 mins exposure (a large



(a)



(b)

Figure 8.1: SPR image of 1 LB layer zinc phthalocyanine (ZnPcBC) (a) as seen by the CCD camera (b) magnified image of the square in figure 8.1 (a).

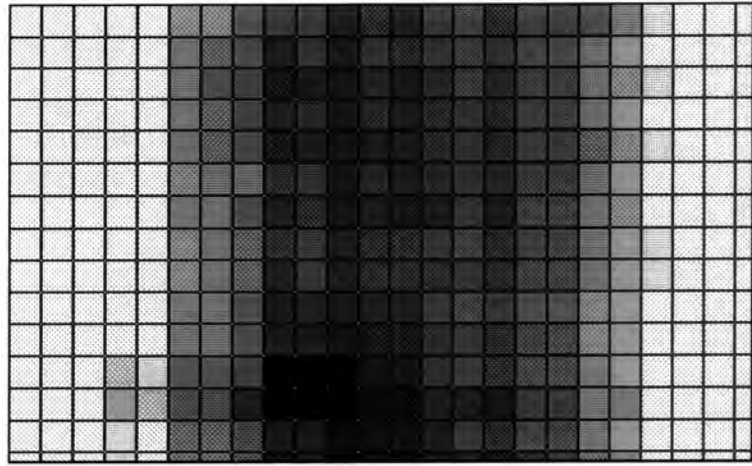
exposure time was chosen so that changes in the CCD image could be seen by the eye), the SPR image (shown in figure 8.2 (c)) had shifted by *ca* 10 pixels to the left and begun to narrow. After a further 60 mins under NO_x (shown in figure 8.2 (d)), the SPR image had become completely bright, due to the SPR point moving beyond the range of the sensor. Following 24 hours in dry nitrogen the SPR image partially recovered to its original position in angle (ie, before the introduction of NO_x). These effects were attributed to a reaction between the ZnPcBC film and the NO_x (reversible) and an oxidation reaction between the NO_x and the silver substrate (irreversible).²

These experiments confirm that the experimental setup, of an SPR system with a CCD camera as detector, can be used to follow dynamic changes in the SPR curve (ie, change in SPR position broadening/narrowing or loss of resonance). The system showed good sensitivity to NO_x and it was hoped that similar responses would be seen with aromatic hydrocarbons.

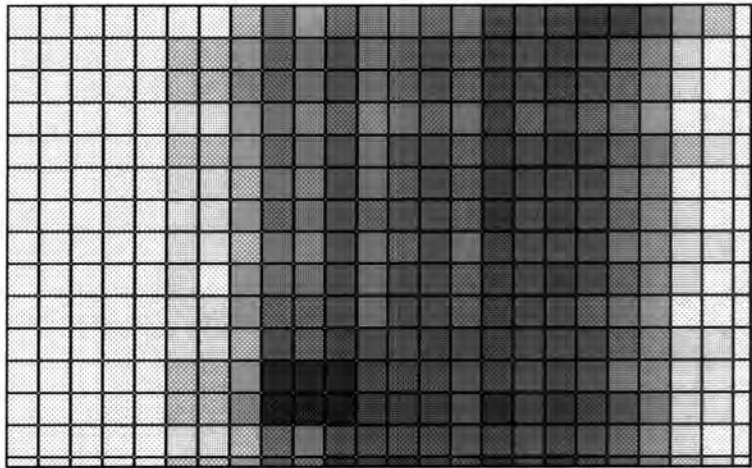
8.2 Polysiloxane exposed to toluene vapour

LB layers of a polysiloxane³ (AMCR22) were exposed to low concentrations of toluene vapour. During these experiments, extended exposure times were used to demonstrate this sensing method to the naked eye. As before, images were processed on computer via 'PC Image' using brightness and contrast techniques.

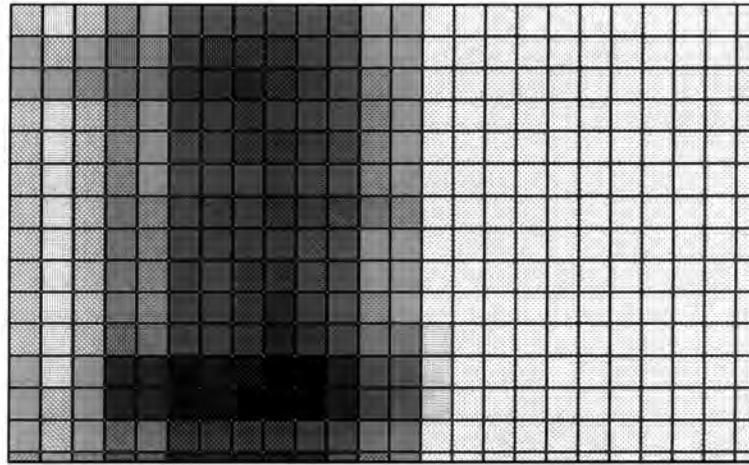
The images shown in figure 8.3 are for 1 LB layer AMCR22 exposed to 100 vpm toluene in a flow of pure nitrogen (100 cc min⁻¹). Figure 8.3 (a) was the initial image



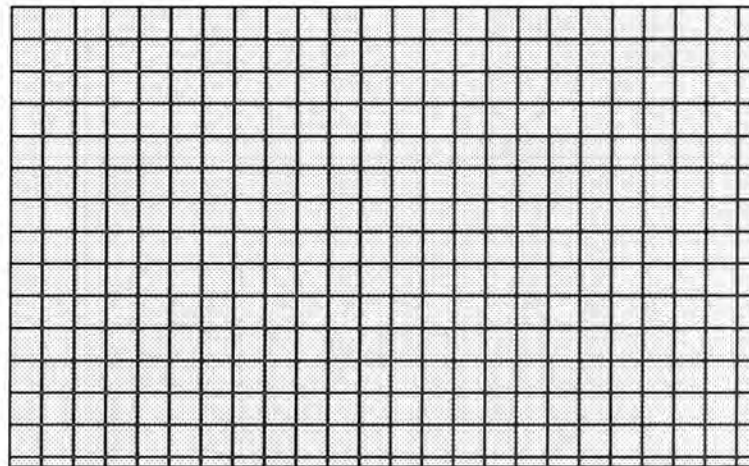
(a)



(b)



(c)

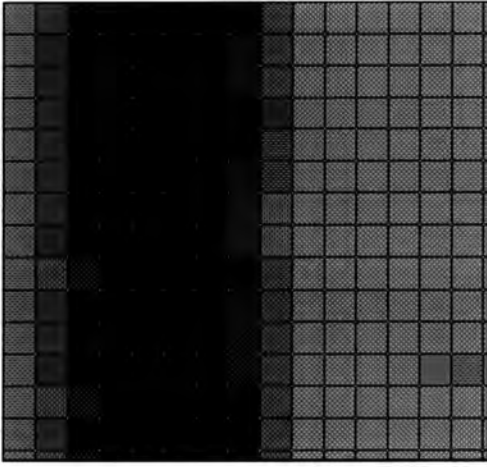


(d)

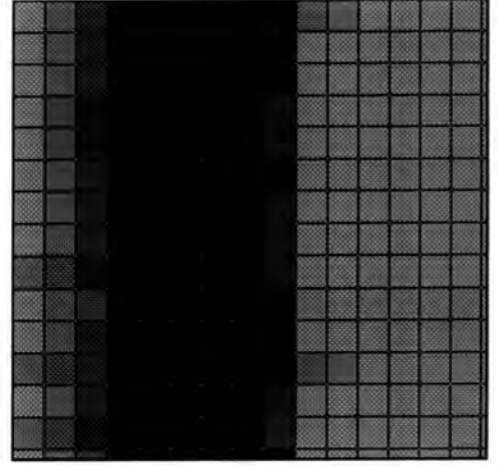
Figure 8.2: SPR images for 1 LB layer ZnPcBC exposed to oxides of nitrogen (a) initial picture (b) after 50 mins exposure to dry nitrogen (c) after 60 mins exposure to 20 ppm NO_x (d) after 120 mins exposure to 20 ppm NO_x .

before the introduction of nitrogen. Figure 8.3 (b) was captured after 20 mins exposure to nitrogen vapour. In this figure the SPR point has moved by one pixel to the right (ie higher angles). This was attributed, again, to the removal of excess water from the LB film. The sample was then exposed to 100 vpm toluene for 17 hours, shown in figure 8.3 (c). In this case, the SPR point has shifted one pixel to the right (*cf* with a 10 pixel shift to the left with NO_x and ZnPcBC) and had narrowed by one pixel. The shift of the SPR point to the right, for AMCR22 and toluene vapour was similar to those detailed in Chapter Seven, where the SPR curve moves to higher angles on the introduction of either toluene, benzene, ethanol or water vapour. Figure 8.3 (d) was captured after the sample had been exposed to air for 4 days, there was no observable shift in the SPR point to its original position (before the introduction of nitrogen vapour), though there was a narrowing in the SPR point.

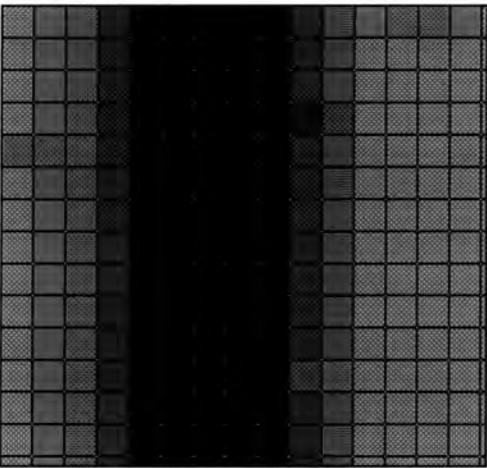
The exposure of toluene to 1 LB layer of AMCR22 showed that it was possible to detect even low concentrations of organic vapours using this technique. The only problem was the long exposure times needed to achieve changes observable by the naked eye. This process could be speeded up by the use of computer pattern recognition software which should be able to detect changes in one pixel by one grey scale. The 'Grey Scale' is a number assigned to a pixel that gives it a shade (or colour), this number for most computers varies between 0 and 255, where 0 is black and 255 is white.



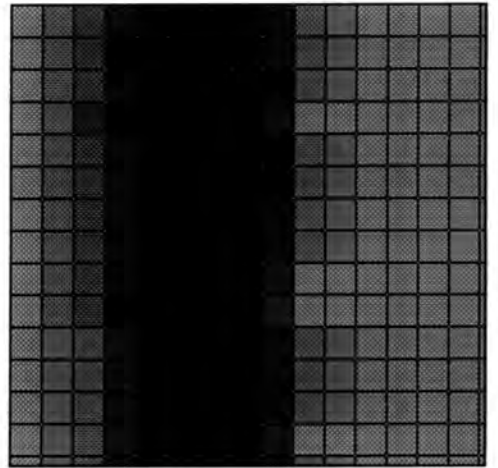
(a)



(b)



(c)



(d)

Figure 8.3: 1 LB layer AMCR 22 exposed to toluene vapour (a) initial picture, (b) after 20 mins exposure to dry nitrogen, (c) after 17 hours exposure to 100 vpm toluene vapour, (d) after 4 days exposure to air.

8.3 Poly(CuMBSH) exposed to benzene and water vapour using a neural network

LB layers of poly(CuMBSH) were exposed to benzene vapour, using the CCD camera SPR system since poly(CuMBSH) had been shown to give the largest change in SPR curve (see Chapter Seven). Images of the SPR point were captured via a CCD camera and stored on the computer. These data were then processed so they could be contained in one file (number of images over a period of time) and then presented to a trained neural network. Benzene and water vapour were used to test the neural network because of their chemical properties, composition and hopefully different reactions with poly(CuMBSH).

8.4 Design of neural network

A three layer neural network was chosen to process the images captured on computer. In most gas sensing systems multilayer feedforward networks are chosen, where each neuron in a layer is connected to every neuron in the next layer⁴ (shown in figure 8.4). There are a number of inputs, with their values corresponding to the 'Grey Scale' value of a cross section of pixels (a single line through the SPR point). These networks are based on a model where each neuron has a number of inputs (weighted sum of the input pixels) and only one output. The neural network was designed to learn using back-propagation (see Chapter Five). A three layer network was chosen to reduce the probability error, which increases as the number of data sets increase. The number of data sets (D) is given by

$$D = 2(m + n)h \quad [8.1]$$

where for a typical network D should be *ca* 100, m is the number of sensors, n is the number of classes (outputs) and h is the number of hidden layers. The network used in this chapter has 60 inputs (see section 8.4.2) and 2 output classes, thus to minimise the number of data sets the number of hidden layers was set to 1 (h). The output classes were set to be either benzene or water vapour.

8.4.2 Data capture and processing

Data were extracted from the images (shown in figure 8.5) using the linedraw facility on PC Image. This enabled the user to draw a straight line across the image n pixels long. The grey scale values of each pixel, with its corresponding x and y co-ordinates were then saved to a file. As for the initial work (with NO_x and toluene) each image was pre-processed using brightness and contrast techniques to enhance the SPR point. In this work, a line 10 pixels long was drawn and the data for each image were saved to an individual file.

The best method for compiling data was to take a representative sample from the whole gas sensing experiment. This was achieved by assuming the movement of the SPR point would be similar to those observed for poly(CuMBSH) and benzene shown in Chapter Seven. Data were then extracted at various intervals along a typical response characteristic, shown in figure 8.6. In this case it was assumed that the turn on and off characteristics were rapid (at about 90 seconds) with a steady state value reached in between. The computer was then programmed, via a macro facility on PC Image, to

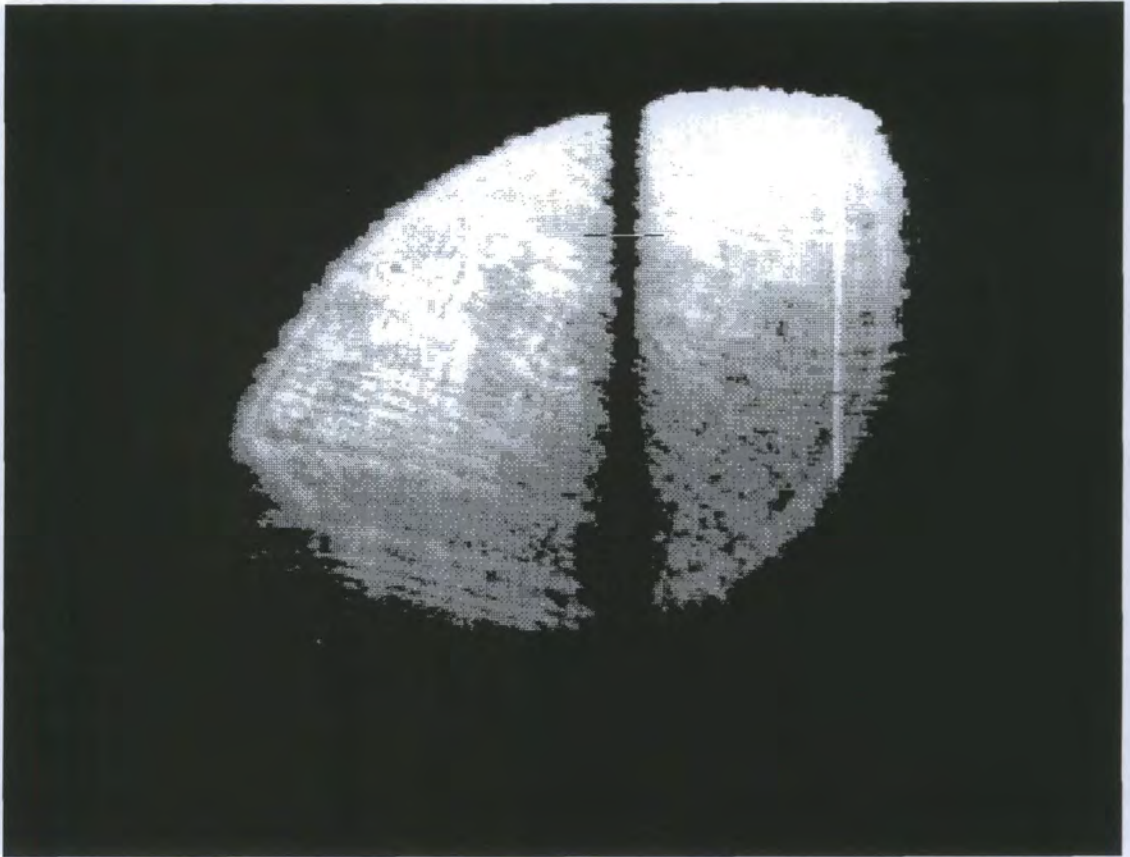


Figure 8.5: Picture of SPR image from 4 LB layers poly(CuMBSH). The line indicates the region of data presented to the neural network.

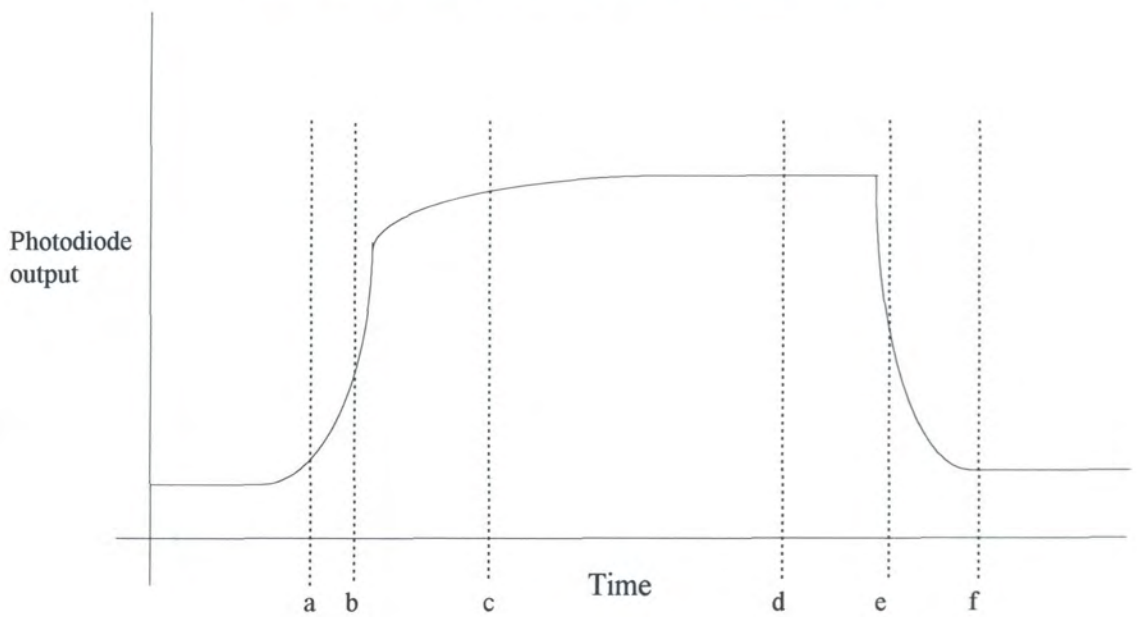


Figure 8.6: Idealised gas sensing trace with points (a) to (f) indicating the times at which data were captured and presented to the neural network.

capture images every 20 seconds, saving each image in a separate file. Each image was then pre-processed using the same contrast and brightness filters and a macro was written to extract data from the same 10 pixels on each image.

Figure 8.6 shows an idealised gas sensing trace (similar to those presented in Chapter Seven) with positions a to f representing the times at which the images were captured. The 6 measurements were chosen as a representation of the whole gas sensing trace. Once the data at each time (one image) had been processed into 10 numerical values they were all put into one file 60 data points long. The output of the system was simple to fix, this was either benzene or water vapour (the two vapours used). The output of the neural network then only had two possibilities, either 10 or 01 (benzene or water, binary format). The data file then had two extra values added to each exposure, indicating the vapour causing the reaction. A representation of this can be seen in table 8.1.

Input data sets from 6 regions selected in figure 8.7						Output data	
region (a)	region (b)	region (c)	region (d)	region (e)	region (f)	benz.	water
data 0-9	10-19	20-29	30-39	40-49	50-59	60	61

Table 8.1: Representation of how data is tabulated and presented to the neural network.

8.4.3 Testing the neural network

4 LB layers poly(CuMBSH) were exposed to 10000 vpm benzene and 40000 vpm water vapour, sequentially. Five Sets of training data for benzene vapour and five sets for

water vapour were presented to the neural network to allow it to train, and then new data were presented to it.

Desired output		Actual output			Output error	
Benzene vapour	Water vapour	Benzene present	Water present		Benzene error	Water error
1	0	0.0587	0.9736		0.9413	-0.9736
1	0	1	0		0	0
1	0	0.9005	0.0513		0.0995	-0.0513
1	0	0.8906	0.0632		0.1094	-0.0632
1	0	0.2368	0.6870		0.7163	-0.6871
0	1	0.1238	0.8771		-0.1237	0.1229
0	1	0.1243	0.8753		-0.1247	0.1247
0	1	0.1191	0.8870		-0.1191	0.1130
0	1	0.1081	0.8941		-0.1081	0.1059
1	0	0.4154	0.5905		0.5845	-0.5906
1	0	0.8289	0.1342		0.1710	-0.1342
1	0	0.0348	0.9841		0.9652	-0.9841

Table 8.2: Output of three layer neural network for data collected from 4 LB layers poly(CuMBSH) exposed to 10000 vpm benzene and 40000 vpm water vapour.

For this test, poly(CuMBSH) was exposed to benzene vapour eight times and water vapour five times. For each exposure, a new film was used. A new data file was created with the first five sets being benzene vapour, the next four being water vapour and the final three sets being benzene. The results of this experiment can be seen in table 8.2. The first two columns are for the desired output values (ie, first 5 benzene vapour, output 10, next 4 water vapour, output 01, last 3 benzene vapour, output 10). The next two columns are the actual output of the neural network, in response to the unseen data. The final two columns show the difference between the two sets of outputs.

It is usual for testing networks to take a threshold value, numbers above this can be rounded up to 1. In the case of this network it was decided that the threshold should be 0.8 (an arbitrary figure). Out of the 12 unseen data sets presented to the network it recognised 8, giving a recognition percentage of 66.7 %. Though this percentage is not high (one would expect over 90 % for a good network), it is above 50 %, indicating that the network shows signs of recognition. There are a number of reasons for the poor recognition. First, the number of training sets could have been too low, in this case only ten were used. Too few sets results in a network that cannot recognise data, yet too many training sets results in a network that is unable to interpret unseen data. Second, the data presented could have been almost random in pattern (rise and fall times and saturation levels) thus the network was unable to classify. This reason is almost certainly incorrect since the network is able to recognise water vapour with a good degree of accuracy.

Out of the two vapours used it is interesting to note that the network recognised 100 % of the water vapour data, whilst the non-recognised data was always benzene vapour. One possible explanation for this could be the difference in concentrations used. Higher water vapour concentrations may produce a more repeatable response, whilst the low benzene concentrations (the maximum that could be generated was used) may produce some spread in response characteristics (ie, response times and saturation value).

8.5 Summary

LB layers of phthalocyanine, polysiloxane and poly(CuMBSH) have been used to test a new system using surface plasmon resonance, with data collected via a charge coupled device camera. This allowed constant monitoring of the SPR image during exposure to NO_x , toluene and benzene vapours. SPR images were captured and stored on computer at regular intervals during exposure to gases or vapours.

On the exposure of zinc phthalocyanine (ZnPcBC) to NO_x , the SPR point started to move to lower angles and the SPR profile began to narrow. The changes in the image were dramatic, though this was due to the high vapour concentration (20 ppm) and long exposure times (60 mins). These data demonstrated that the system using a CCD camera was able to show changes in the SPR profile of a material on exposure to a gas, forming the basis of a sensing system. LB layers of polysiloxane (AMCR22) were then exposed to low concentrations of toluene vapour. This was to determine if the system could detect small changes in the SPR profile due to aromatic hydrocarbon vapours. An experiment was designed so that changes in the SPR image were observable to the

naked eye. However, the response of this experiment was disappointing, with exposure times of 17 hours and little observable recovery in 4 days. The magnitude of response were also small, with a maximum shift in the SPR profile of *ca* 2 pixels (*cf* 10 pixels for NO_x and ZnPcBC). Again, this experiment proved that the system was viable though reactions were difficult to see with the naked eye.

The final experiment used a co-ordination polymer (poly(CuMBSH)) exposed to benzene and water vapour (10000 and 40000 vpm, respectively). In this case reactions were not observable to the naked eye, but passed to a neural network to analyse. The network successfully trained the data and then was tested with 12 different exposures (4 water and 8 benzene), of which it recognised 66.7 % of the new data. Though this recognition percentage is not high it shows that the network was able to distinguish between the two vapours.

This experimental setup forms the basis of a sensing system, with a reactive sensing layer of poly(CuMBSH) and some built in recognition via a neural network. The use of a CCD camera in the SPR system provides more information than normally accessible with a Si photodiode. It especially provided detail about changes in the SPR profile on exposure to certain gases or vapours.

References

- 1 J.N. Wilde, M.C. Petty, J. Saffell, A. Tempore, L. Valli, *Measurement and Control*, 30, **1997**, 269-272.
- 2 G.J. Ashwell, M.P.S. Roberts, *Electronics Letters*, 32 (22), **1996**, 2089-2091.
- 3 N. Kalita, J.P. Cresswell, M.C. Petty, A. McRoberts, D. Lacey, G. Gray, M.J. Goodwin, N. Carr, *Optical Materials*, 1, **1992**, 259-265.
- 4 M.H. Hassoun, "**Fundamentals of Artificial Neural Networks**", *MIT press-London*, **1995**, 197-199.

Chapter Nine

Conclusions and Suggestions for Future Work

9.1 Conclusions

The combination of the technique of surface plasmon resonance (SPR) and thin organic films has produced a relatively successful gas sensor. Two experimental SPR designs were used. In the first, a silicon photodiode was used to record the intensity of the reflected light. The second captured images of the illuminated area of the LB film via a charge coupled device (CCD) camera. This provided more information on the changes in the resonance on exposure to a vapour. The latter system was successfully used in conjunction with a neural network to discriminate between benzene and water vapour. Though the system was able to discriminate between benzene and water vapour, the results were inconclusive (a recognition rate of *ca* 66 %) and large vapour concentrations were needed (10000 vpm benzene and 40000 vpm water). In this work, only a small number of data sets were presented to the neural network (8 sets of benzene vapour and 5 sets of water vapour). Further work needs to be done with larger data sets to obtain a true statistical picture (and thus improve the recognition rate).

Four different materials: a co-ordination polymer Cu 5,5'-methylenbis (N-hexadecylsalicylsalicylideneamine) (poly(CuMBSH)); two tetrasubstituted phthalocyanines, copper tetrakis-(3,3-dimethyl-1-butoxycarbonyl) phthalocyanine (CuPcBC); zinc tetrakis-(3,3-dimethyl-1-butoxycarbonyl) phthalocyanine (ZnPcBC);

and the polysiloxane AMCR23 were exposed to four different vapours and their responses analysed.

The physical, chemical and Langmuir forming properties of the reacted co-ordination polymer (poly(CuMBSH)) and its unreacted monomer (MBSH) were investigated in great detail. The studies reveal that through the polymerisation reaction a change in the orientation of the molecule at the air/water interface and on the substrate occur. Two possible orientations for the monomer have been presented whilst the reacted polymer was assumed to be orientated so the copper atoms within the film were angled at 30° to the substrate surface, adopting a 'zig-zag' conformation.

Poly(CuMBSH), CuPcBC, ZnPcBC and AMCR23 were individually mounted in the SPR system using a silicon photodiode and exposed to concentrations of benzene (100 to 10000 vpm), toluene (100 to 3000 vpm), ethanol (700 to 17000 vpm) and water vapour (700 to 40000 vpm). The results indicated that poly(CuMBSH) was the most sensitive and could detect concentrations of benzene vapour down to 100 vpm. LB layers of poly(CuMBSH) were the most stable, with little degradation in response for samples continually exposed over a period of 30 days. The response times of each vapour were similar, with turn on and off times of *ca* 60 seconds and full recovery achieved within *ca* 60 minutes.

The vapour sensing results indicated that the dipole moment of the vapour and LB layer played a large part in the reaction mechanism. It is easier for vapours to be absorbed

into LB films of similar polarity (ie, non-polar vapour and non-polar LB films). On exposure, the change in the SPR curve was attributed to swelling of the LB film. This effect was most noticeable with poly(CuMBSH) (relatively non-polar) and benzene vapour (non-polar), whilst reactions with polar vapours (such as water) were substantially smaller. The dipole moments of CuPcBC, ZnPcBC and AMCR23 were all substantially greater than poly(CuMBSH). As a result, these materials were not as responsive to benzene. The results obtained for these materials give an indication of the reaction mechanism, though this process needs to be investigated in greater detail.

Though the materials were responsive to each vapour, the magnitude of response in some cases was small. This problem was accentuated by the noise generated in the sensing equipment. The noise was attributed to fluctuations in the intensity of the laser beam, small changes in the concentration of vapour generated and the electrical connections. One way to improve the sensitivity of the system would be to eliminate (or reduce) this problem.

9.2 Suggestions for further work

The fundamental results presented in this work show that organic films and SPR can be used as a vapour sensor. The cross-sensitivity to several vapours (including water) and the slow recovery times are a problem to be overcome to create a practical device.

The vapour sensing mechanism of poly(CuMBSH) has been examined in detail yet the true nature of the interaction between the vapour and the LB film is still unknown.

Experiments could be undertaken to determine how the SPR curve of an LB layer changes on exposure to a vapour. This could be done by recording the full SPR curve at various times after exposure (this technique was tried in this thesis but the results were inconclusive).

To discriminate between different vapours it is necessary to obtain some extra information from the gas sensing data. In human olfactory systems research has suggested that the 'smelling' process is a two stage system.^{1,2} The initial response is due to molecules fitting into one of a number of receptors (ie, lock and key). The second is due to an electrical impulse passed across the molecule and the resulting atomic vibrations analysed. A combination of the two signals are passed to the brain which interprets them. Further work could perhaps concentrate on the design of a hybrid gas sensing system, comprising both optical and conductivity measurements. The initial absorption of the vapour could be monitored by SPR and the adsorption of the vapour monitored by changes in conductivity. The combination of these data could then be passed to a neural network for analysis.

The processing of data by a neural network (in this work) was performed off-line (ie, data were recorded, processed and presented to the network at a later date). This technique is not acceptable for a commercial sensing system, as the data has to be processed in real time. Some work needs to be done on designing a computer program capable of capturing the image from the CCD camera; processing the data into a form acceptable by the neural network; a trained neural network to analyse the sensing data.

References

- 1 R.H. Wright, "**The Sense of Smell**", *CRC Press Inc.*, Florida, **1982**, 19-23.
- 2 L. Turin, *Chemical Senses*, 21 (6), **1996**, 773-791.

Appendix A

Computer Programs

The computer program used in this work was written in Turbo Pascal. The software was used for acquiring storing and displaying the gas sensing data.

```

{FILE NAME : SENSE.PAS }
{
{Purpose      : This program takes readings from a DVM every n seconds }
{              (n - user defined) saves the data to disk and displays the data }
{              on screen. }
{Language    : Turbo Pascal }
{
{Author      : J.N. Wilde }

{The routine checks that the DVM is connected and operational. }

```

Program data_read_and_display;

uses gpib, Crt, dos, graph;

var

ioerr,dvm1,points,aver1,j : integer;

graphdriver, graphmode,x : integer;

impdata,scale_point : real;

instr1,cmdstr : lstring;

data : lstring;

impdata_string : string;

procedure iochk; { I/O error check routine }

begin

case ioerr of

0 : ;

1 : writeln("TIME OUT !!");

else

writeln("INTERFACE ERROR !!");

end;

end; { End of iochk }

{This routine reads data from the DVM}

procedure read_data;

var t,code : integer;

```

begin
    ioerr :=iesend(cmdstr);
    instr1:=          ';
    ioerr:=ieenter(dvml,instr1);
    iochk;
    data:=instr1;
    data:=copy(data,6,7);
    val(data,impdata,code);
    str (impdata,impdata_string);
end;

```

**{This routine sets the size of the display and divides the number of x and y ticks }
{so that they will fit on the screen, or series of screens }**

```

procedure set_page;
var
    a,b,x_ticks,data_point,x_label,x_labelo      : integer;
    y_ticks                                       : real;
    x_string,y_string,x_stringo                  : string;

```

```

begin
    setviewport (0,0,getmaxx,getmaxy,clipon);
    settxtstyle (defaultfont,horizdir,1);
    settxtjustify (centertext,centertext);
    moveto (25,10);
    lineto (25,310);
    lineto (625,310);
    a:=1;
    for a :=1 to 6 do
        begin
            x_ticks := a * 100;
            moveto(x_ticks+25,313);
            lineto(x_ticks+25,307);
            x_label := x_ticks+(600*(j-1));

```

```

        x_label:= 0+(600*(j-1));
        str (x_label,x_string);
        str (x_label,x_stringo);
        outtextxy (25,320,x_stringo);
        outtextxy (x_ticks+20,320,x_string);
    end;
b:=1;
for b :=1 to 5 do
    begin
        y_ticks := getmaxx;
        str (y_ticks,y_string);
        moveto (25,310-(75*b));
        lineto (28,310-(75*b));
        outtextxy(15,160,'0');
        outtextxy(15,10,'25');
        outtextxy(11,310,'-25');
    end;
end;

```

**{The routine maps the data values onto the screen. The first value is mapped to 0 }
{the rest of the points are mapped relative to this. }**

```

procedure display_data;
var
    x_point,y_offset,y_point          : longint;
    y                                  : real;
    points_string                      : string;

begin
    x_point := x + 25;
    y:=(scale_point-impdata)*1000;
    str(y,points_string);
    y_offset:=trunc(y);
    y_point:=(y_offset*6)+160;
    putpixel(x_point,y_point,15);

```

```

    outtextxy(240,460,'Hit any key to stop reading');
    outtextxy(425,460,' data from the DVM.');
```

end;

{*****Main Program*****}

```

var
    i,s,loop,r,d           : integer;
    inpdel,del            : real;
    f                     : text;
    c                     : char;
    fullname,filename,start_point : string;
    hour,minute,second,sec100 : word;
    g,rescale             : real;

begin
    clrscr;
    ioerr:=ieabort;
    dvm1:=24;
    writeln('Enter the integer value for the required frequency of readings,');
    write('[ in seconds] :- ');
        readln(inpdel);
    writeln;
    write('Enter the number of data points to be sampled :- ');
        readln(points);
    writeln;
    writeln('Enter Filename to be saved under (without extension)....');
        readln(filename);
        fullname :='C:\pascal\data\' +filename+ '.dat';
        assign(f,fullname);
        rewrite(f);
```

{ Set the DVM's }

```
cmdstr:='DCL';  
ioerr:=ieoutput(dvm1,cmdstr);           { Clear device to turn-on state }  
iochk;                                   { Error check                       }  
cmdstr:='F1T2R2N1S';  
ioerr:=ieoutput(dvm1,cmdstr);           { Send DVM #1 setting string      }  
iochk;                                   { Error check                       }
```

{ Measurement start }

```
cmdstr:='UNL UNT MTA LISTEN 24 GET';  
gettime(hour,minute,second,sec100);  
writeln('Start time = ',hour,':',minute,':',second);  
graphdriver := detect;  
initgraph(graphdriver, graphmode, '');
```

{ Read in first data point initially }

```
aver1:=1;  
x:=0;  
j:=1;  
read_data;  
append(f);  
writeln(f,impdata);  
close(f);  
set_page;  
start_point:= data;  
scale_point := impdata;  
display_data;  
aver1:=2;
```

{ Read rest of data points with delay }

```
repeat
  d:=1;
  repeat
    delay(4880);
    d:=d+1;
  until d > inpdel;

  read_data;
  append(f);
  writeln(f,impdata);
  close(f);
  display_data;
  aver1:=aver1+1;
  x:=x+1;
  rescale := aver1/(600*j);

  if rescale > 1 then
    begin
      clearviewport;
      x:=0;
      j:=j+1;
      set_page;
    end;

until (aver1 > points) or (keypressed);

closegraph;
writeln;
gettime(hour,minute,second,sec100);
writeln('End time = ',hour,':',minute,':',second);
writeln(aver1 - 1, ' data points collected');
writeln;
writeln('Start voltage: -', start_point, ' V');
```

```
writeln;  
writeln('The data has been saved in ',filename,'.dat');  
end.
```

{ End of Program }

Appendix B

Publications

“Toluene vapour sensing using copper and nickel phthalocyanine Langmuir-Blodgett films”, C. Granito, J.N. Wilde, M.C. Petty, S. Houghton, P.J. Iredale, *Thin Solid Films*, 284-285, **1996**, 98-101.

“Surface plasmon resonance imaging for gas sensing”, J.N. Wilde, M.C. Petty, A. Tempore, L. Valli, *Measurement and Control*, 30 (9), **1997**, 269-273.

“Optical sensing of aromatic hydrocarbons using Langmuir-Blodgett films of a Schiff base co-ordination polymer”, J.N. Wilde, J. Nagel, M.C. Petty, *Thin Solid Films*, in press.

“Structural and optical properties of Langmuir-Blodgett films of a schiff base co-ordination polymer: a material for hydrocarbon vapour sensing”, J.N. Wilde, A.J. Wigman, J. Nagel, A. Beeby, B. Tanner, M.C. Petty, *Acta. Polymer.*, 49, **1998**, 294-300

“Molecular orientation in Langmuir-Blodgett films of schiff base co-ordination polymers as studied by electron spin resonance”, L.M. Goldenberg, J.N. Wilde, V.I. Krinichnyi, J. Nagel, M.C. Petty, in preparation.

“Deposition and characterisation of Langmuir-Blodgett films of an azo-modified polypeptide: azobenzene containing poly-l-lysine”, C. Tedeschi, M.P. Fontana, O. Pieroni, L. Dei, J.N. Wilde, C. Pearson, M.C. Petty, B. K. Tanner, *Submitted to Langmuir*.

